Development of Solid Electrolyte and Reference Materials for Designing Sensor for Measuring Magnesium in Non-Ferrous Alloys

Mohammed Alhaji ADAMU

School of Chemical and Process Engineering
University of Leeds

Submitted in accordance with the requirements for the degree of
Doctor of Philosophy

March 2018

Declaration

The candidate confirms that the work submitted is his own, except where work which has formed part of jointly authored publications has been included. The contribution of the candidate and the other authors to this work has been explicitly indicated below. The candidate confirms that appropriate credit has been given within the thesis where reference has been made to the work of others.

All the results presented in this research were obtained and analysed by the author of the thesis except for the following contributions; Dr Girish M Kale - offered technical advice and editing of manuscripts, including technical content and thesis structure.

1. M Adamu and GM Kale. *Novel Sol-Gel Synthesis of* $MgZr_4P_6O_{24}$ *Composite Solid Electrolyte and Newer Insight into the* Mg^{2+}*-Ion Conducting Properties Using Impedance Spectroscopy. Journal of Physical Chemistry C, 2016,* ***120,*** *17909-17915.*

This copy has been supplied on the understanding that it is copyright[1] material and that no quotation from the thesis may be published without proper acknowledgment.

Assertion of moral rights:

The right of Mohammed Alhaji Adamu to be identified as Author of this work has been asserted by him in accordance with the Copyright, Designs and Patents Act 1988.

Acknowledgments

First and foremost, I would like to extend my deepest gratitude to Dr Girish M Kale, for his endless guidance and support through this project. Your insight and numerous anecdotes made the entire process enjoyable, thank you for the thorough supervision.

I am profoundly indebted to Professor Gin Jose for his willingness to share knowledge, and for ensuring l was properly guided during my first year transfer viva as head of the transfer assessment panel; "The small details of yesterday, crystallised into this joyful ending." I would also like to thank the technical staff in the School of Chemical and Process Engineering for all the help and support rendered throughout my time at the University of Leeds. To LEMAS, John Harrington, Stuart Micklethwaite and Dr Zabeada Aslam for the hands-on help with Electron microscopy (SEM and HR-TEM). Mohammed Javed for the help with Thermal analysis (TGA-DSC). Simon Lloyd for the help with X-ray fluorescence (XRF) and Atomic absorption spectroscopy (AAS). To XRD suite, Dr Tim Comyn, Dr Faye Esat and Dr Jennifer Forrester for the help and training with X-ray diffraction, High-temperature X-ray diffraction and Rietveld refinement. Dr Eric Kumi Barimah for the hands-on help with Laser-Raman scattering and FTIR spectroscopy. Diane Cochrane, Robert Simpson and Ed Woodhouse for the assistance and training, especially with occupational health and safety related issues.

I would also like to thank colleagues in my research group and friends at the University of Leeds, for sharing research experience and for making my time in Leeds thoroughly fulfilling. In no particular order; Dr Farooq Abubakar Atiku for your friendship and technical know-how; My laboratory and research colleagues of the Dr Girish M Kale team for all the valuable research discussions, dynamism, consumables exchanged and collaborations; Dr Gardy Jabbar for your availability; Dr Steven Mudenda for all the valuable time you committed to discussing solid-state chemistry and electroceramics.

To every other person whom our path has crossed, and every office mate whom I have shared a laugh with; Dr Terence Makanyire for the interest in my research progression.

I reserve particular appreciation to the National Zakat Foundation, United Kingdom who provided useful assistance and understanding when l needed it most. The benefit of Zakat to the society is huge and meaningful to all and sundry. Jazak Allah Khair!

I would like to thank the Tertiary Education Trust Fund, TETFund for providing me with the AST&D scholarship for this research. The fund served the purpose for which it was provided and disbursed. I will remain graciously appreciative of the fund.

Finally and most importantly, I would like to reserve a heartfelt eternal appreciation for my wife and lovely daughters for the patience, perseverance and endurance they displayed at every stage of this project and the many travels for academic conferences, writing up, research meetings and viva-voce examination, it attracted. You beautiful three gave me so much hope, assurance, belief and a glimpse into the future, and, am encouraged by the insistence that a bright future is certain. To my parents, brothers, sisters and the global family, your encouragement and support is always appreciated. To Allah (subḥānahu wata ‘ālā وَتَعَالَى سُبْحَانَهُ); The Most Compassionate The Most Merciful, for His wisdom of life and procreations, livelihood, guidance, protection and provision of knowledge towards this lofty achievements. “I bear witness that there is nothing worthy of worship except Allah (subḥānahu wata ‘ālā وَتَعَالَى سُبْحَانَهُ) and l bear witness that Muhammad (ṣallā llāhu ‘alayhi wa-sallam و سلم آله وعلى عليه الله صلى) is the Rasul and Special Messenger of Allah (subḥānahu wata ‘ālā وَتَعَالَى سُبْحَانَهُ).”

* * * ®

Dedication

For Aamanee & Nabeela

Abstract

Novel solid-state electrolytes, $MgZr_4P_6O_{24}$, $MgHf_4P_6O_{24}$, $MgCe_4P_6O_{24}$ and their solid-state solutions were synthesised using a modified sol-gel chemical procedure. Xerogel of this chemical synthesis was subjected to thermal analysis for possible calcination temperature and high-temperature X-ray diffraction to determine transformation point with temperature. Based on the TGA-DSC analysis, the dried xerogel powders were calcined at 800 and 900°C, yielding a pure single phase homogeneous nanopowders with an average crystallite size. Pellets of 13mm diameter (Ø) and 3.8mm thickness were prepared and sintered at various temperatures in the range, $1000 \leq T/^{o}C \leq 1550$. However, 1300°C was adopted as the sintering temperature haven achieved optimum density and stable sample composition at that temperature. XRF, FTIR, Laser-Raman scattering, and HR-TEM are some other characterisation techniques deployed for the structural analysis of these ceramic materials.

$MgHf_4P_6O_{24}$ and $MgCe_4P_6O_{24}$ solid-state electrolytes were synthesised for the novelty and characterised for their electrical and thermodynamic properties. The conductivity and thermodynamic data of the novel solid-state electrolytes, compared with those of $MgZr_4P_6O_{24}$ electrolyte, shows some improvement in the trend of ionic conductivity.

Sintered pellets of the end-members electrolytes and their corresponding solid-state solutions were characterised for their electrical properties and thermodynamics studies using the electrochemical method. The ionic conductivity of the end-members solid-state electrolytes identified $MgZr_4P_6O_{24}$ as most conductive, with bulk conductivity, $\sigma_{bulk} = 7.23 \times 10^{-3}$ Scm^{-1} at 998K followed by $MgCe_4P_6O_{24}$ with $\sigma_{bulk} = 2.14 \times 10^{-3}$ Scm^{-1} at 1017K and then, $MgHf_4P_6O_{24}$ with $\sigma_{bulk} = 4.52 \times 10^{-4}$ Scm^{-1} at 1020K in this order. In terms of ionic mobility, $MgCe_4P_6O_{24}$ solid-state electrolyte with activation energy, $E_a = 0.52 \pm 0.04$eV has shown the highest mobility, followed by $MgHf_4P_6O_{24}$ with $E_a = 0.74 \pm 0.02$eV and $MgZr_4P_6O_{24}$ with $E_a = 0.84 \pm 0.04$eV, respectively.

Therefore, the end-members solid-state electrolytes depict different ionic conductivity and activation energies but have shown chemical stability at 1300°C. The solid-state solutions further shows a unique trend which depicts that ionic conductivity increases with increasing concentration. This research interest however shows that conductivity decreases at two different concentrations, with chemical mole ratio (x) each, that is, it decreases at $x = 0.5$ and $x = 0.8$ for Hf-doped solid-state solution, while for Ce-doped solid-state solution, it decreases at $x = 0.3$ and $x = 0.6$, respectively. It has shown that the rate of conductivity varies for the two doped samples at different temperatures.

Based on available ionic conductivity data, stability of the end-members electrolytes in molten Al, OFHC-molten Cu, Cu-0.5 wt.% Mg and Al-Mg alloy, a biphasic powder mixture of the $MgCr_2O_4$+Cr_2O_3 reference electrode, Mg-sensors were fabricated and tested successfully in molten non-ferrous alloy. A linear dependence of sensor emf on logarithm of Mg concentration ($\log X_{Mg}$) showing that sensor emf increases as Mg concentration increases in the molten Al-Mg alloy at 700±5°C, which complies with the Nernst equation. The Mg-sensor fabricated with $MgZr_4P_6O_{24}$ solid-state electrolyte shows an increase in the sensor emf of about 0.2V, $MgHf_4P_6O_{24}$ based Mg-sensor shows sensor emf of 0.12V as Mg concentration increases and, for $MgCe_4P_6O_{24}$, the sensor emf increased to 0.48V.

In terms of sensor evaluation and performance, sensor testing characteristics such as response and recovery time were determined; Mg-sensor fabricated with $MgHf_4P_6O_{24}$ solid-state electrolyte, shows fast response of the sensor by adding 0.005-1.5 wt.% Mg indicating the Mg-sensor reached a stable emf of 1.92V in about 0.5h, the emf reading equilibrates at this emf for a further 0.5h, the sensor emf then increased by 30mV after the measurand (Mg-rod wrapped in Al-foil) was increased by 0.05 wt.% Mg. After further equilibration for 0.5h, a stable emf of 1.95V was achieved. Subsequently, with additional 0.5 wt.% Mg, the sensor emf increased to about 2.1V which is an increase of about 150mV. The solid-state Mg-sensor then returned to zero after the measurand was discontinued, which indicates that the Mg-sensor has a robust recovery time. For $MgCe_4P_6O_{24}$ Mg-sensor with a measurand ranging 0.005-1.0 wt.% Mg, the Mg-sensor reached a stable emf of 1.5V after the initial 0.005 wt.% Mg was added. The sensor emf further increased to 1.75V and then 2.25V after Mg concentration was increased to 1.0 wt.% at an interval of 250mV after each stage of Mg addition. However, for the $MgZr_4P_6O_{24}$ Mg-sensor with a measurand of 0.005-1.5 wt.% Mg concentration range, a sensor emf of 2.03V was achieved after 0.005 wt.% Mg sample wrapped in Al-foil was inserted. This insertion was done after a long Al-baseline calibration of molten Al was possible for 2.02h. The sensor emf of 2.07V, an increase of 40mV was achieved after the measurand was increased by 0.05 wt.% Mg at an equilibration time of 2.25h. Further equilibration was allowed before 0.5 wt.% Mg was inserted, this then resulted in a sensor emf increase to 2.09V, an increase of 20mV. The addition of 1.0 wt.% Mg and 1.5 wt.% Mg at separate equilibration intervals resulted in an increase of the sensor emf to 2.15V and 2.21V, a sustained increment of 60mV, respectively. As expected, the Mg-sensor then returned to zero after the measurand was removed showing a good Mg-sensor recovery time.

Thermodynamic activity of Mg in molten Al from the Gibbs energy of formation, ΔG_f^o of $MgCr_2O_4$ and MgO was determined by electrochemical method at a temperature of 700±5^{o}C. In this system, the thermodynamic activity of Mg in molten Al as a function of concentration (X_{Mg}) was computed, showing negative deviation from Raoult's law. A linear dependence of the theoretical and experimental emfs on the logarithm of Mg concentration ($\log X_{Mg}$) in molten Al at 700±5^{o}C was determined and used to compute the average transport number of Mg^{2+}-cation in the solid-state electrolytes. However, the average transport number of Mg^{2+}-cation in the stabilised solid-state electrolytes characterised in this research is believed to be approximately 0.85±0.03.

List of Abbreviations

The following is a list of abbreviations used in this thesis:

AAS	Atomic Absorption Spectroscopy
Al	Aluminium
AST&D	Academic Staff Training and Development
BAW	Bulk Acoustic Wave
Cu	Copper
DRAMs	Dynamic RAMs (Random Access Memories)
DSC	Differential Scanning Calorimetry
EDS	Energy-dispersive X-ray Spectroscopy
EIS	Electrical Impedance Spectroscopy
EMF	Electromotive Force
EPA	Environmental Protection Agency
FTIR	Fourier Transform Infrared
GSAS	Generalised Structure and Analysis Software
HR-TEM	High Resolution Transmission Electron Microscopy
HT	High Temperature
HT-XRD	High Temperature X-ray Diffraction
LEMAS	Leeds Electron Microscopy and Spectroscopy Centre
LISICON	Lithium Super Ionic Conductor
LRS	Laser-Raman Scattering

LT	Low Temperature
MCD	Materials Chemistry Division
MCeP	Magnesium Cerium Phosphate
MEMs	Micro-electromechanical Systems
Mg	Magnesium
MHfP	Magnesium Hafnium Phosphate
MLCCs	Multilayer Ceramic Capacitors
MZ-CeP	Magnesium Zirconium-Cerium phosphate
MZ-HfP	Magnesium Zirconium-Hafnium Phosphate
MZP	Magnesium Zirconium Phosphate
NASICON	Sodium Super Ionic Conductor
OFHC	Oxygen-free High Conductivity
PSR	Parkinson-Spencer Refractories
RSC	Royal Society of Chemistry
SAW	Surface Acoustic Wave
SEM	Scanning Electron Microscopy
TEM	Transmission Electron Microscopy
TGA	Thermogravimetric Analysis
X_{Mg}	Mg concentration
XRD	X-ray Diffraction
XRF	X-ray Fluorescence
YSZ	Yttria-stabilised Zirconia

Other abbreviations are defined wherever they are used.

Nomenclature

The following is a list of the symbols used in this thesis and their meanings, where symbols are duplicated, the relevant meaning is indicated in the accompanying text.

2θ	Diffraction angle
E_a	Activation energy
F	Farad
hkl	Miller indices
k	Boltzmann constant
K	Shape factor of particles
Ø	Diameter
S	Siemen
V	Voltage
wt.%	Weight Percent
α, β, γ	Angle between length of unit cells (alpha, beta, gamma)
γ_c	Activity coefficient of unit concentrations
λ	Wavelength of X-rays
ρ_{Al}	Density of Aluminium
ρ_{Mg}	Density of Magnesium
σ	Electrical conductivity
τ	Relaxation time
ϕ	Phase difference

ω	Angular frequency, $2\pi f$
Ω	Resistance
ω_H	Hopping frequency
ω_p	Crossover frequency

Other symbols are defined wherever they are used.

Content

List of Figures

List of Tables

Chapter 1

Introduction

1.1 Overview

“Necessity is the mother of invention”. Ingenious developments in materials have coincided with major stages in the development of civilisations. Materials were handled in accordance with their perceived nature, which had been sensitively learned, but a theoretical understanding of their properties developed slowly and had little or no effect on the practice until this present century [1].

Over the century, the electronics industry has grown exponentially and now has a pervasive influence in modern life, with crucial implications for society. By the year 2000, the microelectronics industry represented 10% of world trade, the largest single sector [2]. The rapid growth of this industry has created a huge requirement for better materials. Consequently, the wide range of applications of ceramics in the electronic industry has resulted in the development of a large number of materials [3-5]. In particular, the so-called *smart* materials [4] play a key role in their application in intelligent systems, with new developments predicted for the next century.

Novel approaches to preparation and processing, connected mainly with increased purity, together with new processing techniques and functional materials, have been developed. New markets have begun to open up in such areas as multilayer ceramic capacitors (MLCCs), micro-electromechanical systems (MEMs), transducers, sensors, actuators, piezoelectric resonators and high density dynamic random access memories (DRAMs) [3-5]. Different composite functional materials continue to enter the market for application as electroceramics in sensor making and other energy saving devices.

In this connection, Magnesium (Mg), the sensing component in this research, is the eight most abundant element in the earth's crust (about 2.5%) and is, after Aluminium (Al), the lightest of structural metals, moderately hard, silvery-white metal with one of the lightest density of all common structural materials, having a specific gravity of 1.74 is readily available as an alloying element for engineering use. Furthermore, the lightness, high specific strength, good machinability, high damping capacity, good castability, low melting temperature, melting energy and corrosion resistance [6] shows the reason why magnesium is important to the automobile, aerospace and other related industries. As the lightest structural metal known, in oxides, MgO possesses some characteristic properties in most electroceramic materials and the combination of low density and good mechanical strength resulting in high strength-to-weight ratio applicable in most aerospace and automobile industries. Because of their low modulus of elasticity, Mg-alloys can absorb energy elastically. When combined with moderate strength, this provides excellent dent resistance and high damping capacity. Mg also has good fatigue resistance and it performs particularly well in applications involving large revolutions at low stress. It is sensitive to stress concentration, therefore notches, sharp corners, and abrupt section changes should be avoided. Mg and its alloys have a traditional base mostly driven by aerospace and automobile industrial requirements for the lightweight materials operating in increasingly demanding harsh condition. Meanwhile, Mg has shown limited ambient temperature formability due to a shortage of independent deformation modes that would accommodate deformation along the c-axis of Mg hcp unit cell, which is different from Aluminium (Al) as a close metal on the periodic table with unconstrained-unlimited formability [7]. In comparison, Al and Mg are two important light weight structural metals with tremendous weight saving potential in automobiles, aerospace and defence applications; they both possess the lightest density of common structural materials ($\rho_{Al} = 2.77$ gcm^{-3}, $\rho_{Mg} = 1.74$ gcm^{-3}) [7-9]. The non-heat-treatable Al-Mg alloys have good applications in the aerospace sector while, the age-hardened Al-Mg-Si alloys showing tremendous combination of strength and formability are important in the automobile industrial complex [7]. Al-scrap contains 0.5-5.0 wt.% Mg, which can result in the formation of an embrittling

Mg silicide during casting of the recovered Al, it must be removed during reclamation by demagging [10], the solid-state potentiometric sensors designed for sensing Mg in molten Al is important as it advances the efficiency of monitoring the composition of Mg in traditional Al-Mg alloy, and related alloys such as Al-Mg-Si, Cu-Mg and other non-ferrous metallic alloys during process recycling and alloying operations by in-line adjustments to the alloying composition [11].

In contrast to Mg, the slightly heavier element, Al has an established leading role in automotive applications for both automobiles and aerospace. With plethora of interest in development of sensory devices for manufacturing and refining metallic and non-metallic alloys, the need for in-line electrochemical solid-state Mg-sensor suitable for sensing Mg concentration in molten non-ferrous metallic alloys is a novel research aimed at developing a new, viable and more efficient technology for continuous monitoring and controlling the refining process of non-ferrous alloys. Currently, the technique used in most metallurgical industries to monitor metal composition during refining is by discretely sampling the metal, casting the sample in the form of disk followed by either destructive or non-destructive chemical analysis [12] which are mostly discontinuous, slow, unreliable and has the tendency to measure total impurity content instead of the dissolved impurity content. And, needs expensive infrastructure to function. Electrochemical sensors have the potential to overcome the disadvantages associated with the conventional techniques. Measurements could be done *in situ* and a fast response time may be expected. Indeed, in this research, electrochemical sensors for the determination of Mg concentration in molten non-ferrous metallic alloys of Al-Mg and Cu-Mg is practically fabricated to overcome the challenges.

Electrochemical sensor[2] designed and developed for in-line analysis of molten metal can provide alternative solutions to resolving the deficiencies of the currently adopted practices in metallurgical and materials processing industries. Novel high-temperature electrochemical sensors with conducting solid-state electrolytes have shown several advantages in the processing of molten metals. Moreso, since conductivities of solid-state electrolytes increase with increasing temperature, the high operating temperature required during sensing of molten non-ferrous alloys in this research is well-suited to

---

[2] The most versatile and highly developed chemical sensors defined Potentiometric, Amperometric and Conductometric.

the electrochemical sensors [13]. The sensing output of the electrochemical solid-state Mg-sensor in this research is determined by the thermodynamic properties of molten non-ferrous alloys (Al-Mg and Cu-Mg) and the reference electrode ($MgCr_2O_4$+Cr_2O_3) in this case, so the Mg-sensor does not necessarily require calibration. The supporting electronics in sensors are relatively simple, since output of the electrochemical sensor is a dc voltage. In addition, the solid-state electrolytes are generally stable compounds because of their ceramic nature hence, can withstand the harsh chemical environment as applicable in the molten non-ferrous alloys.

The successful development and implementation of electrochemical device like high-energy lithium-ion batteries [14-16] in recent years has found applications in a variety of portable devices. In the same period, one of the important technological challenges for battery research is to develop the solid-state electrolytes having high lithium-ion conductivity and high chemical stabilities. Meanwhile, in a solid-state electrochemical sensor, solid-state electrolyte is the heartbeat of the sensory system, it should therefore be carefully selected in order to sense the desired species in molten alloys. The choice of electrolyte is always wider for low temperature applications whereas it is extremely limited for high-temperature applications such as sensing in molten Al-Mg at 700±5°C or molten OFHC-Cu and Cu-0.5 wt.% Mg alloys at 1250°C. The reason is because of the corrosive nature of molten metals, alloys and rapid kinetics of undesired chemical reactions between the solid-state electrolytes and their reference or sensing electrodes at high-temperatures. Solid-state electrolytes are materials capable of conducting ions which has received increased attention in recent years owing to the excellent suitability of the solid-state electrolytes as an ionically conductive materials in high-temperature systems [17]. Among solid-state electrolytes, ceramic electrolytes form a significant and unique class of materials, they display a wide electrochemical stability window, absence of leakage compared to liquid electrolytes and possess a variety of sizes and shapes [18, 19]. Recent research have shown that the ceramic electrolytes are the only solid-state electrolytes with ordered structure [20, 21]. In this research, $MgZr_4P_6O_{24}$, $MgHf_4P_6O_{24}$, $MgCe_4P_6O_{24}$ solid-state electrolytes and the solid-state solutions were synthesised by a modified sol-gel process and then characterised for the design and fabrication of the high-temperature electrochemical solid-state Mg-sensor suitable for sensing Mg concentration in non-ferrous metallic alloys. In knowing that the working environment in non-ferrous metal refining, recycling, alloying is of high-temperature,

Mg^{2+}-cation conducting solid-state ceramic electrolytes with high fracture toughness and an improved thermodynamic stability in a reducing oxygen condition becomes an important consideration during application. Moreso, solid-state Mg-sensor has found applications in Cu-Mg alloying during melting and casting at high-temperature for in-line adjustments to the alloying composition in a high-speed rail, and high-conducting wire making process, thereby enabling effective and efficient monitoring of the Mg concentration in the Cu-Mg alloys [11].

The plethora of recent research interest in solid-state electrolytes is related to electrical conductivity properties of the solids. The presence of high ionic conducting solid-state electrolytes has given rise to development of new electrochemical cells, batteries and other solid-oxide fuel cells that are solids, rather than liquid electrolytes.

Ionic solid-state electrolytes such as α-AgI and other AgI-base complexes, $RbAg_4I_5$, Naβ-Al_2O_3, Kβ-Al_2O_3, Ag_3SBr, AgCl, AgBr, $Na_3Zr_2Si_2PO_{12}$, $Li_{14}ZnGe_4O_{16}$, $LaMnO_3$, Ca^{2+} or Y^{3+} substituted ZrO_2, $YBa_2Cu_3O_7$ have been investigated [22, 23]. Similarly, solid-state electrolytes conducting O^{2-}, H^+, Li^+, Na^+, K^+, Ag^+, F^-, Cl^-, OH^- ions have also been reported showing ionic conductivity of $10^{-3} < \sigma\ (Scm^{-1}) < 10^1$ depending on the materials structure and operating temperature. However, there are no known solid-state Mg^{2+}-cation conductors other than $MgZr_4P_6O_{24}$ or double $Mg_{0.5}Zr_2(PO_4)_3$ [24-26]. Mg^{2+}-cation is stable in the +2 oxidation state and has ionic radius of 57 pm and 72 pm with coordination numbers of 4 and 6 for tetrahedra and octahedra coordinated cation, respectively [27]. In Mg-based phosphates such as the $Mg_{0.5}M_2(PO_4)_3$ (M = Ti, Zr, Hf) [28-31], the coordination number of Mg^{2+}-cation is either 4 or 6. Other Mg^{2+}-cation conducting solids like $Mg_{0.5}Zr_2(PO_4)_3$-based oxides [32-36], $MgHf(WO_4)_3$ [37], $Mg(BH_4)(NH_2)$ [38] and $(Mg_xHf_{1-x})_{4/(4-2x)}Nb(PO_4)_3$ [21] have also been developed and characterised to improve similar and related research interest. A monoclinic symmetry β-$Fe_2(SO_4)_3$-type structure ($P2_{1/n}$) have been studied with interest [39], and are known to have a three-dimensional network linking Zr-O-P framework consisting of corner-shared PO_4 tetrahedra and ZrO_6 octahedra, which is similar to NASICON, with high Mg^{2+}-cation conductivity (i.e., 1.4×10^{-3} Scm^{-1} at 800°C) [21, 40]. Similarly, in the $Mg_{0.5}Zr_2(PO_4)_3$, each of this Mg^{2+}-cation is located at an interstitial site of the Zr-O-P framework with an occupancy of 0.5 [39], the partial occupancy however provides Mg^{2+}-cation vacancies and is expected to facilitate the migration of Mg^{2+}-cations.

In producing the next-generation of electrochemical devices, such as high-temperature electrochemical sensors with thermodynamic inputs, that are applicable in non-ferrous scrap metal refining and virgin metal alloying operations, the miniaturisation of such devices is important, cost, safety and capacity, have also become a crucial task and at the heart is the electrolytic materials representing the key for creating electrochemical devices with these desirable properties [41].

In order to design and develop a simple miniaturised and affordable high-temperature electrochemical sensor, the key components of solid-state electrolytes and reference materials were synthesised through a sol-gel chemical route and a conventional solid-state method, respectively. Advantages of synthesising ceramic materials using the sol-gel route are enormous, the formation temperature is greatly reduced. Since mixing using sol-gel synthesis occurs at a molecular level among the precursors, the method equally homogenises and mixes precursor oxides at molecular level which is likely to increase the reaction rate and decrease the processing temperature, therefore yields reproducibly and consistently pure single homogeneous phase.

In order to monitor the concentration of Mg in molten alloys of Al-Mg at 700±5^{o}C or Cu-Mg at 1250^{o}C for desired properties of Al- or Cu-alloys, a highly conducting Mg^{2+}-cation solid-state electrolyte is desirable for fabricating of solid-state electrochemical sensors for sensing Mg in molten alloys. First attempt was the development of sensors using fused salt containing $MgCl_2$ as solid-state electrolyte [42]. Because of difficulty in handling $MgCl_2$ molten salt and its corrosive nature, Zhang and Fray [42] designed the sensor by impregnating molten salt electrolyte into porous MgO thimbles. The response of solid-state Mg-sensors were found to be reasonably satisfactory. However, the long term stability of the electrochemical sensor needs to be carefully investigated. Another shortcoming for this solid-state Mg-sensor is that $MgCl_2$ is hygroscopic and therefore has a limited shelf life. Researching into new sets of solid-state electrolytes: $MgZr_4P_6O_{24}$ (MZP), $MgHf_4P_6O_{24}$ (MHfP), $MgCe_4P_6O_{24}$ (MCeP) from the solid-state electrolytes series, $MgZr_{4(1-x)}M_{4x}P_6O_{24}$ with [MZP (x = 0), MHfP, MCeP (x = 1); when M = Hf, Ce] and their corresponding solid-state solutions ($0.1 \leq x \leq 0.9$), and stable reference electrodes: $MgAl_2O_4$+α-Al_2O_3 or $MgCr_2O_4$+Cr_2O_3 or $MgFe_2O_4$+α-Fe_2O_3 biphasic powder mixture have been synthesised by sol-gel process for the solid-state electrolytes and then conventional solid-state method for the reference electrodes. The

solid-state electrolytes were carefully selected to solve problems such as handling, corrosion and hygroscopic nature of the electrolytes encountered by other researchers [42]. The sensing/working electrode: Molten Al-Mg alloy at 700±5°C or Cu-Mg alloy at 1250°C were synthesised by adding Mg-rods firmly wrapped in Al-foil sheets of different composition into the molten Al to yield Al-Mg alloy, whereas, Mg-Cu alloy was produced in a graphite crucible while varying the composition of Mg at intervals, thereby forming a master alloy for subsequent use in this research as the need arise.
For characterisation: Thermogravimetric analysis - differential scanning calorimetry (TGA-DSC), X-ray diffractometer (XRD), Electrical impedance spectroscopy (EIS), Fourier transform infrared (FTIR), Laser-Raman scattering (LRS) spectroscopy, X-ray fluorescence (XRF), Scanning electron microscopy (SEM), Transmission electron microscopy (TEM) and associated Energy-dispersive X-ray spectroscopy (EDS) are some of the techniques used for characterisation of the synthesised electrolyte in order to evaluate both physical and chemical compositional changes of the materials.

In choosing a potentiometric sensor for application in high-temperature environment, sensitivity, speed of response, recovery time, reproducibility, chemical stability, size, immunity to environment, cost and selectivity are some useful attributes considered in this research.

A good number of galvanic cells of MZP (x = 0), MHfP (x = 1) and MCeP (x = 1) ceramic solid-state electrolytes and the reference electrodes: $MgAl_2O_4$+α-Al_2O or $MgCr_2O_4$+Cr_2O_3 or $MgFe_2O_4$+α-Fe_2O_3 were used to measure the transport number (t_{Mg}) of the solid-state electrolytes in molten Al-Mg and Cu-Mg alloys by emf method at different Mg-composition expecting Mg^{2+}-cation being the only conducting specie in the solid-state electrolyte. This is believed to from the bulk of the charge carrier which also expresses the response rate of the solid-state Mg-sensor. A review of recent literature to date has shown the paucity of data on the electrical behaviour and design procedure of the novel $MgHf_4P_6O_{24}$, $MgCe_4P_6O_{24}$ and some other phosphate-based solid-state electrolytes in application, which is studied by focusing so much research interest on the electrical behaviour of the solid-state $MgHf_4P_6O_{24}$ and $MgCe_4P_6O_{24}$ electrolytes, subsequently, fabricating high-temperature solid-state Mg-sensors with these electrolytes and stable reference electrodes.

Generally, this research is centrally about the development of electrochemical sensors, fabricated using solid-state electrolytes for measuring Mg concentration in molten non-ferrous metallic alloys at elevated temperatures. The electrochemical solid-state Mg-sensor can withstand harsh physical and chemical environment because of the ceramic nature of the electrolytes.

Increasing demands for improved product quality control, and process efficiency of industrial processes require the development of in-line sensors to provide feedback for process optimisation [43]. Thus, controlling, quantifying and monitoring the amount of Mg in molten Al-Mg, Cu-Mg, Al-Mg-Si alloys and other molten non-ferrous alloys during alloying, refining, casting and other chemical processes is essential during the reclamation of aluminium scraps [10], during copper refining, wire drawing, and other production processes such as in roofing sheet, photoengraving plate, galvanising baths and dry-cell battery where Zn is an alloy of Mg. Electrochemical sensors for in-line sensing ensures significant savings in energy cost for the industries by implications of the automation processes and updating less productive work. The outcome of a typical response of electrochemical sensor for molten Al-Mg or Cu-Mg alloys is presented in a stepwise emf (E/V) vs logarithmic Mg concentration ($\log X_{Mg}$) graph with each step representing change in Mg concentration in the molten non-ferrous alloy [44]. The sensor emf increases as Mg concentration increases otherwise, the sensor is believed to have failed in operation. Oftentimes, Al^{3+} alloy scrap contains excess Mg^{2+} which is demagged [10] by chlorination, solid-flux and electrochemical processes. An *in situ* Mg-sensor is important for improving efficiency of these processes and for in-line adjustment to the alloying composition. The research interest therefore is to interface and cooperate with metallurgical, chemical and other process industries believing that the solid-state electrochemical Mg-sensors would resolve such recurring problems in those industries. The solid-state Mg-sensors designed and fabricated in this research would be achieving the following objectives for the chemical and process industries. The solid-state Mg-sensor will

i. improve the efficiency of various processes in the adjustment of Mg alloy composition. For instance, the monitoring and control of Mg concentration in Al-Mg and Cu-Mg alloys in the automobile and aerospace industry and, in Cu cable industries where Cu-Mg alloys provide suitable substitute for pure Cu in overhead contact wires and cables for high speed trains. Mg is also important as a deoxidiser in the manufacture of Cu-based alloys, such as brass and bronze.

ii. reduce operational cost as a result of automation and optimisation of the production processes thereby improving product yield.

iii. encourage continuous in-line monitoring of Mg concentration in Al-Mg and Cu-Mg alloys. This is an improvement on the discrete approach readily practiced today. A discrete adjustment of the alloy composition require extraction of a sample alloy which is further analysed in the laboratory. An in-line solid-state Mg-sensor would provide an immediate compositional information and avoid errors resulting from changes in composition during holding of the molten alloy at an elevated temperature. For e.g., during the high-temperature holding process, the Mg concentration may decrease due to preferential oxidation or vapourisation. Thus, solid-state Mg-sensor could improve the efficiency (e.g., reduce holding time) and quality control (e.g., composition control) during processing of molten Al-Mg and Cu-Mg alloys. Other non-ferrous alloys such as Zn-Mg will be studied in future.

iv. reduce carbon footprint. This will reduce total greenhouse gas emissions caused in the industry during production process as a result of manual and prolonged use of hydrocarbon in production. It also helps to conserve finite oil reserve and it equally leads to reduction in fuel consumption and CO_2 emissions.

1.2 Objectives of the Research

The objective of this research is to demonstrate the techniques for fabricating a simple, affordable, reproducible, stable and highly sensitive high-temperature electrochemical solid-state Mg-sensors using Mg-based solid-state phosphate electrolytes, as the Mg^{2+}-cation conductor and biphasic powder mixture of $MgCr_2O_4$+Cr_2O_3 reference electrode. The synthesis of $MgZr_{4(1-x)}M_{4x}P_6O_{24}$ solid-state electrolytes by complete substitution or systematic co-doping or partial substitution with Hf^{4+} and Ce^{4+}-cation for producing solid-state solutions in different chemical stoichiometric reactions is to improve the structural and electrical properties of the functional materials.

To achieve this feat, the following investigations were performed:

i. Modified sol-gel synthesis for the solid-state electrolytes, solid-state solutions and, solid-state method for reference materials synthesis.
ii. Use of emf method to research the thermodynamics and chemical stability of both the solid-state electrolytes and reference materials at high-temperatures.
iii. Use of simultaneous TGA-DSC to predict the calcination temperature as well as the transformation reaction (if any). HT-XRD to reveal the transformation temperatures. XRD used to identify phase formation in calcined nanopowders and sintered pellets. FTIR and Laser-Raman scattering used for characterising molecular bonds of the active precursor oxides, SEM for morphologies, TEM for fine detailing, XRF and EDS for elemental compositional analysis.
iv. Electrical characterisation of the platinised sintered pellets at $RT \leq T/\ ^oC \leq 800$ for conductivity measurement.
v. Sensor fabrication and sensing characterisation in relation to reproducibility, sensitivity, response time, stability and immunity to environment. These are relevant properties expected of the fabricated solid-state Mg-sensor.

The final consideration for this high-temperature solid-state Mg-sensor design is cost of synthesis, fabrication and miniaturisation. For industrial applications, the sensor needs to be as cheap as possible, rugged, compact, reliable, selective, sensitive, stable, recoverable, and reproducible, for which the selected component parts characterised for sensor design and fabrication is essential. Therefore, the solid-state electrolytes and reference electrodes should be carefully prepared from reasonably cheap precursor materials and energy conserving procedures. The solid-state Mg-sensor on the other hand should be miniaturised for easy handling and storage. Miniaturisation: “when smaller is better” ensures the solid-state Mg-sensor probe is designed and fabricated to a size small enough to be inserted into the relevant point of application without the regular weight related issues affecting electroceramics of this kind. In effect, since Al is susceptible to corrosion, the automobile and aerospace industry is researching ways to improve the corrosion resistance of Al cables thereby making it a viable, lightweight alternative to Cu automotive cabling.

1.3 Justification of the Research

The solid-state Mg-sensor finds requisite application in alloying, recycling or refining of virgin metals or metal scraps. In the chemical and materials processing industries, the solid-state Mg-sensor is designed and fabricated for monitoring Mg concentration during scrap metal recycling, or refining, and virgin metals alloying. In both cases, the continuous monitoring of Mg concentration in the various non-ferrous alloys during recycling or alloying to adjust the concentration of Mg in-line will improve the process efficiency of the beneficial industries. In view of the high-temperatures involved in Al refining, recycling and alloying, ionic ceramics, i.e., Mg^{2+}-cation conductors having high fracture toughness and thermodynamic stability in a reducing oxygen condition becomes important in high-temperature electrochemical Mg-sensors. Solid-state Mg-sensors therefore benefit research and other sundry process industries by increasing throughput, lower dross production, lower refractory consumption, lower energy loss, lower environmental pollution, and improve automation by reducing production time and sequence.

In specific interest to the researcher, considering that Cu-Mg alloy is now becoming the preferred alloyed copper for high-speed rail applications, as the non-ferrous alloy provides a combination of good electrical conductivity, high tensile strength and good creep resistance. Cu-Mg alloy is considered a viable alloy, apart from meeting these physical property requirements, Cu-Mg alloy is also considered an environmentally benign material with no scientific toxicity hazard. Furthermore, considering the light and reactive nature of Mg and its propensity to form slag when molten, the production of Cu-Mg alloy by adding Mg to the molten Cu is difficult therefore, the composition of Cu-Mg alloy can be maintained during continuous melting and casting within very tight tolerance which can be monitored with a high-temperature solid-state Mg-sensor.

1.4 Structure of the Thesis

Chapter 2 of this thesis outlines the background theory and literature reviewed in this research. Background theory and research progress on sol-gel synthesis approach, characterisation of high-temperature solid-state electrolytes, ionic conductivity of the solid-state electrolytes, thermodynamic and kinetics or transport number computation analysis, sensor mechanism, electrochemical sensors, and solid-state Mg-sensors will be reviewed. Reference electrodes and selection process using phase diagram theory for sensor design and fabrication are considered vital for review.

Chapter 3 of this thesis entails experimental techniques and details. This section will include materials identification, selection, materials synthesis, chemical analysis, and characterisation techniques. Experimental techniques including thermodynamic emf measurement, kinetic or transport properties of Mg^{2+}-cation, stability measurement of solid-state electrolytes in molten OFHC-Cu, molten Al and other molten non-ferrous alloys with varied magnesium will also be discussed in this chapter. Sensor fabrication techniques and sensor testing will close the discussions in this chapter.

Chapters 4 of this research include results of materials synthesis by the sol-gel method, materials characterisation of solid-state electrolytes; MZP (x = 0), MHfP (x = 1), MCeP (x = 1), and their solid-solution $(0.1 \leq x \leq 0.9)$ using $MgZr_{4(1-x)}M_{4x}P_6O_{24}$ series. Results of reference electrodes characterisation, stability analysis on solid-state electrolytes in molten OFHC-Cu, molten Al, sensor fabrication and testing will be included in this chapter. A detailed discussion of the results determined during sol-gel synthesis and sample powder-pellets characterisation of both solid-state electrolytes and reference electrodes will contribute substantial information to this chapter.

Chapter 5 includes comprehensive discussion of the electrical characterisation on the solid-state electrolytes and the solid-state solutions by the electrochemical impedance spectroscopy method. The electrical characterisation will be limited to impedance analysis, electric modulus, temperature dependence and frequency dependence on ionic conductivity, respectively.

Chapter 6 entails thermodynamic measurements by emf method assessing the kinetics or transport properties of Mg^{2+}-cation will be discussed. Investigation of the stability of solid-state electrolytes at high-temperatures as well as the thermodynamic stability of reference electrodes in sensor fabrication will be included. The sensor emf response rate as a function of Mg concentration variation in molten Al at a fixed temperature will be discussed in this chapter. Computation of thermodynamic activity will also be included.

Chapter 7 includes conclusion, recommendations and future work.

Chapter 8 consists of a list of publications, future publications, conference attended with dates, recognitions and grants awarded.

Finally, references and appendix!

Chapter 2

Theoretical Background and Literature Review

2.1 Synopsis

A robust theoretical background and literature review on solid-state Mg-sensor in non-ferrous alloys is necessary to bridge the dearth of information on the solid-state Mg-sensor which is a very important sensor to the metal casting and refining industries. The relevance of this sensor to materials and metallurgical refining industries is huge. The research to investigate areas of possible applications of this sensor is necessary for improving production processes in our metallurgical industries today.

Monitoring and control of Mg concentration in Al-alloys containing Mg for aerospace application and, high Mg concentration (0.4-0.6% Mg) in Cu-Mg alloy for overhead contact wires and cables for high-speed trains. Also, monitoring of Mg concentration in low Mg concentration (0.1-0.2% Mg) in Cu-Mg alloy rod for use in the manufacture of small diameter automotive data communication cables production, this is necessary in order to improve the process efficiency of production. Although the commonly used discrete procedure of specimen for analysis is exact, a more portable, sensitive, stable and cost-effective device capable of working in the harsh and dirty environment for use in indoor and remote sensing applications is needed. This research is designed to develop an electrochemical sensor for the sensing of Mg in molten non-ferrous alloys at high-temperatures.

Sensors using a eutectic mixture of $MgCl_2$ and $CaCl_2$ as the electrolyte have equally been reported [45-47]. Recently, studies on electrochemical sensors for sensing Mg in molten Al have also been reported: Tiwari and Howie [46], Belton and Rao [48], and Tsyplakove and Strelets [49] used molten $MgCl_2$, Mg^{2+}-cation conductor, electrolyte for sensing Mg in molten Al, and to deduce the thermodynamic properties of dilute Al-Mg liquid alloys containing less than 0.15 atomic fraction Mg. Larose, *et al.* [50] used 1-2 wt.% MgO stabilised Na-β''-Al_2O_3, a Na^+-ion conductor, as solid-state electrolyte for sensing Mg in molten aluminium. Fergus and co-workers [11, 51] used MgF_2, F^--ion conductor, as solid-state electrolyte for sensing Mg in molten aluminium. Also, Zhang and Fray [42] used immobilised $MgCl_2$ in porous MgO thimble as an electrolyte for sensing Mg in molten aluminium. In all of the findings investigated, it was clear therefore that the principle of sensing Mg in molten aluminium is based on indirect measurement when solid-state electrolyte is used for designing the Mg-sensor [11, 42, 50, 51]. Sensing mechanisms for different types of electrolytes were discussed by Kale and Kurchania [12]. Furthermore, it was equally important to note that none of the measurements involved the application of a solid Mg^{2+}-cation conductor as an electrolyte in solid-state Mg-sensor. The research work, in this case, entails synthesis and characterisation of solid-state electrolyte materials and designing of novel solid-state Mg-sensor using $MgZr_{4(1-x)}M_{4x}P_6O_{24}$ (when M = Hf, Ce; $0 \leq x \leq 1$) as Mg^{2+}-cation conducting electrolytes which is tested in molten non-ferrous alloys, to determine the chemical stability or sensing Mg in molten Al and Cu, respectively. There are, in principle, many ways to detect chemical species in the environment. Most commonly, the sensing device takes the form of a chemical to electrical transducer. Classically, this would be in the form of electrochemical cells, operating either in the potentiometric or amperometric mode. Indeed, the sensors installed in tens of millions of every new automobiles per year, for the purpose of monitoring the oxygen partial pressure, P_{O2}, of the exhausting gas, are potentiometric devices utilising the oxygen ion solid-state electrolyte, yttria-stabilised zirconia (YSZ). In this case, electromotive force (emf) is generated across the electrolyte due to gradient in P_{O2} between the exhaust manifold and air reference [52].

This chapter is composed mainly of the theoretical models as well as literature reviews of the research. Other literature reviews can be found in the introductory parts of relevant chapters.

2.2 Chemical Synthesis

2.2.1 Sol-gel chemical process

Sol-gel chemical process provides a unique approach to the preparation of ceramics [53]. The starting procedure of this approach is by making solutions of molecular precursors, where an oxide network is achieved by inorganic polymerisation reactions. This method is equally termed wet chemistry method because the reactions occur in solutions. The sol-gel synthesis process [54-56] is an attractive alternative to other methods for the synthesis of ceramics compared to the conventional process for many reasons;

i. that homogeneous multi-component systems can be easily obtained by mixing the molecular precursor solution [57, 58].
ii. that temperatures required for material processing can be noticeably low [59].

The chemistry of the sol-gel process is based on hydroxylation and condensation of molecular precursors; these reactions have been extensively studied in the case of SiO_2 [60]. Unfortunately however, very few data is available for transition metal oxide precursors [53]. Two different processing routes have been followed, depending on whether the precursor is an aqueous solution of an inorganic salt or a metal organic compound. The most versatile precursors for the sol-gel synthesis of oxides are undoubtedly metal alkoxides which are very reactive toward nucleophilic reagents such as water [61]. Historically, metal alkoxides have been employed in the sol-gel process, which readily underdo catalysed hydrolysis and condensation to form a nanoscale oxide or hydroxide particles. Still, in general, metal alkoxides are often used as raw materials in sol-gel process, but many of the alkoxides are very difficult to be obtained because of the high sensitivity to the atmospheric moisture [62-67]. In ordinary sol-gel processing, starting compositions, as well as reaction conditions, are selected so as to maintain the mixture in a homogeneous state throughout the processes including mixing of starting compounds, gelation, aging, drying, and heat-treatment. Structural evolution during the sol to gel and gel to solid transitions need to be fully understood before a real mastery of the sol-gel process can be reached. The properties of a gel and its response to heat treatment are very sensitive to the structure already created during the sol stage. Sols and gels are usually considered as intermediates in the processing of ceramics. Therefore, drying and densification are very important processes [68-70]. The sol-gel synthesis process as illustrated in Figure 2.1 describes all the steps and chemical reactions involved in a sol-gel method; the steps such as preparing the sol (2) from inorganic precursors and monitored reaction (4) from which aqueous gel (6) was prepared which was dried during solvent evaporation (8) to form a dried xerogel powder (10) which was later calcined (11) at specific temperatures and annealing time to form the desired compound (12).

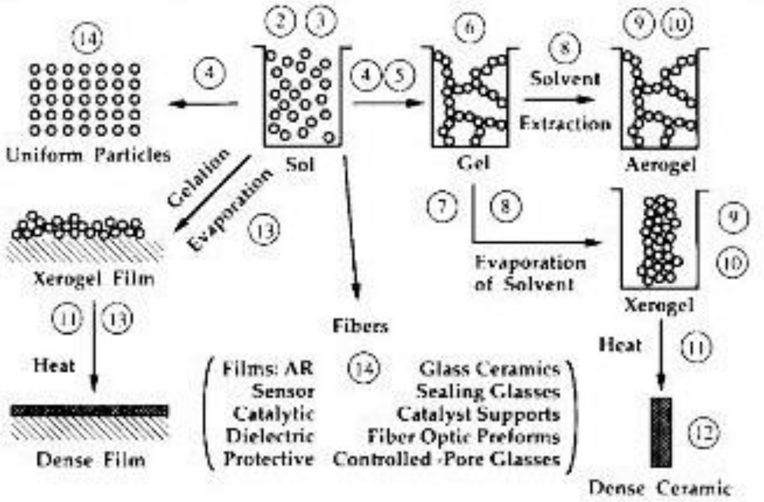

Figure 2-1 Sol-gel synthesis process showing all the steps of sample formation [55].

2.3 Solid-State Electrolyte

Solid-state electrolytes are materials in which the electric current is predominantly by ions [71]. They can be oxides, halides, sulphides and other types of solid materials. They have gained importance due to their role in various scientific and technological applications as they are being used in electrochemical cells to measure chemical potentials in gases, liquids and solids. In addition, they can also be used to control the chemical composition by coulometric titration. The solid-state electrolytes theory and applications, such as in sensors and other electrochemical devices have been discussed in many books [72-78] and review papers [23, 79-84].

In solid-state electrolytes, the conductivity stems from mobile ions rather electrons. Typically, conductivity is dominated by one type of ion only. Solid-state electrolytes already play important roles in commercial gas and ion sensors. In applications, some solid-state electrolytes have been used recently, as nonporous membranes separating two compartments containing chemical species at different concentrations on either side. Moreso, by measuring the potential across such a membrane, one can determine the concentration of the chemical species on one side if the concentration on the other side (i.e., the reference side) is known.

Alternatively, solid-state electrolytes could be described as materials with high ionic conductivity, either of cations or anions but not usually both, and they have shown negligible electronic conductivity. They have also been termed solid-state equivalent of molten salts or strong liquid electrolytes. Also, they can be referred to as superior conductors, fast ion conductors or optimised ionic conductors but a few.

Solid-state electrolytes with an ionic transport number of unity, most time exhibit both ionic and electronic conductivity; these type of solid-state electrolytes are said to be of mixed conductors, intercalation materials or solid-state solution electrodes [83].

The most commonly used solid-state electrolytes are metal-oxides. While many metal-oxide electrolytes conduct oxide-ions, there are metal-oxide electrolytes that conduct other ions, such as protons and metal ions. The most common oxide-ion conducting electrolyte is stabilised zirconia, which has been used in a hydrogen sensor for molten aluminium [85, 86]. However, proton-conducting oxides, such as $BaCeO_3$ and $CaZrO_3$ and modified NASICON, are more commonly used for hydrogen sensors [87-91]. One of the most widely used solid-state electrolytes in sensors for molten aluminium is β-alumina. The most direct use of β-alumina, which conducts sodium ions, is for sodium sensors [92, 93]. However, β-alumina has also been used in sensors for measuring strontium, lithium, and magnesium. In some cases, the β-alumina is ion-exchanged to conduct another ion, e.g., Li^+ [50, 94], while in other cases the surface is modified to create an auxiliary electrode, e.g., Mg [50].

Yttria (Y_2O_3) stabilised zirconia (ZrO_2), which is O^{2-}-conductor at high-temperature (>300°C), for the determination of the oxygen in exhaust gases of automobiles, boilers or steel melts, and, LaF_3 [95], an F^--conductor (even at room temperature), for the determination of F^- are two prominent "classical" examples of solid-state electrolytes used in sensor applications. The role of solid-state electrolytes in sensor applications has been expanding dramatically since the discovery of new solid-state electrolytes, some with room temperature conductivities comparable to that of liquid electrolytes. Examples of more recently developed solid-state electrolytes are Ag^+ conductors, α-AgI, Ag_3SI, $Ag_6I_4WO_4$ and $RbAgI_4$, and, good Na^+-conductors, such as sodium β-alumina ($NaAl_{11}O_{17}$) and NASICON ($Na_3Zr_2PSi_2O_{12}$), as well as new Li^+-conductors, such as $Li_{14}Zr(GeO_4)_4$ and Li_3N. Recently, the Mg^{2+}-conductors that has potential applications as a solid-state electrolyte in high-temperature electrochemical sensors have been developed but were not reported until $Mg_{0.5}M_2(PO_4)_3$ (M = Ti, Zr) [28-30]were characterised. In an ion-conducting solid, a solid-state electrolyte or superionic conductor, a number of ions are not restricted to "normal" lattice positions but are free to move through the lattice upon application of electrical field (i.e., migration) or a concentration gradient (i.e., diffusion). The movement of ions in the solid-state differs from transport in liquids and gases by the fact that in gases and liquids all positive and negative ions are mobile, while the bulk of atoms in solids are "fixed" to a lattice. Ions can only move when sites are available for them to move to. This is possible for two cases:

i. The atom finds a vacancy ahead (Schottky defects).
ii. The atom can move interstitially (Frenkel defects).

A third possibility would be by direct exchange between neighbouring ions, but such exchange would not produce the net charge transfer essential for conductivity.

So conductivity occurs because of imperfections in the lattice. The migration or diffusion of ions from imperfection to imperfection is usually modeled as a process of discrete jumps of a particle over an energy barrier (hopping model) [8]. Another model to explain the behaviour of solid-state electrolytes assume one sub-lattice that behaves as a liquid and another sub-lattice with a fixed configuration. Macroscopically the material then behaves as a solid, whereas the mobile ions move as in a liquid [9].

Intrinsic Defects

Energy is required to form a defect, therefore the formation of defects is always an endothermic process [96]. It may be surprising that defects exist in crystals as a result, and even at low temperatures. It is understood that the formation of defects produces a commensurate gain in entropy, S. Therefore, the enthalpy of formation, H of the defects is balanced by gain in this entropy such that, at equilibrium, the overall change in free energy, ΔG of the crystal owing to defect formation is zero as shown in equation (2.1) [96];

$$\Delta G = \Delta H - T\Delta S \tag{2.1}$$

Further, a finite concentration of imperfections, specifically vacancies and interstitials, will be present even in the purest material because the entropy, S contribution to the Gibbs energy, ΔG requires the presence of this imperfections in solids thermodynamic equilibrium at the temperatures, T above 0 K. These ionic defects, fixed through the thermodynamic equilibrium, are called the intrinsic defects. Overall charge neutrality requires that each negatively charged defects are compensated by a positively charged ionic defect (or by holes), and defect pairs will appear. The two most common defect structures in solid-state electrolytes are vacancy pairs and vacancy-interstitial pairs.

Extrinsic Defects

Extrinsic defects, in contrast to intrinsic defects, can result from the introduction of aliovalent dopant ions (i.e., impurities) into a lattice. For example, in doping zirconia (ZrO_2) with yttria (Y_2O_3), Y^{3+}-cations occupy the Zr^{4+}-cation sites, and the resulting excess negative charge leads to the necessity for an increase in oxygen vacancies to maintain charge neutrality. Also, if $CaCl_2$ is added to a NaCl crystal, each Ca^{2+}-cation replaces two Na^+-cation in order to preserve electrical neutrality, and so one cation vacancy is created [96]. With the exception of the halides, very few pure solids exhibit appreciable ionic conductivity based on intrinsic defects, and it is necessary to greatly increase the concentration of ionic defects by introducing such soluble aliovalent ions. Grain boundaries and dislocations are other examples of extrinsic defects.

Solid-state electrolytes with dominant ionic conductivity resulting from migration of ions through point defect sites in the lattice. The defects are created either by thermal activation in the range $0.7 \leq E_a$ (eV) ≤ 1.4 or by compensation of aliovalent dopants. By comparing with the conductivities of insulating ceramics of $\sigma \leq 10^{-10}$ Scm^{-1}, the conductivities of solid-state electrolytes generally are $\sigma \geq 10^{-5}$ Scm^{-1} with an ionic transport number (t_{ion}) ≥ 0.99

The solid-state electrochemical method has been known as a selective and an accurate way of sensing chemical species in the environment and even in the liquid metal for some time. After the first interpretation of the ion-conduction mechanism in zirconia [97], there have been substantial advances in the development of solid ionic materials that are extensively being used in electrochemical sensors. The most successful among these sensors is the emission control sensor made of stabilised zirconia for automobile engine. It made a revolutionary change in the automobile engine from the use of carburetor to the electronic fuel injection.

The chemically sensitive solid-state devices are based on the electrical response of the solid to its chemical environment. Interest is very high in solids whose electrical properties are affected by the presence of a gas-phase or liquid phase species; this change in electrical properties is observed and then used to detect the species. In addition to sensors based on changes in electrical parameters, many other types of solid-state chemical sensors are based on other principles, such as acoustics [e.g., bulk and surface acoustic wave (BAW and SAW)], optics (e.g., optical waveguides), and thermochemistry [e.g., microcalorie sensor and microenthalpy sensor (or, in more classical form, catalytic bead sensors)].

The major advantages of solid-state sensors are their simplicity in function, small size (possible miniaturisation) and projected low cost. The projected cost for this sensor is low because the size of the solid sample used is small. For some forms of solid-state sensors now under development, the cost is further minimised by the use of batch, planar fabrication technologies in manufacturing the device.

The major disadvantages of most solid-state chemical sensors are lack of stability, lack of reproducibility, and lack of selectivity as well as insufficient sensitivity for certain purposes. These problems were alleviated in this research and outlined accordingly. However, in many applications the disadvantages are not prohibitive, hence solid-state sensors are commercially available and in use.

One of the most important conditions for the use of materials as solid-state electrolytes is its predominantly ionic conductivity, i.e., $t_{ion} \geq 0.99$, where t_{ion} is referred to as ionic transport number, defined as the ratio of the ionic conductivity, σ_{ion} to the total conductivity, σ_{total} as illustrated in equation (2.2)

$$t_{ion} = \frac{\sigma_{ion}}{\sigma_{total}} \qquad (2.2)$$

In any case, when the ionic conductivity, σ_{ion} becomes smaller than 0.99, an accurate knowledge of the conductivity of the solid-state electrolyte becomes important. When solid-state electrolytes are used for emf measurements, one additional experimental requirement has to be fulfilled: i.e., a good and reliable contact between electrodes and electrolytes in order to obtain stable and reversible emf values.

It is known that the electrical conductivity of solids is due to mobile species such as electrons and holes as seen in semiconductors and metals. In solid-state electrolytes or ionic conducting solids, the mobile species are only ions. Some sample compositions such as magnesium cerium phosphate, $MgCe_4P_6O_{24}$ used as a solid-state electrolyte in this research shows the potential of both ionic and electronic properties. $MgZr_4P_6O_{24}$ and $MgHf_4P_6O_{24}$, on the other hand, are ionic.

In the quest for an optimal sensor with the best properties, attempts have been made in improving ionic conductivity of solid-state electrolytes using doping by substitution or partial substitution mechanism with other elements, or oxides which in this case are oxides of Hf and Ce (i.e., HfO_2 and CeO_2) to form solid-state solutions.

2.3.1 Crystal structure of solid-state electrolyte

Double $Mg_{0.5}M_2P_3O_{12}$ (M = Zr, Hf, Ti) [28-30] solid-state electrolytes have been selected and characterised as end-member electrolytes. The crystal structure of double $Mg_{0.5}Zr_2P_3O_{12}$ and $MgHf_4P_6O_{24}$ [98] as presented in Figure 2.2 illustrates the isolated positions of the ZrO_6 octahedra and PO_4 tetrahedra joined together through common vertices to form mixed three-dimensional framework. The specific features of the structure of framework phosphates containing Mg in Figure 2.2 is that the Mg can have different coordination numbers, CN = 4 and 6 [98]. More, it exhibits framework phosphates in which Mg can both enter into composition of the framework and occupy holes. As a consequence, Mg-O chemical bonds are characterised by different degrees of iconicity. Also, the two ZrO_6 octahedra and three PO_4 tetrahedra form a topological framework unit, lantern; as viewed in Figure 2.2, these structural units are packed into zigzag ribbons, as the neighbouring lanterns in one ribbon makes an acute angle of 71^o with the formation of a tiling packing of structural units. In the framework, however, it shows that holes have a complex shape and relatively large volume. Mg^{2+}-cations and are observed to be located in narrow regions of holes between edges of two ZrO_6 octahedra. In the framework however, holes are connected by windows; the widest windows are formed by edges of three PO_4 tetrahedra and three ZrO_6 octahedra. In the framework, holes form three-dimensional network of tunnels therefore, Mg^{2+}-cation can migrate in holes of the structure which then shows the ionic conductivity of $Mg_{0.5}Zr_2P_3O_{12}$ phosphate.

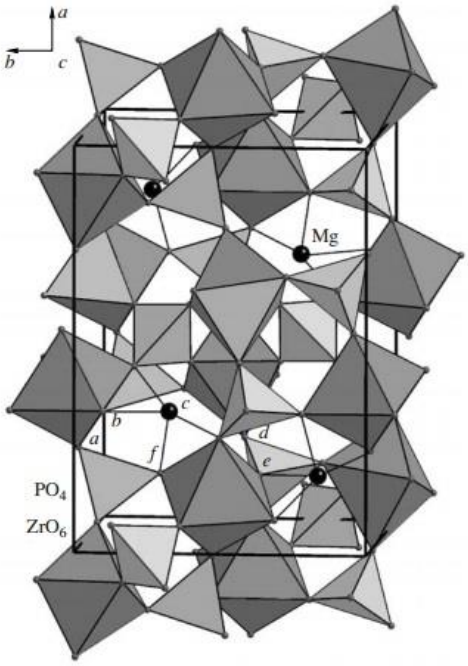

Figure 2-2 Fragment of crystal structure of $Mg_{0.5}Zr_2P_3O_{12}$ at 298K. The coordination of polyhedral of Mg^{2+}-cation and the window between the extra framework positions (*abcdefa*) [98].

$Mg_{0.5}Zr_2P_3O_{12}$ and related composites, such as NASICON, $Na_3Zr_2Si_2PO_{12}$ (x = 2) of monoclinic symmetry have been treated as high-temperature solid-state electrolytes with an ionic conductivity as high as 6.9 x 10-3Ω^{-1}cm^{-1} at a temperature of 1073K [99]. While the NASICON like phosphates have been extensively studied as solid-state electrolyte for electrochemical gas sensors. However, Wang and Kumar [100] and Ikeda *et al.* [101] considered the $Mg_{0.5}Zr_2P_3O_{12}$ phosphate as electrolyte in gas sensors for SO_2 and CO_2.

The available data on crystal structure of $Mg_{0.5}Zr_2P_3O_{12}$ phosphates are contradictory. Ikeda *et al.* [32] believes $Mg_{0.5}Zr_2P_3O_{12}$ phosphate has NASICON crystal structure. Recent research however, shows that it has a primitive monoclinic unit cell [25, 102]. The double $Mg_{0.5}Zr_2P_3O_{12}$ phosphate has no data of structural characterisation and the distribution of Mg^{2+}-cation in the crystal structure is also not clear. Nomura *et al.* [33, 102] assumed that $Mg_{0.5}Zr_2P_3O_{12}$ phosphate undergoes an order-disorder phase transition at 943K. Therefore, the final influence regarding the structural type of the $Mg_{0.5}Zr_2P_3O_{12}$ phosphate can be made only on the basis of the results of complete structural investigations, including those performed at high-temperatures. The data on the structure of the $Mg_{0.5}Zr_2P_3O_{12}$ phosphate under investigation reveals the crystal structure by Rietveld refinement method using GSAS and perhaps, Neutron diffraction in future studies.

The structural parameters of ionic radius, valence, and coordination number (CN) was considered while formulating the substitutional mechanism as applicable in this research. The values relevant to this research are however identified in Table 2.1.

Shannon and Prewitt [27, 103] quoted the coordinated ionic radius for the parameters used in this research and, the similarity of the identical radii of Mg-Zr and -Hf phosphates in six-fold coordination shows the similarity in their chemical properties considering they belong to the same periodic group. However, Mg-Ce phosphates with valence of +3 and +4 shows different ionic radii, different material behaviour as well as crystal structure. According to the refined data [104], the structure shown in Figure 2.3 is characterised by a 3D framework formed by connected PO_4 tetrahedra and MO_9 polyhedra, forming distorted single-cap square antiprisms. Furthermore, it was shown that each oxygen atom forms bridge bonds with two metal atoms, whereas one of the four oxygen atoms of the tetrahedron is bonded to three atoms. More, MO_9 polyhedra with a cation composition share vertices and edges and form the framework structure in Figure 2.3. Vacancies in the M positions of this structure provide a wide spectrum of isomorphous substitutions of Ce(IV) by cations that have lower vacancies, such as other lanthanides and actinides. Such substitutions result in the filling of this vacancies or in partial transition of Ce(IV) to Ce(III) accompanied by incorporation of cation valence $\leq 3+$. This inclusion can in turn favour the formation of compounds that are more energetically favourable.

Phosphorus atoms in the compounds occupy isolated tetrahedra. However, the Ce, Mg cations are located in the nine-vertex polyhedra formed by three monodentant and three bidentant PO_4 groups.

Table 2-1 Ionic parameters relevant to this research [27]

Ion	Valence	Ionic radius/pm	CN
Mg	+2	57.0	4
		72.0	6
Zr	+4	72.0	6
		84.0	8
Hf	+4	71.0	6
		83.0	8
Ce	+3	101.0	6
Ce	+4	87.0	6
		97.0	8
P	+5	17.0	4
O	-2	138.0	4

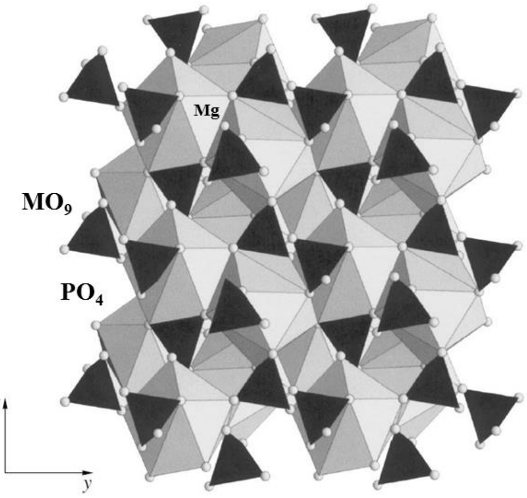

Figure 2-3 Projection of the Ce (PO$_4$) crystal structure onto bc plane at 298K [105].

2.3.2 Defect chemistry

The description of defects nomenclature was first proposed in 1956 [106, 107]. The point defects are considered as dilute species and the solid as solvent. There are essentially three ways of establishment of equilibrium of defects in ionic crystals;

i. Intrinsic defect equilibria. This include Frenkel and Schottky defect equilibria.
ii. Doping, i.e., the intentional manipulation of defect types and concentration by the incorporation of specific dopant into the bulk of a crystal.
iii. Defect reactions at interfaces, e.g. the incorporation of species from the outside into the crystal by way of defects or the opposite, the loss of atoms to the ambience generating defects in crystal.

2.3.3 Types of solid-state electrolytes

Some solid-state electrolytes are listed in Table 2.2. Ionic conductivity in solid-state electrolytes is usually due to lattice defects, and these defects can be caused by;

i. doping with aliovalent ions, which leads to vacancies in the crystal lattice (for example, ZrO_2-based or ThO_2-based oxides)
ii. large cation disorder (as in the AgI-based electrolytes)
iii. structures with a low packing density (tunnel structure and/or layered structure: $Ba_xMn_8O_{16}$, β-alumina) and
iv. glassy or amorphous material (AgBr, AgI) and network structures (NASICON, LISICON).

Table 2-2 Types of solid-state electrolyte

Type	Type of conductor	Examples
Oxide	Anion conductor	ZrO_2-based, HfO_2-based, CeO_2-based, ThO_2-based, Bi_2O_3-based, $CaZrO_3$, etc.
	Cation conductor	β-alumina, β''-alumina, Pyrex, fused silica, $SrCeO_{3-\delta}$
Halide	Anion conductor	MgF_2, CaF_2, SrF_2, BaF_2; PbF_2; LaF_3; $BaCl_2$, etc.
	Cation conductor	CuCl, α-AgI, Ag_3SI, $RbAg_4I_5$, etc.
Oxyhalide	Anion conductor	LaOF
Sulphide	Cation conductor	CaS-based, MgS, etc.
Sulphates	Cation conductor	Li_2SO_4, Na_2SO_4, K_2SO_4
Complex oxides	Proton conductor	$SrCeO_3$-based, $BaCeO_3$-based, $CaZrO_3$-based, $SrZrO_3$-based
Others	Cation conductor	NASICON ($Na_3Zr_2Si_2PO_{12}$), LISICON ($Li_{14}Zn(GeO_4)_4$), AIN(+Al_2O_3), etc.

2.3.3.1 Solid-state solution

Solid-state solutions can be understood to mean a homogeneous crystalline phase of different components dissolved in one another, either in all proportion or over a limited range of compositions. For instance, when two components are mixed together in varying proportions, they do so in one of two different ways, depending on whether they are completely or partly soluble in each other in the solid-state.

In a solid-state solution, the solute atoms are distributed throughout the solvent crystal, the crystal structure of the solvent being maintained. The solute atoms can therefore be accommodated in two different ways;

i. interstitial solid-state solutions, where they occupy interstitial positions, or

ii. substitutional solid-state solutions, where they replace the solvent atoms.

The relative sizes of the solvent and solute atoms determine which is formed. As a rough estimation, interstitial solid-state solutions can only form when the diameter of the solute atom is about 0.6 or less of the atomic diameter of the solvent [108]. Furthermore, when atoms of the two components are more nearly the same size, a substitutional solid-state solution is formed. For complete solid miscibility however, the two components must have the same crystal structure, but even when this is so, if the atoms differ in size by more than 14%, the solubility will be restricted [108].

2.3.4 Ceramic fabrication

There are two essential steps in the fabrication of ceramics from powders: forming of a green compact, mostly done by pressing, and consolidation by a sintering process, during which the strength increases and the porosity decreases. It is necessary for property measurements that the material be in a desired shape. Therefore, samples of known dimension must be fabricated with flat, parallel faces, in order to permit parallel electrode attachment and calculation of the ionic conductivity in impedance analysis.

The next stage in the production of ceramics was to press the calcined powders into shape suitable for sintering. After the calcined powders had been crushed and finely ground, a common uniaxial die pressing technique was used to press the powder into green pellets. To aid pressing and green densification, 1 wt.% binder (Ciba Glascol HA4: Ciba Specialty Chemicals, Bradford, UK) was added into the calcined powders dissolved in acetone, $(CH_3)_2CO$ and dried at 75°C for 1h, prior to pressing.

Special precautions are used in the sintering of electroceramics due to volatilisation of P^{5+}-cation (P_2O_5) as observed in this research. Atmosphere control is important to prevent loss of such important volatile components and to avoid reduction reaction. Therefore, the assembly was surrounded with an atmosphere powder of the same composition as the pellets, taking care to avoid the pellets touching the alumina crucible. An upturned alumina crucible was placed over the pellets and atmosphere powders, and an outer alumina crucible was closed with an alumina lid before insertion into high-temperature sintering furnace. In order to obtain optimum density properties, it was necessary to determine the optimum sintering temperature for maximum possible bulk density without destroying the sample properties. Following sintering, any powder adhered to the ceramic surfaces was removed using SiC abrasive papers.

2.4 Sensors

A sensor is a device that receives a stimulus and responds with an electrical signal [52]. The term stimulus can be interchangeably used as measurand, is the quantity, property, or condition that is received and converted into electrical signal [109]. By signal, it means a signal that can be channeled, amplified and modified by electrical devices [110]. A sensor can also be defined as a device which detects or measures a physical property and records, indicates, or otherwise responds to it. Sensors help interface electronic stimuli to the real world. Importance of sensors, however, contrasts with the limited information available on them. Smart sensors, wireless sensors, microtechnologies are revolutionising sensor design and applications today. Sensors are classified into two mainly, passive and active sensors;

Passive sensors are those that convert stimulus directly into electrical signal without any energy input. Thermocouple and piezoelectric sensors are some practical example of this category.

Active sensors require an excitation energy or external power to convert stimulus into an electrical signal. Thermistors, a potentiometric which requires thermal energy for ionic conduction in solid-state electrolytes, amperometric and conductometric sensors.

In operation, sensor performance can be characterised by some important parameters which are as described;

Sensitivity

This is the change in sensor output per unit change in measurand. Sensitivity is a sensor property that is extremely critical when working with precise control system or the sensing of potentially dangerous measurands [111].

Accuracy

Accuracy is an important characteristic of a sensor, however it truly means inaccuracy. Inaccuracy therefore is measured as highest deviation of a value represented by the sensor from the ideal or true value at input. The true value is attributed to the object of measurement and accepted as having a specified uncertainty [110].

Full Scale Output (FSO)

FSO is the algebraic difference between the electrical output signals measured with maximum input stimulus and the lowest input stimulus applied. This is also referred to as the baseline [52, 110, 112].

Response Time (t_{90})

This is a measure of how fast the response of a sensor is when a new level of stimulus is applied. The response time therefore is the time taken to achieve 90% of its steady-state value after the introduction of the measurand [111]. The response time is denoted as t_{90}.

Recovery Time

This is the time for signal to return to its baseline or the lower steady state output when the stimulus is removed. Recovery time can also be the time it takes the sensor to be within 10% of the value it had before exposure to the measurand. Typically, the response times are much shorter than the recovery times [111].

Resolution

This describes the smallest increments of stimulus or input signal that can be sensed. To have a meaningful output, some sensors may only resolve decade scale [111].

Hysteresis

A hysteresis error is a deviation of the sensor output at a specified point of the input signal when it is approached from the opposite direction [110].

Selectivity

Selectivity is a measure of how selective a sensor is when exposed to different stimuli. This means that the sensor should be able to respond to only one analyte with little or no interference from other substances [52, 110, 112].

2.4.1 Classification of sensors

Commercial sensors are divided into three types according to the detection principle; conductimetric type, potentiometric type and amperometric type. Different types of sensors based on solid-state electrolytes have been developed using the works of Kiukkola and Wagner [113, 114]. Based on their report, the solid-state electrolyte sensors developed are based on one of two principles;

i. the chemical potential difference across the solid-state electrolyte (as observed in a potentiometric sensor) and,
ii. the charge passed through the electrolyte (in amperometric sensor).

The first recognised commercial chemical sensor is a gas alarm sensor, which detects inflammable gases and prevents gas accidents. The sensor is simple, portable, and can be easily installed in most places. These features encouraged mass production and thus, contribute to the production of an inexpensive device. Due to the multitude of sensors that may exist, at first glance, it may appear to be a formidable task to classify sensors in some logical fashion. A possible way to classify sensors may be according to their evolution. Inevitably, the design, fabrication, and utilisation of a sensor are mostly driven by a need. For example, in the case of air to fuel ratio, A/F sensor for automobile, the need was dictated by Environmental Protection Agency (EPA) via the Clean Air Act. The need of the Clean Air Act is to reduce automobile exhaust gases such as CO, CH_x, and NO_x by 90%, but the measurand is not obvious. However, in an attempt to satisfy this need, the identification of a sensor to maintain a stoichiometric A/F mixture in engine combustion resulted. The sensor is therefore used to maintain the A/F ratio to the ideal value where the catalytic conversion of the pollutant gases is performed in an optimum condition. As a potentiometric type, the output of this sensor is obtained as an EMF from the oxygen gas concentration cell.

Sensors in various manufacturing processes may be driven by the need to increase production or decrease cost. A particular biosensor may be driven by the need to rapidly detect a life-threatening disease. A possible evolutionary process associated with the development of a sensor is shown in Figure 2.4.

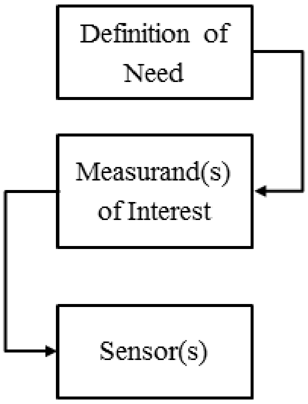

Figure 2-4 An evolutionary process associated with sensor development [111].

Although it is impossible to list all the potential needs that may result in the development of a particular sensor, the needs may be grouped into the various areas shown in Table 2.3

Table 2-3 Possible Need Area for Sensors [111]

Agriculture	Manufacturing
Automotive	Marine
Construction	Medical care
Consumer products	Military
Energy	Oceanography
Environment	Security systems
Fishery	Space
Food technology	Transportation
Forestry	Waste management
Health	

Once the measurand has been identified, the next step in the evolutionary scale is to identify the sensor appropriate to the measurand. The realisation of the sensor can be thought of as the two-step process shown in Figure 2.5. The measurand must undergo a biological, chemical, or physical interaction in order that the measurand may be converted to an entity suitable for creating a sensor output. Some possible measurand interactions are presented in Table 2.4.

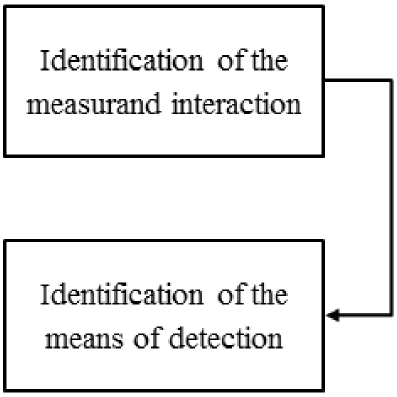

Figure 2-5 Two-step process in the realisation of a sensor [111].

Table 2-4 Possible Types of Measurand Interactions [111]

Biological		Physical	
iii.	Biochemical transformation	iv.	Thermoelectric
v.	Physical transformation	vi.	Photoelectric
vii.	Effect on test organism	viii.	Photomagnetic
ix.	Spectroscopy	x.	Magnetoelectric
Chemical		xi.	Elastomagnetic
xii.	Chemical transformation	xiii.	Thermoelastic
xiv.	Physical transformation	xv.	Elastoelectric
xvi.	Electrochemical process	xvii.	Thermomagnetic
xviii.	Spectroscopy	xix.	Thermooptic
		xx.	Photoelastic

2.4.2 Sensor Properties

There are several properties associated with a sensor that is critical to the sensor performance. Some of the more important properties are listed in Table 2.5. Several of the sensor properties can best be described by referring to a sequence of typical sensor responses as shown in Figure 2.6.

The sensor response or signature that is associated with one of the means of detection such as; biological, chemical, electric, magnetic, or electromagnetic wave, heat, temperature, mechanical displacement or wave, radioactivity, radiation is plotted as a function of time.

Table 2-5 Important Sensor Properties Critical to the Sensor Performance [111]

Response time	Resolution
Recovery time	Dynamic range
Reproducibility	Selectivity
Aging	Size and weight
Stability (short term, long term)	Cost
Sensitivity	

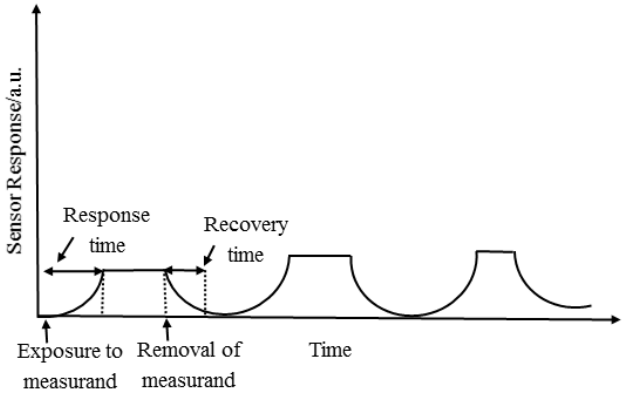

Figure 2-6 A sequence of typical sensor signatures [111]

2.4.3 Electrochemical Sensor

Electrochemical sensors form a group of sensors whose response is a result of an interaction between electricity and chemistry [111]. The fundamental principles of an electrochemical sensor developed with highly conductive solid-state electrolytes is the electrochemical reactions that takes place in the electrochemical cells. These cells are composed of a dense solid-state electrolyte pellet and reference electrodes (pellets and/or powders). The solid-state electrolyte is sandwiched in-between two different electrodes during thermodynamic analysis by emf method and, the reference electrode powder is used in sensor fabrication. Electrochemical sensors are designed to measure the concentration, partial pressure or thermodynamic activity of the analytes.

Meanwhile, Potentiometric, amperometric and conductometric are the three common working modes of electrochemical sensors [110].

For potentiometric sensors, a local equilibrium is established at the sensor interface, where the electrode potential is measured, and information about the composition of a sample is obtained from the potential difference (voltage) between two electrodes due to the redox reactions which takes place at the electrode interfaces. The voltage is measured under conditions of essentially zero current. The voltage is logarithmically dependent on the concentration of the analyte. In considering an electrode reaction in equation (2.3),

$$O_x + ne = Red \qquad (2.3)$$

where O_x denotes an oxidant and Red denotes a reduced product.

The electromotive force, emf developed at the electrode interface under equilibrium conditions follow the Nernstian law, as seen in equation (2.4);

$$E = E^o - \frac{RT}{nF} \ln \left(\frac{C_O}{C_R}\right) \qquad (2.4)$$

Under isothermal conditions of known temperatures, the thermodynamic analysis by emf method can also be described as activity dependent;

$$E = E^o - \frac{RT}{nF} \sum v_{i \ \ln a_i} \qquad (2.5)$$

where E^o is the standard electrode potential, F is the Faraday constant, R is the gas constant, n is the number of electrons transferred in the external circuit to the other electrode and T is the absolute temperature, v_i are the stoichiometric numbers, positive for products (reduced species) and negative for reagents (oxidised species) while a_i are the activities [115]. The concentrations of O_x and Red are C_o and C_R, respectively. The relation between activity and concentration is as shown in equation (2.6)

$$a = \gamma_c C \tag{2.6}$$

where γ_c is the activity coefficient of unit concentrations [112]. Therefore, by measuring the activity at the reference electrode from equation (2.5), the unkown activity of the analyte can be determined. Therefore, substituting this activity into equation (2.6), the concentration can be determined.

It is noted that two half-cell reactions take place simultaneously at the electrodes and only one of the two reactions will involve the sensing. The other half is not interfering, reversible and known. In a nutshell, the emf measured, that is, representative of the concentration of the analyte is the difference between the potentials generated by the reactions on the two electrodes.

Amperometric sensors exploit the use of a potential applied between a reference and a working electrode, to cause the oxidation or reduction of an electroactive species. The applied voltage drives the electron transfer reaction of the electroactive species. The resulting current is a direct measure of the rate of the electron transfer reaction. It is thus reflecting the rate of the recognition event, and is proportional to the concentration of the target analyte. One drawback of amperometric sensors is that they respond to the chemical potential of the element being measured and not directly to the concentration [116]. This is because in process control (which requires direct measurements), concentration is the one being measured and not chemical potential. Therefore an amperometric sensor may not be very well suited for such actuating activities.

On the other hand, conductometric sensors are involved with the measurement of conductivity at a series of frequencies. Charge transfer processes causes polarisation hence the capacitative impedance is obtained. The concentration of charge is obtained through measurement of electrolyte resistance and is therefore not species-selective. As pointed out earlier, this review section focusses on the potientiometric sensors such as solid-state Mg-sensor designed with solid-state electrolyte and reference electrodes. Detailed analysis of various other forms or working modes especially, amperometric and conductometric sensors are available.

2.4.3.1 Basic component of electrochemical sensor

The three major components of an electrochemical sensor are;

i. the working electrode
ii. the reference electrode and
iii. the ion conductive electrolyte

The ion selective electrode is an indicator electrode capable of selectively measuring the activity of a particular ionic species. One electrode is the working (or sensing) electrode whose potential is determined by its environment. The second electrode is a reference electrode whose potential is fixed by the material containing the ion of interest at a constant activity. Since the potential of the reference electrode is constant, the value of the potential difference (cell potential) can be related to the concentration of the dissolved ion [117]. The quality, reliability and operation of an electrochemical sensor rely so much on highly ionic-conductive electrolyte. NASICON, $MgZr_4P_6O_{24}$, and other solid-state electrolytes are reliable electrolytes with ideal properties such as superionic potentiality and improved sinterability which ensures optimum density.

2.5 Conductivity of Solid-State Electrolyte

The solid-state electrolytes, $MgZr_4P_6O_{24}$ and $MgHf_4P_6O_{24}$ are believed to exhibit bulk ionic conductivity while, $MgCe_4P_6O_{24}$ shows the potential of both electronic and ionic. As regards to conduction mechanisms for ionic motion in solid-state electrolytes, three types of these mechanisms are regarded as vital; they are vacancy diffusion, interstitial mobility and interstitialcy motion.

The vacancy mechanism involves movement of atoms through the crystal in which lattice atoms jump to neighbouring unoccupied lattice sites. This is described in Figure 2.7;

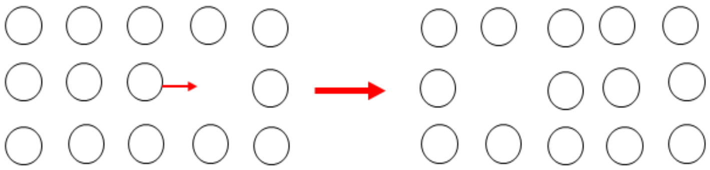

Figure 2-7 Vacancy mechanism for transport ions

The interstitial mechanism involves jump of particles directly from one interstitial site to another as seen in Figure 2.8;

Figure 2-8 Interstitial mechanism for transport ions

The interstitialcy mechanism involves the displacement of a particle located on a regular lattice site into the interstitial lattice by an interstitial particle, which itself then occupies the regular site. The interstitialcy mechanism is presented in Figure 2.9;

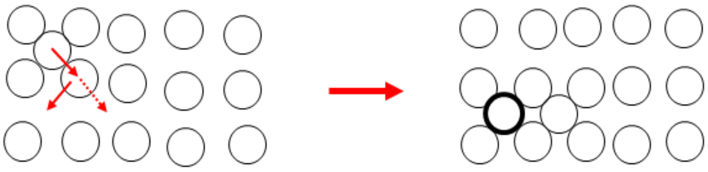

Figure 2-9 Interstitialcy mechanism showing two possible locations of ions after movement.

The electrical conductivity (s) of a solid is related to its defect concentration by

$$s = \sum_i c_i q_i \mu_i + nq_e\mu_e + pq_h\mu_h \qquad (2.7)$$

where c is the ionic defect concentration, q is the charge, μ is the mobility (which is the mean particle velocity per unit potential gradient), and the subscripts i, e and h denote ions, electrons and holes, respectively.

Solid-state electrolyte ion conductivity is generally described by the Arrhenius relation as described in Equation (2.8) [118, 119]

$$\sigma = \left(\frac{C}{kT}\right)\exp\left(-\frac{E_a}{kT}\right) \qquad (2.8)$$

where C is pre-exponential factor, E_a is the activation energy[3] ionic motion, k is the Boltzmann constant (8.617×10^{-5} eV K^{-1}), and T is the absolute temperature (in K).

---

[3] **Activation energy** is an energy barrier that the charge carrying ions must overcome to conduct through the material

Furthermore, the constant C in equation (2.8) is presented as;

$$C = \frac{1}{3}(Ze)^2 n d^2 \omega_o \tag{2.9}$$

where n is the defect density (interstitials in interstitial diffusion or vacancies in vacancy diffusion), d is the unit jump distance of an ion, ω_o is the attempt frequency while the total charge is Ze. The temperature dependence of the microscopic, mobile species diffusion coefficient D is correspondingly represented by an Arrhenius equation of the form $D = D_o \exp\left(-\frac{E_a}{kT}\right)$, where $D_o = \frac{C}{(Z^2 e^2 n)}$, so that the conductivity becomes

$$\sigma = n(Ze)^2 \left(\frac{D}{kT}\right) \tag{2.10}$$

Equation (2.10) is referred to as the Nernst-Einstein equation.

2.6 Reference Electrode

The reference electrode is to maintain a constant and stable chemical potential against which the activity of the unknown species are measured. It must therefore be entirely stable, reversible, good electronic conductivity, compatible with sensing electrode and must not react with the cell components. It must also be independent of any chemical potential changes at sensing electrode [112]. Reference electrodes can either be gaseous [120], liquid or solid materials. A gas reference system decreases the range of application of the sensor as well as sensitivity [121]. One key challenge in developing electrochemical sensors is the identification of stable reference electrodes, since any drift in the reference potential leads to a drift in the sensor output.

The solid-state reference electrode synthesised in this research was based on Figure (2.8), MgO-$MgCr_2O_4$ which is believed to be 50% of the binary phase diagram. The spinel $MgCr_2O_4$ compound was synthesised using Figure 2.10 as a guide in order to achieve a single homogeneous phase of the electrode. In maintaining stability of the reference electrode in molten non-ferrous alloys, the activity of MgO in $MgCr_2O_4$ according to equations (2.11)[122] can be determined and, the activity of MgO is thereafter reduced by the addition of Cr_2O_3 powders in a 1:1 mole ratio to $MgCr_2O_4$ for the synthesis of biphasic powder mixture, which is further calcined at 1090°C for 144h, the reference electrode, $MgCr_2O_4$+Cr_2O_3 is thereafter used as a component part of Mg-sensor.

According to Jacob [122];

$$MgO(s) + Cr_2O_3(cor) = MgCr_2O_4(sp),\ \Delta G_f^o = -45{,}200 + 5.36T(\pm 400)Jmol^{-1} \quad (2.11)$$

Equation (2.11) is rearranged as seen in equation (2.12);

$$MgCr_2O_4(sp) = MgO(s) + Cr_2O_3\ (cor),\ \Delta G^o = +45{,}200 - 5.36T(\pm 400)Jmol^{-1} \quad (2.12)$$

According to Fujii, *et. al.* [123];

$$Mg(l) + \frac{1}{2}O_2(g) = MgO(s),\ \Delta G_f^o = -\ 669350 + 135.0T\ (Jmol^{-1}) \quad (2.13)$$

Equation (2.13) is rearranged as seen in equation (2.14);

$$MgO(s) = Mg(l) + \frac{1}{2}O_2(g),\ \Delta G_f^o = +669350 - 135.0T\ (Jmol^{-1}) \quad (2.14)$$

Therefore, the net anodic and cathodic reaction from equation (2.12) and equation (2.14) is written as;

$$MgCr_2O_4(sp) = Mg(l) + Cr_2O_3\,(cor) + \frac{1}{2}O_2(g),$$

$$\Delta G_f^o = +714550 - 140.36T(\pm 400)Jmol^{-1} \qquad (2.15)$$

The thermodynamic activity of conducting species can be determined from the notion;

$$-nFE = \Delta G = \Delta G_f^o + RTlna_{ion} \qquad (2.16)$$

where n is the number of electrons participating in the electrode reaction (in this research, n = 2), F is the Faraday constant in Coulombs per mol, R is the gas constant, a_{ion} is the thermodynamic activity of the conducting species, E is the measured open potential (in V), and T is the temperature in Kelvin.

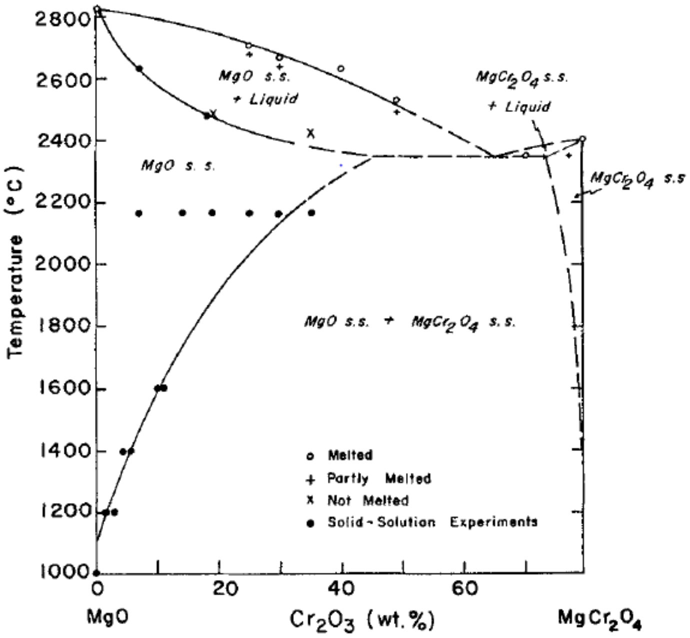

Figure 2-10 Phase equilibrium diagram for the MgO-$MgCr_2O_4$ system [124]

2.7 Solid-State Magnesium-Sensor

In the aluminium, copper and other chemical processing industries, the control of the chemical composition of metals during alloying and recycling is possible while in molten form. Today, the most commonly used technique for measuring composition of metals and other non-ferrous alloys is spectrometric analysis on cast samples [42]. The spectrometric analysis is a very rapid method however, it is retrospective. Online monitoring method will be significant step forward for rapid and accurate composition adjustment of the alloys.

Electrochemical sensors of galvanic cell fabrication based on simple thermodynamic measurements is a positive approach towards achieving online monitoring approach. The interest in making electrochemical sensors for use in molten aluminium is on the increase [50, 125, 126] and in other molten metals [127]. In designing a solid-state electrochemical sensor, the form of electrolyte is important in terms of durability, ease of fabrication, and simplicity of design [51]. The ceramic pellets approach in this research is suitable for the fabrication of Mg-sensor considering that the fabricated sensor being a bulk sensor in probe form is designed for high-temperature applications. Moreover, the solid-state electrolytes used in designing and fabrication of electrochemical sensor today have resolved the limitations identified during in line alloying process [45], such as durability and volatility or consistency of electrolytes.

2.7.1 Sensor design

Electrochemical cell illustrating the working principle of a sensor measuring element M in molten Al is shown as;

air, wire, M (Re)/M^{2+}-cation conductor/M (in Al), wire (2.17)

At equilibrium, the Nernst equation applies for the galvanic cell;

$$-nEF = RT\ln\left(\frac{a_M}{a_{M(Re)}}\right) \qquad (2.18)$$

where n is the units of charge carried, E is the measured open potential (in V) between the two electrode leads measured with a high-impedance, i.e., $\geq 10^{13}\Omega$ Keithley 6517A digital electrometer, F is Faraday constant, R is the gas constant, T is the temperature (in K), a_M is the activity of M in the metallic solution (molten Al), and $a_{M(Re)}$ is the activity of M in the reference material (or electrode).

The basic requirements for viable components in electrochemical cell are;

i. that the solid-state electrolyte has sufficiently high ionic (> 10^{-3} Scm^{-1}) rather than electronic conductivity. The solid-state electrolyte (M^{2+}-cation conductor) is the most important component of the sensor.
ii. that the activity of M in the reference material is reversible and only a function of temperature, and
iii. that the cell can readily reach an equilibrium.

2.8 Summary

This chapter provided insight into theoretical background of this research and it identified the research progress of sol-gel synthesis method, characterisation of the component parts of chemical sensors and electrochemical sensors (that is, the reference electrodes and non-ferrous metallic alloys) by critical literature review system. A robust literature review on chemical sensors, electrochemical sensors and other sensory devices bridge the dearth of information on the solid-state Mg-sensor which is an important sensor in casting, refining and alloying industries. The research data and areas of application of the electrochemical sensor is vital for improving production processes in our industries today. A background theory and research progress on the ionic conductivity of solid-state electrolytes, thermodynamic activity and transport number measurements by emf method, computation theory, stability theory and measurement, and structural analysis of the solid-state electrolyte shows the balance between the literature reviewed and the data achieved in this research. The theory of solid-state solution was extensively reviewed in this research as well. Seeing that the data on novel $MgHf_4P_6O_{24}$ and $MgCe_4P_6O_{24}$ solid-state electrolytes are not available in literature, the data of this research however becomes the reference data for both crystal structure analysis and electrical characterisation in future research. Finally, the design and fabrication of solid-state Mg-sensor was reviewed based on data in literature for Mg-based electrochemical sensors by using $MgZr_4P_6O_{24}$ solid-state electrolyte as ionic conductor. Meanwhile, $MgHf_4P_6O_{24}$, $MgCe_4P_6O_{24}$, and its corresponding solid-state solutions characterised as solid-state electrolytes in high-temperature Mg-sensors add novelty to this research with the new data.

Chapter 3

Experimental Methods

3.1 Synopsis

The starting point of this research is chemical synthesis of inorganic precursor materials. The synthesis of solid-state electrolyte is important because of tremendous increase in the requirements of solid-state electrolyte for various industrial applications. The chemical synthesis route is gaining rapid popularity for large-scale production of fine ceramics [128]. A feature of this research, particularly for solid-state electrolyte ceramics, is the interdisciplinary nature and at present time, chemistry is making an increasing important contribution [129] to the research, development and manufacture of novel ceramic materials, usually in the form of powders [130]. Sol-gel methods for ceramic synthesis, known as soft chemistry routes offer a lower temperature route to ceramic materials compared to the conventional solid-state reactions between oxide powders [130]. Sol-gel processing has been applied mainly to the synthesis of oxide ceramics with an exceptionally small size in the nanometer range. This chapter will describe the sol-gel preparation procedures of solid-state electrolyte ceramic, reference electrodes and experimental techniques adapted for the characterisation of synthesised materials. The equipment and related instruments used will be discussed. The aim of this research is to produce a cheap, stable, durable, reversible and high-temperature electrochemical sensor from its component parts; solid-state electrolytes and reference materials. To achieve the aim of this research, the following approach and principle was deployed;

i. Development of solid-state electrolytes and reference electrodes through the sol-gel synthesis and solid-state methods, respectively. The sol-gel synthesis method is cheap, simple and used to synthesis solid-state electrolytes at much lower temperature with lower carbon footprint compared to solid-state method for reference electrode synthesis.
ii. Since design and fabrication mechanism is made simple and user friendly, the potential to be readily available and affordable is high.

There are several techniques available for the synthesis of chemical powders. The two main approach for synthesis are the chemical method and mechanical method. Both methods have certain merits and demerits to consider. The mechanical method is considered viable for a large-scale production of bulk ceramic powders at low cost and easy adaptability. In conventional solid-state method, high-temperature and prolonged heating renders the particles coarse. Nanopowders prepared by the chemical route have shown improved homogeneity, densification and, chemical precursors deployed therefore can be refined to increase purity. However, in other cases, chemical routes involve complex techniques and the precursor chemicals are more expensive when compared to the conventional solid-state method [128].

This chapter will therefore describe the simple sol-gel synthesis route of the solid-state electrolytes; $MgZr_4P_6O_{24}$ (MZP), $MgHf_4P_6O_{24}$ (MHfP) and $MgCe_4P_6O_{24}$ (MCeP) from $MgZr_{4(1-x)}M_{4x}P_6O_{24}$ series with [MZP ($x = 0$), MHfP and MCeP ($x = 1$); M = Hf, Ce] and their solid-state solutions (with $0.1 \leq x \leq 0.9$). The solid-state synthesis method of a biphasic powder mixture ($MgAl_2O_4$ + α-Al_2O_3 or $MgCr_2O_4$ + Cr_2O_3 or $MgFe_2O_4$ + α-Fe_2O_3) oxides reference electrodes is also described alongside the characterisation techniques deployed on solid-state electrolytes and reference electrodes. Chapter three will end with description of the solid-state electrolytes behaviour in molten-Al, molten OFHC-Cu and Cu-0.5 wt.% Mg alloys at a melting temperature of 660-700^{o}C and 1250^{o}C, respectively with varying holding time for determining the stability property of solid-state electrolytes. The molten OFHC-Cu and Cu-0.5 wt.% Mg alloys was achieved in a graphite crucible at Rautomead International Ltd. (Dundee, Scotland, UK). Other non-ferrous alloying environment, such as, Zn-Mg, Al-Mg-Si, Al-Mg-Sc and Al-Mg-Zn-Si alloys are proposed for further research in future.

The design of an optimised solid-state magnesium sensor having optimum density, a highly conducting solid-state electrolyte and a constant, stable chemical electrode for the sensing of Mg^{2+}-cation in molten non-ferrous alloys is being characterised in this research. The experimental procedure outlined in Figure 3.1 shows the route to follow, and represented as a flowchart in Figure A1 (Appendix).

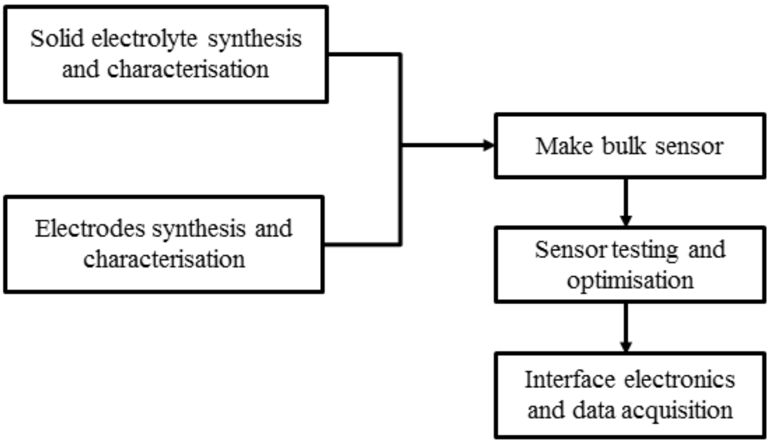

Figure 3-1 Experimental procedure

3.2 Materials Synthesis

This section comprises the synthesis procedures using the precursors in Table 3.1 for synthesising MZP, MHfP, MCeP solid-state electrolytes, its corresponding solid-state solutions, and the reference electrodes used in the designing and fabrication of high-temperature electrochemical sensors in this research. A detailed characterisation of the synthesised solid-state electrolytes, solid-state solutions and reference electrodes are presented and discussed in Chapter 4.

3.2.1 $MgZr_4P_6O_{24}$ (MZP)

Magnesium zirconium phosphate, $MgZr_4P_6O_{24}$ (MZP) from $MgZr_{4(1-x)}M_{4x}P_6O_{24}$ series ($x = 0$) is the primary solid-state electrolyte used in this research for sensor fabrication, testing and thermodynamic measurements. The MZP solid-state electrolyte serve as a reference-base solid-state electrolyte among the characterised series. The solid-state electrolyte is a stable electrolyte in electrochemical Mg-sensor design and fabrication for potential application in other electrochemical devices such as batteries, solid-oxide fuel cells, and electrolysers. A sol-gel method adapted from the works of Mielewczyk *et al.* [131] and Kazakos-Kijowski *et al.*[25] was modified in our materials synthesis laboratory to suit our research needs. The modified sol-gel synthesis method adapted in this research resulted in the formation of a pure single phase monoclinic MZP at a calcination temperature between 870°C to 900°C, which retained a stable phase at a sintering temperature range of between 1000 to 1300°C. The crystal structure of MZP ceramics is refined by the Rietveld method in space group $P2_{1/n}$ ($Z = 4$) at a room temperature of 25°C. It is important to note therefore that the precursor materials used in these syntheses are new and of high solubility in water. A single phase nanopowder was achieved because the sol-gel method homogenises and mix precursor materials at molecular level which likely increases reaction rates among the precursors in solution and decreases processing temperature during sintering of MZP solid-state electrolytes. A single phase nanopowders always ensure effective sintering, doping by substitution and conductivity.

A single phase nanopowder is difficult to obtain because the window of transformation from a single phase to a composite phase material with either minor extraneous peaks or a completely transformed phase is very small, and since calcination temperature is increased in the quest to obtain a single phase polycrystalline nanopowder, it has to be gradual otherwise, the powder starts coarsening and then sinters as a result. There is also a possibility of losing P_2O_5 at very high-temperature. Sintering temperature of the pellets from calcined powder is well monitored to avoid transformation of the already achieved single phase during sintering. The modified sol-gel synthesis route adopted influenced the calcination temperature to be greatly reduced to 800-900°C and for the sintering and phase stability temperature to be maintained at 1300°C. The sol-gel route yields single phase material of high purity and uniform composition with a simplified implementation technique because in the sol-gel procedure, mixing occur at molecular level among the precursors. The sol-gel method is unique and fascinating from both a scientific and practical point of view hence, sol-gel process has gained in recent years increasing relevance in the materials science field, being unanimously recognised for the uniqueness of its advantages in preparing some special materials and biomaterials with remarkable properties such as electrical, magnetic, optical or sensing, and others.

Further, solution chemistry offers many possible routes for “chemical manipulation” which allows different combinations in the synthesis of solids of diverse structures, compositions and morphologies [132].

As interest in electrochemical devices increased rapidly in the past few decades, the uniqueness of high-temperature ceramic materials became research interest dedicated to the optimal combination of host tetravalent Zr^{4+} site in $MgZr_4P_6O_{24}$ open for doping and co-doping in this research. The details of Mg^{2+}-cation conducting behaviour of $MgZr_4P_6O_{24}$ solid-state electrolyte prepared by the modified sol-gel synthesis method for design and fabrication of high-temperature electrochemical Mg-sensor is reported in this research, knowing that electrochemical sensors based on solid-state electrolytes have displayed several advantages in the processing of molten metals [13]. Mg-sensors therefore are fabricated for sensing chemical composition of Mg in molten non-ferrous alloys during refining, casting and alloying operations in related industries [133-135].

Table 3-1 Precursor materials used in this research. *SA:* Sigma Aldrich, *AA:* Alfa Aesar, *FS*: Fisher Scientific, *GF:* Good Fellow, *GP:* General Purpose, *SSE:* Solid-State Electrolyte, *RE:* Reference Electrode, *RM:* Rautomead, *SE:* Sensing Electrode

Chemical	**Source**	**Grade**	**Precursor for:**
$MgCO_3$	SA	$\geq$ 40% Mg	$Mg(NO_3)_2$, RE synthesis
NH_4OH	FS	35% NH_3	Neutralise pH of SSE
HNO_3	SA	70%	$Mg(NO_3)_2$ synthesis
$HfCl_4$	AA	99.9%	$MgHf_4P_6O_{24}$ SSE
$Ce(NH_4)_2(NO_3)_6$	SA	$\geq$ 98.5%	$MgCe_4P_6O_{24}$ SSE
$Ce(NO_3)_3.6H_2O$	SA	99%	$Mg_{0.5}Ce_2P_3O_{12}$ SSE
$ZrOCl_2.8H_2O$	SA	$\geq$ 99.5%	$MgZr_4P_6O_{24}$ SSE
$NH_4H_2PO_4$	AA	99+%	SSE
γ-Al_2O_3	AA	99.7%	RE
Cr_2O_3	SA	98+%	RE
α-Fe_2O_3	SA	$\geq$ 99%	RE
Cu-0.5 wt.% Mg	RM	60%	SE
OFHC-Cu	RM	99.95%	SE
C_3H_6O	FS	100%	GP
Al - Block	GF	97.8%	SE
Mg - Rod	GF	99.9%	SE

The motivation for sol-gel processing is primarily for achieving potentially high level purity and homogeneity of synthesised nanopowders of solid-state electrolytes. The lower processing temperature associated with sol-gels are compared with traditional glass melting or ceramic powders methods [136]. Owing to the possibilities of leading chemical reactions occurring in solution through the sol-gel procedure, obtaining of nanosized materials with predetermined properties is a relatively new technology. One of the advantages considered in preparing oxide materials by using sol-gel method is the possibility of controlling their microstructure and homogeneity. This is important knowing that most applications require homogeneous materials.

Molecular chemical precursors are transformed into an oxide network by hydrolysis and condensation reactions. Two routes are currently used depending on the nature of the molecular precursors: metal alkoxides in organic solvents or metal salts in aqueous solutions [137].

In the case of sol-gel powders, sol-gel process refers to the processing into solution of desired solid materials which do not deposit, so they are not precipitates. They can be sols (composed from discrete units which remain dispersed in the liquid) or gels (made up from solid tri-dimensional networks spread into the whole liquid matrix). The result of the succession of reactions above assumes the following transformation steps of the precursors in aqueous medium: hydrolysis → polymerisation → nucleation → growth. In the case of un-ionised precursors, as alkoxides, the hydrolysis and polymerisation-condensation reactions lead to some linear polymeric structures containing M-O-M bonds, favoured by a slow hydrolysis compared to the polymerisation [138].

The advantages of the sol-gel method in the preparation of mono-component materials refer to the very high purity due to the quality of the available precursors and to the possibility to tailor the textural properties of the product, especially the surface area and the pore size distribution. For the multi-component systems, the following specific advantages can be mentioned: the ability to control both structure and composition at molecular level, the possibility to introduce several components in a single step, and the power to impose kinetic constraints on a system and thereby stabilise metastable phases. Furthermore, the controlled shape and size (usually, mono-disperse), and the nanometer size of the particles must be mentioned.

The chemical compounds Zirconium (IV) oxychloride octahydrate ($ZrOCl_2.8H_2O$), Magnesium nitrate [$Mg(NO_3)_2$], and Ammonium dihydrogen phosphate ($NH_4H_2PO_4$) were used as precursors for the active oxides ZrO_2, MgO and P_2O_5 respectively, in the synthesis of $MgZr_4P_6O_{24}$.

3.2.1.1 Synthesis

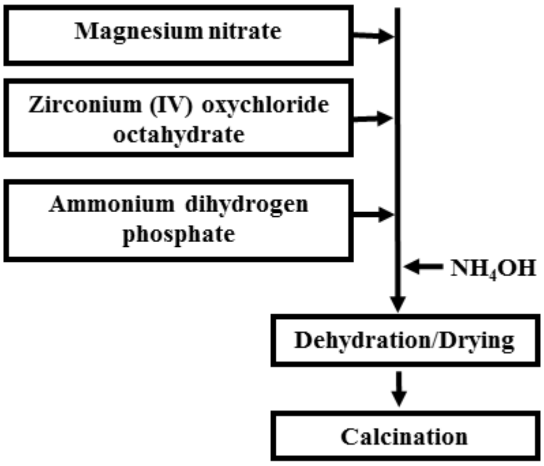

Figure 3-2 Schematic of the MZP synthesis

Appropriate amount of precursor materials were weighed and dissolved in separate beakers of distilled water labelled A, B, C as shown in Figure 3.3. Beaker A contains aqueous $Mg(NO_3)_2$ solution prepared by dissolving appropriate amount of $MgCO_3$ in aqueous HNO_3. Beaker B contains aqueous solution of $NH_4H_2PO_4$ and Beaker C contains aqueous solution of $ZrOCl_2.8H_2O$. The aqueous solutions of $Mg(NO_3)_2$ and $NH_4H_2PO_4$ separately prepared were mixed together while continuously stirring in a beaker with a magnetic stirrer to form a homogeneous sol. To this mixture of the sol, an appropriate amount of aqueous $ZrOCl_2.8H_2O$ solution was added dropwise through the burette to form a homogeneous gel. $ZrOCl_2.8H_2O$ solution acted as a precipitant in the mixture to form a homogeneous acidic gel. The order of mixing these solutions is important to obtain the homogeneous gel. NH_4OH was thereafter added dropwise to the homogeneous gel to neutralise the pH from its initial value of 1.2 to a final pH of 10.2. The final homogeneous gel was stirred for 1h and subsequently, the gel was dried at 100°C for *ca* 24h on a hot plate. The synthesis stoichiometric reaction in equation (3.1) is presented as;

$$Mg(NO_3)_2\,(aq) + 4ZrOCl_2.8H_2O\,(aq) + 6NH_4H_2PO_4\,(aq)$$
$$= MgZr_4P_6O_{24}\,(s) + 6NH_4Cl\,(aq) + 2HCl\,(aq) + 2HNO_3\,(aq) + 36H_2O\,(l) \qquad (3.1)$$

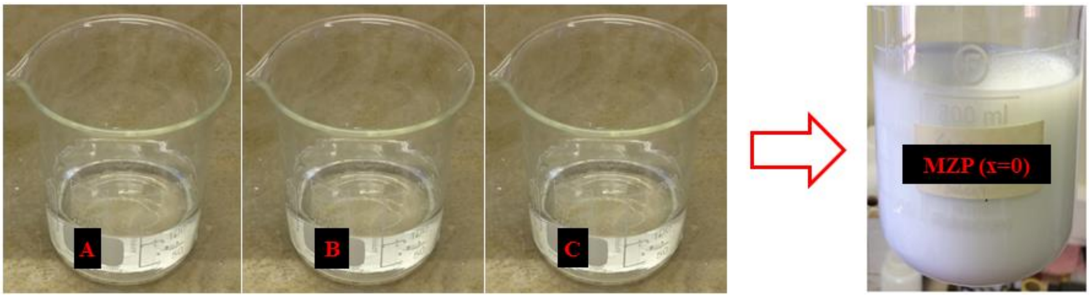

Figure 3-3 MZP synthesis of precursor materials and a resultant gel solution

After drying the gel, the resultant dried powder was mechanically ground with an agate mortar and pestle. The ground xerogel powder is whitish in colour and did not show any clear colour change during thermal analysis and calcination as seen in Figure 3.4.

Figure 3-4 Synthesised MZP of (a) dried xerogel powder (b) calcined nanopowder

The dried xerogel powder was thereafter analysed for its weight loss and heat flow as a function of temperature using the TGA and DSC measurement where the calcination temperature was predicted thereof. The ground xerogel powder was thereafter calcined at 900°C for 3h in a top loading muffle furnace. It was subsequently calcined at 800°C for 0.5h in the same furnace for purpose of comparing the average crystallite size as a function of temperature. To aid pressing and green densification, 1 wt.% binder, Ciba Glascol HA4, was added dropwise into the calcined powders prior to pressing, it was subsequently dried at 100°C for 0.5h and later pressed into pellets of 13mm Ø and

3.8mm thickness using uniaxial press at a compressive pressure of 5kN. The resultant green body-pellets were initially heated between 400-450°C for the purpose of burning out the binder before final sintering at the range of $1000 \leq T/ ^{o}C \leq 1550$ for 24h at $10^{o}C\ min^{-1}$ heating rate. During sintering, the pellets were then embedded in a powder of the same composition in a closed alumina crucible so as to limit loss of P_2O_5 [119] due to volatilisation which easily occurs at high-temperatures. Special precautions are often used in the sintering of phosphate based electroceramics due to the volatilisation of P_2O_5. Atmosphere control is important to prevent loss of volatile components and to also avoid reduction reactions. Therefore, the tile, boat or alumina tray assembly was surrounded with an atmosphere powder of the same composition as the pellet, taking care not to touch the powder. An upturned alumina crucible was placed over the sample pellets arrangement, and an outer alumina crucible was closed with an alumina lid before insertion into a high-temperature sintering furnace. In order to obtain optimum electrical properties, it was necessary to determine the optimum sintering temperature for the maximum possible bulk density without destroying the sample pellets. A constant sintering time (24h) and heating/cooling rate ($10^{o}C\ min^{-1}$) were maintained, while varying the sintering temperature. Following sintering, any powder adhered to the ceramic surfaces was removed using SiC abrasive papers.

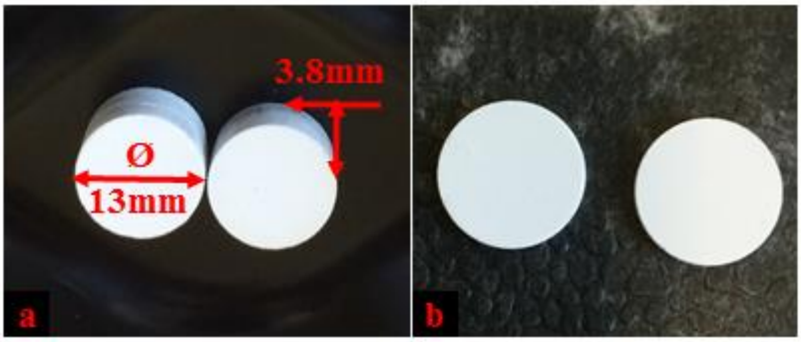

Figure 3-5 Synthesised MZP of (a) green pellets (b) sintered pellets at 1300°C

3.2.2 $MgHf_4P_6O_{24}$ (MHfP)

3.2.2.1 Synthesis

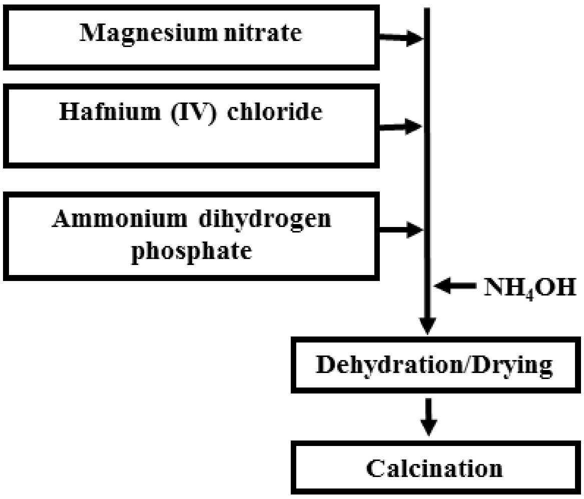

Figure 3-6 Schematic of the MHfP synthesis

$MgHf_4P_6O_{24}$ xerogel electrolyte was prepared by the sol-gel method. An appropriate stoichiometric amounts of the analytical grade of the precursor materials used were weighed and dissolved in separate beakers of distilled water labelled D, E, F as shown in Figure 3.7. Beaker D contains aqueous solution of $Mg(NO_3)_2$ solution. The aqueous $Mg(NO_3)_2$ solution used in this research was prepared by the dissolution of $MgCO_3$ in aqueous HNO_3. The Beaker E contains aqueous solution of $NH_4H_2PO_4$ while Beaker F contains aqueous solution of $HfCl_4$. Meanwhile, the aqueous solutions of $Mg(NO_3)_2$ and $NH_4H_2PO_4$ were mixed together while stirring in a beaker with a magnetic stirrer to form the homogeneous sol. Furthermore, an appropriate amount of aqueous $HfCl_4$ solution was prepared separately and then added dropwise to the homogeneous sol prepared earlier using a burette to produce white wet gel. To neutralise the mixture, concentrated NH_4OH was gradually added dropwise to the homogeneous wet gel to adjust pH of the white gel from the initial pH of 0.2 to a final pH of 8.9. The final white gel solution was stirred for 1h, and then slowly dried at 100°C for *ca* 24h on a hot plate to achieve a dry white xerogel powder. After drying, the xerogel powders were mechanically ground with an agate mortar and pestle. The chemical synthesis stoichiometric reaction is presented in equation (3.2);

$$
\begin{aligned}
&Mg(NO_3)_2\,(aq) + 4HfCl_4\,(aq) + 6NH_4H_2PO_4\,(aq) \\
&\quad = MgHf_4P_6O_{24}\,(s) + 6NH_4Cl\,(aq) + 10HCl\,(aq) + 2HNO_3\,(aq)
\end{aligned}
\tag{3.2}
$$

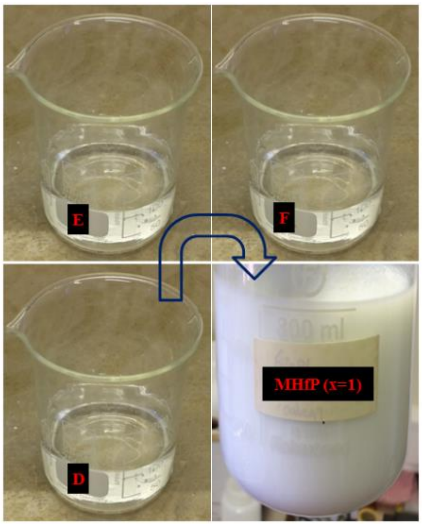

Figure 3-7 MHfP synthesis of precursor materials and resultant gel solution

The ground xerogel powders synthesised using the stoichiometric equation (3.2) did not show any real colour transition from its original whitish colour as observed during thermal analysis and subsequently, during calcination as seen in Figure 3.8.

Figure 3-8 Synthesised MHfP of (a) dried xerogel powder (b) calcined nanopowder

The ground xerogel powder was then analysed for its weight loss and heat flow as a function of temperature using TGA and DSC measurements to determine calcination and transformation temperature. After the TGA-DSC measurement, the dried xerogel powder was calcined at 900°C for 3h in accordance with the TGA-DSC data using the top loading muffle furnace. The xerogel powder was also calcined at 800°C for 0.5h in the same muffle furnace for purpose of comparing the crystallite size as a function of temperature. The calcined powder mixed with 1 wt.% binder, Ciba Glascol HA4, subsequently dried at 100°C for 0.5h and later pressed into pellets of 13mm Ø and 3.8mm thickness using uniaxial press at a compressive pressure of 5kN. The resultant green body-pellets were initially heated between 400-450°C for the purpose of burning out the binder prior final sintering at $1000 \leq T/\ ^{o}C \leq 1550$ for 24h at a heating rate of 10°C min^{-1}. During sintering, the pellets were embedded in a powder of the same composition in a closed alumina crucible in order to protect the loss of volatile oxides, like P_2O_5 [119] from the sintering pellets at high-temperatures. Similarly, a quantity of the same calcined powders was placed on the surface of a tile, boat or alumina trays before the pellets were placed and then covered with the same calcined powders and covered with a crucible lid before sintering in a top-loading muffle furnace. This procedure will therefore prevent any potential reaction between the alumina crucible and the solid-state electrolyte pellets by enabling the calcined powders as a sacrificial material. This may also limit the loss of possible volatiles during sintering. It is quite interesting to note that the green pellets maintained its whitish colour after sintering.

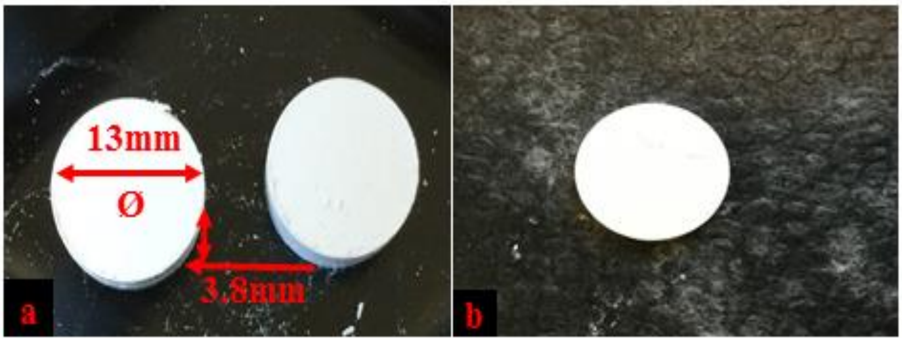

Figure 3-9 Synthesised MHfP of (a) green pellets (b) sintered pellet at 1300°C

3.2.3 $MgCe_4P_6O_{24}$ (MCeP)

3.2.3.1 Synthesis

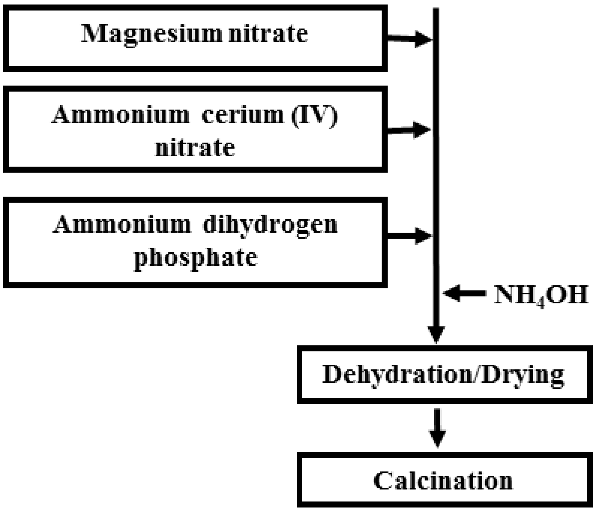

Figure 3-10 Schematic of the MCeP synthesis

$MgCe_4P_6O_{24}$ xerogel electrolyte was also prepared by sol-gel method. Stoichiometric amounts of the precursor materials were weighed and dissolved in separate beakers of distilled water labelled G, H, I as shown in Figure 3.11. Beaker G contains aqueous

$Mg(NO_3)_2$ solution. The aqueous $Mg(NO_3)_2$ solution was prepared by dissolution of an appropriate stoichiometric amount of $MgCO_3$ in aqueous HNO_3. This additional procedure was adopted to achieve a soluble $Mg(NO_3)_2$ solution since $MgCO_3$ like other CO_3^{2-} compounds are insoluble in water. Beaker H contains aqueous $NH_4H_2PO_4$ while Beaker I contains aqueous $Ce(NH_4)_2(NO_3)_6$ solution. The aqueous solutions of $Mg(NO_3)_2$ and $NH_4H_2PO_4$ in beaker G and H were mixed together while stirring in a beaker with a magnetic stirrer to form homogeneous sol. Furthermore, a stoichiometric amount of $Ce(NH_4)_2(NO_3)_6$ solution was prepared separately and then added dropwise to the homogeneous sol prepared earlier using a burette to precipitate a yellow wet gel. The homogeneous gel is acidic as a result of the precipitation therefore, to neutralise the mixture, concentrated NH_4OH was gradually added dropwise to the homogeneous yellow wet gel to adjust pH of the gel from initial 0.1 to a final pH of 8.9. The final yellow gel solution was stirred for 1h, and later dried at 100°C for *ca* 24h on a hot plate so as to achieve dried xerogel powders. The resultant dried xerogel powders was ground mechanically using an agate mortar and a pestle. The synthesis stoichiometric reaction presented in equation (3.3) shows visible colour changes as follows;

$$Mg(NO_3)_2\,(aq) + 4Ce(NH_4)_2(NO_3)_6\,(aq) + 6NH_4H_2PO_4\,(aq)$$
$$= MgCe_4P_6O_{24}\,(s) + 12HNO_3\,(aq) + 14NH_4NO_3\,(aq) \qquad (3.3)$$

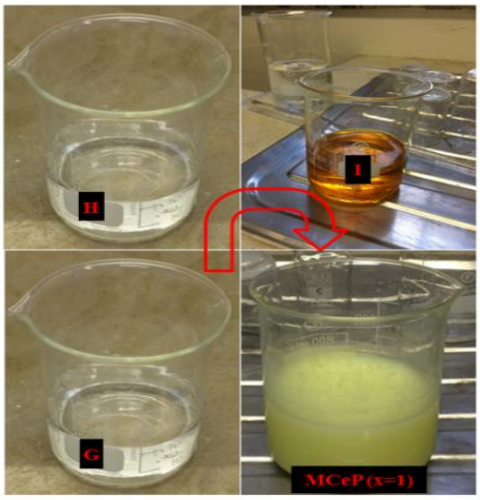

Figure 3-11 MCeP synthesis of precursor materials and resultant gel solution

The ground xerogel powder synthesised according to the stoichiometric equation (3.3) shows a unique colour transition from synthesis → calcination → sintering. The colour transition was observed during thermal analysis (i.e., TGA-DSC measurement) on the dried yellow xerogel powders to a leaf green nanopowders after calcination at 900°C for 3h as presented in Figures 3.12.

Figure 3-12 Synthesised MCeP of (a) dried xerogel powder (b) calcined nanopowder.

The transition from yellow xerogel powders → leaf green powders after calcination may have resulted from the aqueous orange $Ce(NH_4)_2(NO_3)_6$ precursors that precipitates yellow homogeneous gel during synthesis.

The calcination and possible transformation temperature of the dried xerogel powder was predicted by analysing its weight loss and heat flow as a function of temperature using TGA-DSC measurement. After the TGA-DSC measurement, the dried xerogel powder was calcined at 900°C for 3h in agreement with the TGA-DSC data using the top loading and front-loading muffle furnace. The xerogel powder was also calcined at 800°C for 0.5h in the same furnace for purpose of comparing the crystallite size as a function of temperature. The calcined powder mixed with 1 wt.% binder, Ciba Glascol HA4, subsequently dried at 100°C for 0.5h and later pressed into pellets of 13mm Ø and 3.8mm thickness using the uniaxial press at a compressive pressure of 5kN. The resultant green body-pellets were initially heated at 400-450°C for purpose of burning out the binder prior final sintering at $1000 \leq T/^{o}C \leq 1300$ for 24h at a heating rate of 10°C min^{-1}. During sintering, the pellets were embedded in powders of the same composition in a closed alumina crucible in order to protect the loss of volatile oxides such as P_2O_5 [119] in the sintering pellets at high-temperatures. A quantity of the same calcined powder was placed on the surface of a tile, boat or alumina trays before the pellets were placed and later covered with the same calcined powder and then covered with crucible lid before sintering in a top-loading muffle furnace. This procedure will, therefore, prevent any potential reaction between the alumina crucible and the solid-state electrolyte pellets by enabling the calcined powder as a sacrificial material. This process may limit the loss of possible volatiles and contamination during sintering. In Figure 3.13, the trend of colour transition continues from leaf green observed on the calcined nanopowders in Figure 3.12 and the compressed green pellets thereafter to a deep green pellet after sintering at 1300°C for 24h as presented in Figure 3.13.

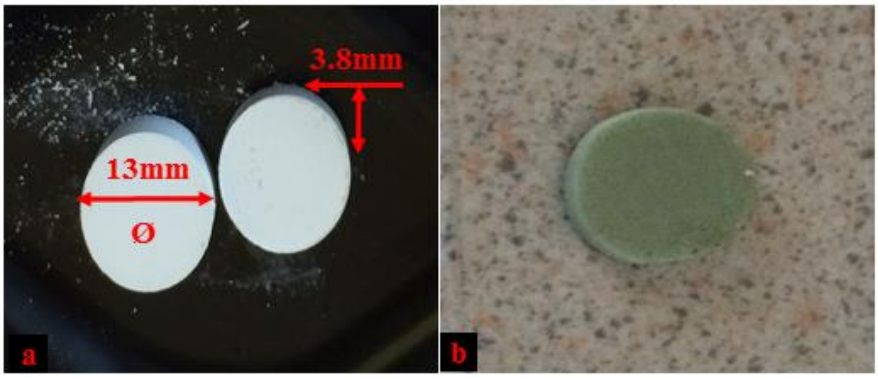

Figure 3-13 Synthesised MCeP of (a) green pellets (b) sintered pellet at 1300°C

3.2.4 Solid-state solutions

$MgZr_{4(1-x)}M_{4x}P_6O_{24}$ solid-state solution with M representing active precursor oxides, HfO_2 and CeO_2 for partial substitution reaction with ZrO_2 oxide using the modified sol-gel synthesis procedures used in the end-members synthesis (when x = 1), and the chemical mole ratio of $0.1 \leq x \leq 0.9$ range was considered in the solid-state solution synthesis. In this research, Zr^{4+} B-site in $MgZr_4P_6O_{24}$ was shared with $Hf^{4+}$and Ce^{4+}, respectively, at different stoichiometric ratio. $MgM_4P_6O_{24}$ (with M = Hf, Ce) was also synthesised when the Zr^{4+} B-site was completely substituted with either HfO_2 or CeO_2 oxides to form the end-members solid-state electrolytes, $MgM_4P_6O_{24}$ (with M = Zr, Hf, Ce). The structural framework of $MgZr_4P_6O_{24}$, with Zr-O-P consisting of corner-shared PO_4 tetrahedra and ZrO_6 octahedra, similar to $Na_{1+x}Zr_xSi_xP_{3-x}O_{12}$ ($0 \leq x \leq 3$), called Sodium Super Ionic Conductor, NASICON, when x = 2 [40] formed with tetrahedral SiO_4 and PO_4, and hexagonal ZrO_6 polyhedral, linked by oxide ions to form a three dimension, 3D network structure, which is suitable for ion migration in all the three dimensions [139].

3.2.4.1 Synthesis

The precursors of $Mg(NO_3)_2$, $NH_4H_2PO_4$, $ZrOCl_2.8H_2O$, $HfCl_4$ and $Ce(NH_4)_2(NO_3)_6$ reagent grade powders were deployed in this solid-state solutions synthesis using the modified sol-gel method developed in our synthesis laboratory. Appropriate aqueous solutions of the precursor reagents were prepared following $MgZr_{4(1-x)}M_{4x}P_6O_{24}$ stoichiometric equation using the number of moles of each precursor compound. The procedures adapted for chemical synthesis of $MgZr_4P_6O_{24}$, $MgHf_4P_6O_{24}$, $MgCe_4P_6O_{24}$ solid-state electrolytes was re-modified in the sense that solution of $ZrOCl_2.8H_2O$ and $HfCl_4$ or $Ce(NH_4)_2(NO_3)_6$ were mixed together according to their number of moles. Different solid-state solutions of $MgZr_{4(1-x)}M_{4x}P_6O_{24}$ were prepared as the number of moles ranging from $0.1 \leq x \leq 0.9$, resulting in 18 different samples for characterisation. As earlier identified, the amount of reacting precursor compound depends on their molar mass and number of moles, therefore, an appropriate solution of $Mg(NO_3)_2$ and $NH_4H_2PO_4$ separately prepared and mixed together forms homogeneous sol labelled J while stirring. Molar solutions of $ZrOCl_2.8H_2O$ and $HfCl_4$, or $ZrOCl_2.8H_2O$ and $Ce(NH_4)_2(NO_3)_6$, were also prepared and mixed together in separate beakers labelled K, L accordingly. In beaker J, an appropriate amount of molar solutions in beaker K and L were added separately to form homogeneous gel of Zr doped with Hf and Ce, respectively. In using the $MgZr_{4(1-x)}M_{4x}P_6O_{24}$ (x = 0.1 and M = Hf, Ce) solid-state solution series, the resulting compound $MgZr_{3.6}Hf_{0.4}P_6O_{24}$ and $MgZr_{3.6}Ce_{0.4}P_6O_{24}$ were synthesised separately and then characterised for their structural and electrical properties. The same procedure was followed in synthesising the $MgZr_2Hf_2P_6O_{24}$ and $MgZr_2Ce_2P_6O_{24}$ (x = 0.5) solid-state electrolyte. Furthermore, $MgZr_{0.4}Hf_{3.6}P_6O_{24}$ and

$MgZr_{0.4}Ce_{3.6}P_6O_{24}$ (x = 0.9) were synthesised and characterised following the same sol-gel synthesis route as adapted in the previous solid-state solutions to complete this series. The acidic homogeneous gels with an average pH of 1.20 were neutralised using NH_4OH which was added dropwise to maintain an average pH of 10.20 for both samples while stirring for 1h, and the gel was later dried at 100°C for *ca* 24h on a hot plate. The dried xerogel powder was ground using an agate mortar and pestle then calcined at 900°C after DSC-TGA analysis and HT-XRD. The crystallographic phases of the calcined nanopowders was determined using XRD at ambient conditions. The calcined nanopowders was then pressed into pellets of 13mm Ø and 3.8mm thickness, then sintered at 1300°C for 24h while the different phases were monitored using XRD. The sintered pellets were further prepared for impedance measurement using Solartron SI1260 FRA.

Characterisation Technique

Thermogravimetric analysis (TGA) and differential scanning calorimetry (DSC) is a combined thermal analysis technique using the simultaneous thermal analyser, STA 8000 model (PerkinElmer, Seer Green, UK) to determine an effective optimisation of calcination conditions, thermal oxidation behaviour, weight loss and thermal stability of dried $MgZr_4P_6O_{24}$, $MgHf_4P_6O_{24}$, and $MgCe_4P_6O_{24}$ xerogel powders, respectively and of the solid-state solutions in controlled atmosphere at a flow rate of $50mL\ min^{-1}$ using a constant heating/cooling rate, $\beta = 10^oC\ min^{-1}$ between 30 and 1000°C. The XRD and HT-XRD measurements on both powders and pellets of the solid-state electrolytes for investigating crystallinity evolution, phase formation and phase transition using a Philips X'Pert diffractometer (PANalytical B.V., Almelo, Holland) and Bruker D8 advance (Karlsruhe, GmbH) at different intervals. The vibrational mode and chemical bonds of the precursor oxides, xerogels and calcined nanopowders of the synthesised solid-state electrolyte powders were characterised using the FTIR and Laser-Raman scattering (LRS) spectroscopy; Nicolet iS10 FTIR spectrometer (ThermoFisher Scientific, Hertfordshire, UK) equipped with a deuterated triglycine sulphate (DTGS)-KBr detector analysed the chemical vibrational mode and bonds of the synthesised xerogel powders and calcined nanopowders. Renishaw inVia Raman spectrometer (Renishaw plc., New Mills, Wotton-under-Edge, Gloucestershire, UK) equipped with a confocal DM 2500 Leica optical microscope (Leica Microsystems GmbH, Wetzlar, Germany), an Ar-ion laser ($\lambda = 514$ nm) was used as the excitation source with a laser power of 25 mW, and thermoelectrically cooled CCD detector (RenCam CCD detector Renishaw plc., New Mills, Gloucestershire, UK) with 50% laser power performance and 2 cm^{-1} spectral resolution. The composition of chemical oxides in the calcined nanopowders were analysed using X-ray fluorescence, XRF (Rigaku Primus WD 4KW, Stockport, UK). Katanax K1 Prime automatic fusion fluxer (Stanmore, UK) was deployed during sample preparation by fusion using Lithium Borates (66.67% $Li_2B_4O_7$, 32.83% $LiBO_2$, 0.5% LiBr) flux for preparing sample fusion beads in-laboratory standards with acceptable precision and accuracy for ED-XRF analysis and the measured data compared with a standard in comparison. The microstructure of representative sample pellets were analysed using SEM (Carl Zeiss EVO MA15, Jena, GmbH) equipped with EDS and Oxford Aztec X-Act EDS spectrometer attached to Carl Zeiss EVO MA15 for the elemental composition analysis of the sample pellets *in situ* at an accelerating voltage of 20 kV. The SEM images were obtained on a freshly broken surfaces of the sample pellets coated with a very thin platinum layer to avoid the sample pellets from charging. The particle size, surface morphology, crystalline phase, lattice fringe of HR-TEM, interplanar spacing, SAED patterns and the EDS elemental composition variation within the nanopowders of the solid-state electrolytes composition and those of their solid-state solutions were investigated by FEI Titan^3 Themis 300 S/TEM and FEI Tecnai G2.

The binder treated calcined nanopowders were pressed into pellets of 13mm Ø and 3.8mm thickness with a uniaxial steel die at a compressive pressure of 5kN after the powders were dried at 100°C, then sintered at 1300°C for 24h (heating/cooling rate, $\beta = 10^{o}C\ min^{-1}$). For measurement of electrical properties, the sintered electrolyte pellets were mildly ground to achieve a flat surface without significantly altering the pellet thickness. Platinum paste (Sigma-Aldrich, UK) was lightly applied to the opposite parallel faces of the sintered pellets and allowed to dry before firing in a tube furnace at 800°C for 0.5h to eliminate organic components, and form contact electrodes. The electrical conductivity was recorded as a function of temperature and frequency using ac-impedance analyser, the Solartron SI1260 Frequency Response Analyser, FRA (Solartron Analytical, Farnborough, Hampshire, UK) in the temperature range from 25 to 800°C and frequency range from 100mHZ to 32MHz and a fixed applied voltage of 100mV, at intervals of 50-100°C depending on the direction of measurements to monitor the reversibility and data accuracy during thermal cycling in this research.

3.2.5 Electrodes

3.2.5.1 Reference electrodes

The reference electrode constitute an integral part of electrochemical measurements. The miniaturisation and simplification efforts of electrochemical measuring systems often fail because of the need of large electrolyte reservoirs and liquid junctions [140]. Solid-state reference electrodes should be thermodynamically and chemically stable, compatibility with solid-state electrolytes and reversible at the operating temperatures and in the measurement atmosphere [112]. Solid-state reference electrodes must not react with any cell components, and are usually more suitable than liquid or bulky gas equivalent [141]. Also, the solid-state reference electrodes maintain a constant, stable and known chemical-electrode potential against which the activity of the unknown species are measured. It must remain completely independent of the changing potential at the measuring electrode. The biphasic powder mixture of $MgAl_2O_4$+α-Al_2O_3 or $MgCr_2O_4$+Cr_2O_3 or $MgFe_2O_4$+ α-Fe_2O_3 were employed as reference electrodes for the design and fabrication of solid-state Mg-sensors necessary for determining the activity of MgO (a_{MgO}), and that it does not form $MgCO_3$ when exposed to an environment containing CO_2 gas because the Gibbs free energy of the reactions, ΔG_f has positive energy change.

The $MgAl_2O_4$, $MgCr_2O_4$ and $MgFe_2O_4$ spinel are synthesised by the conventional solid-state method from $MgCO_3$ and then blend into biphasic powder mixture with the addition of α-Al_2O_3, Cr_2O_3 and α-Fe_2O_3, respectively in equal mole ratio of 1:1 using binary phase diagram:

$$MgCO_3 + \alpha\text{-}Al_2O_3 = MgAl_2O_4 + CO_2 \tag{3.4}$$

$$MgCO_3 + Cr_2O_3 = MgCr_2O_4 + CO_2 \tag{3.5}$$

$$MgCO_3 + \alpha\text{-}Fe_2O_3 = MgFe_2O_4 + CO_2 \tag{3.6}$$

Thermodynamics considerations

From the phase equilibria of $MgO-Cr_2O_3-SiO_2$ ternary system [142], the binary system $MgO-Cr_2O_3$ [143] was applied as reference electrodes in thermodynamic measurement and sensor fabrication. The binary system however shows that only one intermediate compound, $MgO.Cr_2O_3$ or spinel $MgCr_2O_4$ is found with no indication of other solid-state solutions between $MgO.Cr_2O_3$ and either MgO or Cr_2O_3, the spinel phase formed using the conventional solid-state method is confirmed using X-ray diffraction (XRD) analysis [144].

Synthesis

Appropriate molar amounts of precursor carbonates, $MgCO_3$ and the oxides, α-Al_2O_3 or Cr_2O_3 or α-Fe_2O_3 were weighed, mixed and ground separately using an agate mortar and pestle until the powders were homogeneously mixed. The mixture is according to the reactions in Equations (3.4-3.6). The carbonate and oxides were mixed in their solid-state and calcined at 1090°C for 144h to form a single phase $MgAl_2O_4$, $MgCr_2O_4$ and $MgFe_2O_4$ spinel, respectively. X-ray diffraction analysis (XRD) was then used for phase identification of the calcined $MgAl_2O_4$, $MgCr_2O_4$ and $MgFe_2O_4$ spinel powders, respectively. Single spinel phase of the respective calcined nanopowders were used in preparing the $MgAl_2O_4$+α-Al_2O_3, $MgCr_2O_4$+Cr_2O_3 and $MgFe_2O_4$+α-Fe_2O_3 biphasic powder mixture used as reference electrode in this research. But, the thermodynamic data of spinel $MgCr_2O_4$ [122] and $MgAl_2O_4$ [145] was monitored to determine the activity of magnesium oxide, (a_{MgO}) in $MgCr_2O_4$ and $MgAl_2O_4$, respectively, thereby assessing their compatibility and chemical stability against the different solid-state electrolytes characterised for both thermodynamic studies, kinetic (transport number) studies and sensor testing at high-temperatures.

3.2.5.2 $MgCr_2O_4$ + Cr_2O_3

Based on the thermodynamic data and activity of MgO in $MgCr_2O_4$ [122], biphasic powder mixture of $MgCr_2O_4$+Cr_2O_3 was used as the reference electrode for different sensor fabrication in this research. The $MgCr_2O_4$+Cr_2O_3 biphasic powder mixture was considered because it is believed to be the most stable and suitable compound amongst the three synthesised reference electrodes. Also, the reference electrode oxide cannot be easily attacked by either acids or alkali thereby prolonging the life of the sensor. Appropriate amounts of Cr_2O_3 powder is then added to a single phase $MgCr_2O_4$ spinel powders formed at 1090°C for 144h in a 1:1 molar ratio to form a biphasic powder mixture of $MgCr_2O_4$+Cr_2O_3. While the biphasic powder mixture was calcined, the presence of $MgCr_2O_4$ spinel and Cr_2O_3 phase was confirmed by X-ray diffraction. The same procedure was used in preparing a biphasic powder mixture of $MgAl_2O_4$+Al_2O_3 or $MgFe_2O_4$+Fe_2O_3 which served trial purposes only in this research. $MgFe_2O_4$ was not considered because α-Fe_2O_3 has the tendency of being reduced from +3 to +2 thereby rendering the reference electrode unstable whereas, alumina (Al_2O_3) is a stable compound that occurs in various forms (α/β/γ-Al_2O_3) thereby transforming at certain temperature range. The ion of chromium (Cr^{3+}) is stable and is believed to occur in a single form. Some sample pellets were prepared from the calcined biphasic powder mixture for preliminary thermodynamic and kinetic measurements. Chemical stability of the sintered solid-state electrolyte pellets and retention of various phase formations were determined using X-ray diffraction. In fabricating the electrochemical sensors in this research, powder samples of the biphasic powder mixture of $MgCr_2O_4$+Cr_2O_3 was used as the reference electrode.

3.3 Materials Characterisation Techniques

Characterisation is an essential part of all investigations in materials science. During past decade, there have been remarkable innovations in techniques for characterising the structure and properties of ceramics, from atomic scale to the micro-level. Efforts will undoubtedly continue in inventing and developing more powerful and useful techniques for the characterisation of materials. The various experimental techniques used to monitor, examine, analyse, grade and identify chemical composition, structure and properties of the materials in this research are outlined. Some of the experimental techniques deployed for materials characterisation are: Thermogravimetric analysis (TGA), Differential scanning calorimetry (DSC), X-ray powder diffraction (XRD), X-ray fluorescence (XRF), Laser-Raman spectroscopy (LRS), Fourier transform infrared

(FTIR), Scanning electron microscopy (SEM), Transmission electron microscopy (TEM), Energy dispersive X-ray spectrometry (EDS), AC - Impedance spectroscopy.

3.3.1 TGA-DSC

Thermal analysis: defined as a group of techniques in which the physical properties of a substance and/or its reaction product(s) is measured as a function of temperature while the substance is subjected to a controlled temperature programme [146, 147]. Recently, thermal analysis is seen as a group of techniques in which a property of the sample is monitored against time or temperature while the temperature of the sample, in a specified atmosphere, is programmed. The programme may involve heating or cooling at a fixed rate of temperature change, or holding the temperature constant, or any sequence of these [148]. This definition became inevitable to address problems such as, the exclusion of isothermal[4] measurements from thermal analysis, and any measurement that is “sample-controlled” rather than “temperature-controlled” is not covered. The recent definition of thermal analysis reflects the change in complexity of experiments possible with the use of computers and other micro-processors to control the temperature programme and it also embraces isothermal measurements as part of thermal analysis.

TGA and DSC are two techniques used simultaneously for thermal characterisation of dried $MgZr_4P_6O_{24}$, $MgHf_4P_6O_{24}$ and $MgCe_4P_6O_{24}$ xerogel powders and its solid-state solutions in order to determine phase formation, transformation of the samples and to predict their thermal stability. In the simultaneous TGA-DSC measurements, N_2 was used as purging gas for removing corrosive off - gases thereby preserving the lifespan of sample powders and reference furnaces of STA 8000. TGA measures weight/mass change (loss or gain as the case may be), and the rate of sample weight change of the dried xerogel powders (as a percentage of the initial mass applied in some cases) as a function of temperature, time and atmosphere. With this technique, the dried xerogel powders is heated under a flowing gas (preferably, N_2) or synthetic air atmosphere at a flow rate of 50 mL min^{-1} and a constant heating rate (10°C min^{-1}) while the relative difference of the mass during this process is measured. The TGA derivative mass

---

[4] When the sample is heated, held at constant temperature, or cooled in a controlled manner.

change curve (-dm/dT) will appear as declining steps thereby indicating progressive dehydration followed by decomposition of the xerogel powder and then reduction to form the phosphate electrolytes. Sometimes a mass gain is evident when the samples react with oxygen from the synthetic air. To clearly identify the temperature of mass change, the derivative of TGA curve with respect to temperature to obtain reaction peaks is used.

DSC measures the difference in heat flow between a sample powder and a reference substance during a temperature programme. Normally, temperatures of the sample T_s and reference crucible T_r are measured. Depending on the temperature difference between T_r and T_s, heat is supplied to either the sample or furnace crucible in order to balance the temperatures. This additional heat is supplied by the filament of resistance R close to the sample crucible or reference crucible, by joule heating. The additional power P(t), also equal to the heat flux is given as $P = i^2R = dQ/dt$ where i(t) is the filament electric current [149]. The heat flux is also equal to the enthalpy flux, which gives the typical DSC measurement curve.

By measuring the difference in heat flow rate (mW = mJ/sec) between a sample and inert reference as a function of time and temperature, the most obvious transitions recorded are melting or re-crystallisation, but many smaller, much more sensitive events such as, the glass transition (T_g) of the substance are also revealed. Depending on whether the process is either endothermic or exothermic, a peak will be observed. Endothermic peaks are heat flow into the sample from processes such as heat capacity (heating), glass transition, melting, evaporation, while exothermic peaks are due to processes that allow heat to flow out of the sample such as heat capacity (cooling) or crystallisation, cure, oxidation, etc. [150].

3.3.1.1 Experimental Setup

Alumina crucibles with ~20-25mg α-alumina powders of particle size, 13±0.01nm were initially weighed and zeroed accordingly to balance the alumina crucibles for TGA-DSC measurement. The reference crucible contained alumina powder while the sample crucible contained ~15-20mg of the dried xerogel powder sample for TGA-DSC measurement. Both crucibles were placed in a thermal analysis furnace for a simultaneous TGA-DSC measurements performed using an STA 8000 (PerkinElmer, Seer Green, UK) in a controlled air and N_2 atmosphere, respectively at a purge gas flow rate of 50 mL min^{-1} sufficient to remove volatiles more efficiently at a constant heating rate of 10°C min^{-1} over a temperature range from 50 to 1000°C. The xerogel powders measured by simultaneous TGA-DSC method considering the test conditions are perfectly identical and unique for both TGA and DSC, i.e., with the same operating atmosphere, controlled air or N_2 gas flow rate, vapour pressure on the sample, constant heating rate, thermal contact between crucibles and sensor which is common to both measurements. The data derived from TGA and DSC measurements were analysed with the Pyris software (PerkinElmer Inc. Waltham, MA). A schematic representation of the STA 8000 used for the simultaneous TGA-DSC measurements is presented in Figure 3.14

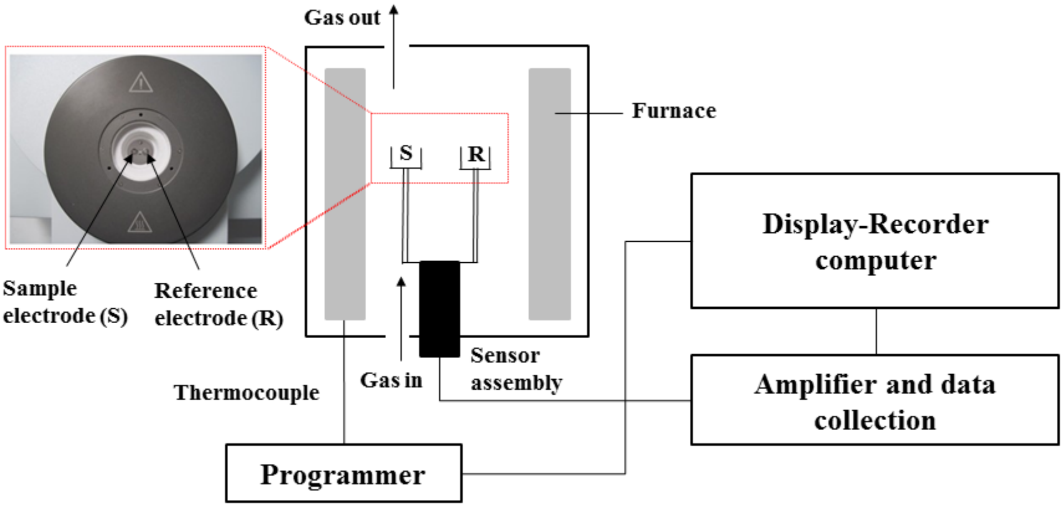

Figure 3-14 Schematic representation of STA 8000 for TGA-DSC measurements showing sample (S) and reference (R) electrode in a thermal analysis furnace.

3.3.2 XRD

A complete description of the structure of a solid requires the determination of the crystal system, space group, unit cell dimensions, atomic coordinates and the actual electron density distribution around the atoms. In order to provide such information, one uses diffraction involving X-rays, electrons or neutrons. The relation between the diffraction pattern and the structure of the crystal is understood in terms of the reciprocal lattice. The direction of scattering depends on the positions and sizes of the scattering elements, whereas intensities of scattering depend on the nature of scattering elements. As a result, information is provided on the structure of materials [151-153]. X-ray diffraction has been commonly used for routine characterisation as well as for detailed structural elucidation. However, many scientists are making increasing use of electron and neutron diffraction to obtain information not provided by the X-ray diffraction method today. The analytical applications of XRD include: characterisation of crystalline materials, determination of unit cell dimensions, measurement of sample purity, distinction between amorphous and crystalline materials, measures interplanar spacing of crystal planes, and quantification of the percent crystallinity of materials. Generally, XRD can be used for investigating the internal structures of compounds. With specialised techniques, XRD can also be used to determine crystal structures using Rietveld refinement method. It can also be used to generate the primary data for analysis of lattice parameters, crystal phases[5], quantitative [154] and structural profile matching of crystalline and amorphous solid materials using specific softwares such as Eva, Topas, X'Pert HighScore Plus and most recently GSAS-EXPGUI [155, 156]. The patterns obtained are characteristics of the particular compounds of which the crystal was formed. The crystal phases identified are confirmed by comparing the measurement data with reference patterns in the Powder Diffraction File (PDF-Card) standards from the Joint Committee on Powder Diffraction Standards - International Centre for Diffraction Data (JCPDS - ICDD also known as ICDD)[157]. X-ray powder diffractometers consist of three basic elements: an X-ray tube (i.e., electron gun or X-ray source), a sample holder, and an X-ray detector as shown in Figure 3.15.

---

[5] Phase denotes atomic structure or chemical composition.

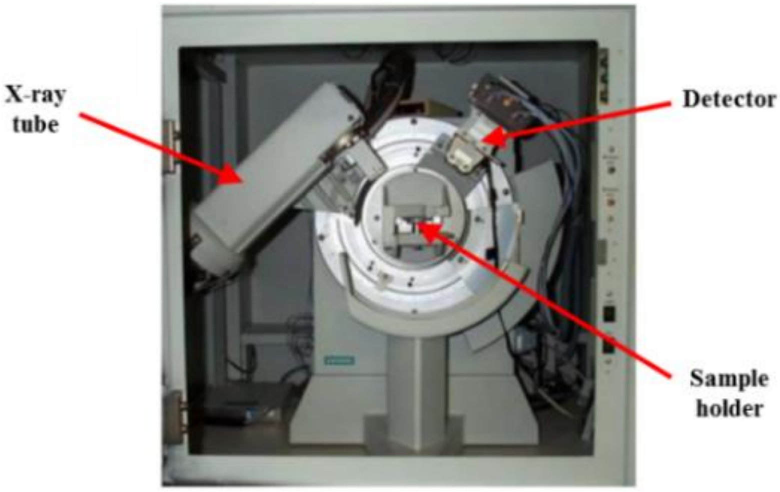

Figure 3-15 X-ray Powder diffractometer [158]

3.3.2.1 Measuring principle

X-rays are electromagnetic radiations. The X-ray powder diffractometer therefore generates X-rays of specific wavelength from an X-ray tube (source)[158]. In this research, the X-ray tube produces X-rays radiation Kα and Kβ. The X-ray radiation Kα consists, in part, of $K\alpha_1$ and $K\alpha_2$. $K\alpha_1$ has a slightly shorter wavelength and twice the intensity as $K\alpha_2$. The X-rays radiation specific to this research target material is CuKα. Copper as the most common target material for single-crystal diffraction, with the monochromatic CuKα radiation has a specific wavelength of 1.5418Å [159]. These X-rays are collimated and directed onto the sample of which some are reflected and some diffracted. In Figure 3.16, as the sample and detector are rotated, the intensity of the reflected X-rays is recorded. When the geometry of the incident X-rays impinging the sample satisfies the Bragg equation, constructive interference occurs and intense peak occurs. The detector records and processes this X-ray signal and converts the signal to a count rate which is visualised through a computer monitor. The geometry of an X-ray diffractometer is such that the sample either rotates or remain fixed depending on the instrument in the path of the collimated X-ray beam at an angle θ while the X-ray detector is mounted on an arm to collect the diffracted X-rays and rotates at an angle 2θ as shown in Figure 3.16. The instrument used to maintain the angle and rotate the sample is termed a goniometer. Data in this research is collected at 2θ from ~10° to 80° present in the X-ray scan with a step size of ~0.0334225° and a time per step of 45.085 s.

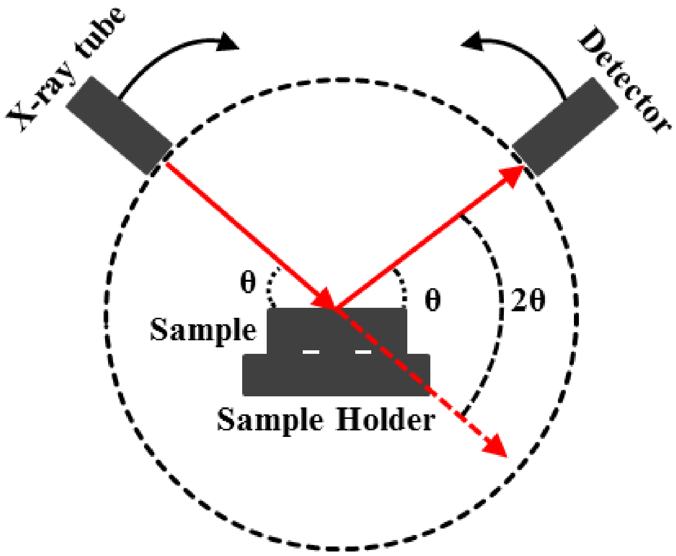

Figure 3-16 XRD sample configuration

A crystalline material will always have planes which will diffract the X-rays and the diffraction pattern depends on the crystal structure of the sample and the wavelength of the X-ray source [160]. Each set of parallel planes has a definite spacing called d-spacing. The diffraction is a constructive interference of the radiation from successive planes and it occurs when the path difference is a multiple of an integral number *n* of wavelengths ($n\lambda$). This diffraction happens at such a unique angle hence the angle and sometimes the intensity becomes the signature of that crystalline material. The Bragg's relationship is illustrated in Figure 3.17. Bragg's relationship for diffraction therefore is derived from Equation (3.7);

$$DC' = C'E = d\sin\theta,\ DC' + C'E = n\lambda = 2d\sin\theta \qquad (3.7)$$

where θ is the angle of incidence, λ is the wavelength of the X-rays and *n* is a positive integer value of the wavelength that fulfils constructive interference.

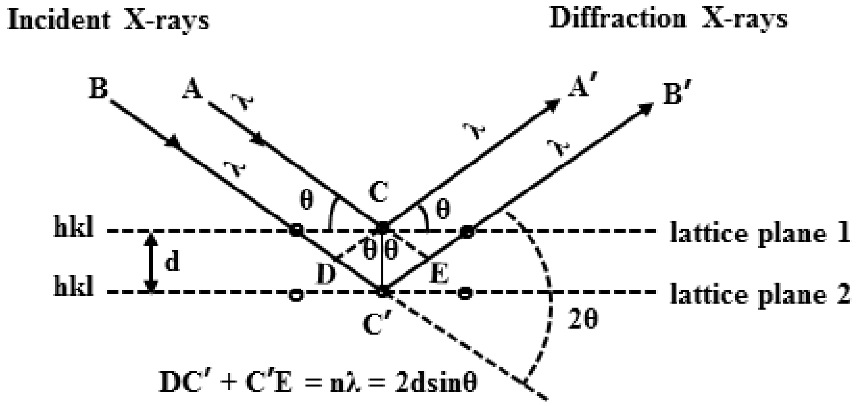

Figure 3-17 Schematic representation for the Bragg condition on a crystal structure

For polycrystalline materials, because of the presence of numerous planes which are all diffracting the X-rays, a sharp and intense peak is recorded. Conversely, for nano-crystalline materials, however, the intensity recorded is very low but broad. This is because of the statistical nature of the counts, the area under the peak should always be constant therefore the peak in nano-crystalline material is always broad while those in polycrystalline materials is sharp and intense.

3.3.2.2 Experimental setup

In this research, x-ray diffraction was used to identify optimum heating temperature, for phase identification, and to determine the crystal structure of materials at a room temperature, in both powder and ceramic pellets form. Philips X'Pert diffractometer and Bruker D8 advance with monochromatic CuKα radiation of wavelength 1.5418Å produced from an accelerating voltage and current of 40kV, 30mA for Philips X'Pert diffractometer and 30kV, 45mA for Bruker D8 advance were used. Lattice parameters of materials were determined from XRD patterns. They are operated in ambient and non-ambient environments. Non-ambient XRD measurement is for high-temperature XRD, HT-XRD using Philips X’Pert diffractometer while ambient XRD measurement was performed for conventional XRD at room temperature using both diffractometers. The sample types and shapes define the type of sample holder to use at every stage of XRD measurements. For instance, powders were loaded and analysed using the round shaped steel or polymeric sample holders (spinner). Pellets were loaded and analysed using a simple fabricated bracket sample holder instead. The powder was firstly compacted and levelled in the round shaped sample holder before it was placed in the XRD machine. The machine when in this mode works under a spinning mode where the sample holder is rotating so that every crystal on the sample is accessed by the X-ray beam. A total time of ~770s with a step size of 2θ equals to 0.0334225° and a time per step of 45.085s were required to complete measurements. The results were stored in digital format and analysed using the HighScore Plus software for the Philips X’Pert diffractometer and Eva software for the Bruker D8 advance equipped with the ICDD database. Pellets were also pressed against the bracket sample holder using plasticine to hold it in place before it was inserted on the XRD machine using a special sample stage. The machine in this mode works on a fixed mode where the sample holder is fixed against the sample stage and the crystal is accessed by X-ray beam in this position. XRD data was collected over a typical scan rate of 0.03°/s from 10.00° to 80.00° 2θ with a step size of 2θ equals *ca* 0.0495° at 35s per step required for the analysis. The data obtained from this measurements were stored in digital format and analysed using the HighScore Plus or Eva. The equipment were calibrated against Si standard and both samples (i.e., powders and pellets) were retrieved since the process is non-destructive.

Polymorphic Phase Identification

In this research, XRD profiles was used to identify crystallographic phases of samples (powders and pellets) by comparing the values of d-spacing and relative intensities of X-ray reflections or peaks with a standard reference database (ICDD). In addition, the relative intensities of each phase present in a mixture of polymorphs could also be estimated by comparing the integrated area under the highest intensity peaks of each crystallographic phase. The integration of the peaks could be performed using the softwares, HighScore, FullProf and/or GSAS for refinement once the crystal and instrument parameters have been optimised.

Similarly, the relative amounts of the separate phases present in a two phase sample compound or polymorphs may, in principle, be calculated from the intensities of the major X-ray reflections for the two phases. In this light, Swart and Shrout [161] have proposed the use of Equation (3.8):

$$\text{wt.\% sample a} = \frac{I_a}{I_a + I_b} \text{ x } 100 \qquad (3.8)$$

This equation should be seen as a first approximation, since its applicability requires comparable maximum absolute intensities of the pair of two phase peaks being used. Here, I_a refers to the intensity of the a-peak and I_b to the intensity of the b-peak, these being the most intense reflections in the XRD patterns of both phases. This equation has been widely employed in connection with the fabrication of PMN and other lead-based complex perovskite materials [161-166]

Crystallite Size

The average crystallite size of calcined solid-state nanopowders is calculated using the Scherrer formula [167-171] proposed in Equation (3.9) according to the broadening of XRD peaks. The relationship between the XRD peak broadening (β) and diameter of the crystallites (D) is given by;

$$D = \frac{K\lambda}{\beta \cos\theta} \qquad (3.9)$$

Where K is the shape factor of the particles (Scherrer constant close to unity, i.e. 0.94), λ is the wavelength of the Cu-kα radiation (usually, $\lambda_{Cu\text{-}k\alpha}$ 1.5406Å), β is the full width at half maxima of the diffraction peaks (FWHM) and θ is the diffraction angle of the X-rays (otherwise called the Bragg's diffraction angle in radians).

Lattice Parameters

For any crystal structure, the interplanar spacing, d depends on the lattice parameters a, b, c (lengths of the unit cells) and α, β, γ (angles between length of the unit cells). Using the relationship between the d-spacing and Miller indices assigned to crystal planes, the lattice parameters could be calculated. For instance, the crystal system of the synthesised solid-state electrolytes in this research is monoclinic system, therefore, the relationship between d and hkl is described according to Equation (3.10);

$$\frac{1}{d_{hkl}^2} = \frac{h^2}{a^2 \sin^2 \gamma} + \frac{k^2}{b^2 \sin^2 \gamma} - \frac{2hk \cos \gamma}{ab \sin^2 \gamma} + \frac{l^2}{c^2} \tag{3.10}$$

Where d_{hkl} is the distance between crystal planes of hkl, λ is the X-ray wavelength, h, k, l is the Miller indices of the diffracting planes, a, b, c is the lattice parameters and γ is the angle between a and b.

3.3.3 Vibrational spectroscopy

Vibrational spectroscopy are molecular-specific and is generally implemented using two principal schemes:

i. absorption, which forms the basis of FTIR spectroscopy and
ii. inelastic scattering of incident radiation that causes a shift in the frequency of the radiation corresponding to the energy difference of the vibrational states of the molecular species. Raman scattering forms the basis of Raman spectroscopy.

3.3.3.1 FTIR

In the FTIR experiment, attenuation of the IR radiation by the sample is measured with transmission of the incident beam. For the FTIR to be operated in transmission mode, the sample was mounted in the micro-DSC in a spectroscopically transparent substrate to allow the passage of the energy from source to detector [172, 173].

FTIR spectra of dried xerogel and calcined powders of the phosphate electrolytes were recorded with the Nicolet iS10 FTIR spectrometer (ThermoFisher Scientific, Hertfordshire, UK), equipped with a deuterated triglycine sulphate (DTGS)-KBr detector to examine the chemical vibrational modes and bonds of the samples. The FTIR spectra range of 4000-400cm^{-1} and a minimum of 36 scans are performed at an average infrared signal of 4cm^{-1} resolution at room temperature.

3.3.3.2 Laser-Raman scattering

Raman spectroscopy is based on inelastic scattering of a monochromatic excitation source from molecules with a routine Raman shift of 4000-100cm^{-1}. Raman shift provide details about vibrational, rotational and other low frequency transitions in molecules. It is used qualitatively for researching molecular structures. Because of the low sensitivity and weak Raman scattering, it is not used for quantitative analysis.

In using Raman spectroscopy, sample powders are illuminated with monochromatic (single wavelength or single frequency) laser light, which could either be absorbed, transmitted, reflected or scattered by the sample powders. The light scattered from the sample powders is due to either elastic collision of the light with the powder’s molecules (Rayleigh scatter) or inelastic collisions (Raman scatter). Whereas Rayleigh scattered light has the same frequency or wavelength of the incident laser light on the sample powders, Raman scattered light returns from the sample powders at different frequencies corresponding to the vibrational frequencies of the bonds of the molecules in the sample powders.

Raman scattering is generally used as complementary to FTIR. However, it offers a special advantage in that it requires almost no sample preparation.

Raman measurement on dried xerogel and calcined nanopowders of magnesium based solid-state electrolytes were recorded at a room temperature using Renishaw inVia

Raman microscope spectrometer (RENISHAW, Gloucestershire, UK). Argon (Ar) ion laser with $\lambda = 514$nm is used as the excitation source with laser power of 25mW. The spectral data were recorded by scanning the 3200-100cm^{-1} region of the magnesium based solid-state electrolyte powders (xerogel and calcined), which were accumulated for 5 scans with 5 sec acquisition time for each scan. One key advantage of Raman analysis is that Raman spectrum can be obtained at a few seconds measuring time. The software WiRE was used to analyse all the data derived during Raman measurement.

Experimental setup

Sample powders (xerogel and calcined) were placed on flat glass slides and mounted in the sample chamber where laser light is focused on it with the help of a lens. The scattered light is thereafter collected using another lens and is focused at the entrance slit of the monochromator. The width of the monochromator slit is set for the desired spectral resolution. Monochromator effectively rejects stray light and serves as a dispersing element for the incoming radiation. Light leaving the exit slit of the monochromator is collected and focussed on the surface of the detector. This optical signal is converted to an electrical signal within the detector. Signal is processed in a computer to develop the final spectrum. A schematic diagram showing typical Raman spectrophotometer is shown in Figure 3.18

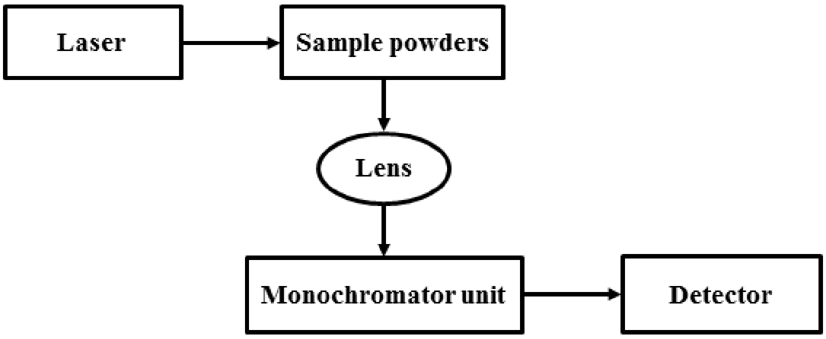

Figure 3-18 Schematic representation of Raman spectrophotometer

3.3.4 Electrical characterisation

3.3.4.1 Impedance spectroscopy

The two [174] and four [175] probe direct current, dc-electrical measurement methods are common techniques for studying electrical properties of materials [176]. However, regarding the characterisation of electroceramic materials, solid-state electrolyte, these techniques are not successful at resolving electrical measurements with contributions from the grain interior, grain boundaries and electrode-electrolyte interface. Interest by several other researchers [177, 178] to measure the inter-granular and intra-granular properties of solid-state electrolytes using miniature electrodes was unsuccessful since the technique is quite complex to implement experimentally. However, alternating current method known as, ac-impedance spectroscopy or electrochemical impedance spectroscopy (EIS), serves as an alternative method capable of resolving the electrical measurements of solid-state electrolytes/electroceramic materials with contributions from the grain interior, grain boundaries and electrode-electrolyte interface.

Furthermore, in this research, ac-impedance spectroscopy is considered a valuable tool for researching into both bulk transport properties of materials and the electrochemical reactions at its interface. Typically, ac-impedance experiments using Solartron SI1260 FRA impedance analyser are carried out over a wide range of frequencies ranging from several milihertz (mHz) to several megahertz (MHz) for the characterisation of different regions of the solid-state electrolyte materials according to their electrical relaxation times or time constants. The Solartron SI1260 FRA impedance analyser guarantees deduction of contribution from the grain interiors, grain boundaries and electrode-electrolyte interface [179, 180]. Impedance spectroscopy data are often obtained in the complex impedance notation $Z^*(= Z' + iZ'')$, this implies, real and imaginary part Z' and Z'' at each frequency are considered. For data interpretation, it can be very useful to convert these data into the modulus $M^*(= M' + iM'')$, capacitance $C^*(=C' - iC'')$, admittance $Y^*(= Y' + iY'')$ or dielectric $\varepsilon^*(= \varepsilon' - i\varepsilon'')$ notation, and the interpretation of the resulting spectra is supported by analogy to equivalent circuits comprising simple components such as resistors and capacitors. In general, such equivalent circuits are not unique, and indeed there exists an infinite set of circuits that can represent any given impedance, but a common practice is to select a physically plausible circuit containing minimal number of components and, somewhat relatively, assign physical significance to the derived parameters [181]. Often, a significant insight into materials behaviour is gained from such analyses, which certainly explains the rise in popularity and functional applications of the impedance spectroscopy as a generic material characterisation tool.

The impedance of any system is defined as $Z = \frac{V_o}{I_o}$, it usually contains both resistive (R) and reactive (L and/or C) components, both of which must be determined. This was achieved by applying an alternating voltage across the solid-state electrolyte samples and a standard resistor that are in series. Different portions of the solid-state electrolyte pellets were characterised by a resistance and a capacitance, usually placed in parallel and, the characteristics relaxation time, τ, of the solid-state electrolytes, parallel RC elements as a product of R and C, is presented in Equation 3.11

$$\tau = RC \tag{3.11}$$

In the frequency domain, RC elements are separable due to the relation in Equation 3.12 which holds at the frequency of maximum loss, ω_{max}, in the impedance spectrum also known as Nyquist plots.

$$\omega_{max} RC = 1 \tag{3.12}$$

By applying a single frequency voltage $V = V_o\sin(\omega t)$, where ω represents the angular frequency $2\pi f$, across the measuring samples, the phase shift and amplitude of the resultant current $I = I_o\sin(\omega t + \phi)$ can be determined. Unless the measuring sample behaves as an ideal resistor there will be a phase difference, ϕ between the applied voltage and the resultant current flowing in the circuit. The phase shift is related to the reactive component of the system. In general, both the magnitude (resistive) and phase shift (reactive) of the impedance of a sample is frequency dependent [180].

Impedance is a vector quantity which can be defined as a complex number, whose magnitude and direction can be expressed by real, Z' and imaginary, Z" components as presented in Equation 3.13

$$Z^* = Z'(\text{resistive}) - iZ''(\text{reactive}) \qquad (3.13)$$

where i is equivalent to √-1, ω is the angular frequency 2πf, Z' is the resistive part of the sample and Z" is the reactive part of the sample. The expression in Equation 3.13 has been applied to a solid-state electrolyte system in impedance spectroscopy [182].

The complex plane in Figure 3.19 is in the form of imaginary, Z" (capacitive) against real, Z' (resistive) impedance.

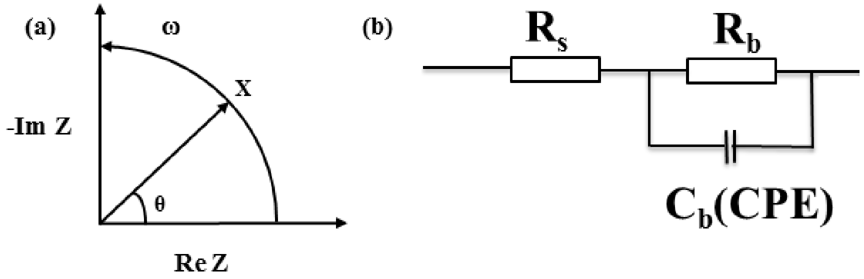

Figure 3-19 Impedance in the (a) complex plane (b) modelled equivalent circuit

Figure 3.19 shows that as the input frequency is varied (that is, when swept from low to high), the complex impedance (locus x), sweeps a semicircle in equal variability. Whenever a semicircle is observed in polycrystalline materials, modelled equivalent circuit contains a resistor and a capacitor in parallel. When several semicircles appear, it is either contributions are from grain interior, grain boundary, electrode-electrolyte effects or the material is multiphase. However, to distinguish if it is due to a second phase, a plot of modulus[6] against frequency is used to resolve the two contributions [180]. A schematic of Nyquist plot showing possible contributions from semicircles and corresponding equivalent circuit is presented in Figure 3.20.

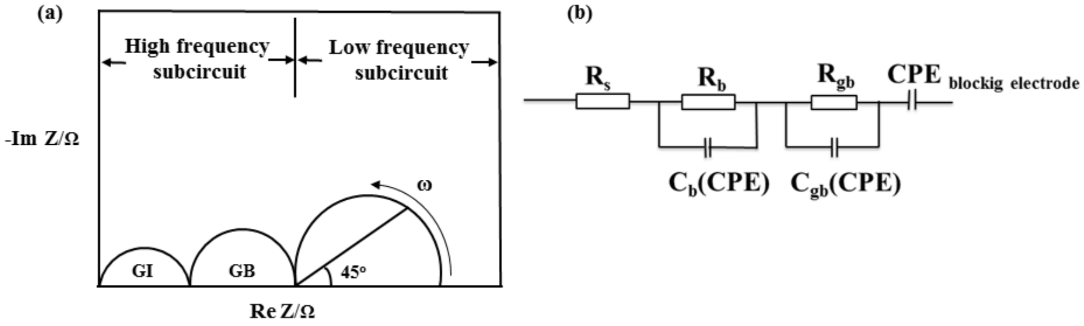

Figure 3-20 Nyquist plots of (a) an ionic conductor (b) modelled equivalent circuit

In Figure 3.20, the first high frequency semicircle is of the contribution from grain interior (GI), the second arc is space charge contribution due to grain boundary (GB). If there is no space charge, the two arcs will combine into a single arc. The third arc may be due to electrode effect [181]. In an ideal situation, each parallel RC element represents a semicircle from which the component R and C values may be extracted by fitting the plot with a corresponding equivalent circuit. R values are obtained from the intercepts on the Z' axis, while C values are obtained from $\omega_{max} RC = 1$, where ω_{max} is the frequency at the highest point on the semicircle. Shapes of plots vary greatly with circuit elements. Sometimes, a quarter circle with 45° line can be observed instead of a semi-circular arc. This represents a Warburg impedance which is an electrical analogy of a diffusion process [73]. Further details of this impedance spectroscopy technique is found in various relevant books and journal papers [179, 180, 183-185].

Conductivity is the product of charge and mobility. In considering the necessity of a fast ion conductivity for solid-state electrolyte in sensor fabrication, the determination of ionic conduction or a mixed ionic and electronic conductor (MIEC) in a solid-state

---

[6] Modulus is a quantity that describes the dielectric relaxation of ions in solid-state materials.

electrolyte is fundamental before it can be applied in sensor fabrication. Connectivity on the FRA impedance analyser comprises the wires which must not be ignored in the complex impedance contribution. Therefore, the overall impedance is a summation of complex impedance contribution from the wires ($Z_{wire}(\omega) = R + i\omega L$), sample electrode interface ($Z_{SEI}(\omega)$) and complex impedance from the sample ($Z_{sample}(\omega)$). Hence, $Z = Z_{sample}(\omega) + Z_{wire}(\omega) + Z_{SEI}(\omega)$ where R and L are the wire resistance and inductance, respectively. To determine the conductivity of solid-state electrolytes in this research, the cross-sectional area A (in cm^2) of the sample pellet as well as the thickness t (in cm) was measured. The ionic conductivity is therefore determined from the relation $\sigma = \frac{t}{(RA)}$, and the units are Ω^{-1} cm^{-1} or Scm^{-1}.

An important parameter for ionic conduction is the activation energy[7]. The lower the activation energy, E_a the easier it is for the ion to migrate from one site to another. This is estimated from the Arrhenius equation showing the temperature dependent conductivity in Equation 3.14

$$\sigma = \frac{\sigma_o}{T} \exp\left(-\frac{E_a}{kT}\right) \tag{3.14}$$

where σ is the ionic conductivity, T is the absolute temperature, k is the Boltzmann constant and σ_o is the pre-exponential factor. When $\log\sigma T$ or $\ln\sigma T$ is plotted against $\frac{1}{T}$, a linear graph is obtained with slope $\frac{-E_a}{k}$ which form the basis for calculating the activation energy of the material.

3.3.4.2 Experimental setup

A sintered solid-state electrolyte pellet was prepared for impedance measurement by lightly grinding the two flat surfaces of the pellet sequentially on dried surfaces of silicon carbide (SiC) papers with grit size P400, P800, P1200, and P2500. Afterwards,

---

[7] Activation energy is an energy barrier that the charge carrying ions must overcome to conduct through the material.

geometric measurements on the sample pellet was achieved to determine the thickness and diameter of the solid-state electrolyte. Then, platinum paste was applied on both flat surfaces of the sample pellet and cured at 800°C for 0.5h in order to provide a good adhesion between platinum and solid-state electrolyte pellets and to also form contact electrode. The applied platinum provide good electrical contacts which also serves as a blocking electrode. The sample pellet was spring loaded in a quartz assembly rig placed inside a Faraday cage within horizontal Lenton LTF1200 tube furnace (Lenton Thermal Designs Ltd., Market Harborough, UK). A type-K thermocouple was inserted close to the sample pellet to subsequently monitor the actual temperature of the sample pellet at the point of impedance measurement. Furthermore, the actual temperature of the experiment was monitored and recorded through a plug and play temperature input device, the NI USB-TC01 to a LabVIEW interface (Business Park, Newbury, UK). The platinum wire clips were then connected to the Solartron SI1260 FRA impedance analyser which interfaced with a computer controlled by the software ZPlot (Scribner Associates, Inc. USA).

A schematic representation of the quartz assembly rig for impedance measurement is presented in Figure 3.21

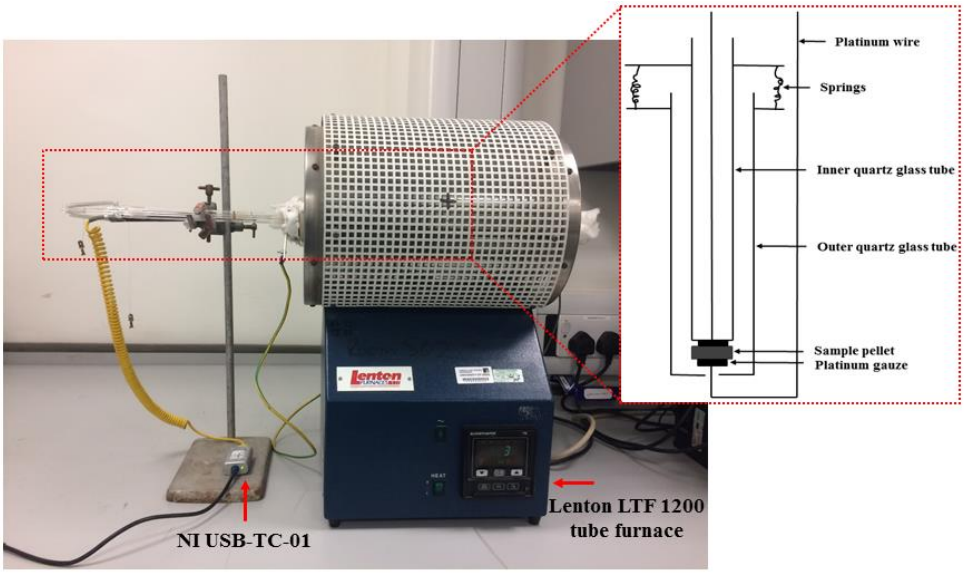

Figure 3-21 Quartz assembly rig for impedance measurements in a Lenton LTF 1200 tube furnace

In this research, the impedance analyser operates at a fixed applied voltage of 100mV and at an impedance furnace temperature range of $25 \leq T/^{o}C \leq 800$. In order to monitor the reversibility properties of the sample pellets, a temperature variance of 50 to 100°C on decreasing and increasing temperature runs, respectively, depending on direction of measurements was applied. The impedance measurements were recorded after the measuring temperature had stabilised without temperature drift.

The assembly rig for impedance measurements in this research comprises a sintered solid-state electrolyte with platinum paste coated on both flat surfaces of the sample pellets, this was then inserted into the quartz rig which made contact with platinum gauze electrode on both faces of the sample pellets. The quartz rig is then spring loaded and inserted into a Faraday cage within a horizontal Lenton LTF1200 tube furnace. The connected platinum gauze-wires were plugged into the Solartron SI1260 FRA impedance analyser for impedance measurements. Furthermore, several impedance measurements and analyses to determine electric modulus and frequency dispersion using ZView or ZSimpWin (Scribner Associates, Inc. USA) software were conducted. The measurement parameters are in Table 3.2

Table 3-2 Measurement parameters for Solartron SI 1260 FRA impedance analyser

DC potential	0.1 V
AC amplitude	100 mV
Frequency range	$0.1 \leq f \leq 3.2 \times 10^{7}$ Hz

3.3.4.3 Thermodynamic and kinetic measurements

A number of solid oxide electrolytes and/or solid-state electrolyte ceramics have been extensively used for thermodynamic measurements and determination of standard free energy of oxides formation and, for kinetic measurements of the transference number phenomena as well [97, 113, 114].

Thermodynamic determination of chemical activities of oxides used in this research was conducted through measurement of emf generated in galvanic cells. A LabVIEW[8] programming language was used to develop an acquisition application program in our laboratory in Leeds, which interfaced with the Keithley 6517A Electrometer (Keithley Instrument, Inc. USA) for acquiring emf data during thermodynamic and transport number measurements. In addition, emf potential (in V) is measured against time (s) at a fixed temperature analysing the thermodynamic and kinetic properties of the solid-state electrolytes. Using the quartz assembly rig in Figure 3.22, a solid-state electrolyte sample pellet was firmly placed between two solid-state biphasic reference electrode pellets in possible stability combination ($MgCr_2O_4$+Cr_2O_3 and $MgAl_2O_4$+Al_2O_3) or ($MgFe_2O_4$+Fe_2O_3 and $MgAl_2O_4$+Al_2O_3) or ($MgFe_2O_4$+Fe_2O_3 and $MgCr_2O_4$+Cr_2O_3), to form electrochemical cell, which was then heated continuously at a temperature interval of 50-100°C in the range 300-800°C at a holding time of 6-12hours. The platinum gauze-wires of the electrochemical cell electrode was plugged into Keithley 6517A Electrometer - LabVIEW connection with a display of real time-temperature-emf data, which was further analysed for the transference number computation.

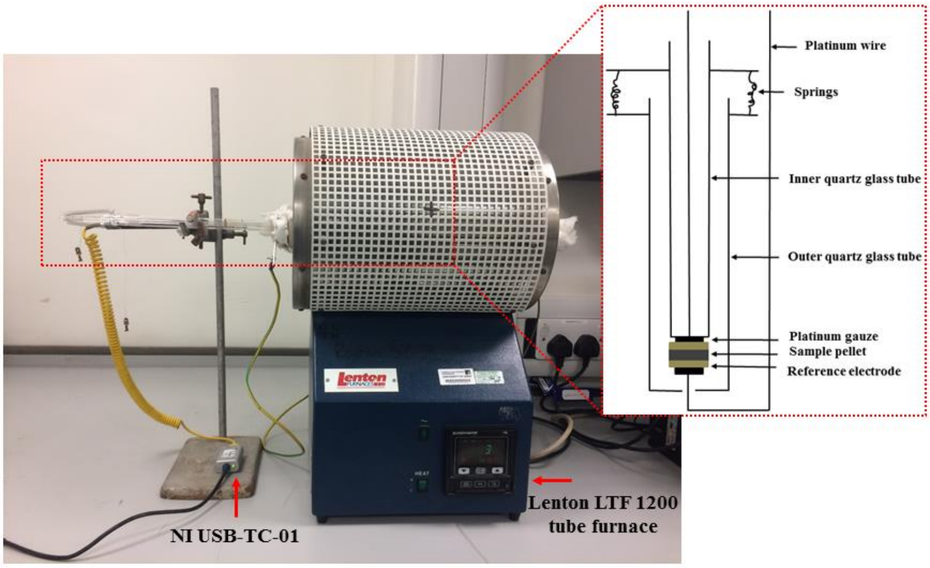

Figure 3-22 Quartz assembly rig for thermodynamic and kinetic measurements in a Lenton LTF 1200 tube furnace

---

[8] **LabVIEW** (**Lab**oratory **V**irtual **I**nstrument **E**ngineering **W**orkbench) is a system-design platform and development environment for a visual or graphical programming for the purpose of creating custom applications that interact with real-world data or signals.

3.3.5 Electron microscopy techniques

In general, microstructural features extend into three dimensions, and are distributed over the volume of solid materials under examination. This implies microstructural characterisation should be based on a 3D model for the material studied. However, in an experimental approach, microstructures are commonly studied in 2D cross-sections or via the examination of thin slices.

Microstructural characterisation/examination usually requires the analysis of a large number of complicated images, with each of them containing microstructural elements required as well as some artefacts produced by the imaging technique. In attempting to derive a quantitative description of a 3D microstructure from measurements on its 2D images, care should be taken such that these images are statistically representative of the microstructure analysed. Sampling is a very significant step of almost any if not all microstructural investigation of a material, and it is relevant to understanding its properties. This requirement should be satisfied by employing the proper stereological sampling procedures designed for specific situations [186].

The number of microstructural investigations using electron microscopy techniques for characterisation of electroceramic materials have increased greatly, and examples of such work are mainly found in commercial literature for solid-state electrolytes and microscopy [187]. Essentially, in order to carry out some microstructural examinations on solid-state electrolytes today, electron microscopy such as SEM, TEM and EDS techniques will most likely be employed. Optical microscopes are secondary devices compare to SEM because of their low magnification and resolution, therefore they are not mostly used in microstructural examinations except on rare occasions.

3.3.5.1 SEM-EDS

SEM

SEM is one of the most versatile characterisation tools for microstructural examination and microstructural characteristics of solid materials in most materials characterisation laboratories. It is used in preference to optical microscopes when higher magnification or an increased depth of field is needed, or when some sort of element or composition analysis is required. Its main displayed practical advantages are: easy observation and straightforward interpretation of the images of virtually any kind of solid specimens; great variety of imaging modes; ease of pixel by pixel image processing and analytical possibilities. SEM generate images of the surface and subsurface of a sample specimen at magnifications in the range of 10x - 100,000x. It also provide details on morphology and crystallographic information of specimen examined. Another important feature of SEM is the three-dimensional (3D) appearance of the specimen image formed by the interaction of high energy electron beam during scanning with electrons in measuring samples, thereby producing secondary and back-scattered electrons. Electron beam is generally scanned in a raster scan pattern, and the beam position is combined with the detected signal to produce an image. The instrumentation of SEM is almost the same as the TEM except that in SEM, bulk specimens are used and a scanning coil is used, which causes the electron beams to move on the specimen point by point line by line. SEM can be used in a back-scattered electron (BSE) mode, secondary electron (SE) mode and specimen current (SC) mode. For the different modes, different detectors are used. In this research however, back-scattered electron imaging shows the spatial distribution of elements or compounds within the top micron experimental samples; whereas, secondary electron imaging shows the topography of surface features a few nanometres across the samples; photon emission provide information on EDS for chemical composition analysis through elemental-mapping and line-scanning.

Operating principles of SEM

In Figure 3.23, the “virtual source” on the top of the diagram represents the electron gun which produces a stream of monochromatic electrons. This can be achieved either by thermionic emission (i.e., passing a current through a filament wire for example, tungsten) or by field emission (i.e., large electric field is created around and dissociates electrons from atoms). The stream is condensed by the first condenser lens (usually controlled by “coarse probe current knob”). This lens is used to form the beam as well as limit the amount of current in the beam. It works in conjunction with the condenser aperture to eliminate the high-angle electrons from the beam. Second condenser lens forms the electrons into a thin, tight, coherent beam and is usually controlled by the “fine probe current knob”. A user selectable objective aperture further eliminates high-angle electrons from the beam then, a set of coils scans (or sweep) the beam in a grid fashion (television-like), dwelling on points for a period of time determined by the scan speed (in microsecond range). The final lens, the objective, focuses the scanning beam onto the part of the specimen desired. As the beam strikes the sample (and dwells for a few microseconds), interactions occur inside the sample and are detected with various instruments. Before the beam moves to its next dwell point, these instruments count the number of interactions and display a pixel on a CRT whose intensity is determined by this number (more reactions brighten the pixel). This process is repeated until the grid scan is finished and then repeated, the entire pattern can be scanned 30 times per seconds.

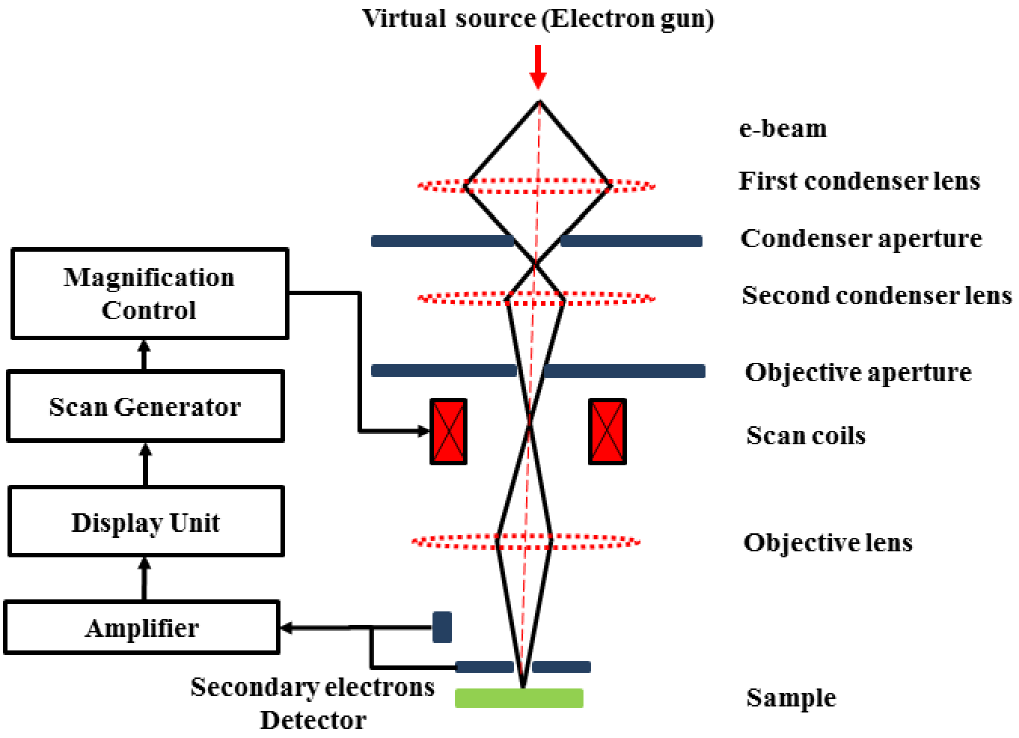

Figure 3-23 Schematic representation of SEM

Specimen electron beam interaction

The interaction of electron beam with a specimen is very important, and illustrated in Figure 3.24

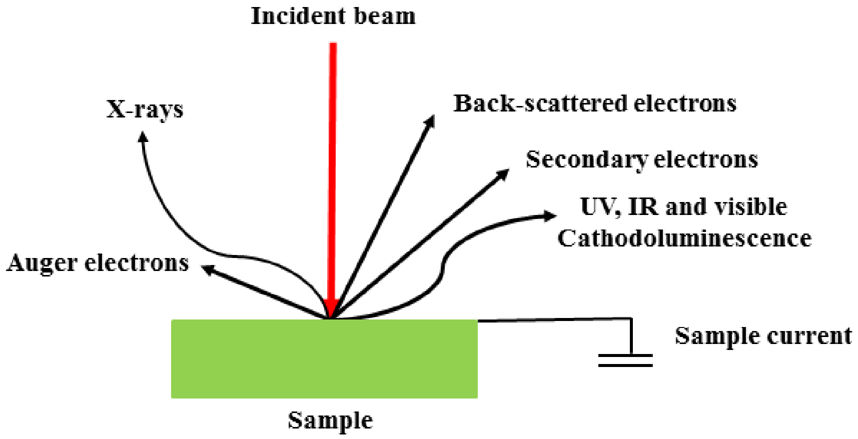

Figure 3-24 Electron specimen interaction in SEM

Figure 3.24 shows how the energetic electrons in the microscope strike the sample and the various reactions that occur are discussed. Back-scattered electrons are formed by elastic scattering of incident electron with the specimen, which is nearly normal to the incident's path. Back-scattered electrons are thus scattered at 180°. They are directly related to the atomic number of elements present in the specimen. It is understood that chemical elements with higher atomic number appears brighter than those with lower atomic number elements. This helps in morphological studies of polycrystalline alloys.

When incident electron beam passes very close to an atom, close enough to induce a generation of low energy electrons from the specimen, the secondary electrons are produced. The energy of the secondary electrons are as low as 5eV, and the secondary electrons are collected with a +100V potential bias used along with a detector.

Auger electrons are also produced by the electron specimen interaction, which is also used for surface characterisation. For the electron beam, after interacting with the bulk specimen also produces characteristic X-rays, characteristic of elements present in the specimen, which are useful for elemental analysis or surface composition analysis.

EDS

The working principles of Energy dispersive X-ray spectroscopy (EDS) analysis in the SEM can be illustrated simply:

As a high energy electron beam reaches the sample pellets surface and interacts with local atoms; inner shell electrons are excited to higher energy states, this creates an electron hole which is filled by an outer shell electrons. In Figure 3.25, an X-ray is emitted due to this change in state; the X-ray energy being of equal magnitude to the change in state, and corresponds to the specific energy levels within each individual element. This allows the identification of actual elements present; the composition of samples with different elemental species can be quantified using this method owing to the quantity of X-rays being affected by abundance of this separate elements. Despite being classified as a surface analysis technique, the electrons still penetrate the surface, up to 1µm depending on the atomic number of elements (the higher the atomic number, the lower the penetration depth), so quantification represents volume instead of surface area.

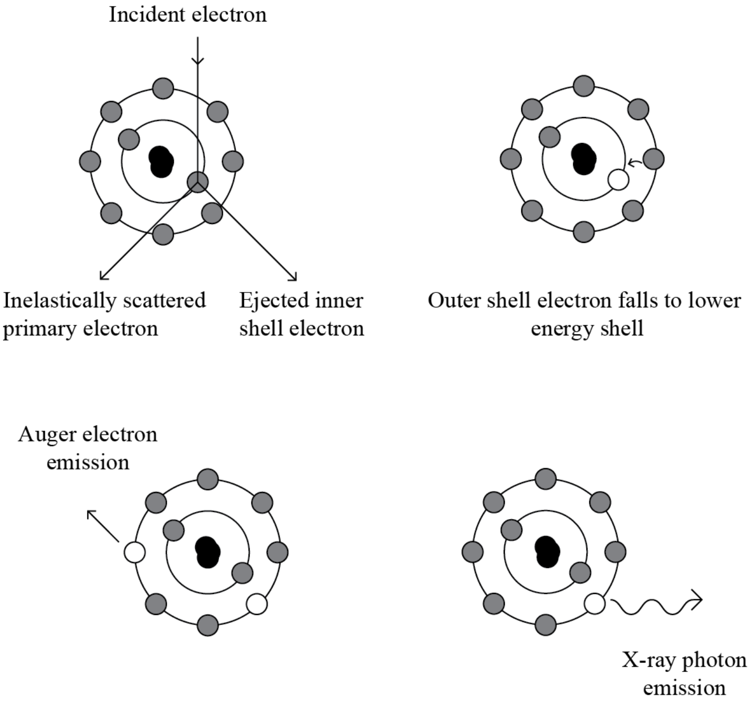

Figure 3-25 Mechanisms of Energy Dispersive X-ray (EDS) Analysis [188]

Experimental setup

The SEM imaging was conducted using the Carl Zeiss EVO MA 15 (Jena, Germany), equipped with energy-dispersive X-ray spectroscopy (EDS) and an Oxford Aztec X-Act EDS spectrometer attached to the SEM for determining the elemental composition of sample pellets at an accelerating voltage of 20kV. The Oxford Aztec X-Act EDS spectrometer enables a simultaneous SE and BSE and, EDS imaging and linescan.

Sample preparation

Sample pellets where fractured and held in a cold resin (3 parts epoxy resin + 1 part epoxy hardener). Pellets of the same dimensions were also embedded in similar resin and then ground using silicon carbide (SiC) paper of grits P400, P800, P1200 and P2500 on a rotary grinding-polishing machine with continuous flowing water. The ground pellets were later polished with fine polishing cloth of 3μ and 6μ, respectively. The possibility of flowing water reacting with solid-state phosphate electrolyte pellets was minimal since the pellets were in sintered form with no evidence of reaction with water. After polishing and rinsing, the sample pellets were dried and then placed on metal stubs with conductive carbon stickers then, carbon paste was later applied to the sample pellets and the metal stubs to provide a reasonable contact between them. The prepared carbon paste sample pellets were then dried for 10 minutes and an e-beam deposition of ~ 5nm platinum (Pt) coating was applied on the sample pellets surface to prevent accumulating charge on the surface due to the high density electron beam. Aztec or INCA software (Oxford Instruments) was used to analyse the EDS.

3.3.5.2 TEM-EDS

The basic components of TEM are similar to those of light microscopy. A beam of electrons from an electron gun is focussed by a condenser lens on to a specimen. The electrons transmitted through an entire image field are focussed by the objective and projector lenses into an enlarged image on a fluorescent screen. High energy electron diffraction is currently operated in TEM, in which diffraction and imaging are closely associated. By combining electron imaging and electron diffraction, the extraction of two different sets of structural data for investigating crystalline materials is permitted.

The strong interaction between crystalline specimens and the electron beam can be used to derive crystallographic information in a number of different ways. Generally, selected area diffraction (SAED), bright- and dark-field imaging techniques are the major output from TEM, which can provide valuable data on defects, deformations, grain boundaries, inclusions, precipitates and new phases at initial stages of growth [151]. In TEM, a bright-field image is formed by electrons which has traversed the specimen without a significant change in direction. Darker areas show where electrons have been deflected out of the beam and intercepted by objective aperture; by atomic scattering if the specimen is amorphous, or by Bragg reflections if from a crystal. However, it is often more informative to form the image using the diffracted electrons rather than the transmitted beam, since one is then using only electrons which have actually interacted with the specimen. Examination modes based on this principle are known as dark-field modes since the final screen is dark, unless there is a specimen present to diffract electrons into the image. The principle is the same as that used in dark-field light microscopy and is similarly useful in showing up low-contrast detail more strongly.

In this research, EDS and structures of the phases formed were elucidated using TEM. Electron energy loss spectroscopy (EELS) or inelastic scattering of electrons; the most versatile technique for investigating vibrational modes on surfaces in vacuum is of characterisation interest in future.

The simplified ray diagram of TEM presented in Figure 3.26 shows how an image is formed by electron beam transmitted through the samples, magnified and focussed by an objective lens and then appear on an imaging screen, a fluorescent screen in most TEMs, plus a monitor, or on a layer of imaging plate, or to be detected by a sensor such as a CCD camera.

It implies that even for non-biological specimens like metallic materials and other materials such as ceramics, cermet, composites; ultrathin specimens are always needed for TEM analysis so that the electron beam can pass through the sample. The greatest advantages of TEM include high resolution, high depth of field (vertical resolution), high magnification and diffraction pattern of micro constituents. Over and above the image viewing, diffraction pattern of a very small selected area of the specimen can also be measured.

In this research however, TEM becomes necessary in order to identify certain minor unindexed phase during X-ray diffraction. Other applications of TEM identified in this research arise through

i. Bright-field and dark-field image formation
ii. Electron diffraction of crystalline regions
iii. Particle morphologies and crystal structures of solid-state electrolytes were investigated by high-resolution transmission electron microscope (HR-TEM). Also, diffraction of selected area enables measurement of interplanar distance of diffracting plane and identification of microconstituents. The particle size determination of nanomaterials and grain size is equally possible using TEM.

Figure 3.26 represent a simplified schematic ray diagram of TEM consisting of an electron source, condenser lens with aperture, specimen, objective lens with aperture, projector lens and fluorescent screen.

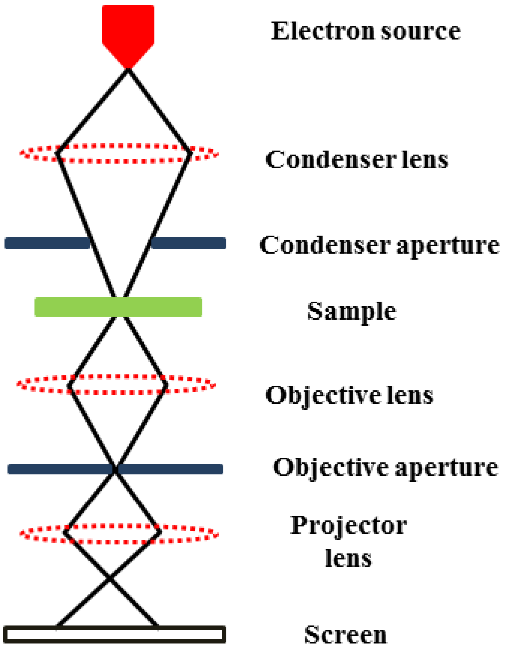

Figure 3-26 A simplified ray diagram of TEM

Experimental setup

TEM imaging of nanopowders of $MgZr_4P_6O_{24}$, $MgHf_4P_6O_{24}$, $MgCe_4P_6O_{24}$ solid-state electrolytes together with their corresponding solid-state solutions nanopowders were investigated using FEI Titan^3 Themis 300 S/TEM and FEI Tecnai G2 (Cambridge, UK). Elemental compositions of the calcined solid-state electrolyte nanopowders were also identified using TEM fitted with high-angle annular dark field (HAADF) detector operated at an accelerating voltage of 300kV equipped with energy dispersive X-ray spectroscopy (EDS, Oxford INCA 350). The data acquired therefore, were analysed using a Velox application software. Imaging, selected area electron diffraction pattern (SAED), HR-TEM, elemental composition (TEM-EDS) and mappings were some data analysed in this research.

Sample preparation

Sample preparation is an important part of TEM analysis. The samples used for TEM analysis were prepared by suspending an ~ 0.2g of calcined $MgZr_4P_6O_{24}$, $MgHf_4P_6O_{24}$, $MgCe_4P_6O_{24}$ together with their solid-state solutions into 20ml of Acetone (C_3H_6O), respectively, followed by ultra-sonication for about 0.5h to disperse nanomaterials. A single droplet of each suspension was placed on a holey carbon coated copper grid at different times; a copper grid (Cu-grid) is commonly used for analysis at an ambient temperature whereas, molybdenum grid (Mo-grid) is used for high-temperature works. The stained Cu-grid was allowed to dry under an infra-red or a standard desk lamp for at least 1hr for moisture and hydrocarbons removal, then placed on a sample holder using a twiser. The sample holder was later inserted into the TEM from outside for imaging analysis. The sample holder is important since it allows for introduction of a sample in ambient condition into the instrument, FEI Titan^3 Themis 300 or FEI Tecnai G2 that is held in vacuum. The sample on a holey carbon coated Cu-grid is then loaded onto the TEM stage for imaging analysis.

3.3.6 XRF

XRF spectroscopy is an excellent technology for qualitative and quantitative analysis of material composition and, it has been widely used recently as routine instrumental analysis technique for the quantification of minerals, slags, oxides, and other ceramic materials [189]. Various applications have been developed for this established XRF technique [190] and Energy dispersive X-ray fluorescence (EDXRF) for simultaneous analysis of elements in order to determine their composition. XRF, also described as a comparative chemical analysis technique capable of analysing a wide range of materials in different forms. The common ways to prepare samples for XRF analysis are solid samples, loose powders, pressed pellets, fused beads and liquids. The fused beads technique was used because it provides a reducing inhomogeneity and particle size effects than loose powders and pressed pellets, it uses more of Lithium borate flux than sample powders, it may also reduce the ability to detect trace elements and the reaction takes place at 1000-1100°C.

3.3.6.1 Sample preparation

In preparing fusion beads samples of various solid-state electrolytes (x=0, 1) and their corresponding solid-state solutions (when x=0.5) for XRF analysis in this research, a 6.3000g of Lithium borates (66.67% $Li_2B_4O_7$, 32.83% $LiBO_2$, 0.5% LiBr) flux was mixed with 0.7±0.0005g of $MgZr_4P_6O_{24}$, $MgHf_4P_6O_{24}$, $MgCe_4P_6O_{24}$, $MgZr_2Hf_2P_6O_{24}$, and $MgZr_2Ce_2P_6O_{24}$ calcined samples nanopowders, respectively, in a 95% Pt/5% Au crucible, in a flux/sample ratio of 9:1 to make up 7g of the total flux/sample weight, and then stir the flux and samples carefully with a spatula to ensure good mixing. The flux/sample mix is then heated between 1000-1100°C. The sample is dissolved in the Lithium borate flux and cast into a mould with a flat bottom using the Katanax K1 prime electric automatic fluxer as presented in Figure 3.27(a). The resultant glass disc or fused beads as seen in Figure 3.27(b) is a homogeneous representation of the prepared samples free of mineral structures and ready for XRF analysis.

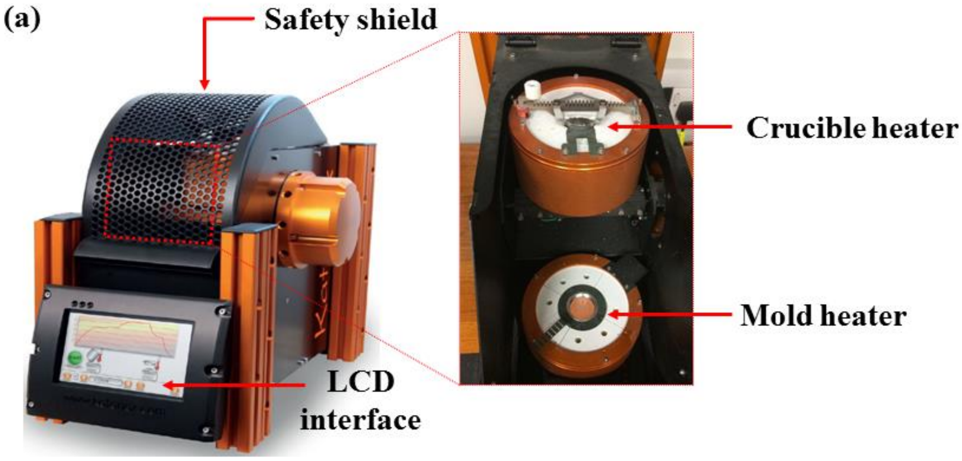

Figure 3-27(a) Katanax K1 Prime Electric Automatic Fluxer (Model-K1P-230-32)

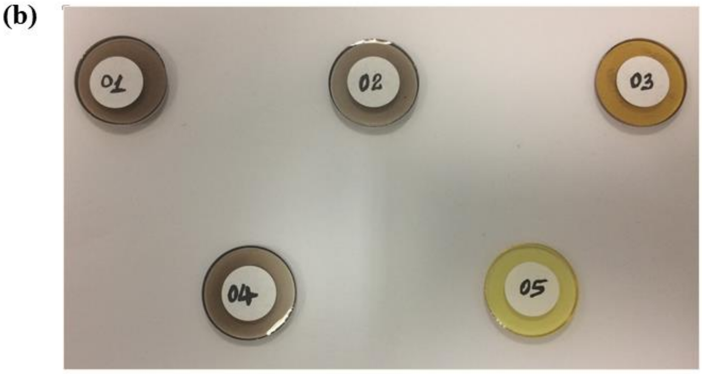

Figure 3-27(b) Fused beads of 01-$MgZr_4P_6O_{24}$, 02-$MgHf_4P_6O_{24}$, 03-$MgCe_4P_6O_{24}$, 04-$MgZr_2Hf_2P_6O_{24}$ and 05-$MgZr_2Ce_2P_6O_{24}$ solid-state electrolyte samples

3.3.7 Stability testing

Testing for stability was meant to investigate the stability of solid-state electrolytes in the working electrodes of molten Al, oxygen-free high thermal conductivity, OFHC-Cu, Al-x[9]Mg and Cu-x[6]Mg alloys. The stability testing of solid-state electrolytes in a

---

[9] Weight percent of Mg in molten Al and Cu, respectively.

pure molten Al was done at 700±5°C for 8h and 24h, respectively, in a pure alumina crucible using top-loading Lenton LTF1600 muffle furnace (Lenton Thermal Designs Ltd., Market Harborough, UK) as shown in Figure 3.28(a). In molten OFHC-Cu and Cu-0.5 wt.% Mg alloy, the stability testing was achieved at 1250°C for 2h and 6.5h, respectively, using Rautomead model RM050 furnace (Rautomead International Ltd., Dundee, Scotland, UK), solid-state electrolyte pellets were detached from the alumina tubes and placed into individual compartment within a graphite holder as presented in Figure 3.28(b). Each compartment had 4-off 5mm Ø holes which allows molten metal to flow in when immersed and to flow out again at the end of the immersion test. The compartments are separated by graphite screwed rod, and the pellets were immersed in molten OFHC-Cu for 2h and Cu-0.5 wt.% Mg alloy for 6.5h at 1250°C, respectively, in a graphite crucible with graphite flake on top of the melt to prevent oxidation of copper at high-temperatures. Furthermore, the RM050 furnace lid was always closed other than when loading and unloading the solid-state electrolytes pellets to prevent oxidation of the crucible.

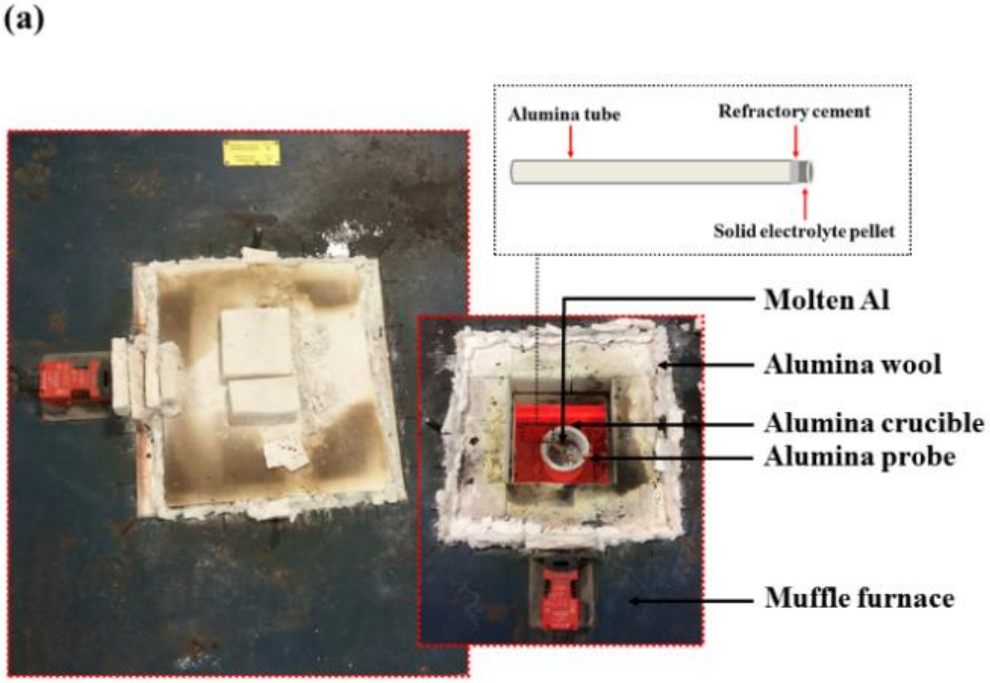

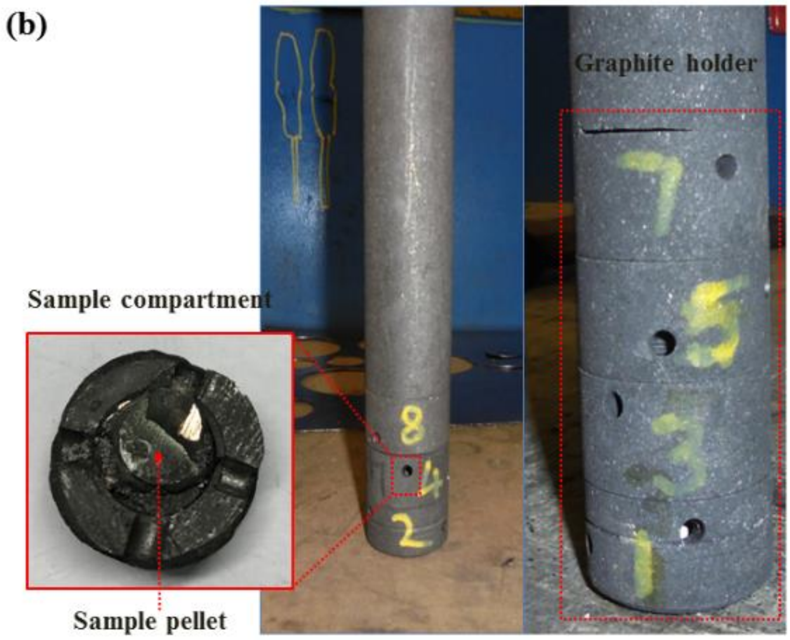

Figure 3-28 Stability testing using (a) top-loading Lenton LTF 1600 muffle furnace for melting pure Al, and (b) graphite holder of sample pellets for melting Cu and Cu-0.5 wt.% Mg in Rautomead model RM050 furnace

In considering that Cu-Mg is not an easy alloy to produce; Due to the light and volatile nature of Mg and its propensity to form slag in molten form, it therefore places unique demand on designing and melting procedures for surmounting all the risk involved in producing molten Cu alloys. Graphite melting and casting crucible furnace technology together with electric resistance heating operation as presently deployed in Rautomead (Rautomead International Ltd., Dundee, Scotland, UK) provides reducing containment environment for molten Cu. The molten Cu should always be maintained in a reducing environment to minimise reaction between the Mg alloying element and any residual oxygen in the molten Cu. Moreso, in preserving the molten Cu, minimum agitation and stirring of the molten Cu was maintained with a protective layer using high quality graphite flakes on the surface of the melt. This technology is applicable for the best upward continuous casting system of oxygen free copper wire rod production. In this case, the unique graphite process eliminates the oxidation problem by providing a naturally reducing oxygen-free environment in which the oxygen present in this Cu reacts with the graphite containment system. The electric resistance heating system technology therefore provides an accurate furnace temperature control without any induced movement or agitation of the melt thereby allowing the furnace to be operated with a minimum superheat metal temperature. In particular, graphite melting crucible furnace technology provides Rautomead correct parameters for the solidification and casting of the Cu-Mg alloys with very minimal oxidation threat.

3.3.7.1 Experimental setup

Alumina tubes of 125mm long were used to prepare the solid-state electrolytes probes for stability testing in pure molten Al at 700±5°C. Some sample pellets of $MgZr_4P_6O_{24}$, $MgHf_4P_6O_{24}$ and $MgCe_4P_6O_{24}$ (x = 0, 1) solid-state electrolytes and the corresponding solid-state solutions of $MgZr_2Hf_2P_6O_{24}$ and $MgZr_2Ce_2P_6O_{24}$ (x = 0.5) were held firmly onto one opened end alumina tubes with pure alumina refractory cement (Parkinson-Spencer Refractories Ltd., Halifax, UK) in preparing the sample probes as presented in Figure 3.29

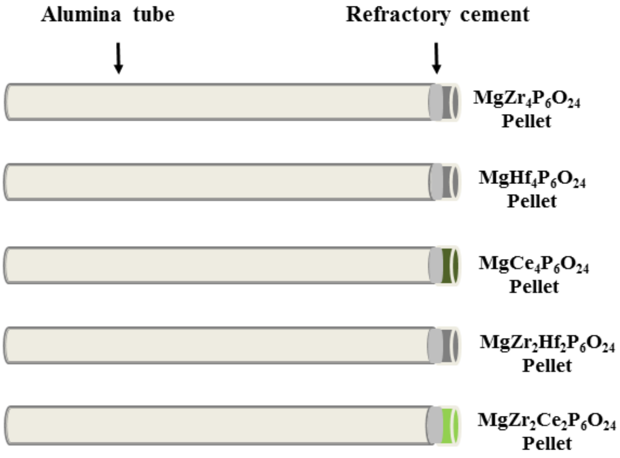

Figure 3-29 Probes showing attached pellets of solid-state electrolytes and solid-solutions

The prepared sample probes were dipped into pure molten Al at 700±5°C for 8h and 24h, respectively, inside the top-loading Lenton LTF1600 muffle furnace described in Figure 3.30(a) and 3.30(b). It is of interest to note that the molten Al is covered by a thin layer of eutectic NaCl-KCl salts that prevents oxidation of the molten Al at high-temperatures. The measuring temperature of 700±5°C is sufficient to completely melt the eutectic NaCl-KCl salts with a minimum melting temperature of 657°C.

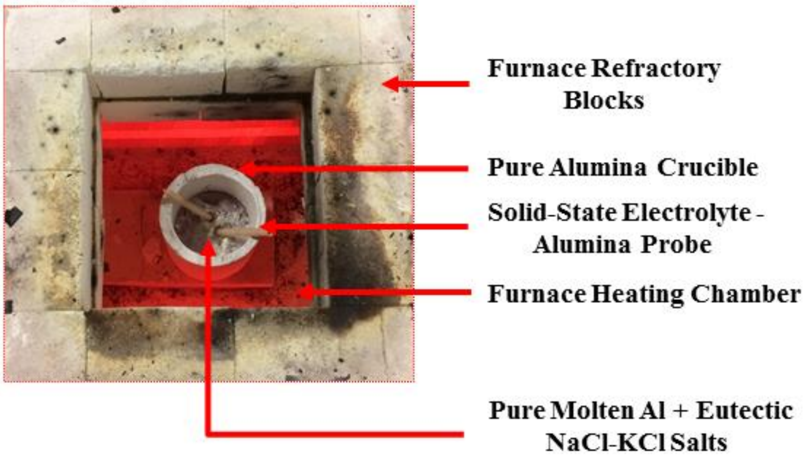

Figure 3-30(a) Top-loading Lenton LTF 1600 muffle furnace chamber for stability testing

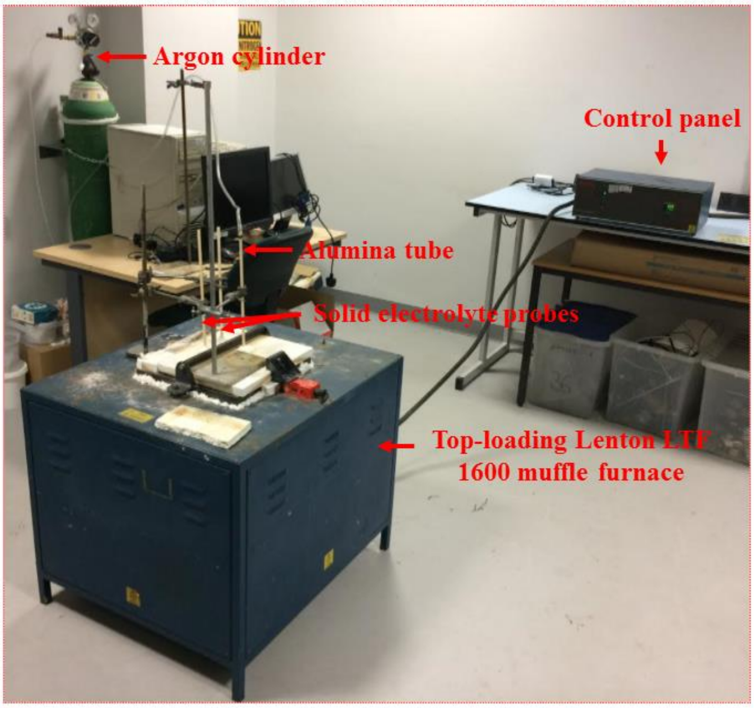

Figure 3-30(b) Top loading Lenton LTF 1600 muffle furnace for stability testing of solid-state electrolytes and their corresponding solid-solutions in molten Al and Cu, respectively

3.3.8 Sensor fabrication

Potentiometric sensors for high-temperature operating systems such as the solid-state Mg-sensors for measuring concentration and activity of Mg in molten Al at 700±5°C are fabricated using a conducting ceramic solid-state electrolytes, a non-reactive wire and a stable, non-reactive biphasic powder mixture reference electrodes. In selecting these component materials, cost and stability are usually considered.

3.3.8.1 Experimental setup

Sample pellets of $MgZr_4P_6O_{24}$, $MgHf_4P_6O_{24}$, and $MgCe_4P_6O_{24}$ solid-state electrolytes were attached to each end of a three different open end 50.8mm long alumina tubes using pure alumina refractory cement (Parkinson-Spencer Refractories Ltd., Halifax, United Kingdom) to form simple alumina probes. A 0.25mm thick annealed Fe-Cr alloy wire (Goodfellow, Cambridge) was coiled, inserted and rammed down into the bottom of the alumina tube along with a biphasic powder mixture of $MgCr_2O_4$+Cr_2O_3 which served as reference electrodes. The three different solid-state Mg-probes were extended by inserting them into a 120mm SiAlON (Silicon Alumina Nitride) ceramic tubes which held them firmly with alumina refractory cement to form bulk solid-state Mg-sensors, respectively, as shown in Figure 3.31

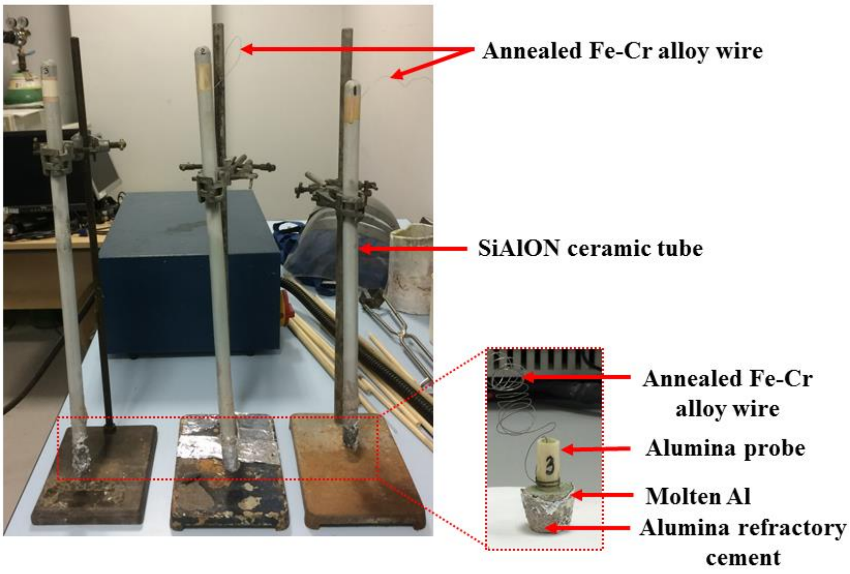

Figure 3-31 Solid-state Mg-sensors. Insert is a simple Mg-sensor before coupling

3.3.8.2 Sensor testing

The general assembly of Mg-sensor testing rig in Figure 3.32 shows both schematic and pictorial representation. A high-density alumina crucible comprising 560g pure Al-block and a eutectic mixture of NaCl-KCl salts was heated at 700±5°C in a non-inductive top-loading Lenton LTF 1600 muffle furnace to form molten Al and a thin layer of eutectic molten salts for protecting the molten Al from oxidation. Solid-state Mg-sensor and a 350mm long and 2mm Ø Mo-rod (Goodfellow, Cambridge) were dipped into the molten Al. The Mg-sensor serving as a primary terminal contact while the Mo-rod serving as counter electrode, which also provide a second terminal contact with the working electrode. Annealed 0.25mm thick Fe-Cr alloy wire of the solid-state Mg-sensor was then connected to the positive terminal of a 10 channel computer controlled high-impedance ($\geq 10^{13}\Omega$) Keithley 6517 A digital Electrometer while Mo-rod was connected to the negative terminal. In ensuring that the emf of electrochemical sensor and thermocouple temperatures were continuously recorded by multi-channel Keithley 6517 A, both connections were visualised on a computer screen through LabVIEW. After long equilibration of Mg-sensor in pure molten Al, Mg concentration in molten Al was varied by alloying it with 0.005-1.5 wt.% Mg, the actual furnace temperature was monitored using K-type thermocouple inserted in the top-loading Lenton LTF 1600 muffle furnace connected through a plug and play NI USB-TC01 temperature input device (Business Park, Newbury, UK) to a LabVIEW platform to monitor real time temperature. Furthermore, a temperature higher than the melting points of pure Al and Mg was maintained throughout the electrochemical Mg-sensors testing in order to obtain Al-Mg alloys of uniform composition. The Cu-Mg alloys were equally prepared at a high-temperature of 1250°C (melting temperature, T_m of Cu = 1085±3°C), to obtain Cu-Mg alloys of uniform composition which is important in determining the activity of Mg in the molten alloys. Uniform composition of molten alloys equally contribute to analysing accurate Mg concentrations in the molten alloys with Atomic Absorption Spectrometer, AAnalyst 400 (PerkinElmer, Waltham, USA). When the emf became stable after each Mg addition, suction samples were withdrawn from the melt using a silica tube of 2mm diameter. The samples were further prepared for AAS analysis. Furthermore, the measured stable emf at each Mg addition was used to calculate the activity of Mg in the molten Al at 700±5°C, as well as the transference number of Mg^{2+}-cation in solid-state electrolytes when the theoretical emf is known.

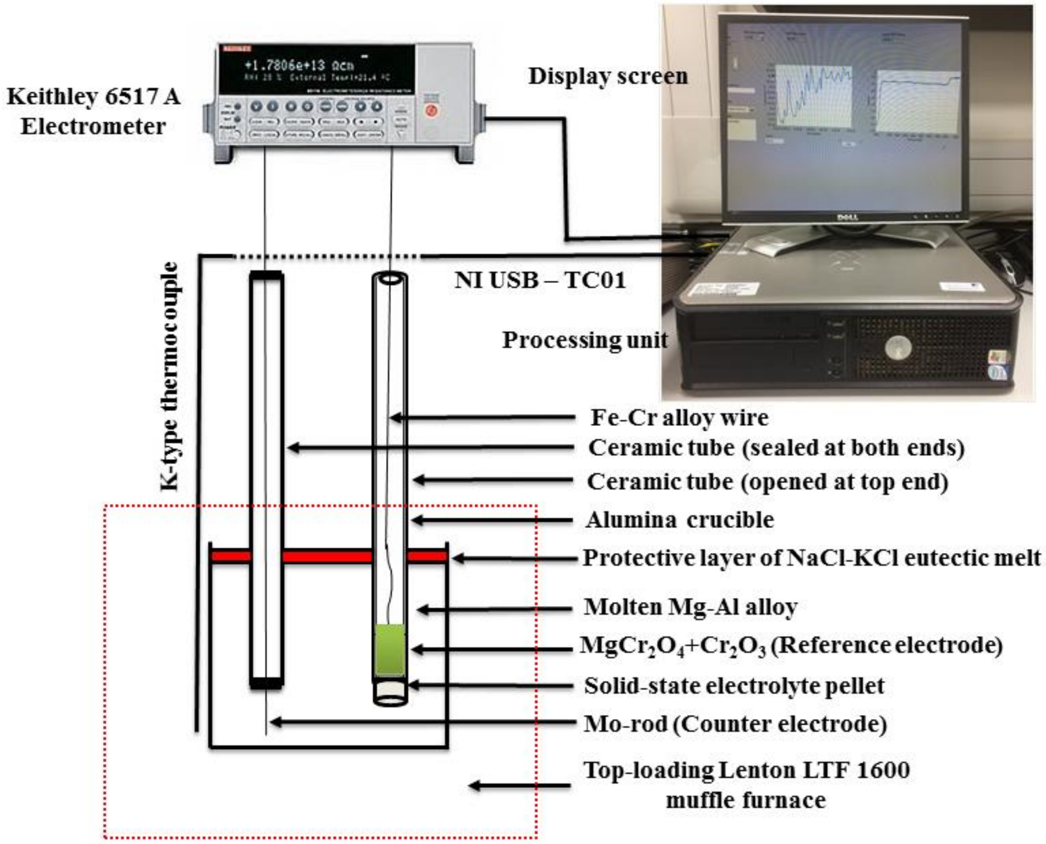

Figure 3-32 Experimental setup of Mg-sensor testing rig

3.4 Summary

This chapter described sol-gel synthesis of solid-state electrolytes characterised in this research. The sol-gel method adapted for the synthesis of solid-state electrolytes was modified in our materials synthesis laboratory to suit our present research needs. High purity solid-state electrolytes; $MgZr_4P_6O_{24}$, $MgHf_4P_6O_{24}$, and $MgCe_4P_6O_{24}$, and their corresponding solid-state solutions were prepared at a relatively low calcination and sintering temperatures after DSC-TGA and HT-XRD analysis. The characterisation techniques; XRD, XRF, FTIR, Laser-Raman scattering, SEM, HR-TEM, EDXRF, EDS and Impedance spectroscopy, for solid-state electrolytes characterisation were described. Finally, a simplified stability measurement on the synthesised electrolytes were determined, the sample pellets were then characterised and successfully adopted in fabricating solid-state Mg-sensors for sensing Mg in molten alloys. The response of Mg-sensors to Mg additions was determined by adding different composition of the Mg-rods wrapped in Al-foil sheet to the pure molten Al at different intervals at a fixed melting temperature of 700±5°C. Characterisation data of the synthesised solid-state electrolytes, electrical characterisation, thermodynamic and/or kinetic analysis, sensor testing are well reported in chapters 4, 5 and 6, respectively.

Chapter 4

Structural Characterisation

4.1 Synopsis

The previous chapter presented synthesis procedures of precursor materials adapted in this research as well as the various characterisation techniques used on the component materials. This chapter, however, reports on the characterisation techniques employed on the solid-state electrolytes - $MgZr_4P_6O_{24}$, $MgHf_4P_6O_{24}$, $MgCe_4P_6O_{24}$, the solid-state solutions synthesis using the modified sol-gel procedures based on the stoichiometric $MgZr_{4(1-x)}M_{4x}P_6O_{24}$ with $0.1 \leq x \leq 0.9$ chemical mole ratio. In synthesising solid-state electrolyte using the modified sol-gel method, the crystallisation temperature is greatly reduced compared to the solid-state process. The sol-gel method also enables the formation of a pure single phase solid-state electrolyte xerogel powders. Furthermore, this chapter provides a detailed discussion of the modified sol-gel synthesis procedures and characterisation results of the solid-state electrolytes (i.e., powders and pellets), reference electrodes, thermodynamic/kinetic mechanism and the working (sensing) electrode in the fabrication of high-temperature electrochemical sensors. In this characterisation, the calcined nanopowders and bulk sintered pellets of the solid-state electrolytes were both measured and compared. Finally, since the ultimate design and fabrication process tend towards a bulk electrochemical sensors for operations in high-temperature environment, the characterisation of solid-state electrolytes sample pellets before and after stability measurements in pure molten Al, Cu, Cu-Mg, and Al-Mg alloys at high-temperature becomes necessary to determine stability of the electrolytes in molten non-ferrous metals-alloys with Mg. The chemical stability measurements of sintered electrolytes and the corresponding solid-state solutions, design, fabrication and testing of high-temperature electrochemical sensors, and the characterisation data reported in this chapter adequately promotes the industrial usefulness and applications of electrochemical sensors today. Furthermore, the electrochemical sensors designed and fabricated in this research, would subsequently be applied at a high-temperature environment, i.e., 700±5°C and 125°C for Al-Mg and Cu-Mg alloys, respectively, and often times, in a harsh corrosive environment.

In fabricating the high-temperature electrochemical sensors, solid-state electrolytes of high stability properties is synthesised and characterised for use as high conducting solid-state electrolytes for sustaining the lifetime of electrochemical sensors. Stability measurements on these electrolytes and solid-state solutions in this research further demonstrates that the selection procedure of appropriate synthesis precursor materials for design and fabrication of high-temperature electrochemical sensors for application in high-temperature operation requires an adequate selection process for the solid-state electrolytes, the reference and sensing electrodes.

The solid-state electrolytes of some magnesium-containing phosphates, $MgM_4P_6O_{24}$ (with M = Zr, Ti) [24, 28, 29, 98] have been widely studied and were observed to be vital electrolytes for use in many process applications. Meanwhile, in complimenting this further, the synthesis of $MgZr_4P_6O_{24}$ using sol-gel process by substituting Zr^{4+} in $MgZr_4P_6O_{24}$ B-site with Hf^{4+} and Ce^{4+}, respectively, using chemical doping method thereby producing highly conducting $MgM_4P_6O_{24}$ (M = Hf, Ce) electrolytes, ensures data on electrical conductivity are now available for sensor design and fabrication. A range of solid-state solutions from $MgZr_{4(1-x)}M_{4x}P_6O_{24}$, with mole ratios, $0.1 \leq x \leq 0.9$ were synthesised by the modified sol-gel process using $Hf^{4+}$and Ce^{4+} as dopants and/or co-dopants, respectively. In order words, to determine an improved ionic conductivity of the solid-state electrolytes, solid-state solutions were synthesised by introducing a low concentration of impurity by a doping process. Such solid-state electrolytes are known as doped or extrinsic electroceramics.

The chemical doping and co-doping of $MgZr_4P_6O_{24}$, and changes in compositions of the resultant solid-state solutions in effect is to substantially improve the structural and electrical properties of the parent solid-state electrolytes. The findings in this research therefore, shows that all the synthesised solid-state electrolytes and the corresponding solid-state solutions are reliably stable with varied ionic conductivities of $MgZr_4P_6O_{24}$, $MgHf_4P_6O_{24}$ and $MgCe_4P_6O_{24}$ electrolytes. An important feature of the three end-members (x = 0, x = 1) solid-state electrolytes is that $MgCe_4P_6O_{24}$ and $MgHf_4P_6O_{24}$ were more stable than $MgZr_4P_6O_{24}$ solid-state electrolyte at a sintering temperature above 1300°C. However, they all show optimum density at this temperature but with different conductivity level. The solid-state solutions were also stable at high sintering temperatures and the conductivity increases with increasing chemical concentrations.

In this research, the xerogel powders of $MgZr_4P_6O_{24}$, $MgHf_4P_6O_{24}$, $MgCe_4P_6O_{24}$ and the solid-state solutions were calcined, several pellets were pressed into discs from the calcined nanopowders for sintering. The pressed pellets were then subjected to various sintering temperatures (T_s) ranging $1000 \leq T/\,^{o}C \leq 1500$, the relative density of the sample pellets were measured and the sintering temperature, $T_s = 1300^{o}C$ was noticed to have achieved an optimum acceptable relative density of ceramic electrolytes higher than 94% [191]. Moreso, $T_s = 1300^{o}C$ assures phase stability and decomposition of sintered solid-state electrolytes was negligible. The calcined nanopowders and dense pellets were analysed using the various characterisation techniques: TGA-DSC, XRD, HT-XRD, XRF, FTIR, Laser-Raman scattering, Densification-porosity, Impedance spectroscopy, SEM-EDS, TEM-EDS, HR-TEM, for analysing the crystallographic structures, ionic conductivity and thermodynamic/kinetic properties of the electrolyte. The solid-state electrolytes are considered suitable candidate electroceramic materials having potential applications in various electrochemical devices such as solid-state batteries, solid oxide fuel cells (SOFC), chemical sensors and electrochemical sensors.

The modified sol-gel procedure developed in our Leeds materials synthesis laboratory is practically comparable with the sol-gel process routes reported in various literature by Mielewczyk *et al.* [131] and Kazakos-Kijowski *et al.* [25] (see appendix A-1).

Thermodynamic and kinetic measurements also revealed the suitability of solid-state electrolytes in high-temperature electrochemical sensors. The electrolytes measured by impedance spectroscopy shows very low electronic conductivity and an improved ionic conductivity. The ionic transport number (t_{ion}) of Mg^{2+}-cation in the ceramic end-members solid-state electrolytes was determined by the thermodynamic measurements using the emf method.

The pelletised $MgCr_2O_4+Cr_2O_3$, $MgAl_2O_4+\alpha\text{-}Al_2O_3$ and $MgFe_2O_4+\alpha\text{-}Fe_2O_3$ biphasic powder mixture were synthesised by the solid-state method and characterised for use as reference electrodes in the preliminary research into thermodynamic measurements by the emf method and in sensor measurements. A stable reference electrode is a vital component in sensor fabrication and testing because any drift in the reference potential would lead to a drift in the sensor output. Meanwhile, the biphasic powder mixture of $MgCr_2O_4+Cr_2O_3$ and $MgFe_2O_4+\alpha\text{-}Fe_2O_3$ pellets were used as the reference electrodes in setting up the galvanic cell for thermodynamic measurements. The biphasic powder mixture $MgCr_2O_4+Cr_2O_3$ was however used in fabricating the solid-state Mg-sensor as reference electrode in this research. The $MgCr_2O_4+Cr_2O_3$ biphasic powder mixture is considered the most stable reference electrode showing no visible phase change. Sintered pellets of $\alpha\text{-}MgAl_2O_4+Al_2O_3$ biphasic powder mixture was considered during thermodynamic measurements and sensor analysis also but for some limitations such as, phase change and instability, the output was not reported rather, it was labelled as trial samples which could be useful in the thermodynamic measurements and sensor research analysis in future.

The working electrode, Al-x[10]Mg alloy was prepared by melting 0.56kg pure Al-block and varying the concentration with Mg-rod at a constant increment of 10% starting at 0.005 wt.% for three different runs that is, 0.005-0.5 wt.% Mg-rod and subsequently, 1.0 wt.% and 1.5 wt.%, respectively at $700\pm5^{o}C$.

Further, 0.46725kg and 0.60kg pure Al-blocks were also melted at different intervals while their concentrations were varied within 0.005-1.5 wt.% and 0.005-1.0 wt.% Mg-rod, respectively. The three sensor testing data reported in this research were those from solid-state Mg-sensors fabricated using $MgHf_4P_6O_{24}$, $MgZr_4P_6O_{24}$, $MgCe_4P_6O_{24}$ solid-state electrolytes, respectively. The solid-state Mg-sensors were fabricated with biphasic powder mixture of $MgCr_2O_4+Cr_2O_3$ for ease of comparison.

The sintered pellets of $MgZr_4P_6O_{24}$, $MgHf_4P_6O_{24}$, $MgCe_4P_6O_{24}$ solid-state electrolytes together with the solid-state solutions, $MgZr_2Hf_2P_6O_{24}$ and $MgZr_2Ce_2P_6O_{24}$ ($x = 0.5$) were measured for their chemical stability in a molten Al at $700\pm5^{o}C$ for 8h and 24h, respectively. Similarly, the chemical stability of the electrolyte pellets and solid-state

---

[10] Weight percent of Mg in molten Al

solutions were also analysed in molten OFHC-Cu and in Cu - 0.5 wt.% Mg at 1250°C for 2h and 6.5h, respectively.

4.2 Solid-state electrolytes

Solid-state electrolytes are materials with high ionic conductivity, either of cation or anion but not usually both, and with negligible electronic conductivity. They are the solid-state equivalent of molten salts or strong liquid electrolytes. Sometimes, they are also called superionic conductors, fast ion conductors or optimised ionic conductors.

The available data in literature shows $MgZr_4P_6O_{24}$ electrolyte as a good Mg^{2+}-cation conductor [24-26, 131]. Mg^{2+}-cations possess several advantages which makes it an attractive material, it has a small ionic radius (0.072nm) with a stable oxidation state (+2), it is not so reactive as other alkali metals and can be stable in various atmospheres [131]. In this research, however, the structure and electrical properties of $MgZr_4P_6O_{24}$, $MgHf_4P_6O_{24}$, $MgCe_4P_6O_{24}$ solid-state electrolytes and the solid-state solutions were studied in relation to their application as high conducting solid-state electrolytes in sensor making and for thermodynamic/kinetic measurement. Phase composition of the synthesised solid-state electrolytes were studied using XRD analysis on the calcined nanopowders and on the sintered pellets to evaluate the phases formed and possible transformation since both processes were achieved at high-temperatures. The powders were calcined at 900°C for 3h and later at 800°C for 0.5h in order to compare the effect of temperature on crystallite size. The pellets were then sintered at 1300°C for 24h. The density measurements on the solid-state electrolytes as defined in this research revealed 1300°C sintering temperature as a more suitable densification temperature.

4.2.1 TGA-DSC

The xerogel powders of $MgZr_4P_6O_{24}$, $MgHf_4P_6O_{24}$, $MgCe_4P_6O_{24}$ electrolytes and the solid-state solutions precursors synthesised by the modified sol-gel process was run in simultaneous TGA and DSC mode to determine the weight loss and heat flow in order to estimate calcining conditions and thermal stability of the dried xerogel powders as shown in Figure 4.1. The nanopowders calcined at 900°C for 3h were further run in a simultaneous TGA and DSC mode to determine phase transformation as well as binder burn-out temperature prepared by adding 1 wt.% Ciba Glascol HA4 binder to calcined nanopowders during pelletising before sintering. The TGA-DSC curves are presented in Figure 4.2

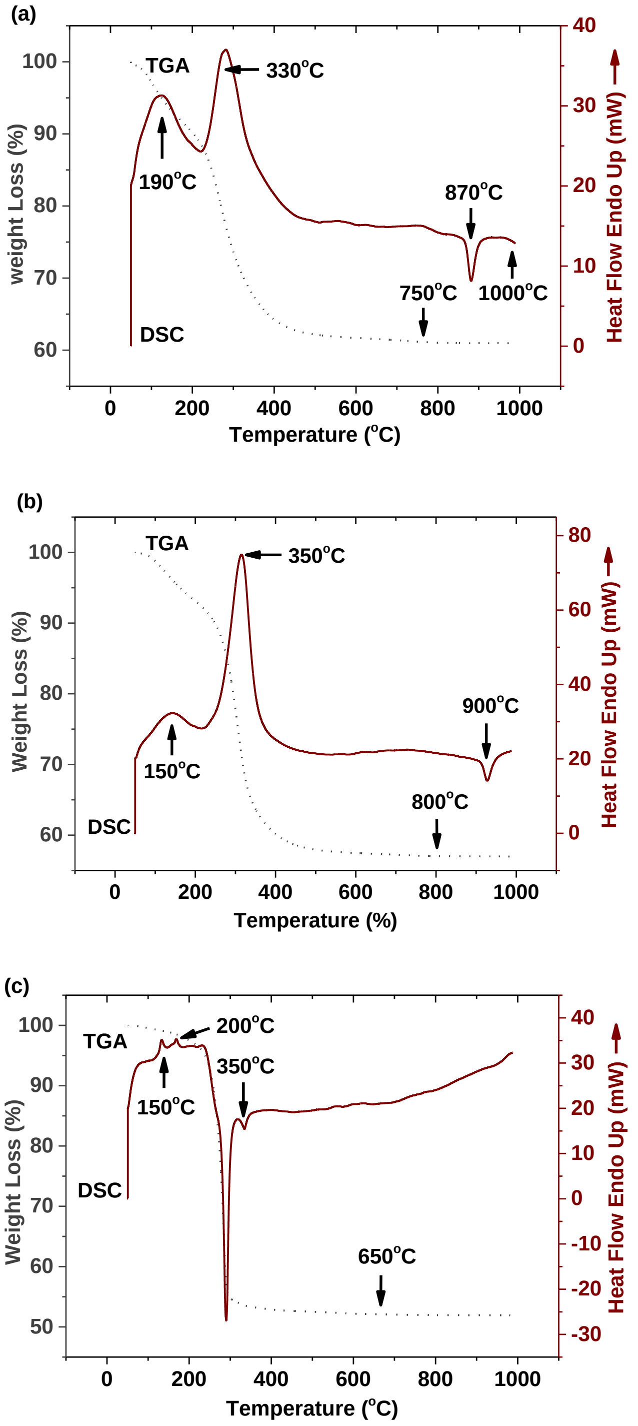

Figure 4-1 TGA-DSC curves of (a) $MgZr_4P_6O_{24}$ (b) $MgHf_4P_6O_{24}$ and (c) $MgCe_4P_6O_{24}$ dried xerogel powders with a scan rate of 10°Cmin^{-1} in air

The xerogel of the three different powders synthesised using a newly modified sol-gel process was run in TGA and DSC mode to determine the weight loss and heat flow in order to estimate the calcining conditions and thermal stability or reaction temperature of the precursor-gel of the xerogel powders. DSC measurements helped confirm any phase transformation as a function of temperature. Figure 4.1(a) depicted TGA-DSC profile curves of $MgZr_4P_6O_{24}$ solid-state electrolyte heated in a uniform temperature range $30 \leq T/^oC \leq 1000$. The TGA curve shows a progressive weight loss of the starting xerogel powders during decomposition process at 30-500°C and it begins to stabilise at 750-870°C, which agrees with the exothermic peak at 870-900°C region. The $MgZr_4P_6O_{24}$ solid-state electrolyte is therefore believed to have been formed at that temperature range. The decomposition pathway on the TGA curve equally shows a sharp drop in weight from 99.9% to 62.6% weight loss which is attributed to the loss of H_2O and decomposition of the various component precursor materials; $NH_4H_2PO_4$, $Mg(NO_3)_2$, $ZrOCl_2.8H_2O$ with decomposition temperatures shown by the endothermic peaks at 190°C, 330°C, and 437°C, respectively. At 190°C, $NH_4H_2PO_4$ decomposed into P_2O_5, H_2O, and NH_3, while $Mg(NO_3)_2$ decomposed into MgO, NO_2, and O_2 at 330°C. Similarly, $ZrOCl_2.8H_2O$ also decomposed into ZrO_2, HCl, and H_2O at 437°C. MgO, P_2O_5, and ZrO_2 formed *in situ* are reactive oxides that yield high purity single phase $MgZr_4P_6O_{24}$ at 870°C and stabilises through 900-1000°C, seen in Figure 4.1(a) and synthesis stoichiometric equation (3.1). Residues of the precursors stoichiometric reactions NH_4Cl, HCl, HNO_3, H_2O vaporises during calcination at 870-900°C thereby forming a pure single phase $MgZr_4P_6O_{24}$ solid-state electrolyte at the temperature.

Figures 4.1(b) and 4.1(c) are the TGA-DSC curves measured in air at a scan rate of 10^oCmin^{-1}. The main decomposition changes observed in the TGA curves in Figures 4.1(b) and 4.1(c) is presented in three different regions. The first region within 30-100°C corresponds to the removal of lattice H_2O. The weight loss in the temperature region 150-500°C is due to decomposition or oxidation of the inorganic precursors-gelled materials such as $Mg(NO_3)_2$, $HfCl_4$, $NH_4H_2PO_4$ for $MgHf_4P_6O_{24}$ synthesis and $Ce(NH_4)_2(NO_3)_6$ for $MgCe_4P_6O_{24}$ synthesis, respectively. There was no further loss of weight above 500±25°C for $MgHf_4P_6O_{24}$ and $MgCe_4P_6O_{24}$ dried xerogel powders, respectively. Similarly, the DSC profile for $MgHf_4P_6O_{24}$ dried xerogel powders in Figure 4.1(b) shows two endothermic decomposition peaks at 150°C and 350°C and an exothermic peak at 900°C. The inorganic precursor, $NH_4H_2PO_4$ decomposes into

$(NH_4)_3H_2P_3O_{10}$ and H_2O molecules at a 140-170°C temperature range which could be responsible for the endothermic peak at 150°C. $Mg(NO_3)_2$ precursor compound also decomposes into MgO, NO_2, and O_2 at a decomposition temperature above 300°C, this could be responsible for the endothermic peak at 350°C. Formation of the reactive oxide, HfO_2 by the oxidation of $HfCl_4$ at 432°C produced $MgHf_4P_6O_{24}$ compound after a stoichiometric reaction with MgO and P_2O_5 reactive oxides at 900°C and indicated as an exothermic peak on the DSC profile in Figure 4.1(b). $MgHf_4P_6O_{24}$ compound started forming at 780°C as shown on the TGA curve with full crystallinity at 900°C. Similarly, the precursor inorganic compound, $Ce(NH_4)_2(NO_3)_6$ also decomposed into the reactive oxide, cubic CeO_2 at 110-150°C and later at 155-190°C in a two-phase decomposition. This decomposition could explain the presence of endothermic peaks at 150-200°C. Meanwhile, the double valence change of cerium: Ce(IV) → Ce(III) → Ce(IV) during thermal decomposition of $Ce(NH_4)_2(NO_3)_6$ [192] explains the change of cerium oxidation state. However, redox reaction of $2Ce^{4+} + O^{2-} \rightarrow 2Ce^{3+} + \frac{1}{2} O_2$, where O^{2-} from the breakdown of N-O bonds in nitrate groups [193] could also account for the sharp drop in weight observed in Figure 4.1(c) which is in excellent agreement with the TGA curve at 200-300°C. A monoclinic $MgCe_4P_6O_{24}$ compound in Figure 4.1(c) could, therefore, be formed from a stoichiometric reaction of CeO_2, MgO, and P_2O_5 reactive oxides starting from 350°C. The low-temperature exothermic peak for $MgCe_4P_6O_{24}$ compound at 350°C could provide useful reasons to consider in calcining and sintering the compound at low temperatures. Furthermore, there were no further peaks on the DSC profile of $MgCe_4P_6O_{24}$ precursors at higher temperatures. By comparison, DSC profiles of $MgHf_4P_6O_{24}$ and $MgCe_4P_6O_{24}$ solid-state electrolytes in Figure 4.1(b) and 4.1(c) shows a sharp endothermic and exothermic peaks at 300-350°C. The observed difference in DSC profile curves of both electrolytes perhaps is in reactivity of the precipitative precursors, $HfCl_4$ and $Ce(NH_4)_2(NO_3)_6$. The inorganic precursors $ZrOCl_2.8H_2O$ and $HfCl_4$ in DSC profile curves of Figure 4.1(a) and 4.1(b), respectively, are in good agreement. Meanwhile, Figure 4.1(c) has no peaks at high-temperatures indicating that the solid-state electrolyte is stable at high-temperatures.

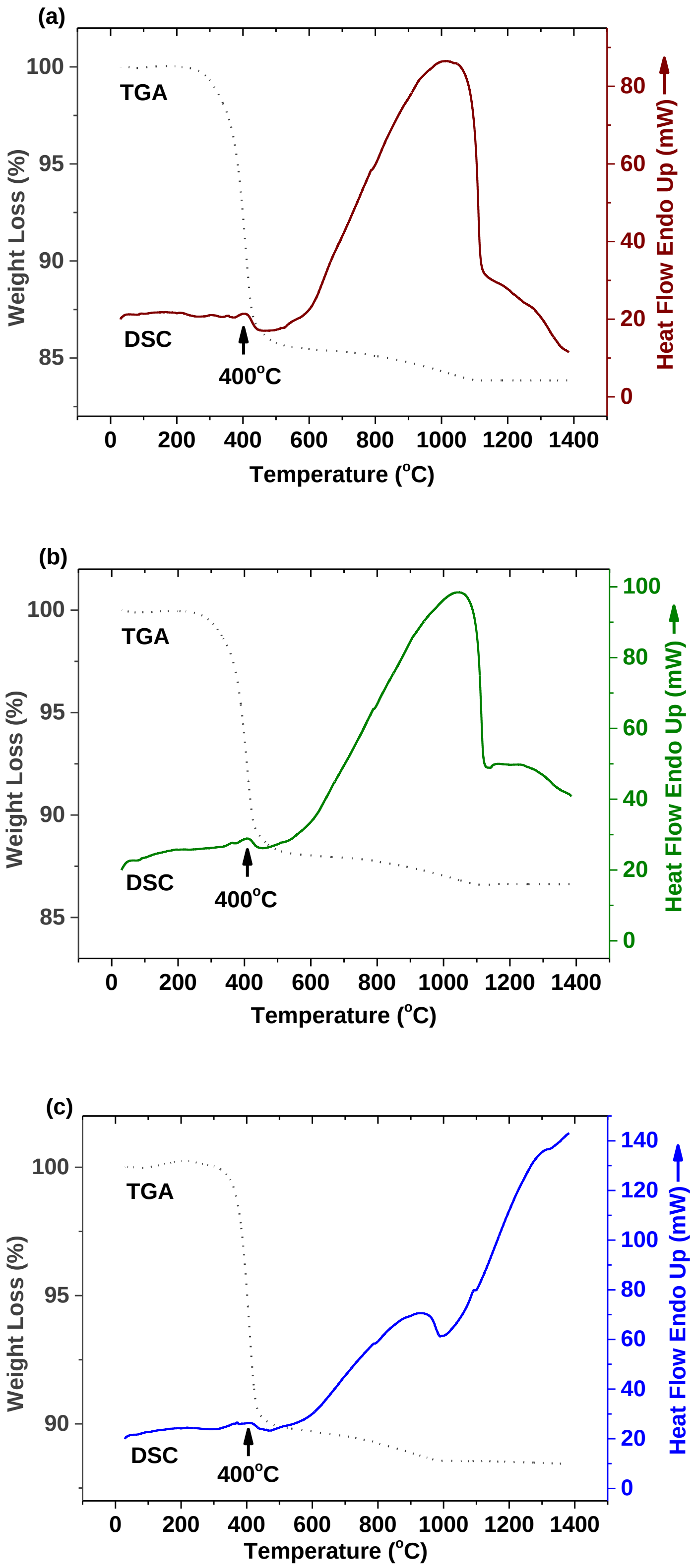

Figure 4-2 TGA-DSC curves of (a) $MgZr_4P_6O_{24}$ (b) $MgHf_4P_6O_{24}$ (c) $MgCe_4P_6O_{24}$ nanopowders calcined at 900°C for 3h showing no phase transformation, with the burn-out temperature of 1 wt.% Ciba Glascol HA4 binder at 400-450°C

Simultaneous TGA-DSC measurements were performed on the single-phase calcined powders of $MgZr_4P_6O_{24}$, $MgHf_4P_6O_{24}$, and $MgCe_4P_6O_{24}$ nanopowders to determine any possible phase transformation and burn-out temperature of 1 wt.% Ciba Glascol HA4 binder added to the calcined solid-state electrolyte nanopowders prior pelletising using uniaxial press then sintering. The TGA-DSC curves are presented in Figure 4.2. The analysed solid-state electrolyte powders with ordered monoclinic symmetry show no transformation from monoclinic to orthorhombic phase at $30 \leq T/^{o}C \leq 900$. However, the solid-state electrolyte sample reported in Figure 4.2(a) transforms to an orthorhombic $Zr_2(PO_4)_2O$ phase at $1350 \pm 25^{o}C$. In contrast, Figure 4.2(b) and 4.2(c) remain stable at high-temperatures, $1000 \leq T/^{o}C \leq 1400$ with no visible phase transformation from monoclinic to orthorhombic. The endothermic peak in the 400-450^{o}C temperature region is attributed to the burn-out temperature of 1 wt.% Ciba Glascol HA4 binder that was added to the calcined nanopowders before pelletising. The peak is common to the three solid-state electrolyte nanopowders with added Ciba Glascol HA4 binder. The second endothermic peak at 900^{o}C could be referred to the formation temperature. This confirms that the solid-state electrolyte nanopowders attained full crystallinity at a temperature of 900^{o}C. The DSC profile curves in Figures 4.2(a), 4.2(b) and 4.2(c) demonstrates that the Ciba Glascol HA4 binder burn-out temperature was identified at 400-450^{o}C since that temperature region is common on the three calcined sample powders and that the solid-state electrolytes are formed at lower temperatures, 800-870^{o}C but attained full crystallinity at 900^{o}C. The DSC profile depicted similar pathways in Figure 4.2(a) and 4.2(b) which confirms that the tetravalent cations, Zr^{4+} and Hf^{4+} in the B-site of $MgZr_4P_6O_{24}$ and $MgHf_4P_6O_{24}$ electrolytes belonging to the same group thereby having similar chemical properties. In contrast, the nanopowders for TGA-DSC measurements in Figure 4.2(c) profile curves, $MgCe_4P_6O_{24}$ solid-state electrolyte containing tetravalent lanthanide cation, Ce^{4+} with a strong basicity which is attributed to the curve presented in Figure 4.2(c). The TGA profile curves, however, are similar, the weight loss at 30-400^{o}C is attributed to the loss of latent moisture from Ciba Glascol HA4 binder, and a complete shrinkage is observed at 1000-1400^{o}C.

4.2.2 XRD

The structural characterisation, phase identification and average crystallite size (D) of the solid-state electrolytes were studied by XRD. Ambient temperature XRD (using the Bruker D8 diffractometer, with Cu-K_{α} X-rays) and non-ambient temperature XRD, also referred to as high-temperature XRD, HT-XRD (using the PANalytical X'pert diffractometer) was conducted on the xerogel and calcined powders, and the sintered pellets too. Dried xerogel powders were subjected to HT-XRD measurements using the X'pert diffractometer in the range from $25 \leq T/^{o}C \leq 900$ at 25-50°C temperature interval to investigate phase transformation, appropriate calcination temperature and the polycrystalline nature of the synthesised nanoparticle compounds as presented in Figure 4.3. The formation of ammonium chloride, NH_4Cl, the crystalline phase at the low temperatures zone (25-150°C) as observed in Figure 4.3(a) and 4.3(b) is presented in Figure 4.3(d).

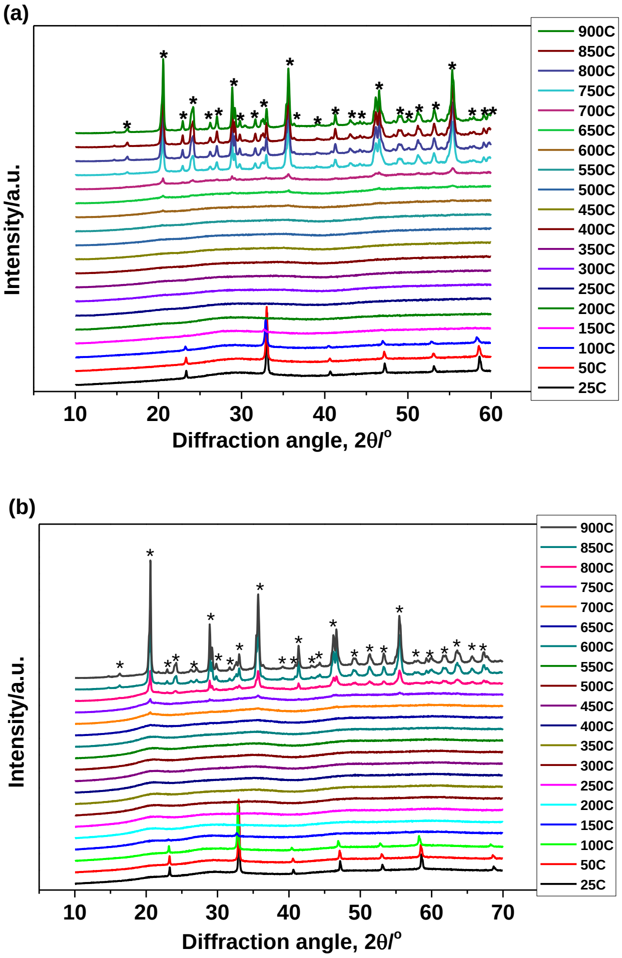

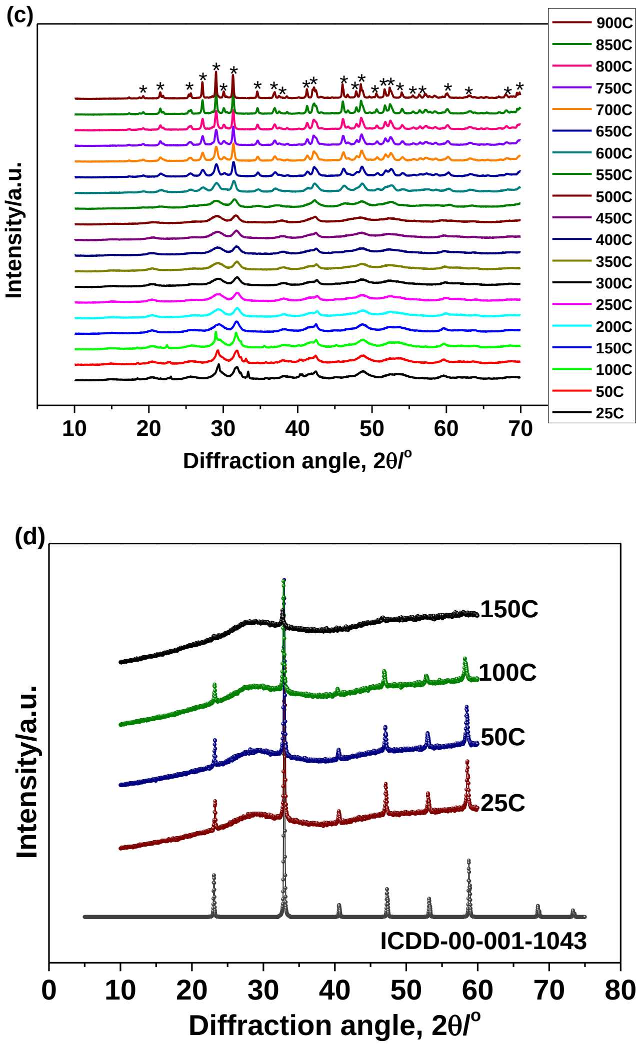

Figure 4-3 High-temperature XRD profiles for (a) $MgZr_4P_6O_{24}$, (b) $MgHf_4P_6O_{24}$, and (c) $MgCe_4P_6O_{24}$ xerogel powders, and (d) NH_4Cl crystalline phase ranging 25-150°C. *Crystalline peak profiles of $MgZr_4P_6O_{24}$, $MgHf_4P_6O_{24}$, and $MgCe_4P_6O_{24}$ solid-state electrolytes, respectively

The HT-XRD measurement on dried xerogel powders presented in Figure 4.3 showing the complete formation of $MgZr_4P_6O_{24}$, $MgHf_4P_6O_{24}$, and $MgCe_4P_6O_{24}$ nanopowders at different crystallisation temperatures. Crystallisation characterisation was therefore based on the TGA-DSC and HT-XRD measurements on some dried xerogel powders to determine the calcining temperatures. Some sample pellets of 13mm Ø and 3.8mm thickness were prepared from the calcined nanopowders using a uniaxial steel die at a compressive pressure of 5kN.

The XRD patterns of the solid-state ceramics electrolytes - $MgZr_4P_6O_{24}$, $MgHf_4P_6O_{24}$, and $MgCe_4P_6O_{24}$ nanopowders calcined at 900°C for 3h and the pellets later sintered at 1300°C for 24h is presented in Figure 4.4, with almost all of the peaks matched and indexed accordingly. However, minor extraneous peaks indicating traces of coexistent second phase, zirconium oxide phosphate [$Zr_2(PO_4)_2O$] was observed on $MgZr_4P_6O_{24}$ pellets sintered at 1300°C for 24h.

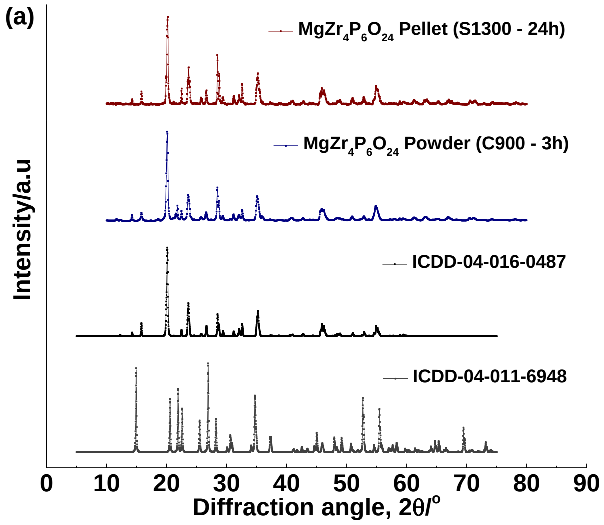

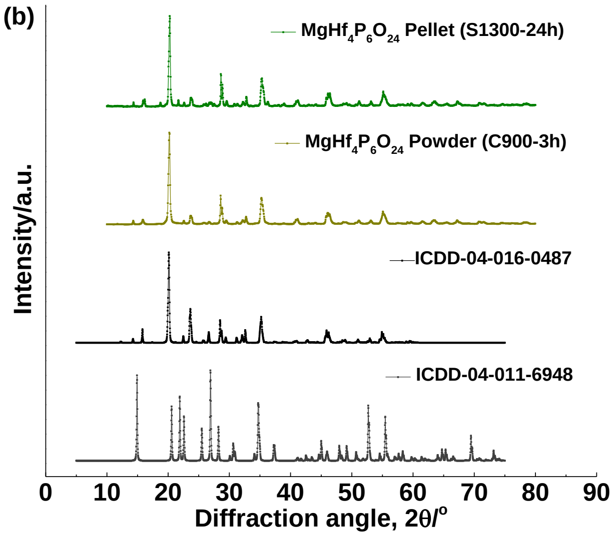

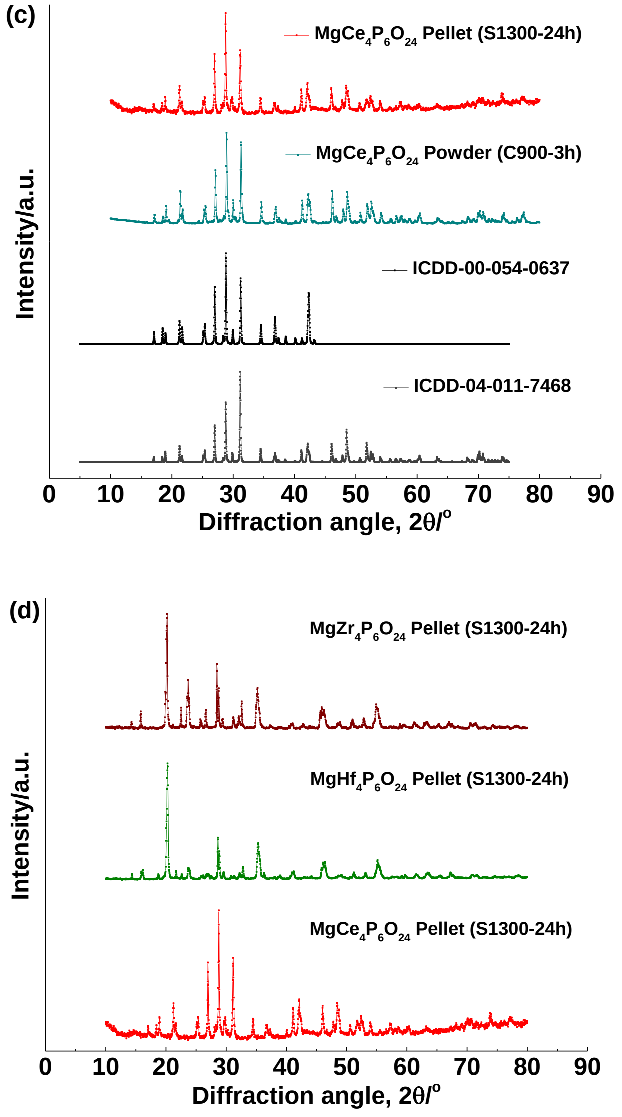

Figure 4-4 XRD peak profiles of (a) $MgZr_4P_6O_{24}$ (b) $MgHf_4P_6O_{24}$ (c) $MgCe_4P_6O_{24}$ powders calcined at 900°C for 3h and pellets sintered at 1300°C for 24h, respectively, and (d) Phases of sintered pellets. All the peaks were then indexed to $Mg_{0.5}Zr_2(PO_4)_3$ [ICDD-04-016-0487], $Zr_2(PO_4)_2O$ [ICDD-04-011-6948], $Mg_{0.5}Ce_2(PO_4)_3$ [ICDD-00-054-0637], and $Mg_{0.167}Ce_{0.667}$ (PO_4) [ICDD-04-011-7468]

Profiles of X-ray diffraction of both powders and sintered pellets of the synthesised xerogels and calcined nanopowders electrolytes measured in ambient and non-ambient modes are shown in Figures 4.3-4.5. An ambient temperature XRD was conducted on both the calcined and sintered pellets while a non-ambient XRD measurement, also referred to as high-temperature XRD, HT-XRD was conducted on the xerogel powders only. Since the TGA-DSC measurements show complete shrinkage at 750-800°C for

$MgZr_4P_6O_{24}$ and $MgHf_4P_6O_{24}$ xerogel powders, and 650°C for $MgCe_4P_6O_{24}$ xerogel as shown in Figure 4.1, the calcination temperature of the xerogel powders was predicted on these results and HT-XRD measurements on the xerogels complimenting TGA-DSC results. HT-XRD profiles in Figure 4.3 shows xerogel powders measured at 25-900°C temperature range, and revealed that the precursor materials crystallised into $MgZr_4P_6O_{24}$ nanopowders from 750°C and then crystallised fully at 800-900°C. Similarly, precursors of $MgHf_4P_6O_{24}$ and $MgCe_4P_6O_{24}$ also crystallised into specific nanopowders starting at 800°C and 650°C, respectively. Based on the TGA-DSC analyses and HT-XRD measurements, the xerogel powders were therefore calcined at 900°C for 3h and, calcination repeated at 800°C for 0.5h on the same xerogel powder composition for the purpose of comparing the crystallite size of the three end-members electrolytes. The HT-XRD profiles for $MgZr_4P_6O_{24}$, $MgHf_4P_6O_{24}$ and $MgCe_4P_6O_{24}$ solid-state electrolytes are presented in Figure 4.3. However, Figure 4.3(a) and 4.3(b) shows that the formation of $MgZr_4P_6O_{24}$ and $MgHf_4P_6O_{24}$ solid-state electrolytes involved intermediate reactions. The xerogels contained a mixture of both amorphous and crystalline phase. In Figure 4.3(a) and 4.3(b), three stages were identified based on their structures. The first stage shows that at 25-150°C, crystalline solid peaks were identified as ammonium chloride, NH_4Cl [ICDD-00-001-1043]. As the temperature increases, the crystalline solid peaks at 150°C diminishes into a minor peak which finally forms amorphous powders at 200-650°C. In Figure 4.3(d), the polycrystalline peaks of NH_4Cl are believed to have been formed during synthesis of $MgZr_4P_6O_{24}$ and $MgHf_4P_6O_{24}$ gels, and subsequent reaction between a hydrochloric acid (HCl) and ammonia solution (NH_4OH) which was added drop-wise in order to control the pH. The gel formed during synthesis of $MgZr_4P_6O_{24}$ and $MgHf_4P_6O_{24}$ compounds are quite acidic because of the reactions with $ZrOCl_2.8H_2O$ and $HfCl_4$, respectively, these compounds contribute the Cl^- which freely combines with H^+ in solution to form HCl as shown in Equation (4.1)

$$H^+_{(aq)} + Cl^-_{(aq)} \rightarrow HCl_{(aq)} \qquad (4.1)$$

NH_4OH was then added to the gel of both $MgZr_4P_6O_{24}$ and $MgHf_4P_6O_{24}$ compound before dehydration to produce NH_4Cl and H_2O as shown in Equation (4.2)

$$NH_4OH_{(l)} + HCl_{(aq)} \rightarrow NH_4Cl_{(aq)} + H_2O_{(l)} \qquad (4.2)$$

The second stage shows that at 200-650°C, the HT-XRD profiles in Figure 4.3(a) and 4.3(b) were completely amorphous which could be attributed to the decomposition temperature range of the precursors, $Mg(NO_3)_2$, $NH_4H_2PO_4$ and $ZrOCl_2.8H_2O/HfCl_4$ and that the decomposition rate of the precursors could be responsible for suppressing the crystalline peaks of NH_4Cl at higher-temperature which got completely diminished at this temperature range which was identified on the TGA-DSC profiles presented in Figure 4.1(a) and 4.1(b), respectively. At this temperatures, no peak was registered which means the resulting solid-state electrolyte materials were not formed at this stage. The third stage also shows the formation of a highly crystalline and single phase solid-state electrolytes at 700-900°C. In Figure 4.3(a) and 4.3(b), the formation of $MgZr_4P_6O_{24}$ and $MgHf_4P_6O_{24}$ solid-state ceramic electrolytes represent a gradual and progressive change in the diffractogram peaks, indicating a final stage of reactions and crystallisation. The minor and full crystal peaks identified at 700-900°C were indexed as $MgZr_4P_6O_{24}$ and $MgHf_4P_6O_{24}$ compounds which fully crystallised as temperature increases. Calcining temperatures in this research was influenced by the full crystalline peaks at 800-900°C and characterised single phase compounds. Figure 4.3(c) shows the HT-XRD profiles of $MgCe_4P_6O_{24}$ xerogel powders at 25-900°C. The formation of crystalline and single phase $MgCe_4P_6O_{24}$ compound started at 650°C and remained uniformly stable as the temperature increases, the crystalline peaks were identified to be in perfect agreement with Figure 4.1(c), showing that the TGA-DSC profile curves at 650-1000°C remaining constant with no visible trace of endothermic - exothermic peaks indicating any phase transformation. Based on this discovery, the xerogel powders were then calcined at 900°C for 3h and subsequently at 800°C for 0.5h, by comparing the average crystallite sizes of the electrolytes. The calcined nanopowders were seen as a single phase $MgZr_4P_6O_{24}$, $MgHf_4P_6O_{24}$ and $MgCe_4P_6O_{24}$ of monoclinic crystal system and a space group of $P2_{1/n}$, using the standard powder diffraction file (PDF-card) from International Centre for Diffraction Data (ICDD) database. Further, pellets pressed from the calcined nanopowders were sintered at a different temperature range, $1000 \leq T/^{o}C \leq 1500$ for 24h in order to achieve a dense and well-sintered pellets. Density and porosity measurements on the sample pellets also influenced the need to sinter the sample pellets at a high-temperature; 1300°C was considered in this research. Figure 4.4 therefore, shows crystalline single phase $MgZr_4P_6O_{24}$, $MgHf_4P_6O_{24}$ and $MgCe_4P_6O_{24}$ nanopowders calcined at 800-900°C and the pellets sintered at 1300°C. In Figure 4.4(a) and 4.4(b), it can be seen that highly crystalline single phase solid-state electrolyte powders, $MgZr_4P_6O_{24}$ and $MgHf_4P_6O_{24}$ electrolytes were formed at 900°C and indexed accordingly. The $MgZr_4P_6O_{24}$ pellets sintered at 1300°C shows a few minor extraneous peaks indicating traces of coexistent second phase. The profiles on Figure 4.4(a) and 4.4(b) shows that the solid-state electrolyte is stable with a single phase at 800°C to 900°C which agrees with the findings of Kazakos-Kijowski *et al.* [25]. In Figure 4.4(a) and 4.4(b), the nanopowders calcined at 900°C for 3h shows a single phase solid-state electrolyte indexed against double $Mg_{0.5}Zr_2(PO_4)_3$ [ICDD-04-016-0487]. The sintered pellets were however indexed against $Zr_2(PO_4)_2O$ [ICDD-04-011-6948] to determine some minor extraneous peaks that were identified during X-ray diffraction measurements and analysis. Figure 4.4(a) further revealed the minor second phase as an orthorhombic $Zr_2(PO_4)_2O$ compound at 22.54° 2θ which confirms that the sintered $MgZr_4P_6O_{24}$ pellets is stable at 1300°C [24]. Similarly, $MgHf_4P_6O_{24}$ nanopowders calcined at 900°C and the pellets sintered at 1300°C shows great stability as the sintering temperature increases, and extraneous peaks were not found. The $MgZr_4P_6O_{24}$ and $MgHf_4P_6O_{24}$ pellets were therefore sintered at 1300°C in this research to achieve stable and densified pellets. As the sintering temperature of $MgZr_4P_6O_{24}$ pellet increases to 1450°C, 1470°C and then 1500°C, extraneous peaks became pronounced, and highly densified but with a completely transformed phase. At a sintering temperature range of 1450-1500°C, the sintered pellet was analysed as an orthorhombic $Zr_2(PO_4)_2O$ compound different from the $MgZr_4P_6O_{24}$ solid-state electrolyte in structure and chemical composition. $MgHf_4P_6O_{24}$ solid-state electrolyte remains stable at $900 \leq T/\,^{o}C \leq 1500$. However, the pellets were sintered and a highly densified pellet was achieved at 1300°C. The diffraction spectra in Figure 4.4(a) and 4.4(b) are similar in structure and they exhibit sharp peaks which indicates excellent crystallinities and long-range crystallographic orders well indexed for both calcined nanopowders and sintered pellets [194]. The similarity and lattice parameters of Zr and Hf analogues are believed to be of the same order because of the similar sizes of Zr^{4+} and Hf^{4+}[195]. Figure 4.4(c) also shows the stability of $MgCe_4P_6O_{24}$ compound at an increasing temperature. The nanopowders and sintered pellets of cerium based solid-state electrolytes were indexed against a $Mg_{0.5}Ce_2(PO_4)_3$ [ICDD-00-054-0637], and $Mg_{0.167}Ce_{0.667}(PO_4)$ [ICDD-04-011-7468] which revealed no extraneous peaks at $900 \leq T/^{o}C \leq 1500$. Figure 4.4(d) also shows some similarities in profile peaks of $MgZr_4P_6O_{24}$ and $MgHf_4P_6O_{24}$, unlike $MgCe_4P_6O_{24}$ compound. It shows according to Figure 4.4, three end-members electrolytes maintained stability at $900 \leq T/\ ^{o}C \leq 1300$ temperature range. As stated, $MgZr_4P_6O_{24}$ transforms from the monoclinic system to orthorhombic $Zr_2(PO_4)_2O$ at temperatures higher than 1300°C. However, $MgHf_4P_6O_{24}$ and $MgCe_4P_6O_{24}$ remains stable at higher temperatures but 1300°C was considered the sintering temperature in this research for the purpose of comparison and to also reduce excess carbon footprint. Zr is considered in many aspects, chemically identical to Hf; similarities in the chemistry of their oxides, ZrO_2 and HfO_2 are also noticed. However, they present significant differences in physical properties, but both Zr^{4+} and Hf^{4+} have similar ionic radii (0.72Å and 0.71Å for six-fold coordination), respectively [27, 103], with very different electronic density (atomic numbers = 40 and 72), respectively. For instance, Hf has a high absorption cross section for thermal neutrons, more than 500 times that of Zr [196]. The lanthanide, Ce exist as Ce^{3+} and Ce^{4+}, both having different ionic radii (1.01Å and 0.87Å for six-fold coordination), respectively [27, 103], with the same electronic density (atomic number = 58). Unlike with Hf^{4+}, the complete substitution of Zr^{4+} with Ce^{4+} has different chemistry of their oxides and changes in both ionic and crystal radii.

Furthermore, $MgZr_4P_6O_{24}$ sample pellets sintered using modified two-step sintering method at 1090°C for 1h and then, 900°C for 75h presented in Figure 4.5 shows the stability of $MgZr_4P_6O_{24}$ solid-state electrolytes at 800-900°C, with no transformation. The possibility of $MgZr_4P_6O_{24}$ solid-state electrolytes with single phase at 800-900°C was possible after the reversible two-step sintering method is also shown in Figure 4.5

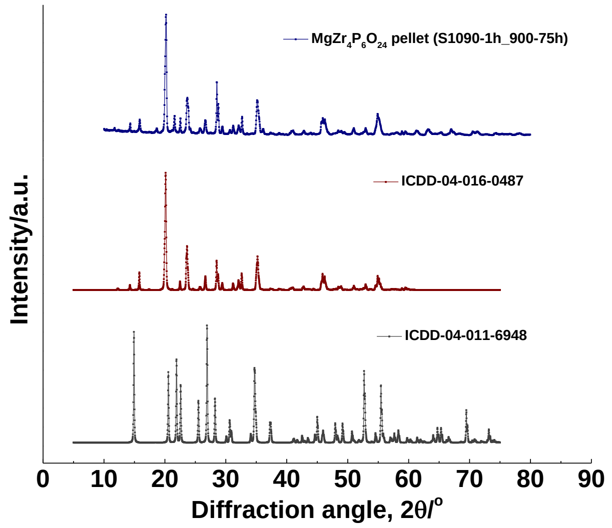

Figure 4-5 Ambient temperature XRD of $MgZr_4P_6O_{24}$ pellet sintered using two-step sintering method at 1090°C for 1h, and then 900°C for 75h. All the peaks are indexed to ICDD 04-016-0487 and ICDD 04-011-6948

Figure 4.5 shows the ambient temperature x-ray diffraction profiles for $MgZr_4P_6O_{24}$ pellet sintered at 1090°C for 1h, cooled down gradually to 900°C and then annealed at this temperature for 75h. Since $Zr_2(PO_4)_2O$ compound is a minor second phase in the sintered $MgZr_4P_6O_{24}$ compound at $1000 \leq T/{}^{\circ}C \leq 1500$, the minor second phase was identified at 1090°C. This is in perfect agreement with the TGA-DSC measurement curves in Figure 4.1(a) at sintering temperatures ≥ 1000°C. Furthermore, knowing that $MgZr_4P_6O_{24}$ sample pellet retains a pure single phase at 900°C, the pellet was cooled down gradually to 900°C and annealed for 75h. It is proven therefore that $MgZr_4P_6O_{24}$ compound is stable at 800-900°C [25] and transform thereafter with the possibility of achieving a reversible transformation to a single phase $MgZr_4P_6O_{24}$ compound with diminished characteristic peaks [24]. Hence, the tendency of $MgZr_4P_6O_{24}$ compound and the minor extraneous second phase, $Zr_2(PO_4)_2O$ to revert back to pure single phase of the solid-state electrolyte is practicable if annealed at 900°C for a prolonged period when the $MgZr_4P_6O_{24}$ compound is sintered in the vicinity of 1000°C, considering that the loss of P_2O_5 is likely to be less, also that diffusion kinetics in solid-state materials is likely to be slow. Hence, the dissociation of $MgZr_4P_6O_{24}$ to $Zr_2(PO_4)_2O$ is believed to occur at high-temperatures according to equation (4.3)

$$MgZr_4P_6O_{24}\ (s) \rightarrow 2Zr_2(PO_4)_2O\ (s) + P_2O_5\ (g) + MgO\ (s) \qquad (4.3)$$

In an attempt to determine the average crystallite size of solid-state electrolytes at increasing temperature; $MgZr_4P_6O_{24}$, $MgHf_4P_6O_{24}$ and $MgZr_4P_6O_{24}$ xerogel powders were also calcined at 800°C for 0.5h, the powder x-ray diffraction profiles were then observed to be in structural agreement with the nanopowders at 900°C for 3h. The profiles of the solid-state electrolyte nanopowders at 800°C for 0.5h and 900°C for 3h, respectively, as seen in Figure 4.6, showing peak indices and average crystallinity difference of the nanopowders as a function of temperature. The analysis of x-ray diffraction profiles is the usual and standard way to measure the crystallite size of nanocrystals [197] using the Scherrer equation. During calcination or sintering, many crystallites of the same orientation coalesce together and form a large grain having a certain orientation. Crystallite size is normally estimated from the FWHM of the x-ray diffraction peak and corresponds to regions of coherent diffraction domain inside the material. Table 4.1 represent average crystallite sizes obtained at different calcination conditions. Evidently, the calcination temperatures effect grain growth, consequently the crystallite size increases as a function of calcination temperatures. In comparison, the crystallite size difference of 8±1nm, 23±2nm, and 16±1nm, for $MgZr_4P_6O_{24}$, $MgHf_4P_6O_{24}$ and $MgCe_4P_6O_{24}$ solid-state electrolytes, respectively, indicating crystal orientation and grain growth variation in the three characterised materials. The density of ZrO_2, HfO_2 and CeO_2 active precursor oxides, 5.68g/cm^3, 9.68g/cm^3 and 7.22g/cm^3, respectively, contribute to the size formation of the crystals as temperature increases.

Some quantities of $MgZr_4P_6O_{24}$, $MgHf_4P_6O_{24}$ and $MgZr_4P_6O_{24}$ dried xerogel powders were also calcined at 800°C for 0.5h. The various phase formation of the calcined nanopowders were determined using powder X-ray diffraction analysis whereas, the average crystallite size was calculated with Scherrer equation as presented in Equation (4.4);

$$D_{hkl} = \frac{K\lambda}{\beta_{hkl}\cos\theta} \qquad (4.4)$$

where D_{hkl} is crystallite size in the direction perpendicular to the lattice planes, hkl are the Miller indices of the planes being analysed, K is a numerical factor frequently referred to as the crystallite-shape factor of the particles or Scherrer constant [198], λ is the wavelength of x-rays, β_{hkl} is line broadening or full width at half the maximum intensity of the XRD peaks (FWHM) in radians and θ is the diffraction angle of the X-rays (Bragg angle). The numerical factor K also depends on the definitions of the average crystallite size and the width. In this case, the structure of the formula is not affected by these definitions, but the numerical value of K may change appreciably [198, 199]. Using the definition of D_{hkl}, and in the absence of detailed shape information, K = 0.94 is a good approximation [198, 200].

In comparing the average crystallite sizes at different calcination temperature, powder X-ray diffraction data from $MgZr_4P_6O_{24}$, $MgHf_4P_6O_{24}$ and $MgZr_4P_6O_{24}$ nanopowders calcined at 800°C for 0.5h, then at 900°C for 3h, were analysed using the Scherrer equation as presented in Figure 4.6 and the effect of calcination conditions on average crystallite sizes are given in Table 4.1

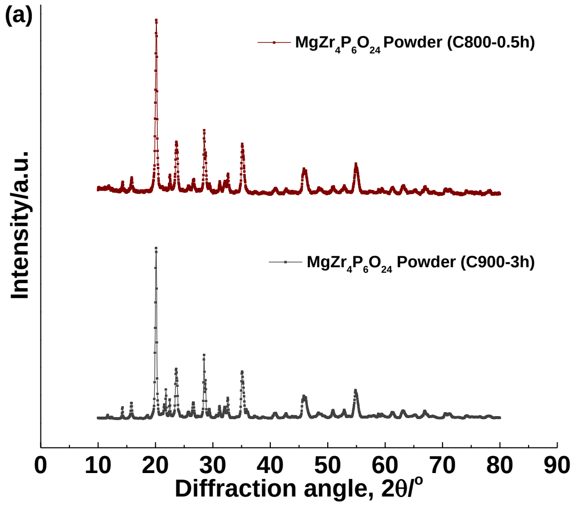

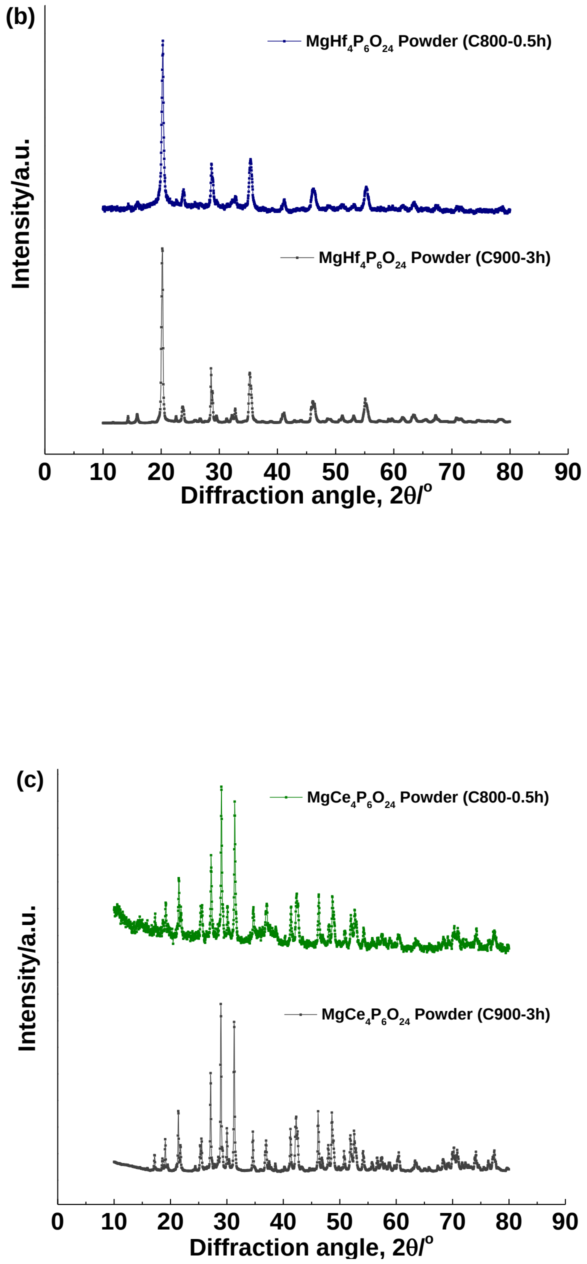

Figure 4-6 Powder XRD pattern of (a) $MgZr_4P_6O_{24}$ (b) $MgHf_4P_6O_{24}$ (c) $MgCe_4P_6O_{24}$ nanopowders calcined at 800°C for 0.5h, and then 900°C for 3h for purpose of comparing crystallite size as a function of temperature

Table 4-1 Comparison of the effect of calcination temperature on average crystallite sizes of $MgZr_4P_6O_{24}$, $MgHf_4P_6O_{24}$ and $MgCe_4P_6O_{24}$ nanopowders

Compound	Calcination temperature (°C)	Crystallite size from Scherrer equation (nm)
$MgZr_4P_6O_{24}$	800	32±2
	900	39±1
$MgHf_4P_6O_{24}$	800	20±2
	900	42±2
$MgCe_4P_6O_{24}$	800	37±2
	900	52±1

The powder XRD patterns of $MgZr_4P_6O_{24}$, $MgHf_4P_6O_{24}$ and $MgCe_4P_6O_{24}$ compounds in Figure 4.4 shows a pure single phase nanopowders with an ordered crystal structure indexed by monoclinic system with $P2_{1/n}$ space group (Z=4), the lattice cell parameters for crystallised $MgZr_4P_6O_{24}$ and $MgHf_4P_6O_{24}$ nanopowders are; a(Å) = 12.4218(2), b(Å) = 8.9025(2), c(Å) = 8.8218(2), β(deg) = 90.4660(1) and V(Å^3) = 975.53(2) [ICDD-04-016-0487]. Similarly, the lattice parameters of $MgCe_4P_6O_{24}$ nanopowders are; a(Å) = 6.794(1), b(Å) = 7.020(1), c(Å) = 6.468(1), β(deg) = 103.46(1) and V(Å^3) = 300.03 [ICDD-04-011-7468] at 298K. The refined crystal structures of $MgZr_4P_6O_{24}$, $MgHf_4P_6O_{24}$ and $MgCe_4P_6O_{24}$ compounds are presented in Figure 4.7. The unit cell lattice parameters and R-factor values obtained at 298K through Rietveld refinement (whole-profile) method are included in Table 4.2

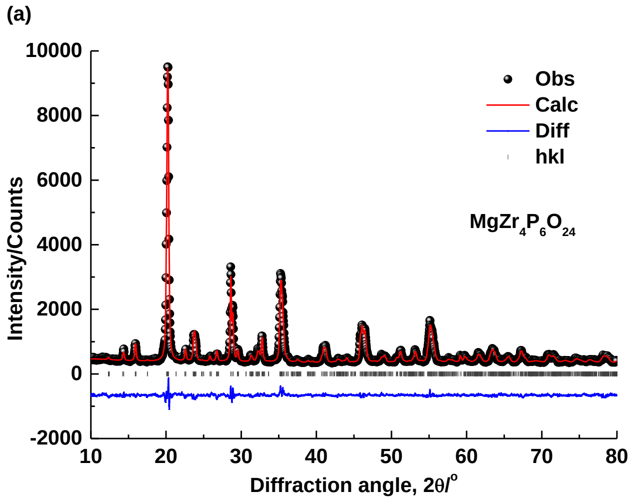

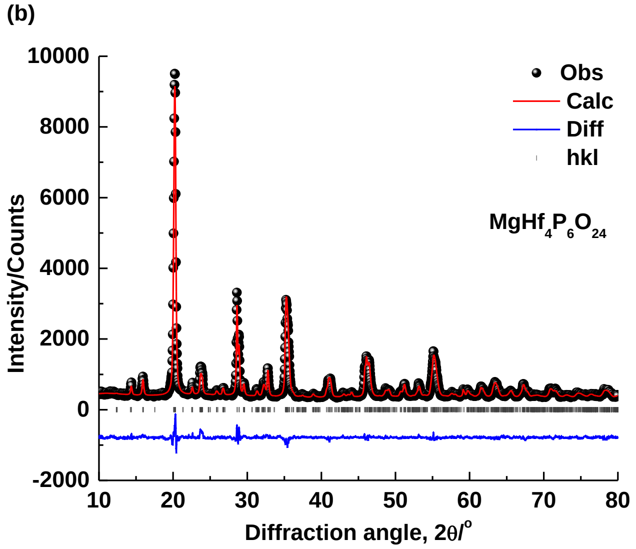

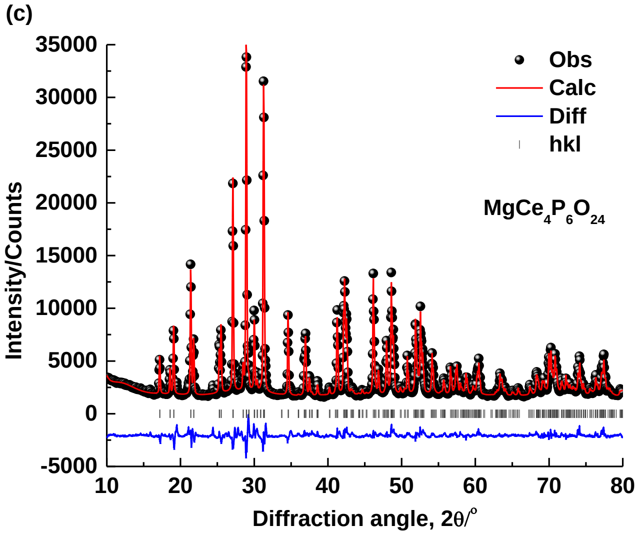

Figure 4-7 The experimental (black sphere) and calculated (red line) XRD pattern of (a) $MgZr_4P_6O_{24}$ (b) $MgHf_4P_6O_{24}$ (c) $MgCe_4P_6O_{24}$ solid-state electrolyte showing the difference between the experimental and calculated spectra (blue bottom line). Dark gray vertical bars indicating allowed Bragg reflection positions of contributing phases in the calculated XRD pattern

Table 4-2 Main characteristics, unit cell parameters, and the structure refinement of $MgZr_4P_6O_{24}$, $MgHf_4P_6O_{24}$ and $MgCe_4P_6O_{24}$ solid-state electrolytes at 298K

In brackets, the standard deviation in units of the last decimal.

	$MgZr_4P_6O_{24}$	$MgHf_4P_6O_{24}$	$MgCe_4P_6O_{24}$
Space group, Z	$P2_{1/n}$, 4	$P2_{1/n}$, 4	$P2_{1/n}$, 4
Radiation	CuKα X-ray	CuKα X-ray	CuKα X-ray
Wavelength(s), Å	1.54056	1.54056	1.54056
	1.54439	1.54439	1.54439
2θ scan range, deg	10 - 80	10 - 80	10 - 80
Unit cell parameters:			
a, Å	12.3850(8)	12.3850(8)	6.80118(24)
b, Å	8.8775(6)	8.8773(8)	7.02575(25)
c, Å	8.8001(7)	8.8000(7)	6.47691(20)
β, deg	90.529(5)	90.528(5)	103.4669(21)
V, Å^3	967.52(12)	967.48(12)	300.979(18)
Number of reflections	198	236	781
Refinement parameters	18	19	44
Residual values, %:			
R_{wp}	5.43	5.52	6.57
R_p	4.25	4.35	4.80
$\chi 2$	1.680	1.738	13.38

In Figure 4.7, the Rietveld refinement based on the X-ray diffraction profiles of the $MgZr_4P_6O_{24}$, $MgHf_4P_6O_{24}$ and $MgCe_4P_6O_{24}$ compounds are presented. Unit cell lattice parameters of the X-ray diffraction profiles in Figure 4.4 and the refined unit cell parameters and R-factor values presented in Table 4.2 are in excellent agreement. The difference in unit cell parameters is minimal at 298K. The crystal structure refinement was by continuously adding refined parameters with a continuous graphic simulation of the background to stabilise the R-factors into constant value [98]. The structural model of $Mg_{0.5}Zr_2P_3O_{12}$ compounds [98] and $Mg_{0.5}Ce_2P_3O_{12}$ [105] with their atomic coordinates, thermal displacement parameters U_{iso}, site occupancies q of the space group $P2_{1/n}$ were used as the starting models in the refinement of the crystal structures of $MgZr_4P_6O_{24}$, $MgHf_4P_6O_{24}$, and $MgCe_4P_6O_{24}$ compounds to generate new sets of their corresponding atomic coordinates, xyz, thermal displacement parameters, U_{iso}, and site occupancies, q (appendix T-1, T-2 and T-3). The experimental and calculated x-ray diffraction patterns in Figure 4.7 are also in excellent agreement.

4.2.3 Densification and porosity

Obtaining high-density sample pellets can be very challenging. Sintering $MgZr_4P_6O_{24}$, $MgHf_4P_6O_{24}$ and $MgCe_4P_6O_{24}$ solid-state electrolytes at high-temperature can result in phase decomposition and formation of second phases. In order to achieve a balance between the appropriate temperature and optimum density, the various sample pellets characterised for examination in this research were subjected to a sintering process for 24h in the temperature range, $1000 \leq T/{}^{o}C \leq 1500$. In this research, the measurements of experimental densities, ρ_{expt}, of the sintered ceramic sample pellets were achieved by a method based on the Archimedes principle. The theoretical density, ρ_{theor}, is the density of a material calculated from the number of atoms per unit cell and the unit cell parameters determined by X-ray diffraction, according to Equation (4.6)[201]. The relative density of the samples $MgZr_4P_6O_{24}$, $MgHf_4P_6O_{24}$ and $MgCe_4P_6O_{24}$ solid-state electrolytes was computed using the ratio of theoretical density and experimental density and the resulting data is presented in Figure 4.8

$$\text{Relative density, } \rho_{rel} = \frac{\rho_{theor}}{\rho_{expt}} \qquad (4.5)$$

$$\text{Theoretical density, } \rho_{theor} = \frac{m}{v} \equiv \frac{N_C A}{N_A V_C} \qquad (4.6)$$

The porosity of the sample pellet as a fraction varying between 0 and 1, or a percentage varying between 0% and 100% is determined using the following relation:

$$\text{Porosity, } \phi = 1 - \frac{\rho_{theor}}{\rho_{expt}} \qquad (4.7)$$

Where N_C is the number of atoms in a unit cell, A is the atomic weight (g/mol), N_A is the Avogadro's number (6.022×10^{23}/mol) and V_C is the volume of the unit cell (cm^3).

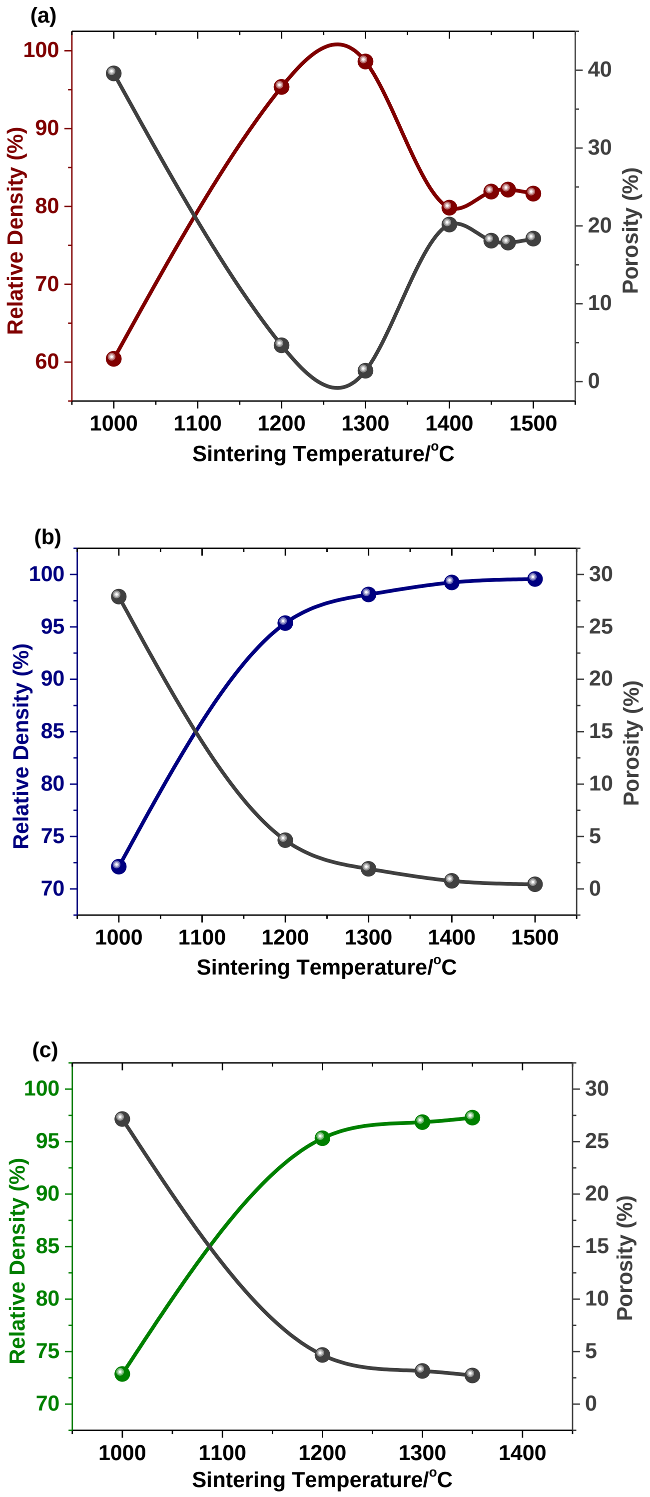

Figure 4-8 Dependence of percentage-relative density and porosity of the sample pellets (a) $MgZr_4P_6O_{24}$, (b) $MgHf_4P_6O_{24}$ and (c) $MgCe_4P_6O_{24}$ compounds on sintering temperature

There are two essential steps in the fabrication of ceramic pellets from powders: forming of a green compact, mostly done by pressing, and consolidation by a sintering process, during which the strength increases and the porosity decreases. It is necessary for property measurement that the material should be in the desired shape. Impedance spectroscopy measurement is a major characterisation requirement in this research. In obtaining a highly densified sample ceramic pellets, high sintering temperatures is a conventional sintering practice for solid-state electrolytes. To obtain a pure stable phase pellets, the sintering temperature is carefully selected and since some composite pellets transform at relatively high-temperatures, the balance in sample pellet purity, stability and sintering temperatures has to be reached. For instance, the $MgZr_4P_6O_{24}$ sample compound transforms into $Zr_2(PO_4)_2O$ phase at a sintering temperature higher than 1300°C [24], thereby changing the crystal structure or phase of the compound and limiting $MgZr_4P_6O_{24}$ as Mg^{2+}-cation conducting ceramic material. $MgHf_4P_6O_{24}$ and $MgCe_4P_6O_{24}$ compounds however still maintain stability at higher-temperatures. One effect of heating a phosphate based compound at a high-temperature is the loss of P_2O_5 oxide from zirconia precipitate as a result of its volatility [119], the change in phase observed in the $MgZr_4P_6O_{24}$ compound was attributed to the loss of P_2O_5 at high-temperature. However, $MgHf_4P_6O_{24}$ and $MgCe_4P_6O_{24}$ sample pellets were stable at high sintering temperatures. Figure 4.8 shows the dependence of relative densities on sintering temperatures of $MgZr_4P_6O_{24}$, $MgHf_4P_6O_{24}$, and $MgCe_4P_6O_{24}$ compounds. Figure 4.8(a) however, shows that the optimum relative density of ~99% and the least porosity of ~1% was achieved at a sintering temperature of 1300°C, which was used in predicting a suitable sintering temperature for the sample pellets. The optimum relative density of ~99% for $MgZr_4P_6O_{24}$ pellet is in perfect agreement with Mori *et al.* [191], that acceptable relative density of ceramic solid-state electrolytes should be higher than 94%. Furthermore, the relative density of $MgZr_4P_6O_{24}$ sample increases continuously from 60% to 99% as sintering temperature increases from 1000°C to 1300°C. At this sintering temperature, a maximum relative density of ~99% of the theoretical density was achieved as stable monoclinic system with which $MgZr_4P_6O_{24}$ solid-state electrolyte is fabricated for sensor application. The sintering temperatures in 1300-1500°C range shows significant transformation from monoclinic $MgZr_4P_6O_{24}$ to orthorhombic $Zr_2(PO_4)_2O$ phase which shows a downward trend in the relative density from 99% to 82% at a sintering temperature of 1400°C, this was verified according to equation (4.3). Therefore, high volatility of P_2O_5 oxide at high sintering temperature can be a contributing factor for the decrease in density of the $MgZr_4P_6O_{24}$ composite pellet suggesting that 1300°C is an ideal optimum sintering temperature. The variation of porosity of $MgZr_4P_6O_{24}$ sample pellet as a function of the sintering temperature is also shown in Figure 4.8(a). The porosity of sample pellets decreases with increasing sintering temperatures. This was observed in the temperature range 1000-1300°C, the porosity decreases rapidly, which reduces from 40% to 1%. Therefore, the sintering temperature of 1300°C with the porosity of 1% yields the least porous and most stable $MgZr_4P_6O_{24}$ sample pellets. The sintering temperatures in the 1300-1500°C range showing an increase in porosity from 1% to 18% with a crystal structure transformation from a monoclinic $MgZr_4P_6O_{24}$ phase to an orthorhombic $Zr_2(PO_4)_2O$ phase according to equation (4.3). Similarly, solid-state $MgHf_4P_6O_{24}$ and $MgCe_4P_6O_{24}$ sample pellets presented in Figure 4.8(b) and (c) shows that relative density increases continuously with sintering temperature, from $1000°C \leq T \leq 1500°C$, and $1000 \leq T/°C \leq 1350$, respectively, with 24h of annealing time. In Figure 4.8(b), therefore, the sample pellets begin to show some densification (~95%) at temperature higher than 1100°C and exhibit an optimum density of about 98% at 1300°C for 24h. Furthermore, the increment in density between 1300-1500°C is only ~1%, signifying that a saturation point has been reached for the densification of $MgHf_4P_6O_{24}$ sample pellets. The porosity of ~2% was achieved at 1300°C which is considered good enough for the solid-state electrolyte sample pellets in sensor application. Figure 4.8(c) also shows progressive percentage-relative density at increasing sintering temperatures range of 1000-1350°C. The sample pellet shows progressive densification from ~95% to ~97%, indicating that optimum density could be achieved at a lower sintering temperature. In this research, 1300°C sintering temperature at annealing time of 24h was considered suitable for purpose of comparison and that since the difference in percentage-relative density is only ~1% from 1200-1350°C, a saturation point was already achieved at 1300°C. Using 1300°C as sintering temperature according to the density profile, a pure stable phase was also achieved for the characterised solid-state ceramic electrolytes.

4.2.4 Vibrational spectroscopy

4.2.4.1 Fourier transform infrared (FTIR) spectroscopy

FTIR spectroscopy for analysing the interactions among atoms or ions in phosphate-based solid-state electrolytes showing the induced changes in vibrational modes of the electrolyte powders to analyse its vibrational spectra. The FTIR vibrational spectra of $MgZr_4P_6O_{24}$, $MgHf_4P_6O_{24}$ and $MgCe_4P_6O_{24}$ solid-state electrolytes presented in Figure 4.9 was recorded in the observed bands or wave number range of 400-4000 cm^{-1} and this complement X-ray diffraction information in Figure 4.3 and Figure 4.4 for a more accurate composition of phases at various temperatures. The spectroscopic FTIR and X-ray diffraction techniques also allow transformation of phases during calcination of xerogel powers analysed. The various phase formation of $MgZr_4P_6O_{24}$, $MgHf_4P_6O_{24}$, and $MgCe_4P_6O_{24}$ compounds is primarily confirmed using FTIR spectrum analysis.

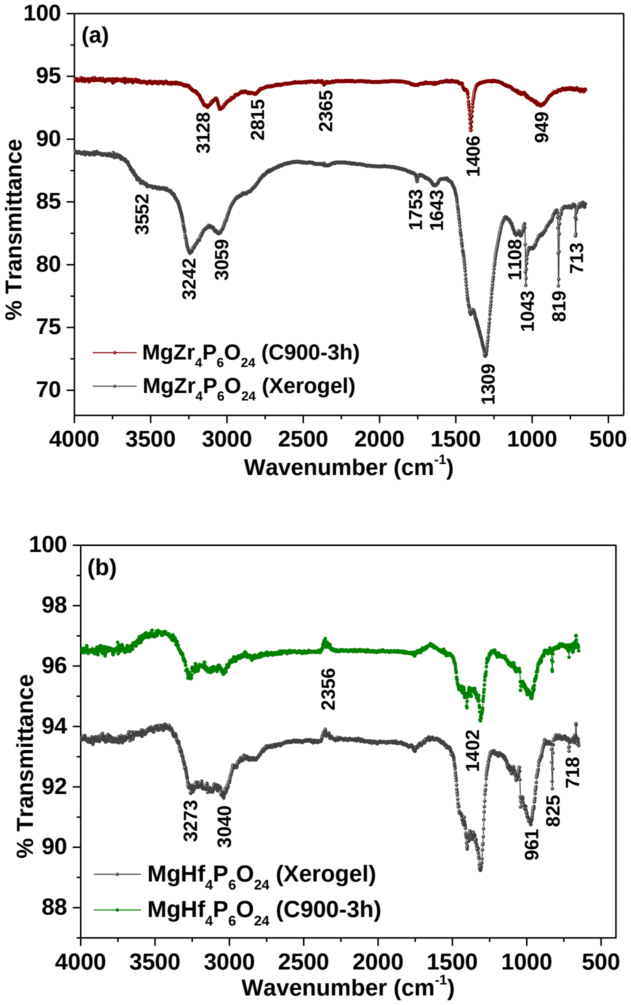

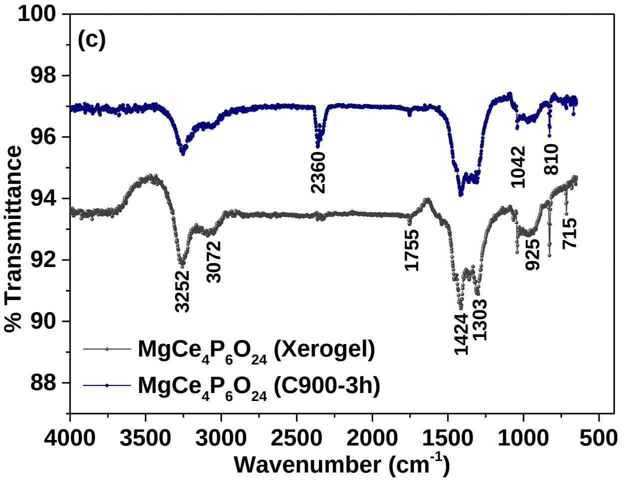

Figure 4-9 FTIR spectra of (a) $MgZr_4P_6O_{24}$, (b) $MgHf_4P_6O_{24}$ and (c) $MgCe_4P_6O_{24}$ precursors (xerogel) and nanopowders calcined at 900°C for 3h, respectively

Figure 4.9 shows the FTIR transmittance spectra of $MgZr_4P_6O_{24}$, $MgHf_4P_6O_{24}$ and $MgCe_4P_6O_{24}$ xerogel and calcined sample powders recorded in the wavenumber range of 400-4000 cm^{-1} and is used for analysing the interactions among atoms or ions in the solid-state electrolytes. These interactions induce changes in vibrational modes of the sample powders. In Figure 4.9(a), several transmittance bands were observed at 713, 819, 949, 1043, 1108, 1309, 1406, 1643, 1753, 2365, 2815, 3059, 3128, 3242 and 3552 cm^{-1} representing transmittance spectra for both xerogel and calcined compound. The xerogel and calcined compound shows common transmittance band at 949, 1406, 1753-2365, 2815-3059 and 3552 cm^{-1} depicting symmetric P-O stretching in P_2O_5 oxide, asymmetric stretching C=O of samples exposed to the atmosphere [202], ZrO_2 active oxide and Mg-O stretching from $Mg(NO_3)_2$ precursor [203], respectively. The xerogel transmittance band range at 713-819 cm^{-1} corresponds to ZrO_2 active oxide in the $MgZr_4P_6O_{24}$ solid-state electrolyte. Other xerogel bands formed at 1108, 1309, 1643, 3128-3242 and 3552 cm^{-1} correspond to symmetric P-O stretching of solid-state electrolyte and N-O stretch, due to the presence of nitrate [204] in $Mg(NO_3)_2$, respectively. The transmittance band 1643 and 3128-3242 cm^{-1} range correspond to H-O-H and O-H stretching vibration from H_2O molecules and hydroxyl groups which is believed to have been present in the crystalline lattice of sample powders [205]. The transmittance bands in Figure 4.9(b) represent the bands within which $MgHf_4P_6O_{24}$ solid-state electrolyte is formed. The common band between the xerogel and calcined powders is 2356 cm^{-1} absorption bands which correspond to asymmetric stretching of C=O samples exposed to the atmosphere [202] and, the transmittance band at 1402 and 3040 cm^{-1} for Mg-O stretching which is a result of MgO from Magnesium nitrate, $Mg(NO_3)_2$ [203]. Other transmittance bands at wavenumber 718, 825, 961 and 3273 cm^{-1} were also observed. The transmittance band at 718 cm^{-1} correspond to Hf-O [206] stretching suggesting the presence of HfO_2 oxide in synthesised $MgHf_4P_6O_{24}$ solid-state electrolyte. The bands 825 and 961 cm^{-1} correspond to P-O symmetric and asymmetric stretching of the phosphates, respectively, 3273 cm^{-1} corresponding to the O-H stretching vibration from hydroxyl groups and water molecules which may have been present in the crystalline lattice of the sample powders [205]. In Figure 4.9(c), the transmittance bands wavenumbers at 715, 810, 925, 1042, 1303-1424, 1755, 2360, 3072 and 3252 cm^{-1} corresponding to the active oxides of $MgCe_4P_6O_{24}$ synthesis. 715 and 925 cm^{-1} bands correspond to P-O symmetric and asymmetric stretching of the phosphate compound, respectively from P_2O_5. The transmittance bands at 810, 1042, 1755 and 2360 cm^{-1} have common bands between the xerogel and calcined sample powders. The transmittance band wavenumber at 810, 1042 and 1755 cm^{-1} correspond to Ce-O stretching [207] which indicates the presence of CeO_2 active oxide in the synthesised $MgCe_4P_6O_{24}$ compound. The C=O asymmetric stretching on the spectrum indicating the sample powders exposed to the atmosphere is seen on 2360 cm^{-1} band. The wavenumber bands at 1303-1424 region and 3072 cm^{-1} correspond to Mg-O stretching of MgO from the precursor inorganic $Mg(NO_3)_2$ [203]. The broader band at 3252 cm^{-1} O-H symmetric stretching vibration from the hydroxyl groups and water molecules which may have been present in the crystalline lattice of the powders [205]. The active oxides identified with their wavenumber bands indicate the presence of the required phases in the compounds synthesised.

4.2.4.2 Laser-Raman scattering (LRS) spectroscopy

In order to monitor the formation of $MgZr_4P_6O_{24}$, $MgHf_4P_6O_{24}$ and $MgCe_4P_6O_{24}$ polycrystalline compounds from their various active precursor oxides, the Raman spectra presented in Figure 4.10 shows the strength of the active oxides bonding.

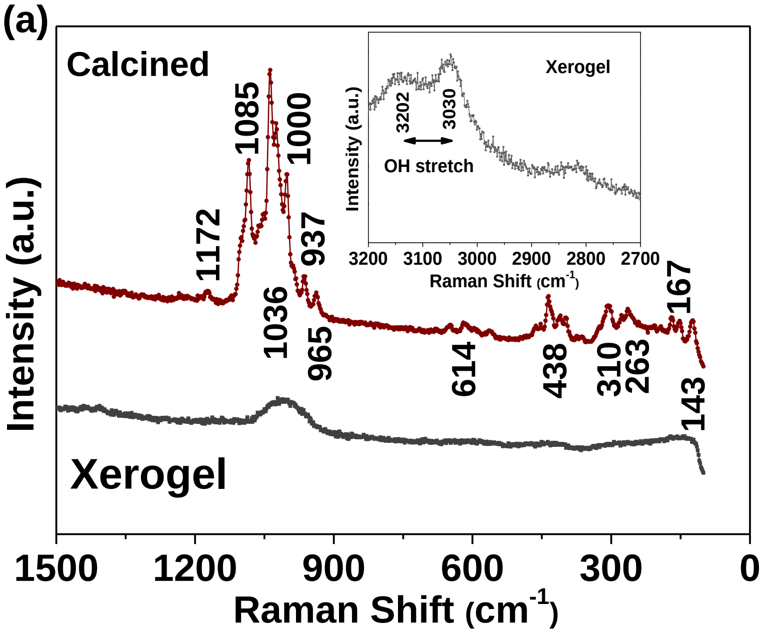
(a)
Calcined
Xerogel
Intensity (a.u.)
1500
1200
900
600
300
0
Raman Shift (cm^{-1})
1172
1085
1000
937
1036
965
614
438
310
263
167
143
Xerogel
3202
3030
OH stretch
Intensity (a.u.)
3200
3100
3000
2900
2800
2700
Raman Shift (cm^{-1})

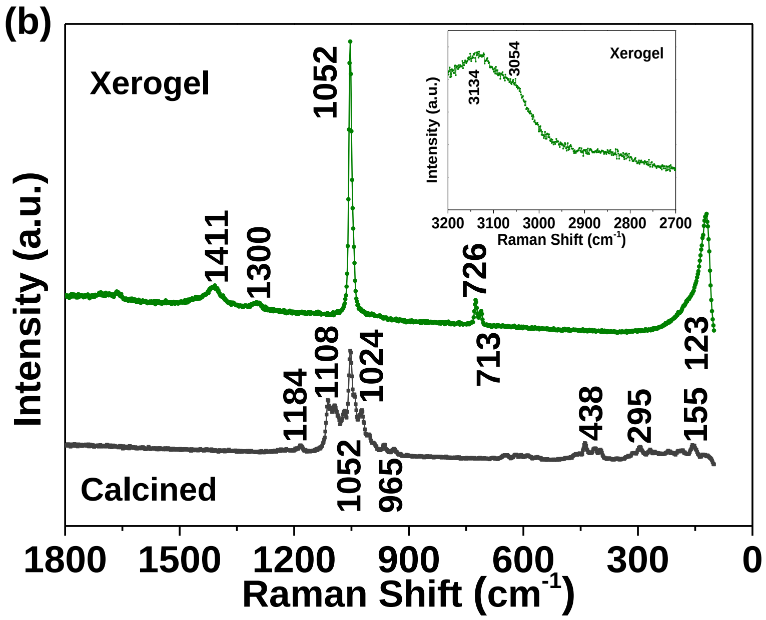
(b)
Xerogel
Calcined
Intensity (a.u.)
1800
1500
1200
900
600
300
0
Raman Shift (cm^{-1})
1052
1411
1300
726
713
123
1184
1108
1024
1052
965
438
295
155
Xerogel
3134
3054
Intensity (a.u.)
3200
3100
3000
2900
2800
2700
Raman Shift (cm^{-1})

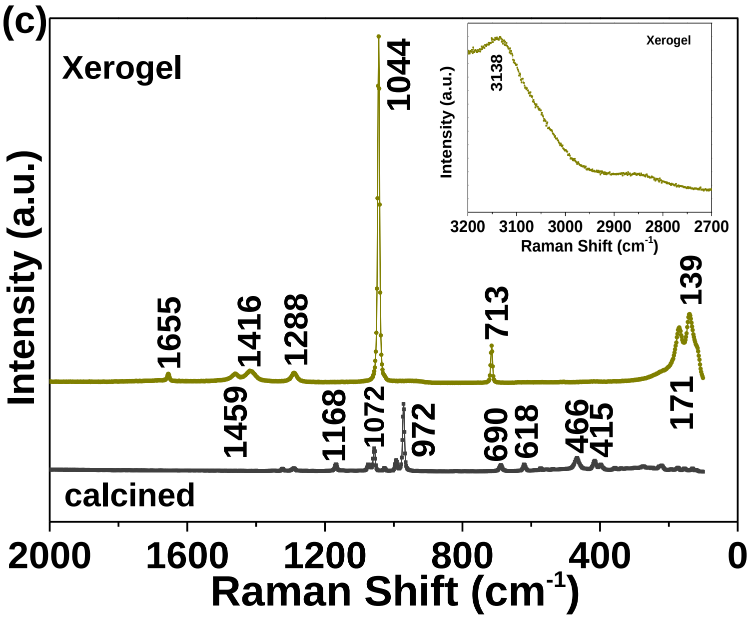

Figure 4-10 Raman spectra of (a) $MgZr_4P_6O_{24}$, (b) $MgHf_4P_6O_{24}$ and (c) $MgCe_4P_6O_{24}$ solid-state electrolyte (xerogel and calcined) compounds. Insert is Raman peaks of xerogel powders at 2700-3200 cm^{-1} Raman shift

In determining the vibrational frequencies of the bonds of $MgZr_4P_6O_{24}$, $MgHf_4P_6O_{24}$ and $MgCe_4P_6O_{24}$ molecules using laser Raman spectroscopy, Figure 4.10 present the Raman spectra of the xerogel and calcined phase of their molecules. The spectrum was recorded in the wavenumber range of 0-3500 cm^{-1}. The active oxides of MgO, CeO_2, HfO_2, and P_2O_5 are precursors samples of $MgZr_4P_6O_{24}$, $MgHf_4P_6O_{24}$ and $MgCe_4P_6O_{24}$ synthesis with other product of the reaction such as CO stretch, OH stretch and NH_4Cl. In Figure 4.10(a), the Raman spectra of the calcined sample powders have 12 peaks while the xerogel sample powders show 2 peaks at 143 and 1036 cm^{-1} corresponding to C=O asymmetric stretch mode of the carbonyls group (-C=O) and vibrational stretch CO mode, respectively. The Raman spectra at 143-167 cm^{-1} which shows the Raman peak at 143 cm^{-1} for the xerogel powder expanding to 167 cm^{-1} in the calcined powders also correspond to the carbonyls group (-C=O). The xerogel powders also depict OH stretch mode at 3030-3202 cm^{-1} which correspond to the hydroxyl groups residing in the solid-state electrolyte, $MgZr_4P_6O_{24}$ compound. The other Raman peaks at 263-614, 937-965, 1000-1085 and 1172 cm^{-1} correspond to the zircon band (Zr-O) which indicates the presence of oxide of zirconium, phosphate band $(PO_4)^{3-}$ indicating the presence of phosphate group in the solid-state electrolyte, the CO vibrational stretch at 1000-1085 cm^{-1} Raman peaks and the symmetric phosphate group $(O\text{-}P\text{-}O)_s$, respectively.

Figure 4.10(b) represent the Raman spectra of xerogels and calcined sample powders of the $MgHf_4P_6O_{24}$ compound. The xerogel and calcined sample powders have two and one major peaks, respectively, this is attributed to the high spectral background originating from fluorescence. The OH stretch modes at 3054-3134 cm^{-1} Raman shift range are of the hydroxyl groups residing in the $MgHf_4P_6O_{24}$ compound. The C-O vibrational stretch modes found at 1024-1108 cm^{-1} Raman shift range [208] are of carbonyls group (-C=O). The peaks at 713-965 cm^{-1} and 1184-1411 cm^{-1} bands identified as PO_4^{3-} [209] indicates the presence of the phosphate and symmetric phosphate group $(O\text{-}P\text{-}O)_s$, respectively. Hf-O symmetric vibrational stretching mode found at 123-438 cm^{-1} Raman shifts [210], suggesting the strength of Hf-O bond in $MgHf_4P_6O_{24}$ solid-state electrolyte indicating that the solid-state electrolyte could be thermodynamically stable at elevated temperatures and oxygen potential gradients.

The Raman spectra of the $MgCe_4P_6O_{24}$ solid-state electrolyte for both xerogel and calcined powders shown in Figure 4.10(c) depicts two major peaks for the xerogel powders and one peak for the calcined nanopowders. The 3138 cm^{-1} band of the OH stretch mode suggest the hydroxyl groups are present in the $MgCe_4P_6O_{24}$ solid-state electrolyte. The C-O vibrational stretch modes at 1044-1072 cm^{-1} Raman peaks for xerogel and calcined powders and, the asymmetric stretch modes at 139-171 cm^{-1} Raman bands represent the carbonyls group (-C=O) [208] in $MgCe_4P_6O_{24}$ samples. The bands 618, 690, 713, 972, 1168, 1288, 1416-1459 and 1655 cm^{-1} representing PO_4^{3-} [209], therefore showing the phosphate group in the solid-state electrolyte. The Ce-O symmetric stretching modes at 415-466 cm^{-1} bands are the characteristic Raman peaks of Ce^{4+} [211, 212].

4.2.5 X-ray fluorescence (XRF)

XRF characteristic analysis was performed to determine the chemical composition of the sample precursor oxides in solid-state electrolytes; $MgZr_4P_6O_{24}$, $MgHf_4P_6O_{24}$ and

$MgCe_4P_6O_{24}$ and, the solid-state solutions of $MgZr_2Hf_2P_6O_{24}$ and $MgZr_2Ce_2P_6O_{24}$ as presented in Figure 4.11. The fast and non-destructive characteristic XRF are usually excited in sample powders by the external radiation sources, such as X-ray tube or isotope source. The sample preparation techniques for XRF characteristic analysis is usually very minimal.

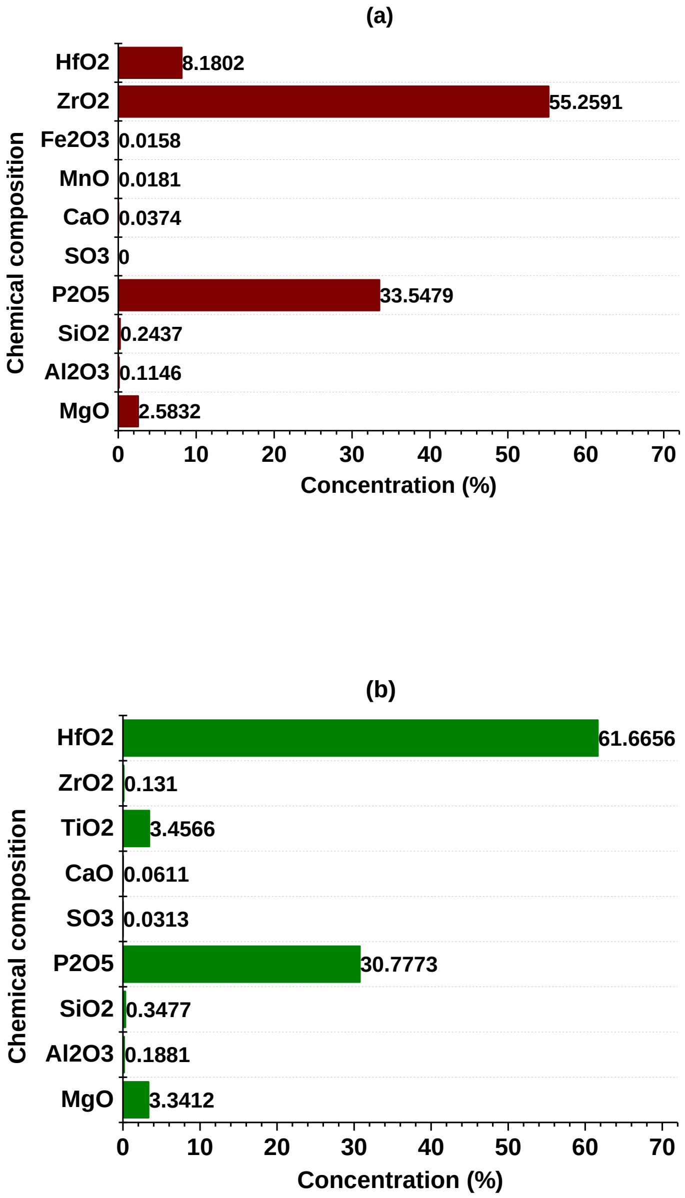

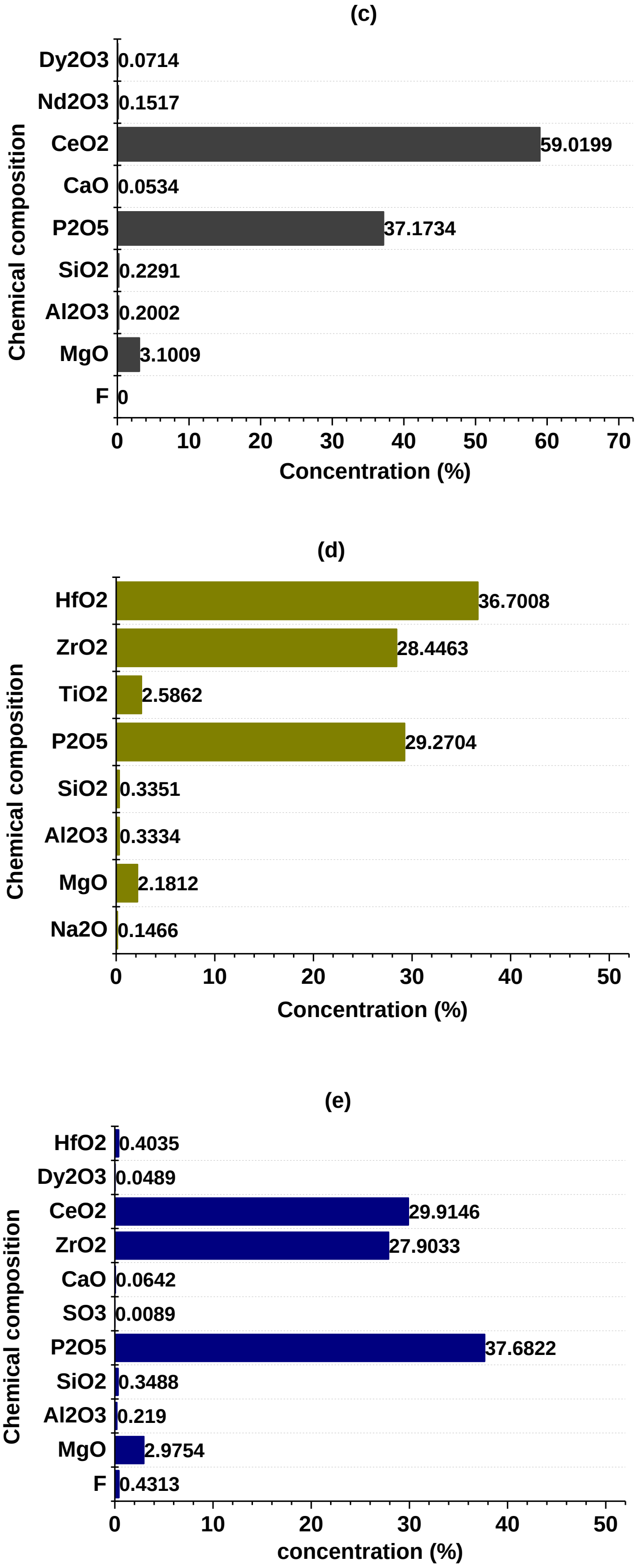

Figure 4-11 XRF analysis of (a) $MgZr_4P_6O_{24}$, (b) $MgHf_4P_6O_{24}$ and (c) $MgCe_4P_6O_{24}$ (d) $MgZr_2Hf_2P_6O_{24}$ and (e) $MgZr_2Ce_2P_6O_{24}$ solid-state electrolyte nanopowders

XRF was performed to understand the chemical compositions of the chemical oxides present in the solid-state electrolytes. Figure 4.11 represents the chemical composition and percentage concentration in the solid-state ceramic electrolytes characterised in this research. In Figure 4.11(a), the active oxides ZrO_2, P_2O_5, and MgO are present in reasonable quantities while the other substances are present in traces. However, the oxide HfO_2 with 8.1802% concentration could have occurred in the compositions because of some similar chemical properties with ZrO_2. The percentage concentration of the active oxides confirms the formation of the chemical analysis of $MgZr_4P_6O_{24}$ solid-state electrolyte. Figure 4.11(b) shows the chemical composition of HfO_2, P_2O_5, MgO and TiO_2, where the major oxides are present in reasonably sufficient quantities whereas, the other oxides are present in traces. The TiO_2however with a reasonable percentage concentration, 3.4566% is not considered a vital oxide in the synthesis of $MgHf_4P_6O_{24}$. The chemical composition of $MgCe_4P_6O_{24}$ presented in Figure 4.11(c) shows the percentage concentration of CeO_2 with 59.0199%, P_2O_5 with 37.1734% and MgO with 3.1009% and, are considered major quantities in the total composition, the other oxides however were observed to appear in traces. In Figure 4.11(d) and 4.11(e), the XRF composition of solid-state solutions, $MgZr_2Hf_2P_6O_{24}$ and $MgZr_2Ce_2P_6O_{24}$ (when X = 0.5), shows that chemical composition of the oxides, HfO_2, ZrO_2, P_2O_5, MgO in Figure 4.11(d), are present in major quantities for $MgZr_2Hf_2P_6O_{24}$ synthesis while oxides occur in traces. Similarly, Figure 4.11(e) shows that CeO_2, ZrO_2, P_2O_5 and MgO active oxides are present in major quantities for $MgZr_2Ce_2P_6O_{24}$ synthesis while the other chemical compositions are observed to be in trace amounts. However, TiO_2 (2.5862%) in Figure 4.11(d) is shown in the composition analysis, but not a part of the total composition in chemical synthesis precursors of solid-state solutions.

4.2.6 Morphology of ceramic solid-state electrolytes

4.2.6.1 SEM-EDS

One of the foundations of researchers in materials science research is recognition that the properties of materials are related to their microstructure and morphologies. Since the existence of such relationships can be observed in various areas of interest today, the basic approach of the researcher is to investigate the microstructure of engineering materials in order to optimise the syntheses and properties for subsequent engineering applications. The morphologies of $MgZr_4P_6O_{24}$, $MgHf_4P_6O_{24}$ and $MgCe_4P_6O_{24}$ solid-state electrolytes (sintered at 1300°C and annealed for 24h) by SEM performed on a cross-section of the fracture surface of the electrolytes are displayed in Figure 4.12, equipped with an EDS spectrum for each solid-state electrolyte.

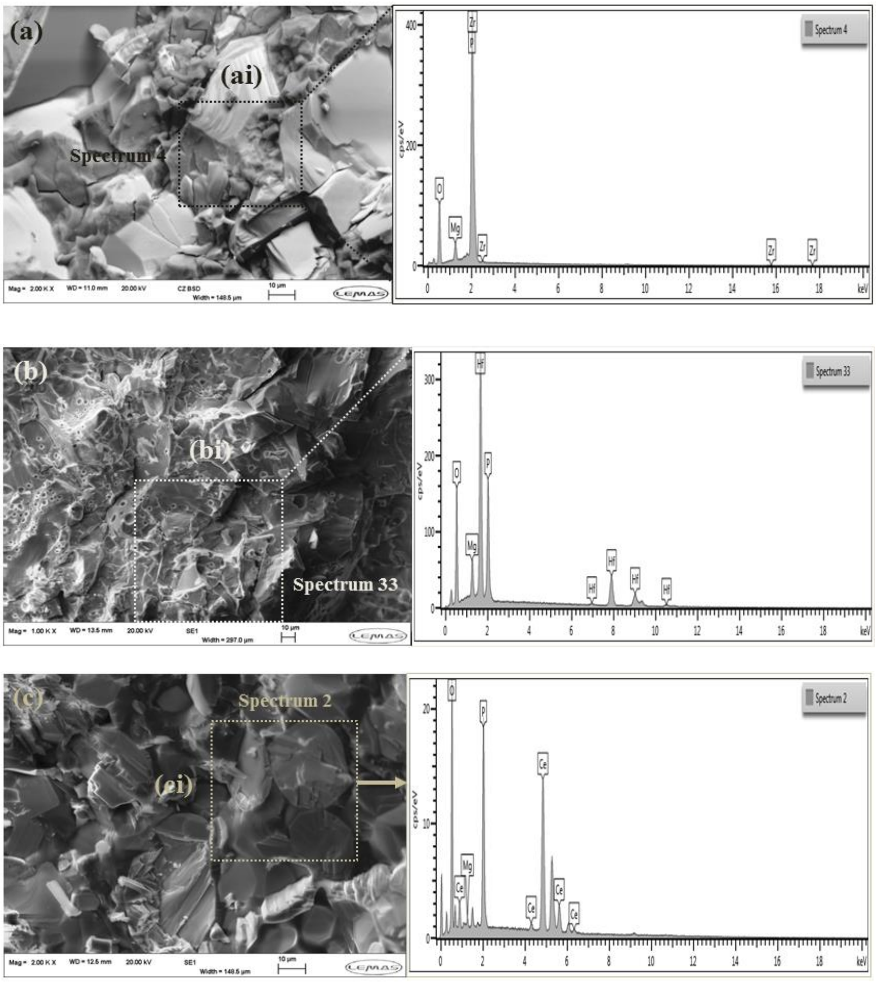

Figure 4-12 SEM micrographs fracture surfaces of (a) $MgZr_4P_6O_{24}$, (b) $MgHf_4P_6O_{24}$ and (c) $MgCe_4P_6O_{24}$ ceramic pellets sintered at 1300°C and annealed for 24h, showing their corresponding EDS spectrum (ai-ci)

The elemental analysis, percentage atomic fraction and atomic ratio extracted from the EDS spectrum of each solid-state electrolyte in Figure 4.12 is presented in Table 4.3, showing how the EDS data compares with the theoretical atomic fraction of the solid-state electrolytes.

Table 4-3 Average elemental composition of the EDS spectra from fracture surface of the $MgZr_4P_6O_{24}$, $MgHf_4P_6O_{24}$, and $MgCe_4P_6O_{24}$ ceramic pellets sintered at $1300^{o}C$ for 24h

Element	Atomic Fraction (%)	Atomic Ratio
$MgZr_4P_6O_{24}$		
Mg	2.83	1.00
Zr	11.68	4.13
P	16.53	5.84
O	68.96	26.13
Total	100.00	
$MgHf_4P_6O_{24}$		
Mg	2.83	1.00
Hf	9.50	3.36
P	17.41	6.15
3	70.27	24.83
	100.00	
$MgCe_4P_6O_{24}$		
Mg	3.12	1.00
Ce	9.28	2.97
P	17.29	5.54
O	70.31	22.54
Total	100.00	

Figure 4.13 is EDS mapping across the fracture surfaces of $MgZr_4P_6O_{24}$, $MgHf_4P_6O_{24}$ and $MgCe_4P_6O_{24}$ ceramic pellets showing the homogeneity of the component oxides and possible phase reactions. Furthermore, EDS linescan of the solid-state electrolytes is displayed in Figure 4.14 showing all the phases and microstructural reactions.

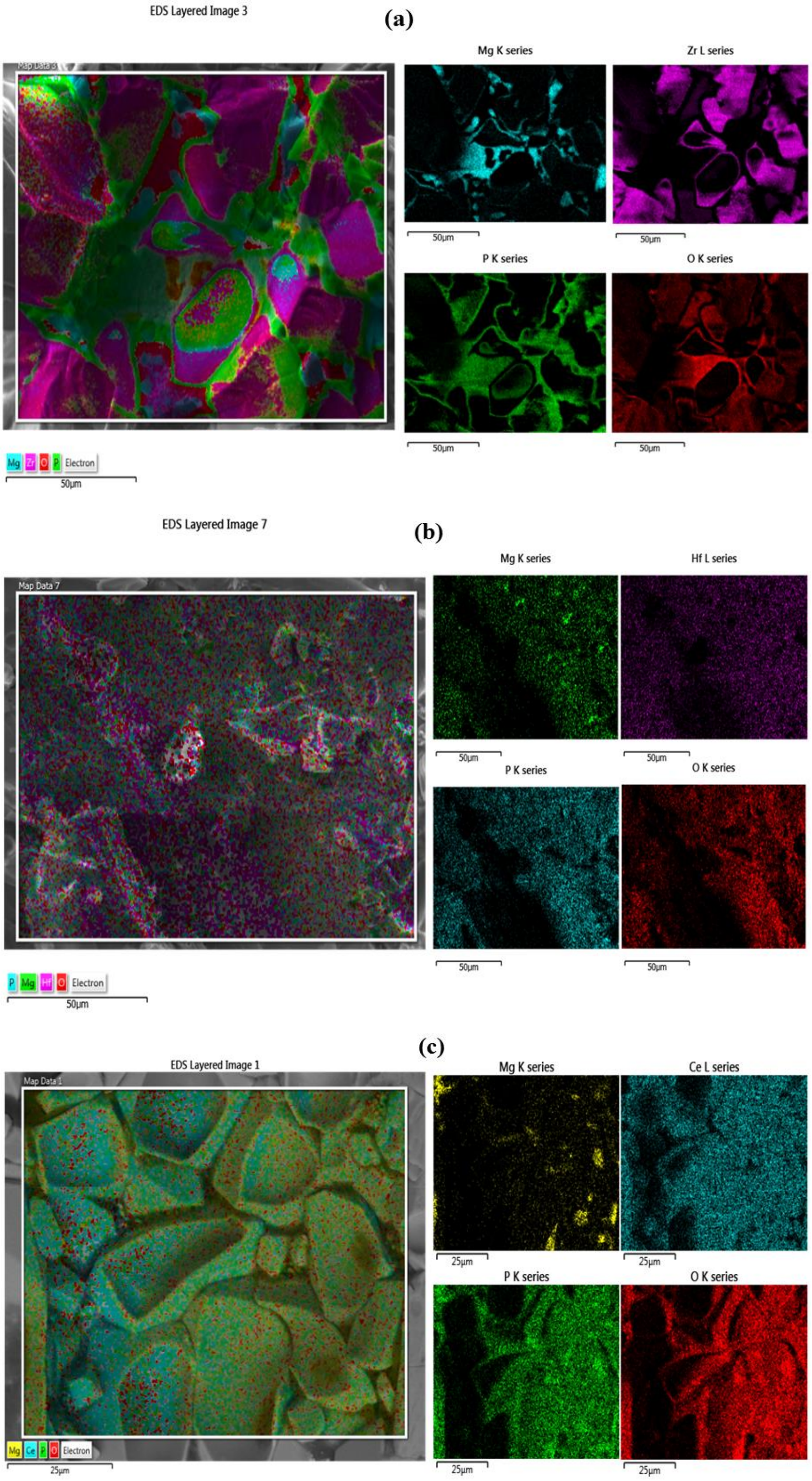

Figure 4-13 Mapping across the fracture surface of (a) $MgZr_4P_6O_{24}$, (b) $MgHf_4P_6O_{24}$ and (c) $MgCe_4P_6O_{24}$ ceramic pellets sintered at 1300°C and annealed for 24h

Figure 4.12 is micrographs of $MgZr_4P_6O_{24}$, $MgHf_4P_6O_{24}$ and $MgCe_4P_6O_{24}$ fracture surface ceramic pellets sintered at 1300°C for 24h. It is clear from Figure 4.12(a), (b) and (c) that the three ceramic pellets show a dense structure with little porosity which is in a perfect agreement with the relative densities of $MgZr_4P_6O_{24}$, $MgHf_4P_6O_{24}$ and $MgCe_4P_6O_{24}$ solid-state electrolytes; 99%, 98%, and 97%, respectively, determined from the physical dimensions and the theoretical density calculated from the crystal structure of the electrolytes. Moreso, the fracture mode is almost totally intergranular and that there are no secondary phases observed at the grain boundaries or segregation to the grain boundaries. The EDS points and square identification from a number of sites showed that the ceramic pellets are homogeneous and the elemental composition averaged from different locations which shows the composition of $MgZr_4P_6O_{24}$ solid-state electrolytes of stoichiometric concentration. However, the elemental composition of some points or square identification of $MgHf_4P_6O_{24}$ and $MgCe_4P_6O_{24}$ sample pellets are non-stoichiometric because the atomic ratio of some elements shown in Table 4.3 are much smaller than the required standard hence, they could not be standardised by approximation. In demonstrating the atomic ratio of Hf in the elemental compositions of $MgHf_4P_6O_{24}$ solid-state electrolyte from Table 4.3, the least atomic fraction, 2.83 is used to divide through all the other percentage atomic fraction to determine the atomic ratio of the different elements. For instance, dividing 9.50 by 2.83 result in 3.36, which is the atomic ratio of Hf in the elemental composition, suggesting $MgHf_4P_6O_{24}$ may be slightly non-stoichiometric as identified having a reduced Hf^{4+}. The presence of excess O^{2-} (24.83) in $MgHf_4P_6O_{24}$ further suggest a non-stoichiometric relation. Similarly, the atomic ratio of the composition was determined by dividing through the percentage atomic fraction by the least value, 3.12 in this case. The measured atomic ratio, 1.00, 2.97, 5.54 and 22.54 were then compared with the theoretical atomic ratio of the solid-state electrolyte $MgCe_4P_6O_{24}$. The atomic ratio 1.00 and 5.54 therefore compares excellently with Mg and P whereas, Ce (2.97) and O (22.54) elements in $MgCe_4P_6O_{24}$ solid-state electrolyte shows a slight reduction in Ce^{4+} and O^{2-} oxides suggesting a non-stoichiometric chemical relation considering an atomic % difference of ~1.00 is observed to occur in the Ce and O element. This also shows that the bulk compound is slightly non-homogeneous and therefore non-stoichiometric as identified earlier.

The EDS elemental mapping and linescan spectra across the fracture surfaces of the solid-state electrolytes; $MgZr_4P_6O_{24}$, $MgHf_4P_6O_{24}$ and $MgCe_4P_6O_{24}$ ceramic pellets are displayed in Figures 4.13 and 4.14, respectively. Figure 4.13 shows a clear identification of the component elements in the map spectrum of the three solid-state electrolytes analysed in this research. The different component elements further displays the stoichiometric chemical relation defined by atomic ratio of the solid-state electrolyte. The component maps presented in different colours are reflective of the EDS layered image whereby the component maps are well defined. In Figure 4.13(a), the presence of Mg, Zr, P and O are clearly identified on the EDS layered image in different colours which shows that the sample component analysed is homogeneous. Similarly, the elemental maps distribution of $MgHf_4P_6O_{24}$ and $MgCe_4P_6O_{24}$ solid-state electrolytes is described in Figure 4.13(b-c). In both cases, all the component elements were distinguished with clear unique colours corresponding to their homogeneous distribution on the EDS layered images.

The linescan across the fracture surface of the solid-state electrolytes shown in Figure 4.14 further reveals the homogeneity of the precursor oxides or component elements in the synthesised solid-state electrolytes.

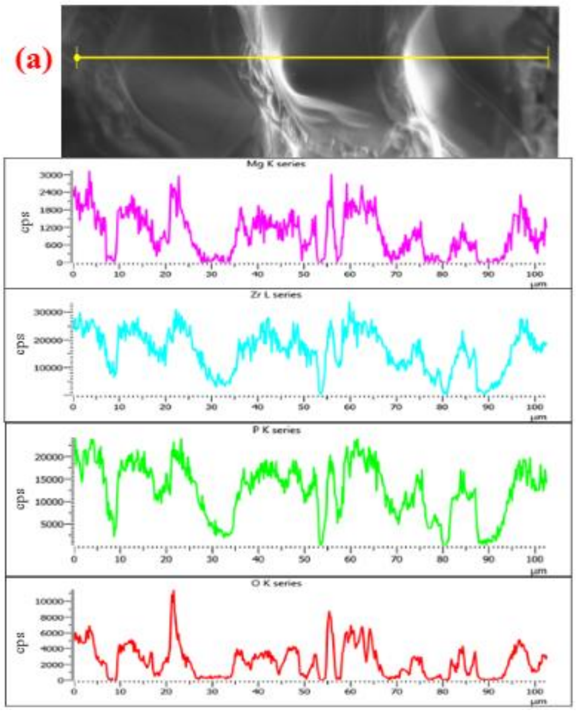

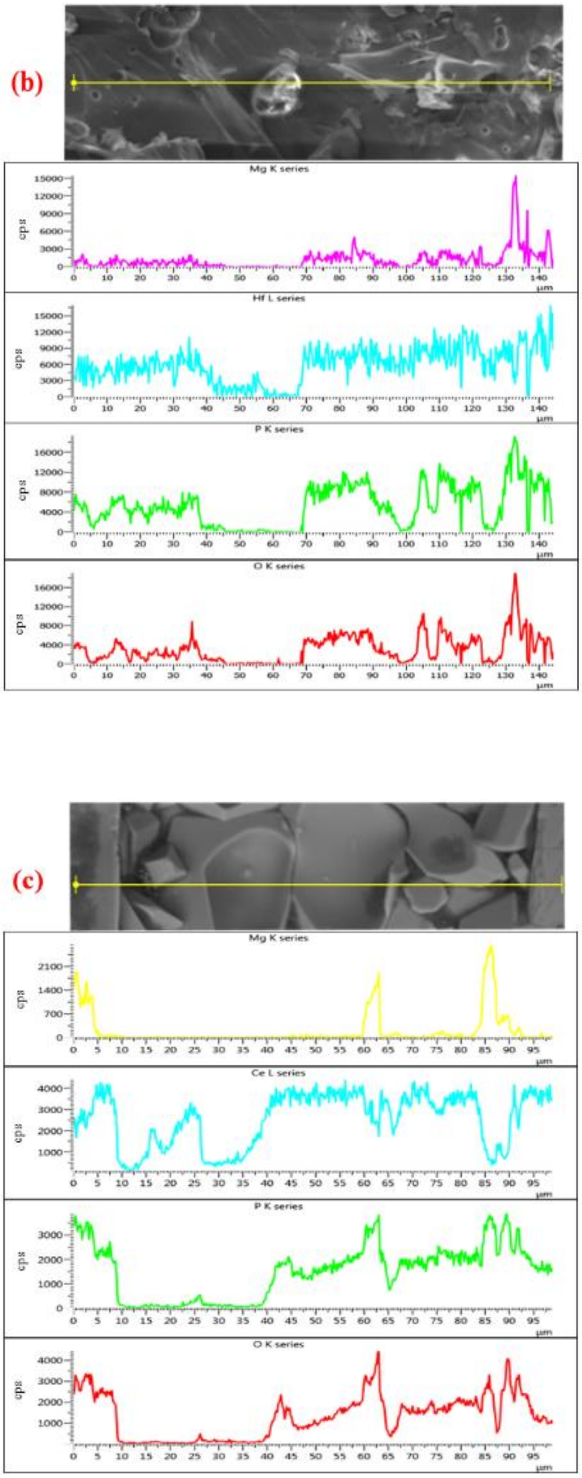

Figure 4-14 Linescan across the fracture surface of (a) $MgZr_4P_6O_{24}$, (b) $MgHf_4P_6O_{24}$ and (c) $MgCe_4P_6O_{24}$ ceramic pellets sintered at 1300°C and annealed for 24h

Figure 4.14 represent linescan across the fracture surface of $MgZr_4P_6O_{24}$, $MgHf_4P_6O_{24}$ and $MgCe_4P_6O_{24}$ solid-state electrolytes. The linescan in Figure 4.14(a-c) reveals core homogeneity of the fracture sample pellets and, the intensity of the individual elements shows uniformity across the surface area analysed. Figure 4.14(b) in particular shows reduced intensity of the $MgHf_4P_6O_{24}$ sample on 40-70μm concentration stretch which is believed to be an indented location on the sample pellet. During a linescan analysis, electron scanning is expected to be surface related therefore, it could not penetrate the hollow or indentation. Figure 4.14(c) showing reduced intensity on 10-40μm for P, O and Mg, Ce in different intensity, could be related to the non-stoichiometric reaction observed in $MgCe_4P_6O_{24}$ electrolyte. Moreso, the percent atomic fraction is ~1.00 short in reference to Ce-P-O elemental composition. The spread of Mg component in the electrolyte composition shows varied intensity at 0-5μm, 60-65μm and 82-89μm, meaning Mg is not homogeneously spread in the sample pellet.

4.2.6.2 TEM-EDS

TEM is considered a vital technique for materials characterisation because, it provides the desired information on morphology, composition, and crystal structure of different nanopowders calcined at different temperatures. The select-area electron diffractions, SAEDs in this research are the crystallographic data obtained using TEM techniques [213]. Bright-field TEM images of $MgZr_4P_6O_{24}$, $MgHf_4P_6O_{24}$, and $MgCe_4P_6O_{24}$ solid-state electrolytes in Figure 4.15 represent the amorphous and crystalline nanoparticles orientation.

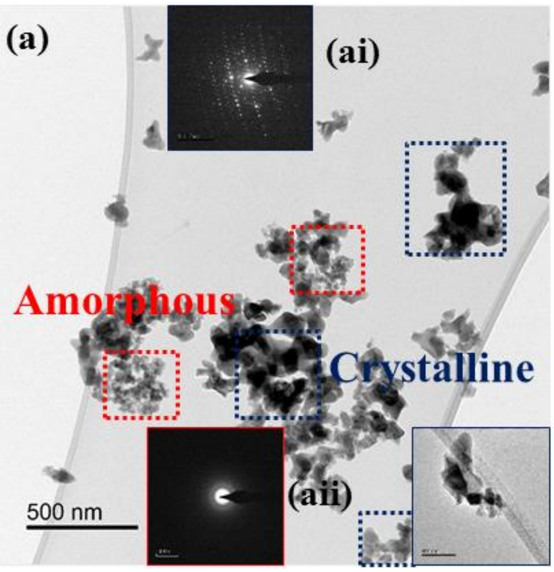

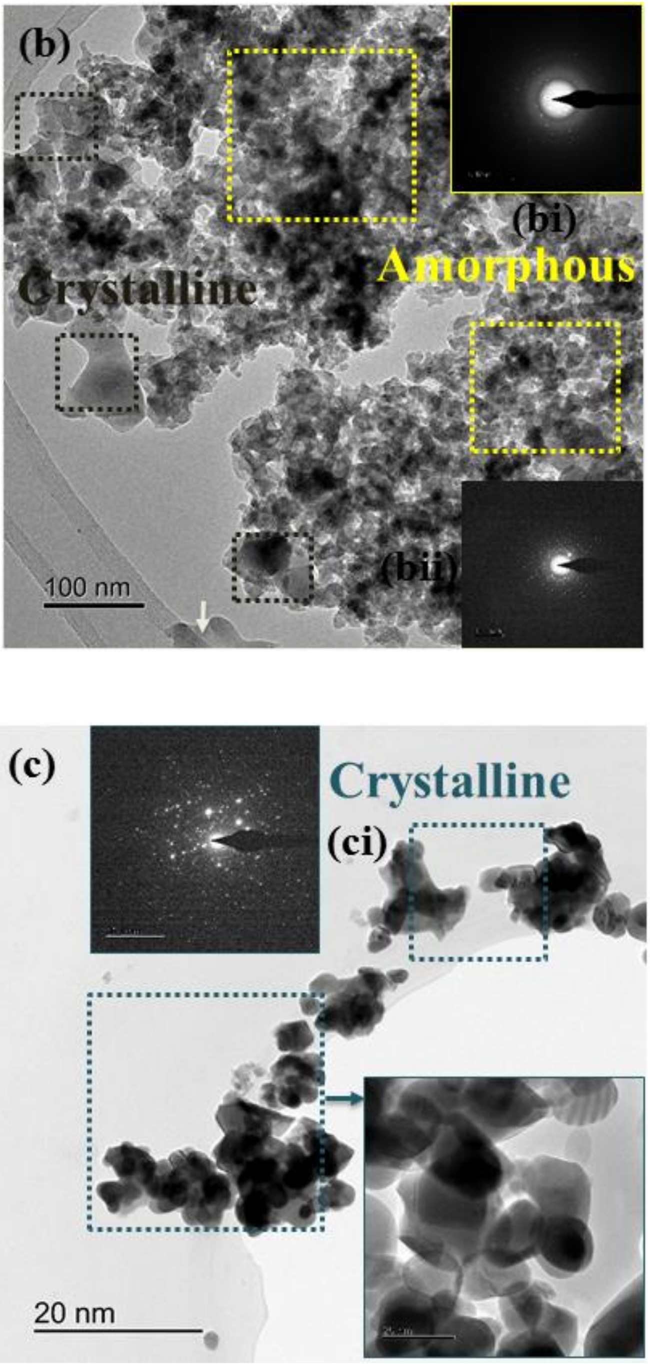

Figure 4-15 Bright-field TEM image of (a-aii) $MgZr_4P_6O_{24}$, (b-bii) $MgHf_4P_6O_{24}$, and (c-ci) $MgCe_4P_6O_{24}$ nanopowders and their corresponding SAEDs showing amorphous and crystalline particles (insert) of the solid-state electrolytes calcined at 800°C

Figure 4.15 represent the Bright-field TEM images of $MgZr_4P_6O_{24}$, $MgHf_4P_6O_{24}$, and $MgCe_4P_6O_{24}$ nanoparticles calcined at 800°C. The TEM images in Figure 4.15(a) and Figure 4.15(b) display traces of both amorphous and crystalline nanoparticles indexed SAED pattern corresponding to amorphous or crystalline orientation at different zone, differentiated by their diffraction rings. The SAED pattern with structural spots clearly showing no aligning diffraction rings indicating a single crystalline structure whereas, those with clear diffraction rings show amorphous structure [214]. The TEM images indexed in relation to SAED pattern (ai-aii) in Figure 4.15(a) shows amorphous pattern scattered around more pronounced crystalline pattern. Similarly, Figure 4.15(b), showing broad fine amorphous pattern dominating the crystalline pattern at 800°C. Figure 4.15(c) however, shows only crystalline pattern with no trace of the amorphous pattern observed at 800°C. The MgCe$_4$P$_6$O$_{24}$ nanopowders showing even distribution on the SAED pattern describing the crystallinity of the sample is as shown in Figure 4.15(c). The crystal orientation shown in Figure 4.15(a-c) depicts a transition in the amorphous and crystalline structures which is temperature dependent. Nanopowders calcined at 800°C shows a departure from the crystal orientation of the nanopowders calcined at 900°C, considering that the nanopowders calcined at 900°C shows a semblance of sintered particles, this however provided unreliable data for further TEM examination. The TEM images of the solid-state electrolytes nanopowders calcined at 900°C for 3h has been presented in the appendix Figures from A-2 to A-8 for purpose of comparing their crystallite size with respect to calcination temperature.

In investigating the particle morphologies and crystal structures of the nanoparticles, the high-resolution TEM (HR-TEM) micrographs and SAEDs in Figure 4.16(a-aiii) for the MgZr$_4$P$_6$O$_{24}$ solid-state electrolyte showing different crystal lattice fringes, interplanar spacing of HR-TEM and surface grafting particles compare with the X-ray diffraction standard database.

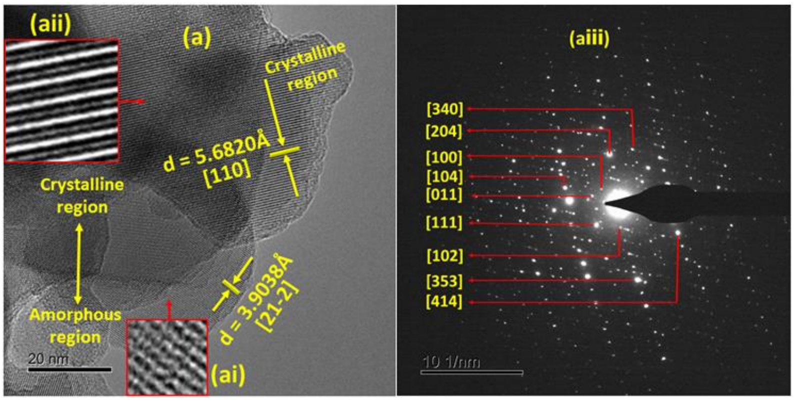

Similarly, Figures 4.16(b-biii) and 4.16(c-ciii) showing HR-TEM micrograph images and SAEDs for $MgHf_4P_6O_{24}$ and $MgCe_4P_6O_{24}$ solid-state electrolytes, respectively, as presented. The crystal lattice fringes, interplanar spacing, phase difference and surface grafting are also displayed.

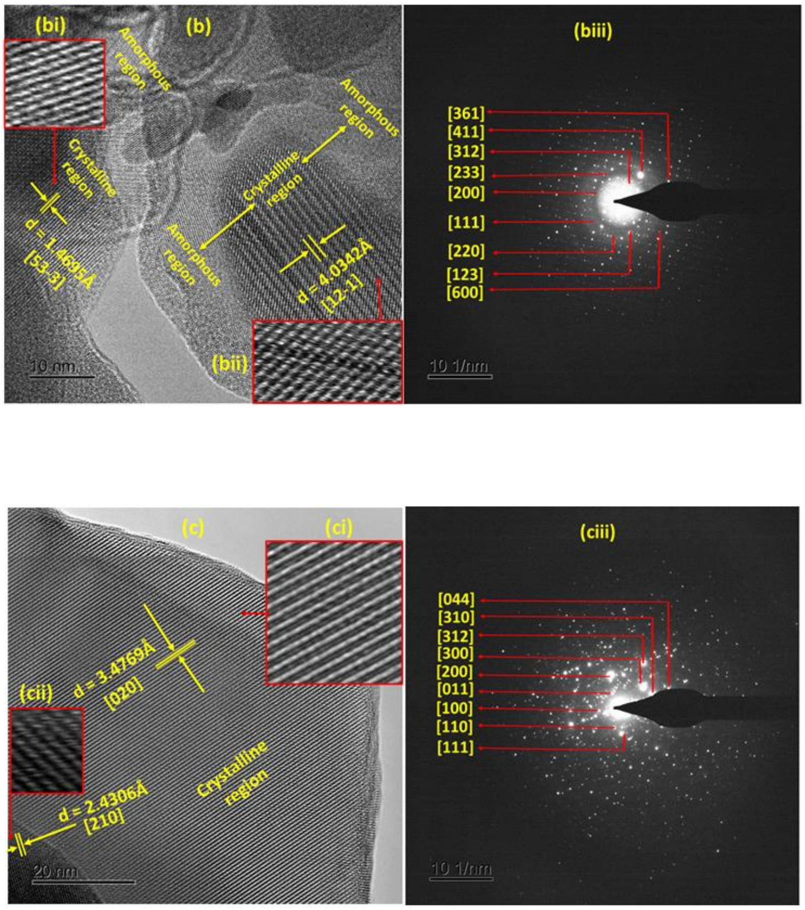

Figure 4-16 HR-TEM micrograph images and their corresponding SAED patterns for (a-aiii) $MgZr_4P_6O_{24}$, (b-biii) $MgHf_4P_6O_{24}$, and (c-ciii) $MgCe_4P_6O_{24}$ nanoparticles prepared by calcining the precursor xerogel at 800°C for 0.5h showing details of d-spacing from lattice fringes of HR-TEM and SAED patterns

The particle morphologies and lattice crystal structures of $MgZr_4P_6O_{24}$, $MgHf_4P_6O_{24}$, $MgCe_4P_6O_{24}$ nanopowders were investigated using HR-TEM, and their corresponding SAED pattern shown in Figure 4.16(a-c). The micrographs illustrated in Figure 4.16(a) shows two different lattice fringes in the amorphous and crystalline region attributed to [21-2] and [110] interplanar spacing of $MgZr_4P_6O_{24}$ nanoparticles with amorphous layer surrounding the crystalline particles. The crystal lattice fringes corresponding to

3.9038Å and 5.6820Å atomic spacing, are characteristics of monoclinic $MgZr_4P_6O_{24}$ solid-state electrolytes. The d-spacing of the surface grafting nanoparticles in Figure 4.16(ai-aii) shows a uniform trend of core crystallinity, whereas the SAED pattern in Figure 4.16(aiii) indexed to the (100) zone axes of monoclinic $MgZr_4P_6O_{24}$ electrolyte, showing clear homogeneity and pure single phase of the $MgZr_4P_6O_{24}$ nanoparticles at 800°C. The d-spacing from SAED patterns in Figure 4.16(aiii) compares well with the XRD profiles in Figure 4.6(a). Similarly, the HR-TEM micrographs in Figure 4.16(b) shows that two different lattice fringes were also observed, which are attributed to the [12-1] and [53-3] interplanar spacing of $MgHf_4P_6O_{24}$ nanoparticles. The crystal lattice fringes corresponding to the 4.0342Å and 1.4695Å atomic spacing, are characteristics of a monoclinic $MgHf_4P_6O_{24}$. The d-spacing of the surface grafting nanoparticles of $MgHf_4P_6O_{24}$ nanoparticles in Figure (bi-bii) equally shows good core crystallinity like the $MgZr_4P_6O_{24}$ nanoparticles but with some traces of amorphous nanoparticles. The monoclinic $MgHf_4P_6O_{24}$ nanoparticles depicts a single homogeneous phase since the SAED pattern described in Figure 4.16(biii) are easily indexed to the (100) zone axes. The d-spacing parameters from SAED patterns in Figure 4.16(biii) compares perfectly with XRD data in Figure 4.6(b), and both data were found to be in excellent agreement. Figure 4.16(c) shows that the HR-TEM and SAED patterns were used to investigate the particle morphologies and crystal structures of $MgCe_4P_6O_{24}$ nanoparticles calcined at 800°C. The HR-TEM micrographs described in Figure 4.16(c) illustrated the two different lattice fringes observed as insert (ci-cii) in Figure 4.16(c) were attributed to the [020] and [210] interplanar spacing of monoclinic $MgCe_4P_6O_{24}$ nanoparticles. The crystal lattice fringes, corresponding to the 3.4769Å and 2.4306Å atomic spacing are characteristics of monoclinic $MgCe_4P_6O_{24}$ solid-state electrolyte. The d-spacing of the surface grafting nanoparticles insert in Figure 4.16(ci-cii) shows a perfectly good core crystallinity with no trace of amorphous nanoparticles. The nanoparticles depict a pure homogeneous phase at 800°C which compares with XRD parameters in Figure 4.6(c). A detailed analysis of the different crystal lattice fringes in HR-TEM micrographs and d-spacing parameters from SAED patterns of $MgZr_4P_6O_{24}$, $MgHf_4P_6O_{24}$, $MgCe_4P_6O_{24}$ solid-state electrolyte nanoparticles synthesised by calcining dried precursor xerogel powders at 800°C and 900°C, respectively showing the dependence of temperature on both the average crystallite size and crystal lattice parameters, as the findings at 900°C have been presented in the appendix Figures from A-2 to A-8.

The corresponding EDS mapping images of the solid-state electrolyte nanopowders are presented in Figure 4.17 showing uniform spatial distribution of the component elements with a corresponding atomic ratio of the electrolytes. The high-angle annular dark-field (HAADF) imaging revealing a qualitative electron tomography with unique insights into the physical, crystallographic, composition and chemical information of the polycrystalline solid-state electrolytes characterised in this research.

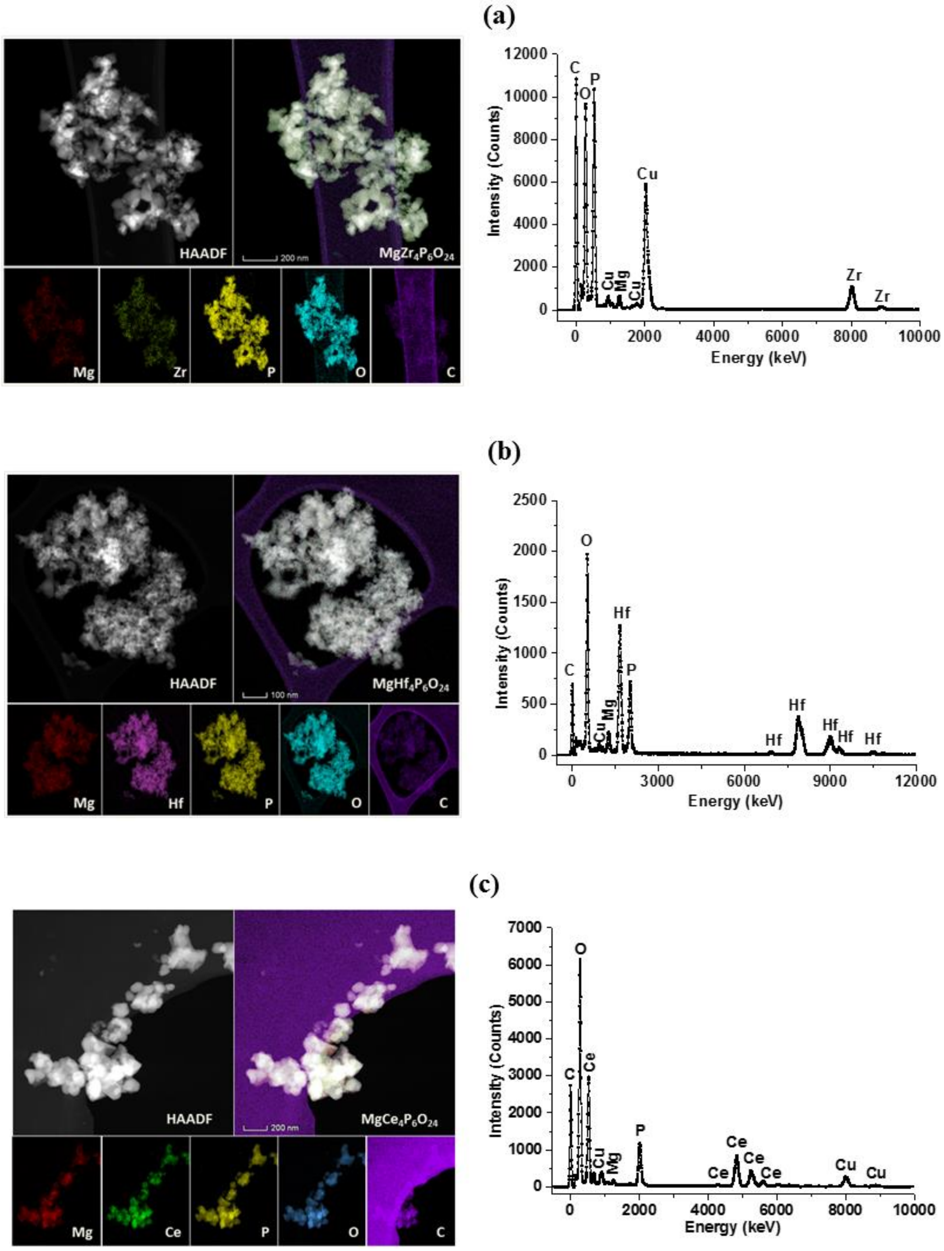

Figure 4-17 HAADF and EDS elemental maps of (a) $MgZr_4P_6O_{24}$, (b) $MgHf_4P_6O_{24}$ and (c) $MgCe_4P_6O_{24}$ nanopowders calcined at 800°C for 0.5h

Figure 4.17 depicts the high-angle annular dark-field (HAADF) and EDS elemental maps of $MgZr_4P_6O_{24}$, $MgHf_4P_6O_{24}$, and $MgCe_4P_6O_{24}$ nanopowders calcined at 800°C. Figure 4.17(a) shows the corresponding elemental map of $MgZr_4P_6O_{24}$ nanopowders. The spectra in this map however shows a uniform spatial distribution of Mg, Zr, P and O with the corresponding atomic ratio for $MgZr_4P_6O_{24}$ indicating homogeneous phase as evident in the elemental EDS spectrum in Figure 4.17(a) which compares with the HT-XRD profiles in Figure 4.3(a) showing $MgZr_4P_6O_{24}$ solid-state ceramic electrolyte xerogels forming crystalline peaks confirming the presence of $MgZr_4P_6O_{24}$ in Figure 4.6(a) illustrating $MgZr_4P_6O_{24}$ solid-state electrolyte as having a pure homogeneous single phase at 800°C. Similarly, the elemental maps of $MgHf_4P_6O_{24}$ nanoparticles is shown in Figure 4.17(b). The EDS spectra in Figure 4.17(b) shows a uniform spatial distribution of Mg, Hf, P, and O with atomic ratio for $MgHf_4P_6O_{24}$, which also appears as a pure homogeneous phase at 800°C. The spectrum was compared with HT-XRD in Figure 4.3(b) which revealed the formation of $MgHf_4P_6O_{24}$ at 800°C and it displays both stability and homogeneity at this temperature, with no trace of extraneous peaks indicating a pure single phase at 800°C. Furthermore, the spectra in Figure 4.17(c) with a uniform spatial distribution of Mg, Ce, P, O corresponding to the atomic ratio for $MgCe_4P_6O_{24}$ solid-state electrolytes nanoparticles, which shows uniform elemental EDS spectrum that compares with the HT-XRD profile in Figure 4.3(c). Based on the simultaneous TGA-DSC examination in Figure 4.1(c), $MgCe_4P_6O_{24}$ nanoparticles has shown the potential of forming a pure single homogeneous phase at 650°C, which is quite evident in the HT-XRD profiles showing crystallinity at a similar temperature as observed in Figure 4.3(c).

The elemental analysis, percentage atomic fraction and atomic ratio extracted from the EDS elemental maps of each solid-state electrolyte in Figure 4.17 is presented in Table 4.4, showing how the EDS composition compares with the theoretical atomic fraction of the solid-state electrolytes.

Table 4-4 Average elemental composition of EDS elemental maps from nanopowders of the $MgZr_4P_6O_{24}$, $MgHf_4P_6O_{24}$, and $MgCe_4P_6O_{24}$ solid-state electrolytes calcined at 800°C for 0.5h

Element	Atomic Fraction (%)	Atomic Ratio
$MgZr_4P_6O_{24}$		
Mg	2.73	1.00
Zr	9.34	3.42
P	17.94	6.57
O	69.99	25.64
Total	100.00	
$MgHf_4P_6O_{24}$		
Mg	2.80	1.00
Hf	11.50	4.11
P	16.57	5.92
O	69.13	24.69
Total	100.00	
$MgCe_4P_6O_{24}$		
Mg	2.71	1.00
Ce	8.70	3.21
P	17.65	6.51
O	70.94	26.18
Total	100.00	

Table 4.4 shows the average elemental composition derived from EDS elemental maps of the $MgZr_4P_6O_{24}$, $MgHf_4P_6O_{24}$, $MgCe_4P_6O_{24}$ solid-state electrolyte nanopowders. The percent atomic fraction of $MgZr_4P_6O_{24}$ nanoparticles showing non-stoichiometric composition, atomic ratio of the constituent element Zr (=3.42) is slightly lower than the theoretical value whereas, P (=6.57) and O (=25.64) are higher in composition than the theoretical values of 6 and 24, respectively. This indicates that the measured nanopowder is non-homogeneous. $MgHf_4P_6O_{24}$ solid-state electrolyte however shows homogeneous composition as the percent atomic fraction of the measured nanopowder agrees excellently with the theoretical values. The $MgCe_4P_6O_{24}$ solid-state electrolyte

also shows a slight difference between the measured and theoretical values of the EDS elemental composition, this indicating non-homogeneous composition. The measured nanopowders comprising Mg (=1.00), Ce (=3.21), P (=6.51) and O (=26.18), is slightly different from the theoretical atomic ratio of 1:4:6:24, this further shows therefore that the measured sample powder is non-homogeneous and of non-stoichiometric reaction.

4.2.7 Solid-state solution

In using the stoichiometric $MgZr_{4(1-x)}M_{4x}P_6O_{24}$ synthesis series (M = Hf, Ce and the mole ratio $0.1 \leq x \leq 0.9$), 18 solid-state solutions where synthesised and characterised with XRD and SEM-EDS for its structural properties and, the electrical properties by impedance analysis. The synthesised xerogel powders were calcined at 900°C for 3h and sintered at 1300°C for 24h. After following standard laboratory procedures of the sol-gel synthesis method earlier modified, the synthesised dried xerogel powders were calcined based on the TGA-DSC and HT-XRD crystalline phase stability temperature of 800-900°C for calcining the end-members solid-state electrolytes; $MgM_4P_6O_{24}$ (M = Zr, Hf, Ce) and the corresponding solid-state solutions. The HT-XRD profiles of the solid-state solutions, $MgZr_{3.2}Hf_{0.8}P_6O_{24}$ and $MgZr_{3.2}Ce_{0.8}P_6O_{24}$ (when x = 0.2) in the temperature range $25 \leq T/^{o}C \leq 900$ is presented in Figure 4.18(a) and Figure 4.18(b), respectively, and the XRD pattern of the polycrystalline solid-state solutions calcined at 900°C for 3h and then sintered at 1300°C for 24h is presented in Figure 4.19(a) and Figure 4.19(b), and code-named, even and odd sample pellets. Further characterisation techniques such as SEM-EDS, impedance measurement and stability measurement of the solid-state solution pellets preparatory for sensor fabrication was also carried out.

In a nutshell, the synthesised solid-state ceramic solutions were characterised for their structural and electrical properties using the HT-XRD, XRD and SEM techniques for the structural analysis, and impedance spectroscopy for electrical characterisation. As solid-state solutions synthesised using the stoichiometric synthesis series that includes the end-members electrolytes, the data acquired from this solid-state solutions should show some improvement on structural and electrical properties of the end-members solid-state electrolytes. The end-members electrolytes, $MgZr_4P_6O_{24}$, $MgHf_4P_6O_{24}$, and $MgCe_4P_6O_{24}$ are synthesised with the mole ratio on the stoichiometric series as shown: when x = 0, $MgZr_4P_6O_{24}$ and x = 1, $MgHf_4P_6O_{24}$ and $MgCe_4P_6O_{24}$, respectively.

4.2.7.1 HT-XRD

The synthesised dried xerogel powders of $MgZr_{3.2}Hf_{0.8}P_6O_{24}$ and $MgZr_{3.2}Ce_{0.8}P_6O_{24}$ solid-state solutions were heat-treated at a temperature range, $25 \leq T/^oC \leq 900$ in order to predict the calcining temperature of the sample powders. The analysed peak profile is presented in Figure 4.18(a-b).

In using $MgZr_{4(1-x)}M_{4x}P_6O_{24}$ (M = Hf, x = 0.2):

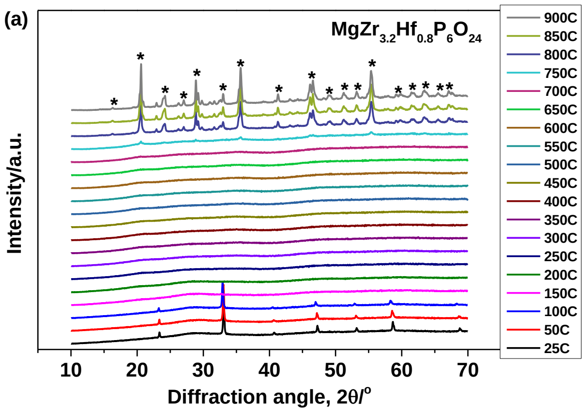

In using $MgZr_{4(1-x)}M_{4x}P_6O_{24}$ (M = Ce, x = 0.2):

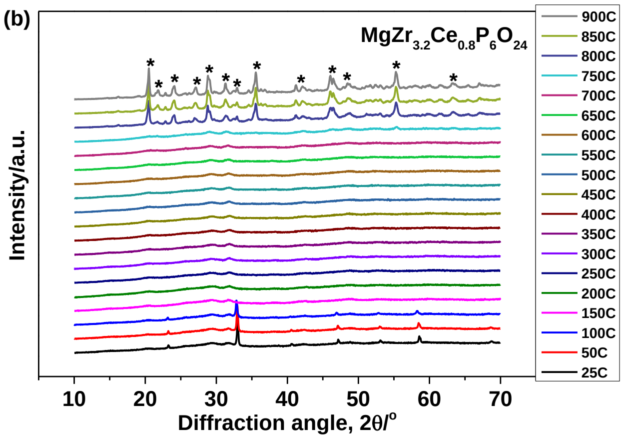

Figure 4-18 HT-XRD profile peaks for (a) $MgZr_{3.2}Hf_{0.8}P_6O_{24}$, (b) $MgZr_{3.2}Ce_{0.8}P_6O_{24}$ dried xerogel powders, heat-treated at a temperature range, $25 \leq T/^oC \leq 900$, showing NH_4Cl crystalline phase at a temperature range of 25-150°C. *Crystalline peak profiles of the solid-state solutions, respectively

Figure 4.18(a-b) demonstrates HT-XRD profile peaks of the measured sample xerogel powders heat-treated at 25-900°C. Figure 4.18(a) depicts the HT-XRD profile peaks of $MgZr_{3.2}Hf_{0.8}P_6O_{24}$ solid-state solution indicating the heat-treated xerogel powders started crystallising at 800°C, showing visible crystalline peaks which were indexed to $Mg_{0.5}Zr_2(PO_4)_3$ [ICDD-04-016-0487]. The profile peaks identified in Figure 4.18(a) compares with Figure 4.3(a-b), respectively. In Figure 4.3(a-b), crystallisation started at 750°C whereas, it started at 800°C according to the profile peaks observed in Figure 4.18(a), this shows therefore that the inclusion of Hf^{4+}- cation dopant must have been responsible for the increase in temperature. Figure 4.18(b) illustrates the HT-XRD peak profiles of $MgZr_{3.2}Ce_{0.8}P_6O_{24}$ solid-state solution, this shows therefore that the profile peaks became visible at 800°C and maintaining stability at higher temperatures. The peak profiles were indexed to monoclinic $Mg_{0.5}Zr_2(PO_4)_3$ [ICDD-04-016-0487] and $Mg_{0.167}Ce_{0.667}(PO_4)$ [ICDD-04-011-7468]. The profile peaks in Figure 4.3(c) was formed at much lower temperatures whereas, in Figure 4.18(b) it formed at 800°C, this further identifies the effect of doping on crystallisation temperature. Furthermore, the HT-XRD analysis was used to predict the calcination temperature of the solid-state electrolytes. Based on the HT-XRD profile peaks identified in Figures 4.18(a) and 4.18(b), the xerogel powders were calcined at 900°C for 3h and sintered at 1300°C for 24h, which perfectly agrees with the calcination and sintering temperatures of the end-members synthesis of $MgZr_4P_6O_{24}$, $MgHf_4P_6O_{24}$, $MgCe_4P_6O_{24}$ solid-state electrolytes, for comparison purpose. The peak intensities and positions in the HT-XRD spectra of the solid-state solutions in Figure 4.18(a-b) further confirms the presence of Zr-Hf and Zr-Ce phosphate phase, therefore showing that solid-state solutions were successfully formed at 800-900°C.

4.2.7.2 XRD

The XRD peak profiles of $MgZr_{4(1-x)}M_{4x}P_6O_{24}$ (when M = Hf, and $0.1 \leq x \leq 1.0$) solid-state solutions were designated into odd numbers (x_o = 0.1, 0.3, 0.5, 0.7, 0.9) and even numbers (x_e = 0.2, 0.4, 0.6, 0.8, 1.0) for purpose of presentation and comparison. The peak profiles of both number range, $0.1 \leq x \leq 1.0$ were indexed against $Mg_{0.5}Zr_2(PO_4)_3$ [ICDD-04-016-0487], and $Zr_2(PO_4)_2O$ [ICDD-04-011-6948], accordingly.

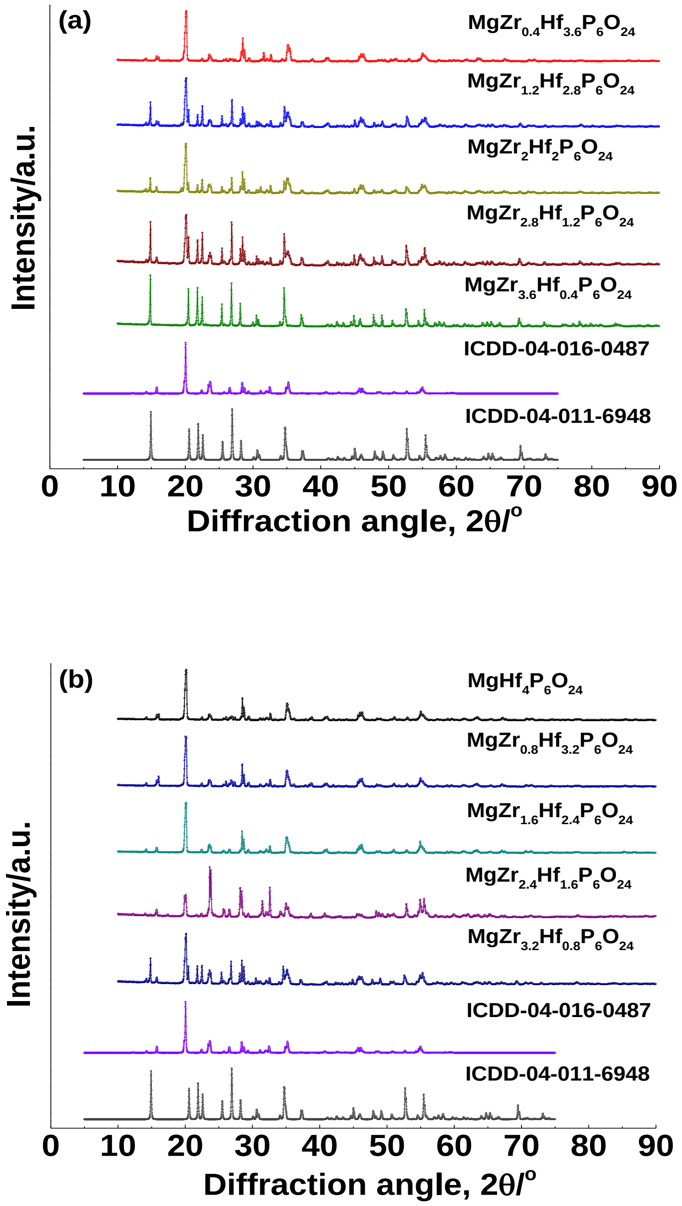

Figure 4-19(a) XRD peak profile of (a-b) $MgZr_{4(1-x)}M_{4x}P_6O_{24}$ (M = Hf, $0.1 \leq x \leq 1.0$) pellets sintered at 1300°C. All the peaks were indexed against $Mg_{0.5}Zr_2(PO_4)_3$ [ICDD-04-016-0487], and $Zr_2(PO_4)_2O$ [ICDD-04-011-6948]

Similarly, the peak profiles of $MgZr_{4(1-x)}M_{4x}P_6O_{24}$ (when M = Ce, and $0.1 \leq x \leq 1.0$) solid-state solutions were designated into odd numbers (x_o = 0.1, 0.3, 0.5, 0.7, 0.9) and even numbers (x_e = 0.2, 0.4, 0.6, 0.8, 1.0) for ease of presentation and comparison. The XRD peak profiles were indexed against $Mg_{0.5}Ce_2(PO_4)_3$ [ICDD-00-054-0637], and $Mg_{0.167}Ce_{0.667}(PO_4)$ [ICDD-04-011-7468], accordingly.

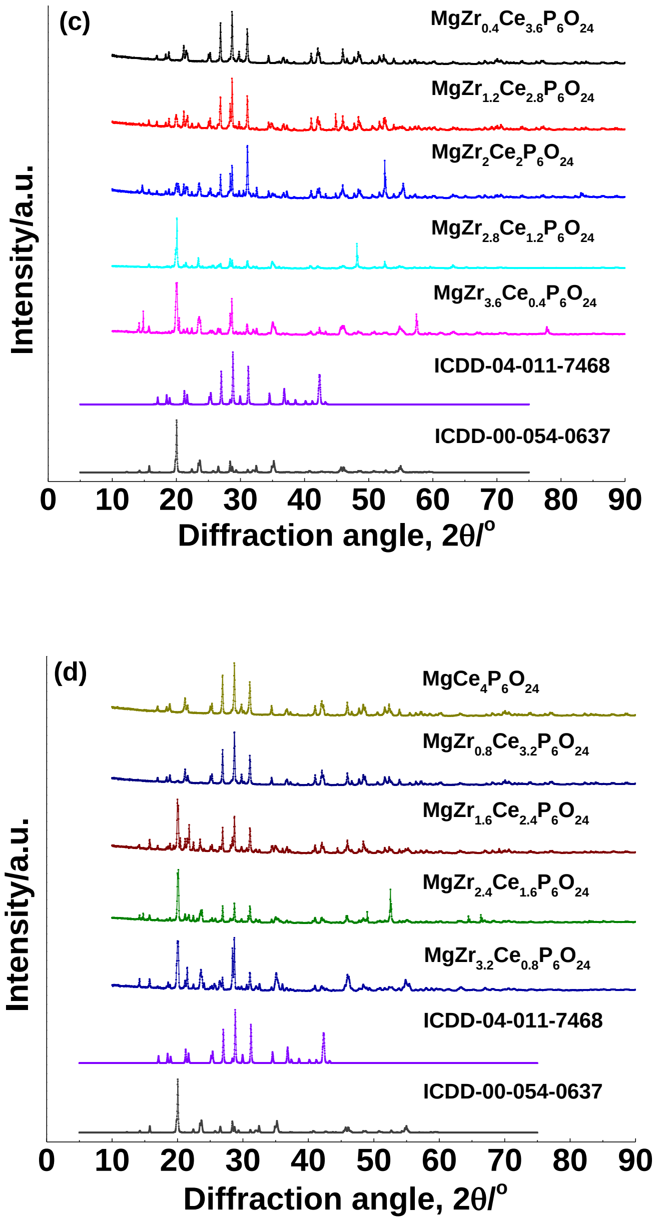

Figure 4-19(b) XRD peak profile of (c-d) $MgZr_{4(1-x)}M_{4x}P_6O_{24}$ (M = Ce, $0.1 \leq x \leq 1.0$) pellets sintered at 1300°C. All the peaks were indexed to $Mg_{0.5}Ce_2(PO_4)_3$ [ICDD-00-054-0637], and $Mg_{0.167}Ce_{0.667}(PO_4)$ [ICDD-04-011-7468]

The XRD profile peaks of $MgZr_{4(1-x)}M_{4x}P_6O_{24}$ (when M = Hf, Ce; $0.1 \leq x \leq 1.0$) solid-state solution series calcined at 900°C and sintered at 1300°C is presented in Figure 4.19(a) and Figure 4.19(b), respectively.

Figure 4.19(a) however, present the profile peaks of 10 solid-state solutions by doping the base electrolyte with Hf^{4+}- cation in the B-site of $MgZr_4P_6O_{24}$, which further shows a particular trend as the substitution progresses. The solid-state solutions were shown as even, X_e and odd, X_o numbers solid-state solutions for purpose of comparison and convenience of presentation. It was observed therefore in Figure 4.19(a) that the solid-state solutions with mole ratio, x = 0.1 and 0.4 shows different profile peaks from the indexing standard, $Mg_{0.5}Zr_2(PO_4)_3$ [ICDD-04-016-0487], and $Zr_2(PO_4)_2O$ [ICDD-04-011-6948]. However, the solid-state solution with mole ratio, x = 0.1 shows a complete transformation to $Zr_2(PO_4)_2O$ [ICDD-04-011-6948]. The other profile peaks of Zr-Hf phosphate solid-state solutions therefore agrees with the indexing standard. Similarly, Figure 4.19(b) present the profile peaks of solid-state solutions synthesised by doping the base electrolyte with Ce^{4+}- cation in the B-site of $MgZr_4P_6O_{24}$ electrolyte resulting in 10 different solid-state solutions, indexed to $Mg_{0.5}Ce_2(PO_4)_3$ [ICDD-00-054-0637] and $Mg_{0.167}Ce_{0.667}(PO_4)$ [ICDD-04-011-7468]. Furthermore, Figure 4.19(b) shows that the solid-state solutions which are believed to be in excellent agreement according to the indexing standard shows also that the 10 solid-state solutions are homogeneous and stable. The Zr-Ce phosphate solid-state solutions therefore maintains high stability at high-temperatures.

From the peak intensities and positions in the XRD spectra of the $MgZr_{4(1-x)}Hf_{4x}P_6O_{24}$ and $MgZr_{4(1-x)}Ce_{4x}P_6O_{24}$ (when $0.1 \leq x \leq 1.0$) solid-state solutions in Figure 4.19(a) and Figure 4.19(b), it was clear that the solid-state solutions phase were successfully produced in each instance in the structural orientation of their respective end-member electrolytes. In Figure 4.19(a), the addition of Hf^{4+}-cation can also be seen to gradually transform the Hf-doped phase from $Zr_2(PO_4)_2O$ [ICDD-04-011-6948] as noticed with $MgZr_{3.6}Hf_{0.4}P_6O_{24}$ (when x = 0.1) to peaks of $Mg_{0.5}Zr_2(PO_4)_3$ [ICDD-04-016-0487] of $MgZr_{3.2}Hf_{0.8}P_6O_{24}$ (when x = 0.2) which confirms the formation of the $Mg_{0.5}Zr_2(PO_4)_3$ phase. The continuous addition of Hf increases the intensity of the relevant peaks, which is accomplished by a decrease in the diffraction angle, 19.99° 2θ. A particular shift in peak position was observed at 23.65° 2θ for $MgZr_{2.4}Hf_{1.6}P_6O_{24}$ (when x = 0.4), However, this initial shift in peak position is seemingly not affected by continuously increasing Hf as stability is achieved at x = 0.5 solid-state solution peaks subsequently stabilising in 20.11° 2θ comparable to the $MgHf_4P_6O_{24}$ solid-state electrolyte.

In Figure 4.19(b), the solid-state solutions formed by doping the Zr^{4+} with Ce^{4+}-cation in the mole ratio ranging $0.1 \leq x \leq 0.9$ were indexed with monoclinic $Mg_{0.5}Ce_2(PO_4)_3$ [ICDD-00-054-0637] and $Mg_{0.167}Ce0.667(PO_4)$ [ICDD-04-011-7468]. The solid-state solutions (when x = 0.1, 0.2, 0.3, 0.4) shows their peak positions compares excellently with $Mg_{0.5}Ce_2(PO_4)_3$ [ICDD-00-054-0637] as the peak intensities at 19.99° 2θ relative to the doping concentration agrees with Zr-P-O structure. The peak position shifts to 31.05° 2θ at x = 0.5 and then stabilises at the peak position of 28.73° 2θ which indexed $Mg_{0.167}Ce_{0.667}(PO_4)$ [ICDD-04-011-7468]. The solid-state solutions at $0.5 \leq x \leq 1.0$ was therefore considered for the design and fabrication of solid-state Mg-sensors. The Zr-Ce phosphate doped solid-state solution series shows an increasing stability relative to temperature.

4.2.7.3 Lattice constant

Figure 4.20 shows the lattice constant of $MgZr_{4(1-x)}M_{4x}P_6O_{24}$ (M = Hf, Ce; $0 \leq x \leq 1.0$) solid-state solutions. The $MgZr_{4(1-x)}Hf_{4x}P_6O_{24}$ and $MgZr_{4(1-x)}Ce_{4x}P_6O_{24}$ lattice constant increases linearly with the doping content. However, lattice constant deviations in this research were noticed at x = 0.1 and 0.4 for $MgZr_{4(1-x)}Hf_{4x}P_6O_{24}$ and at x = 0.2 and 0.5 for doped $MgZr_{4(1-x)}Ce_{4x}P_6O_{24}$ solid-state solutions, respectively.

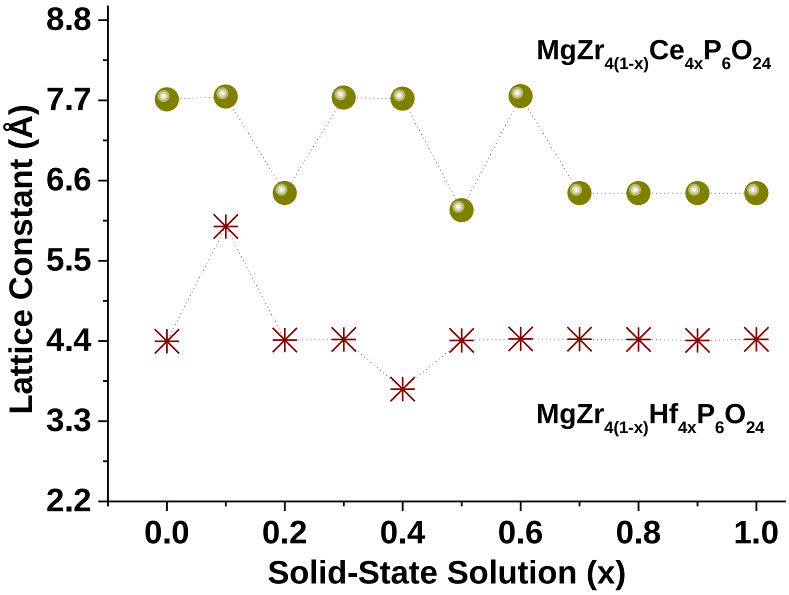

Figure 4-20 Lattice constant of doped $MgZr_{4(1-x)}Hf_{4x}P_6O_{24}$ and $MgZr_{4(1-x)}Ce_{4x}P_6O_{24}$ as a function of dopant content in the composition range of $0 \leq x \leq 1.0$

In Figure 4.20, lattice constant of doped $MgZr_{4(1-x)}Hf_{4x}P_6O_{24}$ and $MgZr_{4(1-x)}Ce_{4x}P_6O_{24}$ solid-state solutions as a function of dopant content in the $0 \leq x \leq 1.0$ composition range is illustrated. The lattice constant in Figure 4.20 therefore increases linearly with increasing doping content (in this case, HfO_2 and CeO_2) in different composition range which manifest the successful synthesis of a pure phase solid-state solution in their complete composition range without any severe distortion of their monoclinic crystal system and no additional peaks from secondary phases were observed however, some deviations were noticed in the composition range of the solid-state doping content. The $MgZr_{4(1-x)}Hf_{4x}P_6O_{24}$ nanocrystals in Figure 4.20 shows deviation from linearity at x = 0.1 and 0.4, which shows that as the $MgZr_4P_6O_{24}$ solid-state electrolyte is doped with HfO_2, the lattice constant of doped $MgZr_4P_6O_{24}$ nanocrystal electrolyte increased from 4.3951Å to 5.9704Å then stabilised at x = 0.2 dopant content. The lattice constant also decreased to 3.7393Å at x = 0.4, then the nanocrystal stabilised at x = 0.5 where equal concentration of the Zr^{4+} and Hf^{4+} dopant content was achieved. This shows in Figure 4.20 that as the homogeneous phase is achieved, subsequent addition of dopant content ensures stability and that the lattice constant maintained the crystal structure of monoclinic system of $MgHf_4P_6O_{24}$ electrolyte. Similarly, the $MgZr_{4(1-x)}Ce_{4x}P_6O_{24}$ nanocrystal solid-state series indexed to double $Mg_{0.5}Ce_2(PO_4)_3$ [ICDD-00-054-0637] and $Mg_{0.167}Ce_{0.667}(PO_4)$ [ICDD-04-011-7468], shows different lattice constant on the same materials, the end-member solid-state electrolyte, $MgCe_4P_6O_{24}$ and doped Zr-Ce solid-state solutions having the same monoclinic crystal structure. Figure 4.20 shows lattice constant deviation at x = 0.2 and 0.5 dopant content; while the x = 0, 0.1, 0.3, 0.4, 0.6 dopant content corresponds to double $Mg_{0.5}Ce_2(PO_4)_3$ [ICDD-00-054-0637], the x = 0.7, 0.8, 0.9 and 1.0 dopant content corresponds to $Mg_{0.167}Ce_{0.667}(PO_4)$ [ICDD-04-011-7468]. The two indexed monoclinic crystal system shows homogeneous single phase which becomes a pure homogeneous single phase at x = 1.0 for $MgCe_4P_6O_{24}$ solid-state electrolyte. The lattice crystal deviation at the x = 0.2 and 0.5 is believed to result from different crystal structure orientation of ZrO_2 and CeO_2, since the transition metals; Zr and lanthanides, Ce belongs to different periodic group thereby showing different physical and chemical properties including their crystal structures unlike Zr and Hf that belongs to the same periodic group with similar properties and crystal structures. However, lattice constant of these doped electrolytes, $MgZr_{4(1-x)}Hf_{4x}P_6O_{24}$ and $MgZr_{4(1-x)}Ce_{4x}P_6O_{24}$ solid-state solutions in Figure 4.20 clearly shows x = 0.5 as the transition dopant content with which stability of the crystal structure is achieved.

4.2.7.4 SEM-EDS

Linescan across the surface of polished solid-state $MgZr_{4(1-x)}M_{4x}P_6O_{24}$ (when M = Hf, Ce; $0.1 \leq x \leq 0.9$), was carried out to determine the purity and homogeneous phase of solid-state solution electrolytes synthesised using sol-gel process by doping the Zr^{4+}-cation in B-site of $MgZr_4P_6O_{24}$ electrolytes with Hf^{4+} and Ce^{4+}, at respective intervals. Microstructure constituent elemental maps were determined by observing the polished surface of the sample pellets in SEM. Moreso, SEM-EDS technique was equally used to confirm whether or not respectively, Hf^{4+} and Ce^{4+} dissolved in the $MgZr_4P_6O_{24}$ electrolyte to form solid-state solutions of uniform and adequate proportion.

Figure 4.21 represent the linescan and EDS-elemental maps of (a) $MgZr_{3.2}Hf_{0.8}P_6O_{24}$, (b) $MgZr_2Hf_2P_6O_{24}$, and (c) $MgZr_{0.8}Hf_{3.2}P_6O_{24}$ for solid-state solutions synthesised by doping $MgZr_4P_6O_{24}$ with Hf^{4+} in the mole ratio, x = 0.2, 0.5 and 0.8, respectively.

Similarly, the linescan and EDS-elemental maps of the Ce-doped constituents are also reported in Figure 4.22 using the same concentration mole ratio.

EDS-Linescan and elemental maps showing the dissolution of HfO_2 and CeO_2-based dopants in the solid-state solutions with varying concentration mole ratio is presented in Figure 4.21 and Figure 4.22 for x = 0.2, 0.5 and 0.8, respectively. The mole ratio, x = 0.2, 0.5 and 0.8 of the corresponding solid-state solutions were reported to show the structural and morphological changes of the doped sample material and, changes in its electrical properties as a result of possible defects with reference to the end-members electrolytes, $MgZr_4P_6O_{24}$, $MgHf_4P_6O_{24}$, and $MgCe_4P_6O_{24}$, for which their electrical properties are already known. The purpose of doping the base solid-state electrolytes with HfO_2 and CeO_2 in this research is towards improving the ionic conductivity of end-members electrolytes by altering the defect structures which underlie the physical and chemical properties of the electrolytes.

$MgZr_{3.2}Hf_{0.8}P_6O_{24}$ (x = 0.2)

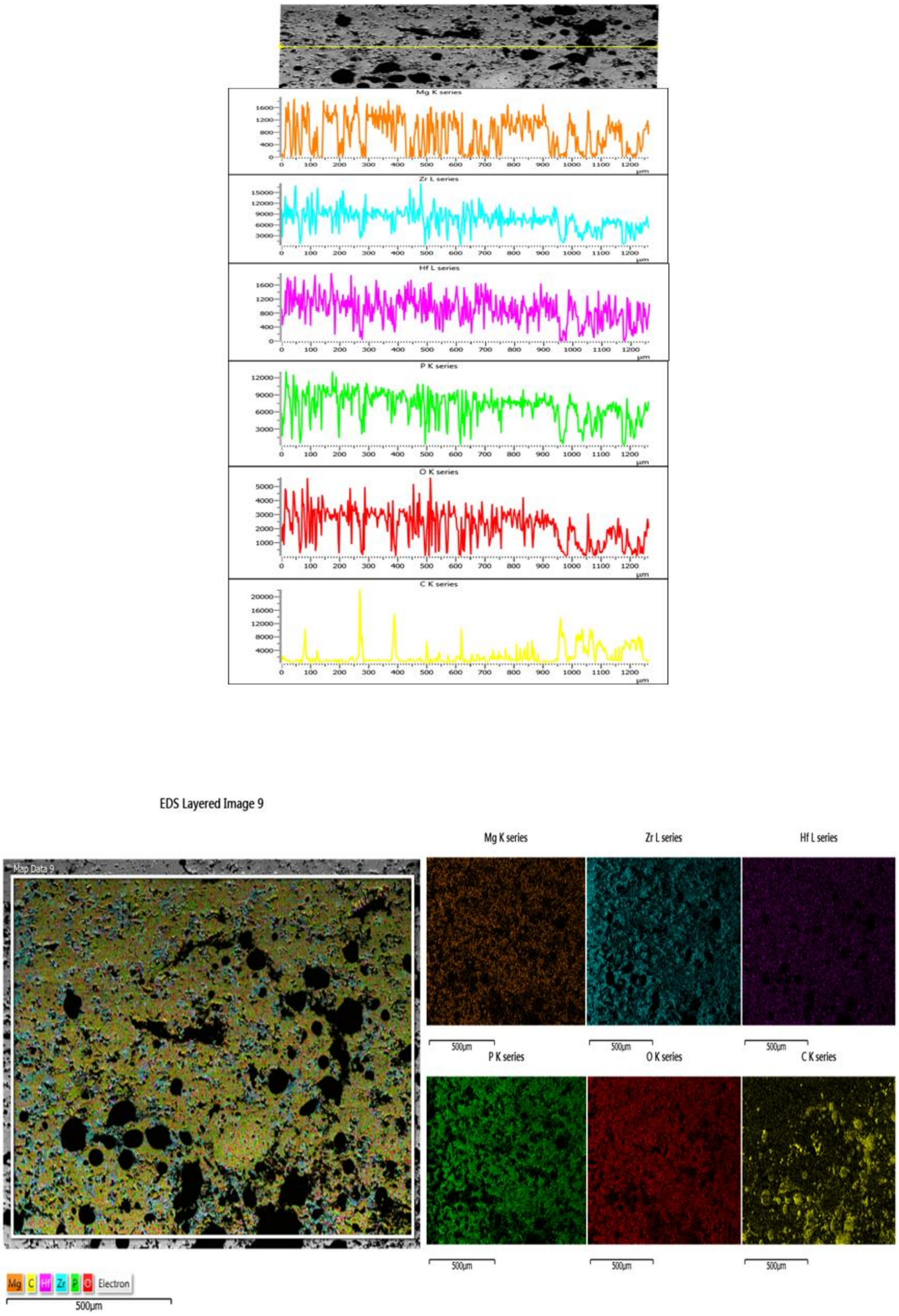

Figure 4-21(a) Linescan and elemental map of $MgZr_{3.2}Hf_{0.8}P_6O_{24}$ solid-state solution

$MgZr_2Hf_2P_6O_{24}$ (x = 0.5)

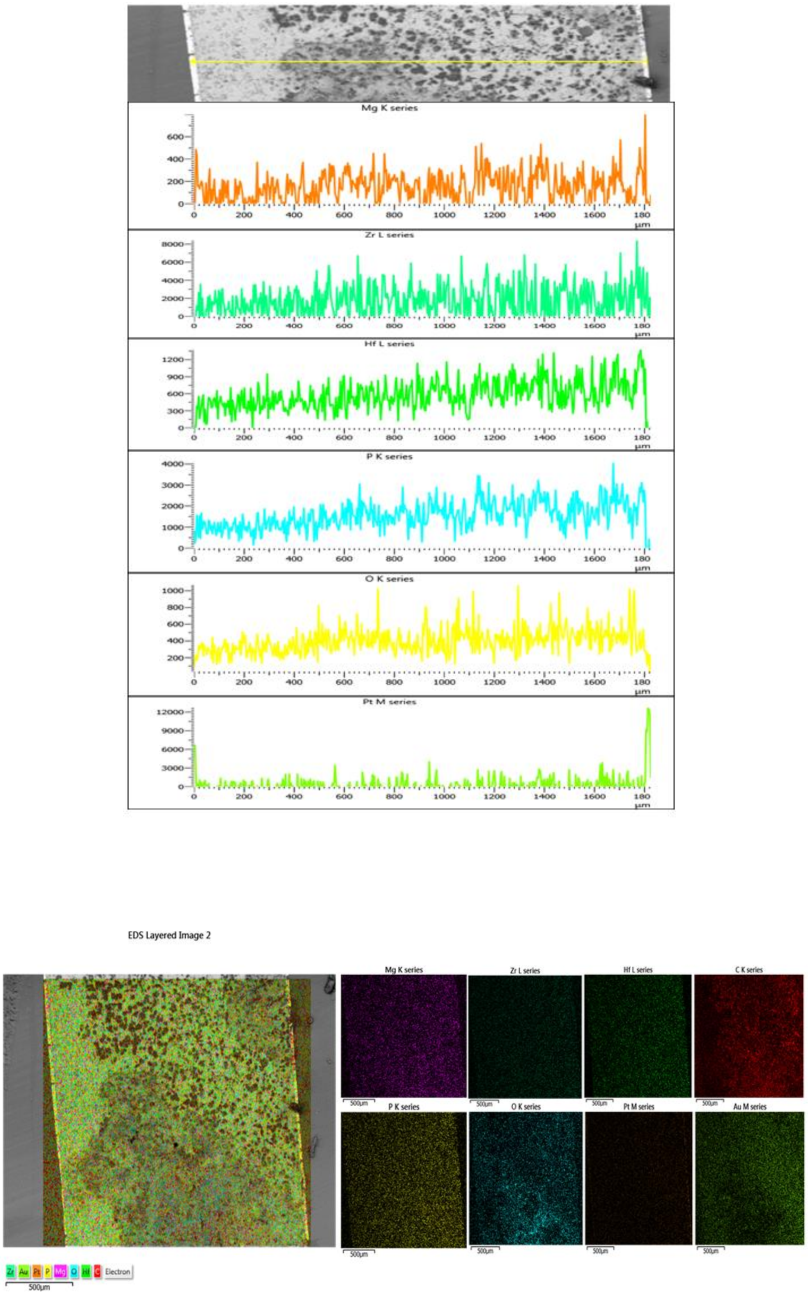

Figure 4-21(b) Linescan and elemental map of $MgZr_2Hf_2P_6O_{24}$ solid-state solution

$MgZr_{0.8}Hf_{3.2}P_6O_{24}$ (x = 0.8)

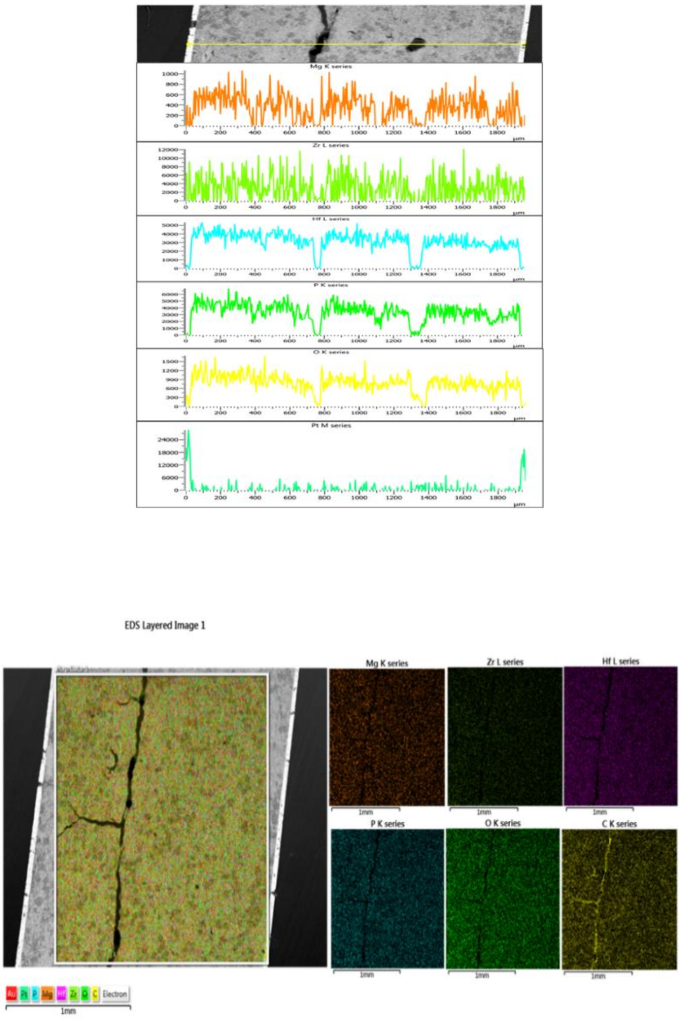

Figure 4-21(c) Linescan and elemental map of $MgZr_{0.8}Hf_{3.2}P_6O_{24}$ solid-state solution

Figure 4.21(a) is the EDS-linescan and elemental mapping data of $MgZr_{3.2}Hf_{0.8}P_6O_{24}$ solid-state solution sample pellet sintered at 1300°C for 24h which revels homogeneity of the sample composition and the interface reactions. The constituent elements in the solid-state solution were identified, the carbon stain picked during sample grinding on a SiC paper was also identified as intense positive peaks on the linescan spectrum. The EDS layered image of this sample did not show any definite interface reaction, this might be due to the fact that ZrO_2 and HfO_2 share very similar chemical properties hence could dissolve into each other and the sample pellet shows notably more dense pellet sintered at 1300°C for 24h. The addition of Hf dopant to form solid-state solution did not alter the sintering temperature considering that HfO_2 and ZrO_2 with similar chemical properties have shown similar sintering temperature. The EDS-linescan and elemental maps of $MgZr_2Hf_2P_6O_{24}$ electrolyte in Figure 4.21(b) shows a sample pellet with equal composition of ZrO_2 and HfO_2 (x = 0.5) with similar structural orientation. The EDS image shows finer sample surface with carbon stain believed to have been attracted from SiC paper. The elemental maps shows a clear homogeneous sample and the elements were identified on the linescan with significant intensity of the elements including platinum, Pt which shows on the linescan spectra from the cross sectional area of the ground sample pellet prepared for impedance analysis. The linescan in this case shows no clear evidence of any interface reaction between Pt and the bulk solid-state solution. However, the doping creates a finer and evenly distributed grain size relative to the $MgZr_4P_6O_{24}$, $MgHf_4P_6O_{24}$, and $MgCe_4P_6O_{24}$, end-members electrolytes. In Figure 4.21(c), the $MgZr_{0.8}Hf_{3.2}P_6O_{24}$, with more Hf than Zr shows fine distributed grain size relative to the pure end-members solid-state electrolytes (x = 0, 1). In this situation, the linescan indicates homogeneous spread of constituent elements with Mg and Zr showing uniform intensity while the other elements showing reduced intensity at certain regions of the entire composition, this shows a likely non-stoichiometric composition. The spot and vertical crack on the sample shows presence of carbon stain most likely from SiC paper during sample grinding and an internal crack that was only visible at SEM magnification, this could have occurred during sintering or impedance measurement with reversible temperature cycle.

$MgZr_{3.2}Ce_{0.8}P_6O_{24}$ (x = 0.2)

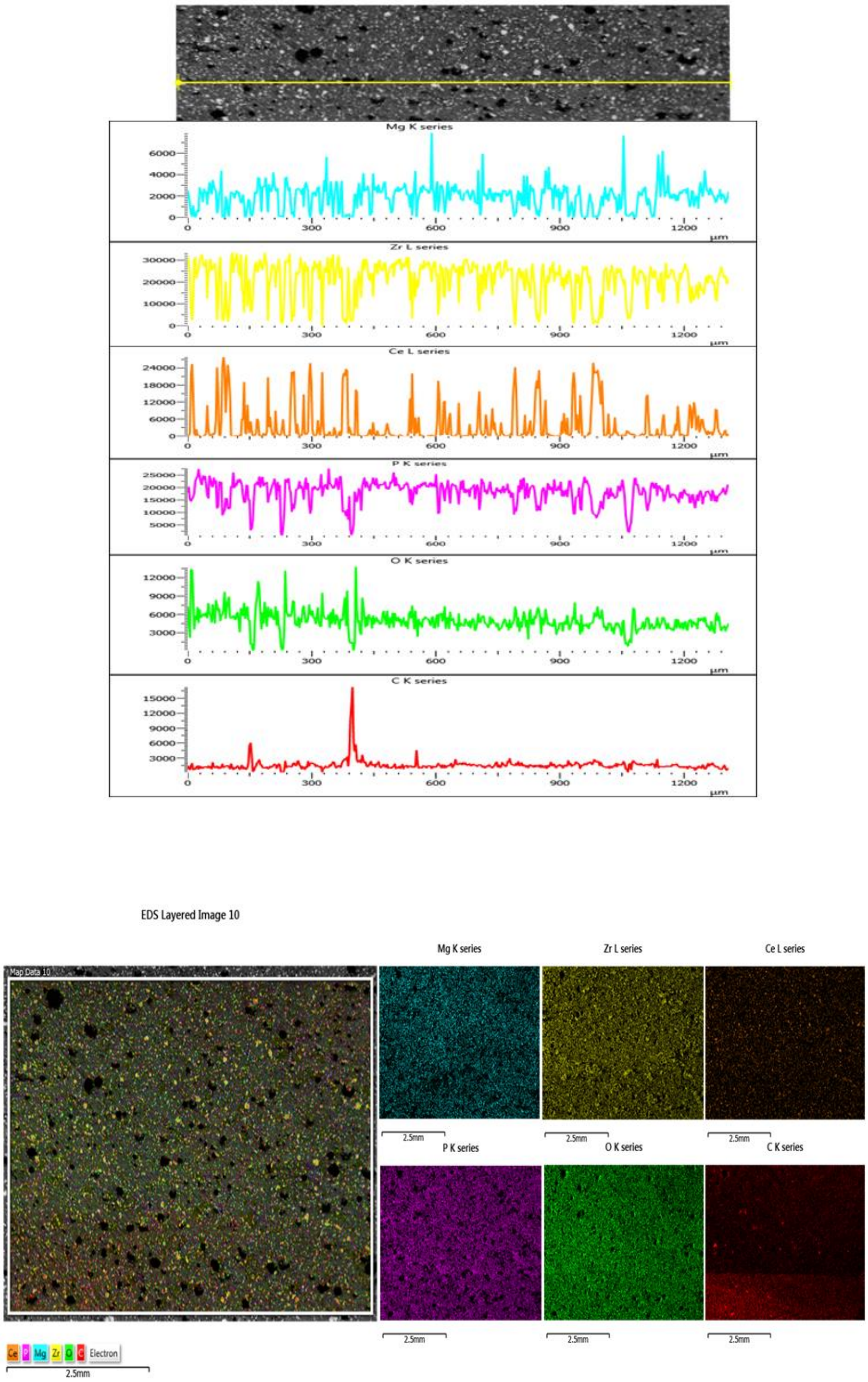

Figure 4-22(a) Linescan and elemental map of $MgZr_{3.2}Ce_{0.8}P_6O_{24}$ solid-state solution

$MgZr_2Ce_2P_6O_{24}$ (x = 0.5)

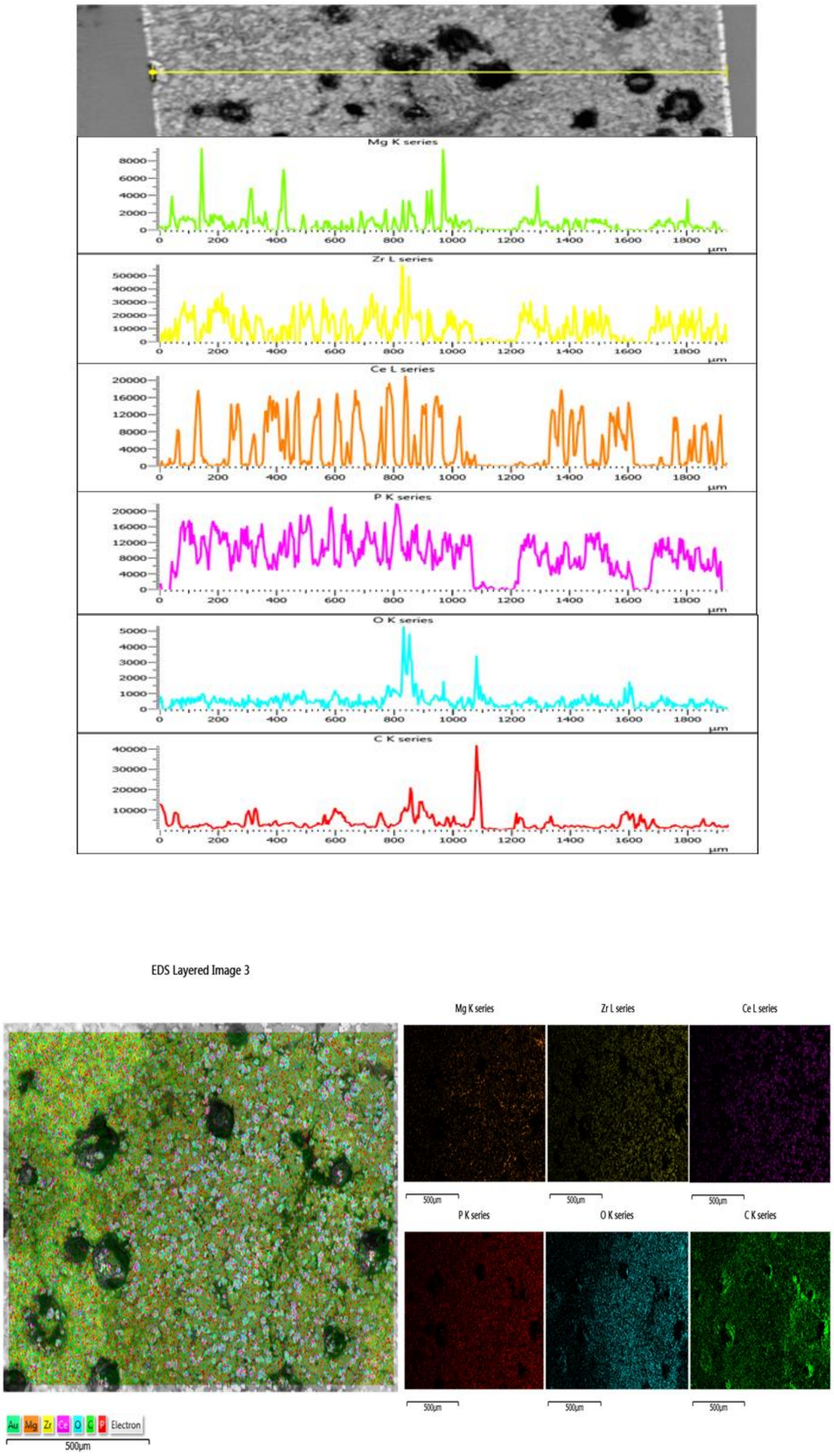

Figure 4-22(b) Linescan and elemental map of $MgZr_2Ce_2P_6O_{24}$ solid-state solution

$MgZr_{0.8}Ce_{3.2}P_6O_{24}$ (x = 0.8)

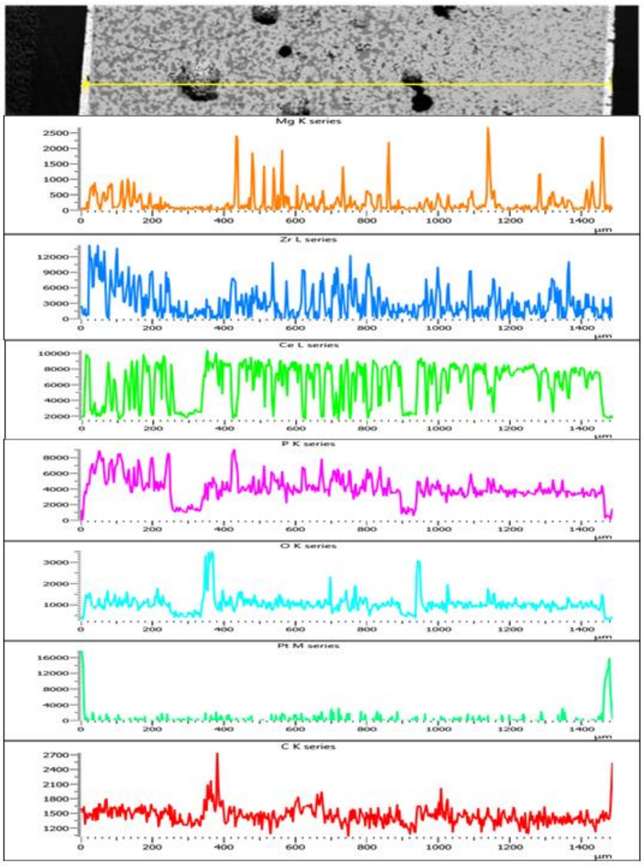

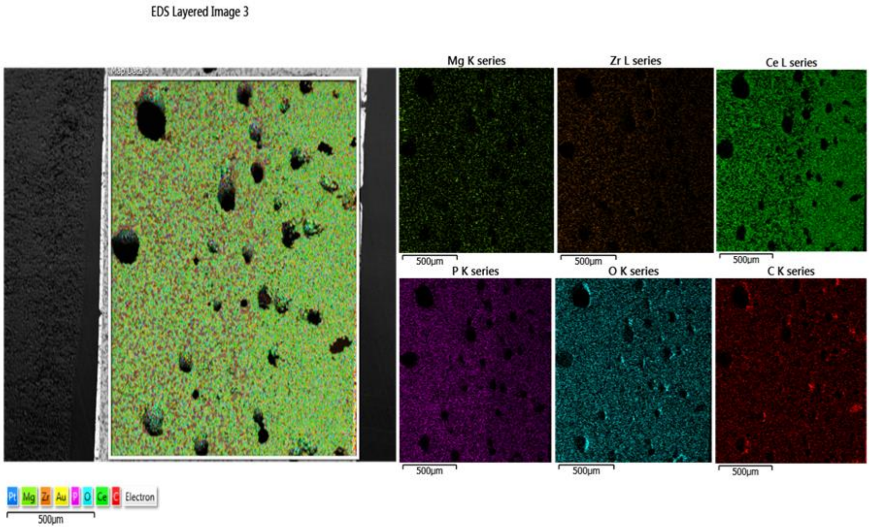

Figure 4-22(c) Linescan and elemental map of $MgZr_{0.8}Ce_{3.2}P_6O_{24}$ solid-state solution

Similarly, $MgZr_{3.2}Ce_{0.8}P_6O_{24}$ shows a solid-state solution with more ZrO_2 than CeO_2 (x = 0.2), it was evident on the linescan that Ce doping creates fine and homogeneous grain size distribution relative to the end-member Ce-electrolyte (x = 1) which shows a dense pellet considering that Ce-based electrolytes sinter at much lower temperature compared with the Zr- and Hf-based electrolytes. The Mg profile also shows uniform distribution of the grain size but Zr reflects reduced intensity across the line spectrum, this could be because Ce is heavier than Zr, therefore creating a CeO_2 structural defects in the form of vacancies for further reaction. As addition of Ce increases, the Ce peaks becomes even broader and Zr starting to show positive intensity. Mg also shows clear presence in the solid-state solution. The grain size at x = 0.5 becomes bigger than those at x = 0.2, this shows that more of the Ce dopant is saturating the Zr position making it assuming the CeO_2 crystal structure. The elemental maps show homogeneous phase distribution of the constituent elements. The sample becomes even finer and dense at x = 0.8, this is because the Ce dopant is fully saturating and possibly displacing the Zr component. At this stage, CeO_2 provides fine grain size compared to Zr which could result in a non-stoichiometric reaction. The EDS-maps however shows improved grain sizes compared to those of $MgZr_2Ce_2P_6O_{24}$.

4.2.8 Reference electrodes

Biphasic powder mixture of $MgCr_2O_4$+Cr_2O_3 was used in this research as the reference electrode because of its stability at high-temperature. However, $MgAl_2O_4$+α-Al_2O_3 and $MgFe_2O_4$+α-Fe_2O_3 were equally used during the trial experiments but were found to be limited in application at high-temperatures and had to be discontinued. The reference electrode therefore was synthesised by the conventional solid-state method at 1090°C for 144h. The long annealing time became necessary since a single spinel phase of the solid-state $MgCr_2O_4$ is observed to be formed at a temperature range of 1200-2400°C according to the phase equilibrium diagram in Figure 4.23, the sintering temperature of 1090°C was adopted because of furnace limitation while a much longer annealing time was used to compensate for the low temperature regime. Meanwhile, calcined biphasic powder mixture of $MgFe_2O_4$+α-Fe_2O_3 were pelletised into sample various pellets and sintered using the same operational condition as $MgCr_2O_4$+Cr_2O_3. The pellets were used for thermodynamic measurements by electromotive force (emf) method but biphasic powder mixture was used for sensor fabrication and Mg-sensor testing. The phase formation of the synthesised reference electrodes were analysed by X-ray diffraction.

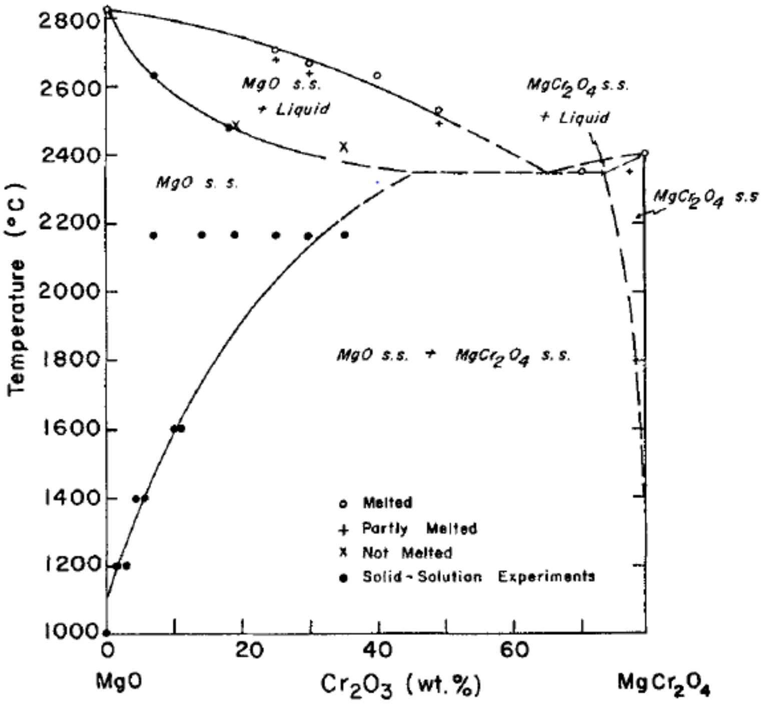

Figure 4-23 Phase equilibrium diagram for the MgO-$MgCr_2O_4$ system [124]

Structural phases of the synthesised biphasic powder mixture of solid-state $MgCr_2O_4$, Cr_2O_3, $MgFe_2O_4$ and α-Fe_2O_3 and their corresponding pellets were analysed by XRD formalism. The synthesis approach and relevant temperature was deduced from the Mg0-$MgCr_2O_4$ phase equilibrium diagram as described in Figure 4.23 [124]. Although the phase equilibrium only shows 50% of the process as illustrated in equation (4.8), the other half not shown on the equilibrium diagram entails the formation of a biphasic powder mixture, the solid-state $MgCr_2O_4$+Cr_2O_3 which is achieved by adding on a 1:1 molar weight ratio, Cr_2O_3 powder to the product of equation (4.8) and then sintered at 1090^{o}C for 144h in order to achieve a sintered pellet at such low temperature. The sintered pellets could be used as reference electrodes in thermodynamic measurement while the atmosphere powder initially provided for shielding likely volatiles of green pellets during sintering could be used alternatively as reference electrode in fabricating the solid-state Mg-sensors.

$$MgO(s) + Cr_2O_3(cor) \rightarrow MgCr_2O_4(sp) \qquad (4.8)$$

4.2.8.1 XRD

The X-ray diffraction peak profiles of biphasic powder mixture of $MgCr_2O_4$+Cr_2O_3 and $MgFe_2O_4$+α-Fe_2O_3 solid-state reference electrodes calcined at 1090°C for 144h is shown in Figure 4.24(a) and Figure 4.24(b), respectively.

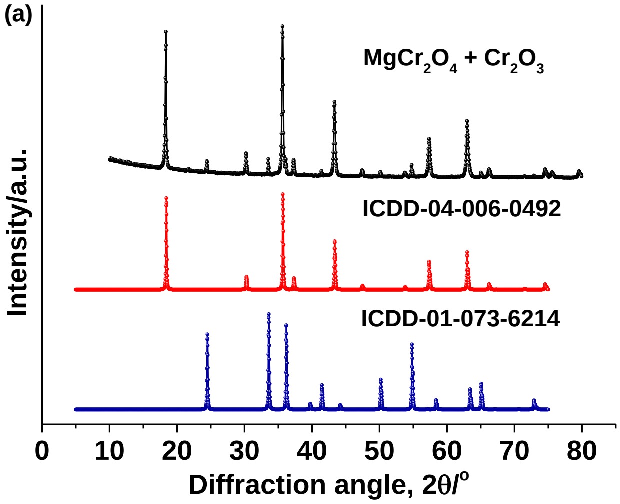

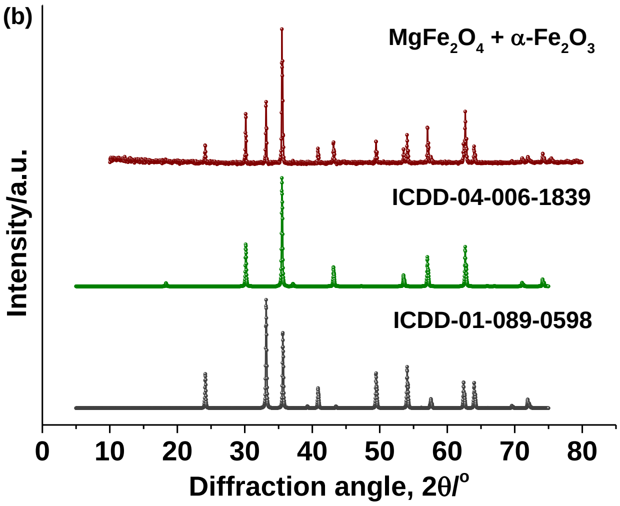

Figure 4-24 XRD peak profiles of (a) $MgCr_2O_4$+Cr_2O_3 and (b) $MgFe_2O_4$+α-Fe_2O_3 system

Similarly, the $MgFe_2O_4$ was equally synthesised and analysed as a single phase spinel compound, then equal amount of α-Fe_2O_3 was added in 1:1 molar weight ratio to form the biphasic powder mixture. The resultant calcined biphasic powder mixture and the sintered pellets achieved at 1090°C for 144h, respectively, were further analysed using X-ray diffraction. Figure 4.24(a) and Figure 4.24(b) shows the peak profiles of solid-state $MgCr_2O_4$+Cr_2O_3 and $MgFe_2O_4$+α-Fe_2O_3 compound, they both depicts a biphasic powder mixture of their constituent compounds in almost the same proportion and were indexed accordingly.

4.3 Conclusions

The synthesised solid-state electrolytes and corresponding solid-state solutions were characterised using various techniques. The characterisation techniques employed in this research: HT-XRD, TGA-DSC, XRD, XRF, HR-TEM, EDS, FTIR, SEM, Laser-Raman scattering, and Densification-porosity revealed structural details of the solid-state electrolytes and the corresponding solid-state solutions. The reference electrodes ($MgCr_2O_4$+Cr_2O_3, $MgFe_2O_4$+α-Fe_2O_3) and working electrodes (non-ferrous metallic alloys) were analysed with X-ray diffraction and SEM characterisation. The structural characterisation summary of this research are outlined as follows;

i. TGA profiles of the $MgZr_4P_6O_{24}$, $MgHf_4P_6O_{24}$ and $MgCe_4P_6O_{24}$ dried xerogel powders suggest possible calcination temperatures at 750°C, 800°C and 650°C, respectively which agrees perfectly with the HT-XRD analysis in this research. DSC profile curves however relates that the exothermic peak at 870°C depicts a phase formation of $MgZr_4P_6O_{24}$ solid-state electrolyte, while the exothermic peak at 900°C and 350°C, suggest a formation of $MgHf_4P_6O_{24}$ and $MgCe_4P_6O_{24}$ solid-state electrolytes phase, respectively.

ii. Ambient temperature powder XRD was used for the phase identification of the calcined nanopowders and sintered pellets of the solid-state electrolytes, and possible transformation which were indexed to the ICDD standard database. The XRD analysis further revealed that the solid-state electrolyte nanopowders calcined at 800-900°C, and the pellets sintered at 1300°C has a homogeneous, pure single phase at this temperatures.

iii. The sintering temperature was confirmed from density-porosity measurement. In this research however, the optimum relative density range of about 94-99% result in dense pellets for impedance analysis at different temperatures.

iv. The morphology of the solid-state electrolyte ceramic revealed that the fracture surface pellet is dense with little porosity and the elemental composition agrees with the atomic ratio of constituent element. The polished surface of the solid-state solution also revealed homogeneous phase with different dopant addition. The homogeneity of the solid-state solution was determined using XRD and linescan across the surface of the polished sample pellets. HR-TEM and SAED shows nanoparticles structures, that it shows single crystallinity with elemental composition agreeing with stoichiometric and non-stoichiometric reactions. The crystal lattice fringes and corresponding d-spacing of their surface grafting nanoparticles present a clear characteristics of monoclinic system.

v. The lattice constant of the solid-state solutions shows the pure homogeneous formation of the solid-state solutions. The deviations observed at $x = 0.1$ and 0.4 of $MgZr_{4(1-x)}Hf_{4x}P_6O_{24}$ nanocrystals shows an increase in the particle size of the nanocrystals. The addition of HfO_2 doping oxide provides Mg^{2+}-cation vacancies which is expected to facilitate migration of Mg^{2+}-cations, while the rate of migration is proportional to the doping concentration. Similarly, lattice constant of $MgZr_{4(1-x)}Ce_{4x}P_6O_{24}$ solid-state solutions revealed deviations at $x = 0.2$ and 0.5, which is believed to serve as transition compositions stabilised thereafter considering that the solid-state solutions indexed to $Mg_{0.5}Ce_2(PO_4)_3$ and $Mg_{0.167}Ce_{0.667}(PO_4)$ have different lattice constant.

vi. The sintered pellets were further characterised for their electrical properties and chemical thermodynamic behaviour as a function of temperature.

vii. Based on the conductivity data and thermodynamic stability, sintered pellets and biphasic powder mixture reference electrodes were used for sensor design, fabrication and testing, and for thermodynamic examination. The electrical and thermodynamic characterisation data are presented in chapter 5 and chapter 6, respectively.

Chapter 5

Electrical Characterisation

5.1 Synopsis

Electrical conduction usually occurs during a long range migration of either electrons or ions. Conduction in inorganic materials is of interest in this research since ionic and electronic conduction is observed in solid-state materials [215]. Typical conductivities for different materials listed in Table 5.1 shows the values of both ionic and electronic conduction. The specific conductivity (σ) of a crystal is normally considered in solid-state materials. Meanwhile, the specific conductivity of a solid-state material includes the conductivity of a crystal of sample pellet with a cell constant of unity, i.e., a unit cross-sectional area and unit length. The units of specific conductivity is measured in $\Omega^{-1}cm^{-1}$ and Scm^{-1} where 1 siemen, $S \equiv 1\ \Omega^{-1}$. In general, conductivities are known to be temperature dependent, and as for all types of materials, except metals, conductivity increases as temperature increases [215]. In metals, however, conductivity is highest at low temperatures and in some other metals, superconductivity phenomenon prevails close to absolute zero [215]. Since defects often effects conductivity; the presence of ionic defects result in ionic conductivity, while electronic defects result in electronic conductivity [216], electronic conductivity is undesirable in a solid-state electrolyte. Meanwhile, for a solid-state electrolyte to be effective, ionic to electronic conductivity ratio should be ≥ 100 [216].

Table 5-1 Typical values of electrical conductivity

	Material	σ (Ω^{-1} cm^{-1}) [83, 215]
Ionic conduction	Ionic crystals	$< 10^{-18} - 10^{-4}$
	Solid-state electrolytes	$10^{-3} - 10^{1}$
	Strong (liquid) electrolytes	$10^{-3} - 10^{1}$
Electronic conduction	Metals	$10^{1} - 10^{5}$
	Semiconductors	$10^{-5} - 10^{2}$
	Insulators	$< 10^{-12}$

In electrical characterisation, some characteristic properties that defines the impedance measurements and were considered in this research are as outlined:

The total electrical conductivity, σ_t of a solid can be defined as;

$$\sigma_t = \sum_i \sigma i \tag{5.1}$$

where σ_i is the partial conductivity of each of the charge carriers (in Scm^{-1}) present in solids. These charge carriers can be either electronic in nature (i.e., electrons or holes), or atomic in nature and are usually defects of either the anionic or cationic sub-lattice. Each of the partial conductivities however, can be expressed as;

$$\sigma_i = C_i Z_i e \mu_i \tag{5.2}$$

where C_i is the number of carriers of type i (in cm^{-3}), Z_i is the number of electronic charges carried by these carriers, e is the elementary electron charge (in C), and μ_i is the mobility of the i charge carriers in the solid (in Ω cm^{2}V^{-1}) [215, 217].

The transport number, t_{ion} for any charge carrier i is defined using the parameters in equation (5.3);

$$t_{ion} = \frac{\sigma_{ion}}{\sigma_t} \tag{5.3}$$

with σ_{ion} and σ_t denoting the ionic and total conductivity, respectively.

Empirically, temperature dependence of the conductivity can be defined as presented in equation (5.4) of the form;

$$\sigma T = A\exp\left(-\frac{E_a}{kT}\right) \tag{5.4}$$

where A is a constant, E_a is the activation energy of the oxide ion, k is the Boltzmann constant (= 8.617 x 10^{-5} eV K^{-1}), and T is the absolute temperature (in K).

In this research, sample pellets of $MgZr_4P_6O_{24}$, $MgHf_4P_6O_{24}$, $MgCe_4P_6O_{24}$ solid-state electrolytes together with the corresponding solid-state solutions, were subjected to series of conductivity measurement using electrochemical impedance spectroscopy. The impedance spectroscopy, relationship between conductivity and temperature, and frequency were equally considered. Electrical properties in electroceramics are usually achieved with either the two-probe or four-probe direct current (dc)-electrical analysis [176]. The alternating current (ac)-impedance method, operating as an electrochemical impedance spectroscopy (EIS), serves as an alternative method for resolving electrical measurements of solid-state electroceramics with contributions from the grain interior, grain boundaries, and electrode-electrolyte interface. Electrochemical impedance is usually determined from semicircles, corresponding to a lumped RC combination. In an electrochemical impedance analysis, when more than one semicircle is observed, it relates to the grain boundary at low frequency regions, depending on structures of the solid-state materials, and in other situation, it can also mean a second phase situation.

However, the inclined spike at 45^o observed as the electrode-electrolyte interface in the low frequency region of Nyquist plots can be attributed to a polarisation effect or simply put, the electrode effect [84]. Moreso, the impedance, Z of RC circuit [217] is defined as shown in equation (5.5);

$$Z(\omega) = R_s - i(\omega C_s)^{-1} \tag{5.5}$$

where R_s and C_s are the equivalent series resistance and capacitance, respectively, ω is the frequency, and i as the imaginary quantity. When RC are in equivalent parallel circuit, the corresponding R_p and C_p circuits are defined as,

$$R_p = \frac{1 + \omega^2 R_s^2 C_s^2}{\omega^2 R_s C_s^2} \tag{5.6}$$

$$C_p = \frac{C_s}{1 + \omega R_s^2 C_s^2} \tag{5.7}$$

Conductivities of platinised pellets solid-state electrolytes were calculated from;

$$\sigma = \frac{t}{ZA} \tag{5.8}$$

where t, A are known as the thickness and cross-sectional area, respectively. Z is the impedance of the solid-state electrolytes, which are obtained from the ac-impedance measurement after fitting appropriate equivalent circuits to the data.

5.2 Conductivity Measurement

5.2.1 Impedance analysis ($MgZr_4P_6O_{24}$)

Electrochemical impedance analysis of a platinised $MgZr_4P_6O_{24}$ solid-state electrolyte pellets in Figure 5.1 shows the electrical properties of Mg^{2+}-cation conducting species, in $MgZr_4P_6O_{24}$ solid-state electrolytes measured with two-probe method at 197-764°C temperature range and from 100mHz to 32MHz. The ac-impedance method was used in this research to resolve the electrical measurements with contributions from the grain interior, grain boundaries and electrode-electrolyte interface. However, Figure 5.1(a) and Figure 5.1(b) demonstrates impedance measurements at both the low and high-temperature regions through an ac-impedance spectroscopy method. The electric modulus in Figure 5.1 shows the points of relaxation for impedance measurements at different temperatures suggesting a conduction mechanism that is thermally activated type of a correlated hopping of Mg^{2+}-cations. The impedance spectra in Figure 5.1(a) however shows a single slightly depressed semicircle at higher frequency followed by the low frequency spike inclined at 45°, and the border frequency, f_b separating both the high and low-frequency regions, was observed at frequency region 50.7kHz and 12.7kHz, respectively, for low- and high-temperature impedance. The inclined spike at low frequencies of $MgZr_4P_6O_{24}$ solid-state electrolyte Nyquist plot defines it as an ionic conductor [179, 218] and the slightly depressed semicircle attributed to constant phase element, CPE appears to suggest the non-Debye relaxation type [219], similar to the solid-state electrolytes reported earlier [220], since the centre of the depressed semicircle is located below the real axis. However, the inclined spike in low-frequency region is also believed to be attributed to polarisation effect at the electrode-electrolyte interface [84]. The semicircle in Figure 5.1(a) and Figure 5.1(b) can also be expressed in terms of an equivalent circuit built from a combination of the resistance, R_p and capacitance, C_p with a CPE relation [221] as presented in equation (5.9);

$$Z = \frac{1}{C(j\omega)^n} \tag{5.9}$$

In using the CPE relation in equation (5.9), C representing an ideal capacitance iff n = 1, j = $(-1)^{1/2}$ and ω is the angular frequency. In real terms, the equivalent circuit consists of a series combination of parallel RC circuit elements and a series resistor, R_s. Grain resistance denotes a lumped resistance, while grain boundary resistance is represented by a resistance attached in parallel to a capacitor [222].

LT region (390-391°C)

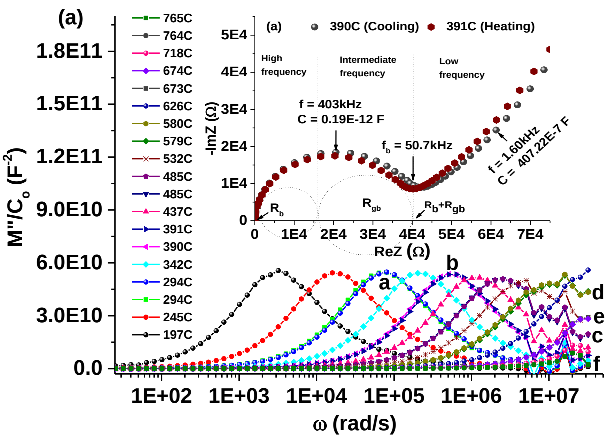

HT region (764-765°C)

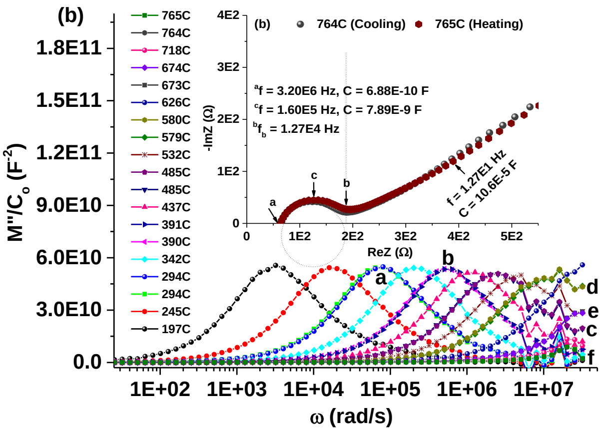

Figure 5-1 Nyquist plots and electric modulus of $MgZr_4P_6O_{24}$ compound measured at (a) 390°C-391°C (b) 764°C-765°C temperature range at various temperatures in the frequency range 100mHz - 32MHz. *f_b is border frequency of the Nyquist plots. *a-f showing reproducibility behaviour of the solid-state electrolytes

As impedance analysis temperature increases from 390°C to 764°C, the depressed bulk semicircle gradually became smaller relative to the inclined spike. This shows that as bulk resistance, R_b is decreasing, the reversibility of charge migration of the electrode-electrolyte, interface is increasing [223]. The semicircle in Figure 5.1(b) however, started off the origin indicating there is a finite resistance, R_s representing lumped electrode-electrolyte interfacial resistance in series with a parallel combination of R_b and CPE_b which represents a grain resistance and constant phase element as presented in Figure 5.1(c);

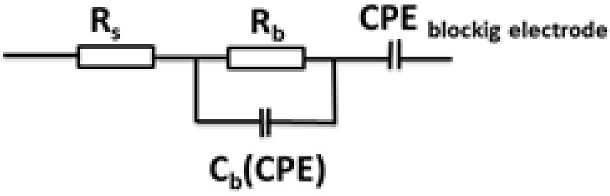

Figure 5-1(c) Equivalent circuit of $MgZr_4P_6O_{24}$ sample measured at 390-391°C, and 764-765°C

The capacitance, C of the solid-state electrolyte was calculated at different temperature as outlined in Figure 5.1, using frequency, f at the maximum point of the semicircle. In using the relation, $C = (2\pi fR)^{-1}$ where f and R represent the frequency and resistance of electroceramics, the capacitance and related interpretation is outlined in Table 5.2:

Table 5-2 Capacitance values and their possible interpretation

Solid-State Electrolyte	Frequency (Hz)	Resistance (Ω)	Capacitance (F)	Phenomenon Responsible [179]
$MgZr_4P_6O_{24}$ (390-391°C)	4.03×10^5	2.08×10^6	0.19×10^{-12}	bulk
45° electrode spike	1.60×10^3	2.44×10^1	407.22×10^{-7}	sample-electrode interface
$MgZr_4P_6O_{24}$ (764-765°C)	3.20×10^6	7.23×10^1	688.0×10^{-12}	bulk
	1.60×10^5	1.26×10^2	7.89×10^{-9}	grain boundary
45° electrode spike	1.27×10^1	11.82×10^1	10.6×10^{-5}	sample-electrode interface

5.2.2 Temperature dependence of ionic conductivity

In thermally activated processes, temperature dependence of conductivity is expressed by the Arrhenius relation in equation (5.10)

$$\sigma T = \sigma_o(T)\exp\left(-\frac{E_a}{kT}\right) \qquad (5.10)$$

where $\sigma_o(T)$ represent the pre-exponential factor which is a function of charge carrier concentration, temperature and material structural parameters, k known as Boltzmann constant (8.617 x 10^{-5}eVK^{-1}), E_a is the activation energy of conduction and T is the temperature (in K). It can be deduced form Arrhenius equation (5.10) that conductivity profile follows the exponential relation $\sigma \propto \exp\left(-\frac{1}{T}\right)$ whereas, the activation energy, E_a can be calculated from the slope which in itself is determined by linear regression analysis. The slope therefore corresponds to the relation in equation (5.11);

$$\text{slope} = -\frac{E_a}{1000k} \qquad (5.11)$$

where k (= 8.617 x 10^{-5} eVK^{-1}) is the Boltzmann constant and E_a(eV) is the activation energy which is a measure of energy barrier to ion transport.

The linearity plot presented in Figure 5.2 shows ionic conductivity of $MgZr_4P_6O_{24}$ solid-state electrolyte at different temperatures. The linearity of the plot suggests there is no significant phase changes within 197-764°C temperature range of measurement. This also suggest $MgZr_4P_6O_{24}$ solid-state electrolytes as a good ionic conducting material. The activation energy, E_a was determined from the gradient of Arrhenius plot by fitting the ionic conductivity data with the Arrhenius equation as presented in equation (5.12);

$$\sigma_t T = A\exp\left(-\frac{E_a}{kT}\right) \qquad (5.12)$$

where σ_t is the total conductivity, A is the pre-exponential factor, E_a is the activation energy of conduction, k is the Boltzmann constant and T is temperature (in K).

Based on the relation in equation (5.12) and the data of this research, ionic conduction as a thermally activated transport, shows that conductivity increases exponentially as temperatures increase. Therefore, in this research, $MgZr_4P_6O_{24}$ solid-state electrolyte shows a bulk conductivity of 7.23 x 10^{-3} Scm^{-1} at 725°C, which is a slight improvement on 6.92 x 10^{-3} Scm^{-1} at 800°C achieved in an earlier research [224]. The activation energy, E_a of the solid-state electrolyte, calculated from the slope of $\ln\sigma_{dc}T$ - $1000T^{-1}$ in Figure 5.2 equates to 0.84±0.04eV. It shows that $MgZr_4P_6O_{24}$ solid-state electrolyte with low E_a (0.84±0.04eV), provides a shorter profile of Mg^{2+}-cation mobility thereby resulting in an improved conductivity (7.23 x 10^{-3} Scm^{-1}).

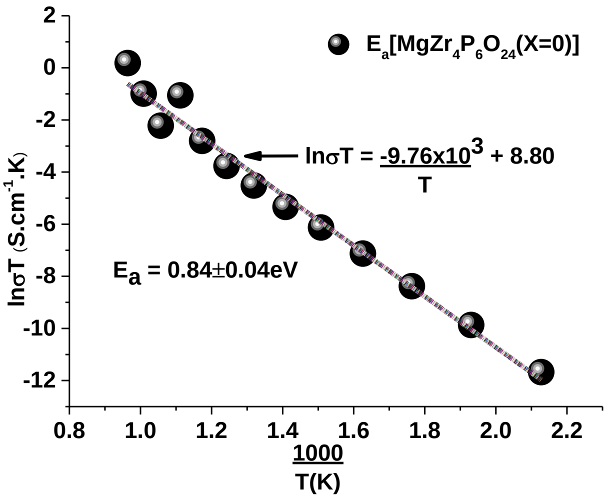

Figure 5-2 Bulk ionic conductivity of $MgZr_4P_6O_{24}$ solid-state electrolyte as a function of temperature

5.2.3 Frequency dependence of ionic conductivity

Frequency dependence of real impedance (ReZ) for $MgZr_4P_6O_{24}$ solid-state electrolyte at different temperatures is presented in Figure 5.3. The ionic conductivity dispersion plots of $MgZr_4P_6O_{24}$ solid-state ceramic electrolyte shows three regions of interest in this research;

i. low-frequency dispersion,
ii. intermediate-frequency plateau, and
iii. extended dispersion at high frequency [225-228].

The low-frequency dispersion regions in ionic conductivity corresponds to electrode polarisation at the electrode-electrolyte interface [84]. At this frequency, the ionic conductivity of $MgZr_4P_6O_{24}$ solid-state electrolyte is high enough to accumulate a significant amount of charge at the electrode-electrolyte interface, which reduces the effective applied field across the measured sample resulting in possible conductivity [195, 229, 230].

Intermediate-frequency plateau represents the dc-conductivity and does not depend on frequency, but on temperature, which agrees excellently with conductivity relationship as shown in Figure 5.2. The switch over from the intermediate-frequency region to the extended dispersion region at high frequency, signals onset of conductivity relaxation, which shifts toward higher frequencies as the temperature increases, representing ac-ion conductivity. The observed dispersion of this conductivity with frequency agrees with the prediction of the jump relaxation model in solid-state electrolytes [231]. According to this model, as frequencies tend to zero ($f \rightarrow 0$), ion can jump from one site to another neighbouring vacant site which contributes to ionic conductivity [231]. However, at high frequencies, the probability of the ion to jump back to its initial site increases due to the available short time frame. The high probability for the correlated forward-backward hopping at high frequencies together with the relaxation of the dynamic cage potential is responsible for the high frequency dispersion [232]. In any case, since the crossover frequency is temperature dependent, it could be observed in Figure 5.3 that crossover frequencies, ω_P, shift towards high-frequency as temperature increases. Meanwhile, the logarithmic plot between dc-conductivity and crossover frequency, ω_P, in Figure 5.3 insert gives a slope of unity which agrees excellently with conductivity formalism [231], which implies that both dc- and ac-conductions are closely correlated and that they are of the same mechanism [233]. Alternatively, the characteristic angular frequency, ω_P, is activated with the same thermal activation energy as dc-conductivity [230, 231, 233, 234].

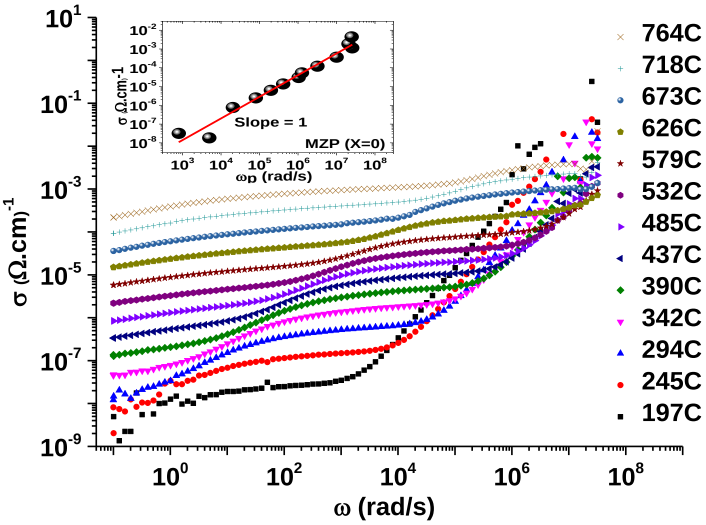

Figure 5-3 Ionic conductivity dispersion plots of $MgZr_4P_6O_{24}$ solid-state electrolyte at various temperatures. Insert is a plot of logσ vs logω_p

At high-frequency dispersion, angular frequency-dependent ionic conductivity, $\sigma_{ac}(\omega)$ increases and this is well described by the Jonscher universal power law [227, 235] as shown in equation (5.13)

$$\sigma_{ac}(\omega) = \sigma_{dc} + A\omega^n \tag{5.13}$$

where $\sigma_{ac}(\omega)$ is the ionic conductivity, σ_0 is the limiting zero frequency conductivity (σ_{dc}) of the electrolytes, A is the pre-exponential constant, $\omega = 2\pi f$ is the angular frequency and n is the power law exponent which represents the degree of interaction between the mobile ion and is less than 1 ($0 < n < 1$) [228]. The value of n is extracted from the slope of log$\sigma_{ac}(\omega)$ versus logω when $\sigma_0 \rightarrow$ zero. Therefore, the conductance spectra in Figure 5.3 shows that when measurement temperature increases, transition from the dc-conductivity plateau to ionic conductivity dispersion region shift towards higher frequency range (10^3-10^7 rad/s). However, at high frequencies, conductance spectra at different temperatures converge thus indicating that ionic conductivity is independent of temperature at high frequencies [236-239].

A comparison of dc-conductivity from the intermediate-frequency plateau with ionic conductivity using Arrhenius relation is presented in Figure 5.4. The close correlation in the total conductivity connotes that the conduction is from the same majority charge carrier, Mg^{2+}-cation, and that the composite solid-state electrolyte is purely ionic. This further suggest a transport number, $t_{ion} > 0.99$ for Mg^{2+}-cation in $MgZr_4P_6O_{24}$ solid-state electrolyte as well as their comparable activation energy, $E_a(ac) = 0.84\pm0.004eV$ and $E_a(dc) = 0.87\pm0.004eV$.

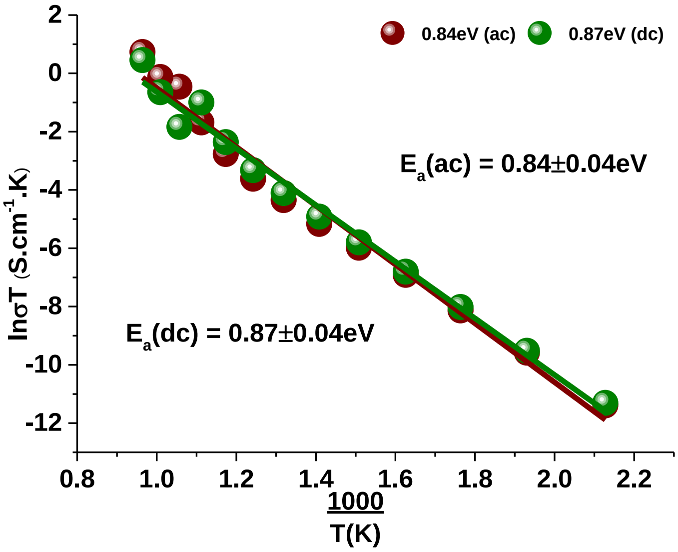

Figure 5-4 Comparison of dc-conductivity extracted from the low-frequency plateau with ionic conductivity of $MgZr_4P_6O_{24}$ solid-state ceramic electrolyte calculated using Arrhenius equation

5.2.4 Impedance analysis ($MgHf_4P_6O_{24}$)

Impedance analysis of $MgHf_4P_6O_{24}$ solid-state electrolyte as illustrated in Figure 5.5 demonstrate the electrical properties of Mg^{2+}-cation conducting specie in $MgHf_4P_6O_{24}$ solid-state electrolyte. Figure 5.5 however, identifies contribution from grain interior, grain boundary and electrode-electrolyte interface in the high, intermediate and low frequencies region of the Nyquist plots for impedance analysis [182]. The impedance spectra is measured at the 182-747°C and 100mHz-32MHz temperature and frequency range, respectively. The bulk and grain boundary resistance of the measured sample pellet is denoted as R_b and R_{gb}, respectively. The impedance spectra in Figure 5.5(a) however, shows a single slightly depressed semicircle at higher-frequency followed immediately by the low-frequency spike inclined at angle of 45°. The appearance of such an inclined spike at low-frequencies therefore demonstrates the measured sample $MgHf_4P_6O_{24}$ as an ionic conductor like the $MgZr_4P_6O_{24}$ sample pellets [179, 218]. The slightly depressed semicircle in Figure 5.5 is attributed to the CPE parameter and it appears to suggest non-Debye type of relaxation behaviour [219] since the centre of the depressed semicircle is located below the axis, which is similar to other solid-state electrolytes [220], in particular the $MgZr_4P_6O_{24}$ solid-state electrolyte characterised in this research. Furthermore, the real impedance, ReZ(Ω) obtained from intersection of semicircle at a lower frequency with the x-axis, corresponds to the dc resistance. Also, the observed slightly depressed semicircle can result from the ionic migration in the bulk of solid-state electrolyte which is indicative of sintered sample pellets confirming the absence of grain boundary effects. Meanwhile, inclined spike in the low-frequency region may be attributed to the polarisation effect at the electrode-electrolyte interface [84], which is similar to the outcome of $MgZr_4P_6O_{24}$ impedance analysis. The border frequency, f_b in Figure 5.5 corresponds to 6.38kHz, 1.60kHz and 2.02kHz for the solid-state electrolyte at 273°C, 690°C and 747°C, respectively.

To research the relaxation dynamics of ionic species, the electric modulus formalism in Figures 5.5(a) and Figure 5.5(b) was used. The variations of imaginary component (M''/C_o) as a function of frequency (ω) at different temperatures show clearly resolved peaks at unique peak frequencies, with the peaks showing a tendency to shift towards a higher frequency region with an increase in temperature. This behaviour suggests a conduction mechanism which is a thermally activated type of correlated hopping of Mg^{2+}-cations. Reproducibility mechanism can be found in Figure 5.5(a) considering that no clear temperature profile deviation was observed at 273-275°C.

LT region (273-275°C)

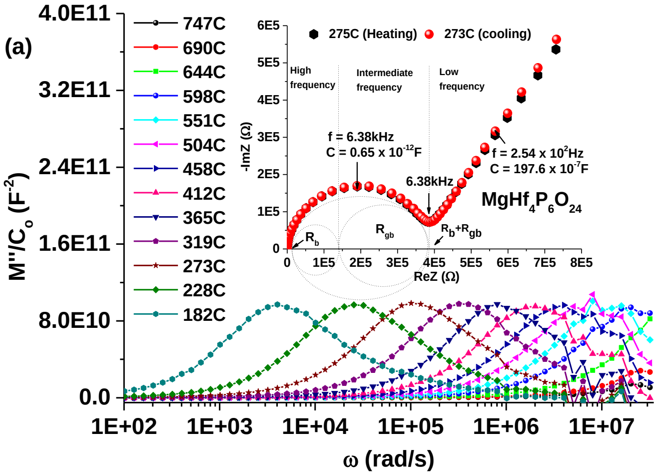

HT region (690°C and 747°C)

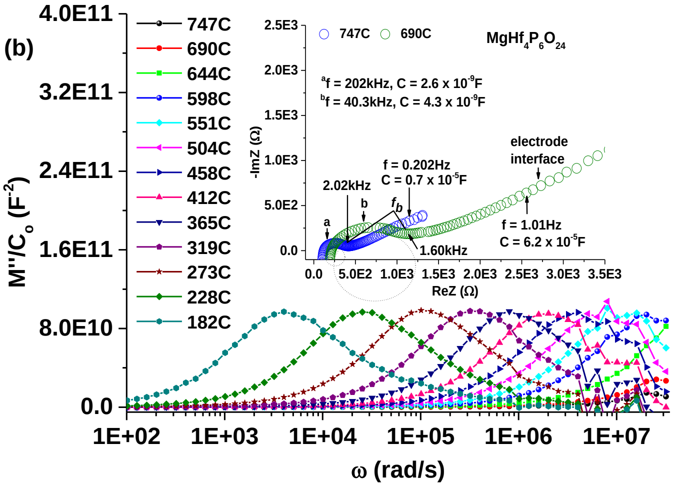

Figure 5-5 Nyquist plots and electric modulus of $MgHf_4P_6O_{24}$ compound at (a) 273-275°C (b) 690°C and 747°C temperatures in the 100mHz-32MHz frequency range

As impedance temperature increases from 273°C in Figure 5.5(a) to 690°C and then 747°C in Figure 5.5(b), the depressed bulk semicircle gradually becomes smaller and, the inclined spike on the electrode-electrolyte interface gradually bent downward to become a depressed semicircle. This implies that as R_b is decreasing the reversibility of charge migration at electrode-electrolyte interface is increasing [223]. Furthermore, the semicircles observed in Figure 5.5(b) are not starting from the origin which means there is a finite resistance (R_s) representing a lumped electrode-electrolyte interfacial resistance in series with a parallel combination of R_b and CPE_b thereby representing a grain resistance and constant phase element, CPE as shown in the equivalent circuit in Figure 5.1(c).

Several points were deduced from Figure 5.5; the calculated value of the capacitance of the Nyquist plots of $MgHf_4P_6O_{24}$ solid-state electrolyte at different temperatures using frequency at the maximum point of the semicircle in Figure 5.5(a) and Figure 5.5(b) is illustrated in Table 5.3:

In using the relationship, $C = (2\pi fR)^{-1}$ where f and R are considered the frequency and resistance of the solid-state electrolyte electroceramic circuit;

Table 5-3 Capacitance values and their possible interpretation

Solid-State electrolyte	Frequency (Hz)	Resistance (Ω)	Capacitance (F)	Phenomenon Responsible [179]
$MgHf_4P_6O_{24}$ (273°C)	6.38×10^3	3.85×10^5	0.65×10^{-12}	bulk
45° electrode spike	2.54×10^2	3.17×10^5	197.6×10^{-7}	sample-electrode interface
$MgHf_4P_6O_{24}$ (690°C)	40.3×10^3	9.18×10^2	4300×10^{-12}	bulk
45° electrode spike	0.101×10^1	2.54×10^3	6.2×10^{-5}	sample-electrode interface
$MgHf_4P_6O_{24}$ (747°C)	2.02×10^5	3.03×10^2	2600×10^{-12}	bulk
45° electrode spike	2.02×10^{-1}	11.47×10^2	0.7×10^{-5}	sample-electrode interface

5.2.5 Temperature dependence of ionic conductivity

The ionic conductivity of $MgM_4P_6O_{24}$ (when M = Hf, Zr) solid-state electrolytes as a function of temperature is shown in Figure 5.6. In this analysis, ionic conductivity of both the $MgHf_4P_6O_{24}$ and $MgZr_4P_6O_{24}$ electrolytes were measured and compared, with the prior knowledge that they belong to the same periodic group and haven shown the potential of being used interchangeably in structural and electrochemical applications. However, in Figure 5.6, several points are outlined; firstly, the linearity of the plots suggest there are no significant structural and phase changes noticed in the impedance temperature range. This further shows therefore $MgHf_4P_6O_{24}$ and $MgZr_4P_6O_{24}$ solid-state electrolytes as comparable ionic conducting samples. The activation energy, E_a which includes the energy of the formation and migration of ions in the solid-state electrolytes were determined from the gradient of Arrhenius plots by fitting the ionic conductivity data with Arrhenius equation as shown in equation (5.10).

Ionic conduction is a thermally activated transport, the conductivity of both samples increases exponentially as temperatures increase. $MgHf_4P_6O_{24}$ and $MgZr_4P_6O_{24}$ solid-state electrolytes therefore exhibit the conductivity data of 4.52×10^{-4} Scm^{-1} at 747^oC and 7.23×10^{-3} Scm^{-1} at 725^oC, respectively. However, the bulk activation energy, E_a of $MgHf_4P_6O_{24}$ and $MgZr_4P_6O_{24}$ electrolytes in Figure 5.6 deduced from the slope of $\ln\sigma_{dc}T$ - $1000T^{-1}$ plots are 0.74±0.02eV and 0.84±0.04eV, respectively. Therefore, the $MgHf_4P_6O_{24}$ solid-state electrolyte with lower $E_a = 0.74\pm0.02eV$ has a higher mobility of Mg^{2+}-cations but exhibit a lower conductivity ($\sigma_{ac} = 4.52 \times 10^{-4}$ Scm^{-1}) at 747^oC while $MgZr_4P_6O_{24}$ solid-state electrolyte with higher $E_a = 0.84\pm0.04eV$ exhibiting a higher conductivity ($\sigma_{ac} = 7.23 \times 10^{-3}$ Scm^{-1}) at 725^oC. The conductivity data of both samples in Figure 5.6 therefore shows that $MgZr_4P_6O_{24}$ measured between $197\text{-}725^oC$ is a better-conducting solid-state electrolyte than $MgHf_4P_6O_{24}$ measured between $182\text{-}747^oC$ temperature range. However, the $MgHf_4P_6O_{24}$ sample remains chemically more stable at high-temperatures compared to the $MgZr_4P_6O_{24}$ [24]. Moreso, the crossover point in Figure 5.6 for the bulk ionic conductivity is 394^oC. This suggest therefore that $MgZr_4P_6O_{24}$ is a marginally better ionic conductor than $MgHf_4P_6O_{24}$ electrolyte at temperatures greater than 394^oC whereas, at temperatures below 394^oC, $MgHf_4P_6O_{24}$ is better than $MgZr_4P_6O_{24}$. This could be due to the enhancement of ionic conductivity due to space-charge region effect [240] since $MgZr_4P_6O_{24}$ is a composite electrolyte whereas $MgHf_4P_6O_{24}$ is a single phase solid-state electrolyte.

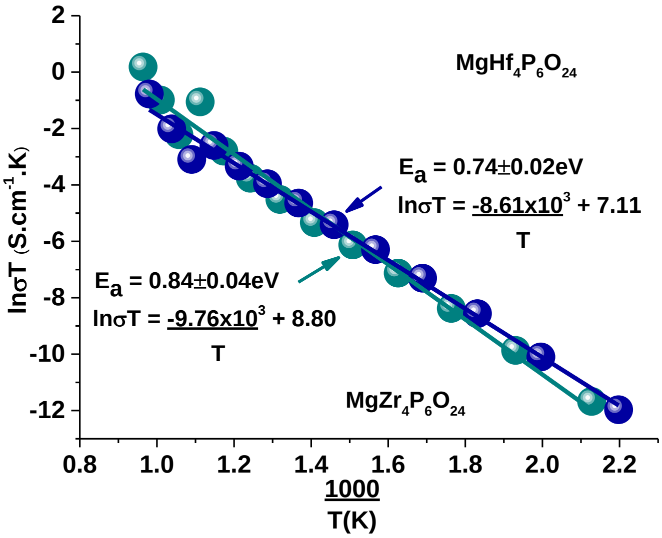

Figure 5-6 Bulk ionic conductivity of $MgHf_4P_6O_{24}$ and $MgZr_4P_6O_{24}$ solid-state electrolytes as a function of temperature

5.2.6 Frequency dependence of ionic conductivity

Figure 5.7 illustrates the characteristic frequency dependence of the real impedance, ReZ for $MgHf_4P_6O_{24}$ at different temperatures. The spectral analysis of Figure 5.7 and Figure 5.3 agrees showing that both materials can be used interchangeably within the impedance temperature range measurement. In comparison with $MgZr_4P_6O_{24}$, the low frequency dispersion, intermediate frequency plateau and extended dispersion at high frequency characterised the ionic conductivity dispersion of $MgHf_4P_6O_{24}$ [225-228]. The low-frequency dispersions in ionic conductivity arise from electrode polarisation; at these frequencies, ionic conductivity of the sample is highly activated to accumulate a significant amount of charge at the electrodes, which reduces the effective applied field across the measured samples and hence the apparent conductivity [208].

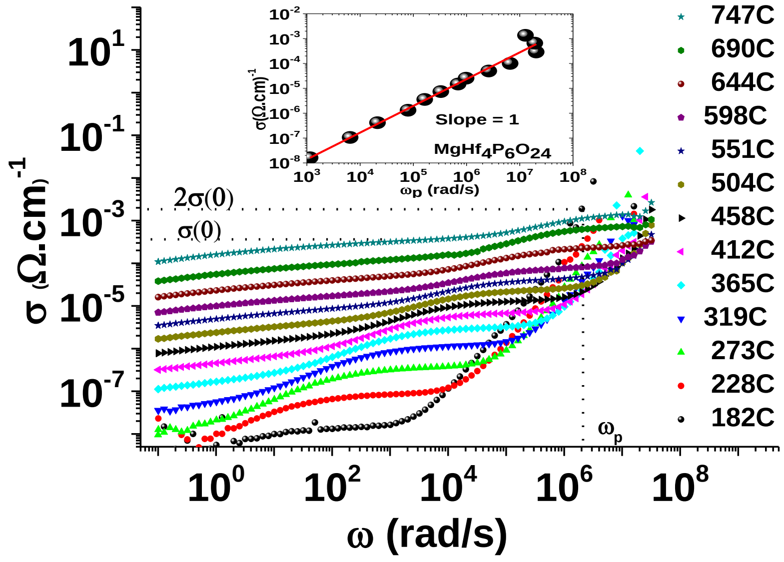

Figure 5-7 Ionic conductivity dispersion plots of $MgHf_4P_6O_{24}$ solid-state electrolyte compound at various temperatures. Insert is a plot of $\log\sigma$ vs $\log\omega_p$

At the intermediate-frequency plateau region, the conductivity does not depend on frequency, and the value of conductivity at the plateau region agrees substantially with the ionic conductivity plots in Figure 5.6. The switch over from frequency independent region to the frequency dependent region signals the onset of conductivity relaxation, which shifts toward higher frequencies as the temperature increases. The observed dispersion of conductivity with frequency is in general agreement with the prediction of the jump relaxation model in solid-state electrolytes [71]. According to this model, at very low frequencies, when frequency tend to zero, an ion can jump from one site to its neighbouring vacant site which successfully contributes to ionic conductivity. At high frequencies however, the probability for the ion to jump back to its initial site increases due to the short time periods available. High probability for the correlated forward-backward hopping at high frequencies together with the relaxation of the dynamic cage potential is responsible for the high frequency dispersion observed in $MgZr_4P_6O_{24}$ and $MgHf_4P_6O_{24}$ solid-state electrolyte [241].

Figure 5.8 describes a comparison of dc-conductivity obtained from the intermediate-frequency plateau with ionic conductivity analysis for $MgHf_4P_6O_{24}$ and $MgZr_4P_6O_{24}$

solid-state electrolytes. Furthermore, the conductivity behaviour of $MgHf_4P_6O_{24}$ solid-state electrolyte displays the tendency of the electrolyte exhibiting a total conductivity comparable to the $MgZr_4P_6O_{24}$ composite solid-state electrolyte [24] which is ionic.

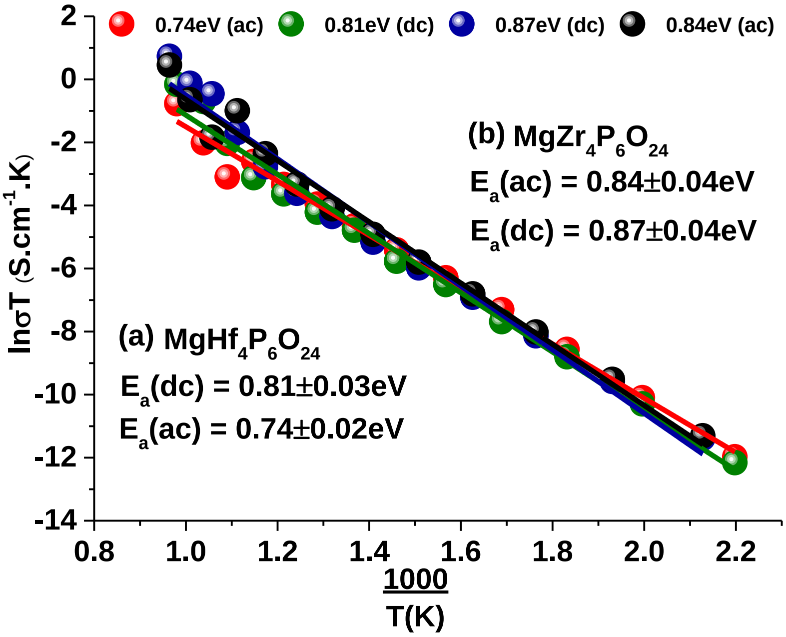

Figure 5-8 Comparison of dc-conductivity obtained from the low-frequency plateau with ionic conductivity of $MgHf_4P_6O_{24}$ and $MgZr_4P_6O_{24}$ solid-state electrolyte using the Arrhenius equation

5.2.7 Impedance analysis ($MgCe_4P_6O_{24}$)

In general, impedance spectroscopy entails the measurement of complex quantity, Z* (impedance) of platinised pellets as a function of angular frequency. The description of impedance is as shown;

$$Z^* = \frac{U(\omega)}{I(\omega)} = /Z/e^{i\varphi} = Z' - iZ'' \qquad (5.14)$$

Measurements of magnitude /Z/ and phase φ allows the computation of the real (Z') and imaginary (Z'') part of impedance, and this which are plotted against each other in the impedance spectra as a function of frequency.

Electrochemical impedance spectroscopy is a technique for investigating the electrical properties of solid-state electrolytes. Impedance of an ionic conductor measured by a two-probe method contain contributions from the grain interior, grain boundaries and electrode-electrolyte interface. Figure 5.9 shows impedance spectra for $MgCe_4P_6O_{24}$ in the frequency range 100mHz-32MHz at various temperatures ranging between 94-744°C. The impedance spectra in Figure 5.9 shows double depressed semicircles at high and intermediate frequencies with no visible presence of the low frequency spike inclined at 45°. The semicircles observed in Figure 5.9 can be presented in the form of an equivalent circuit using a combination of resistance and capacitance, R_b, C_b and R_{gb}, C_{gb} with the constant phase element (CPE) behaviour. However, the capacitance, $C = 9.2 \times 10^{-12}$ F and $C = 4.9 \times 10^{-9}$ F for high and intermediate frequency semicircles, respectively, defines the high-frequency semicircle as a displaying bulk phenomenon whereas, the intermediate frequency portrays a grain boundary phenomenon.

LT region (184-186°C)

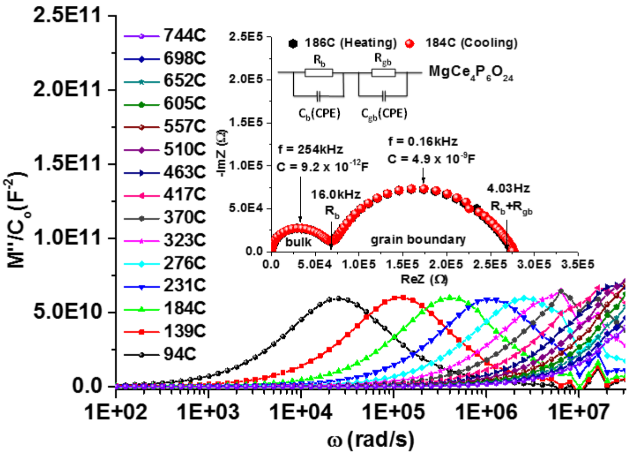

Figure 5-9 Nyquist plot and Electric modulus of $MgCe_4P_6O_{24}$ solid-state electrolyte at various temperatures in the frequency range 100mHz-32MHz. Insert is equivalent circuit

The electric modulus in Figures 5.9 revealed the relaxation potential of $MgCe_4P_6O_{24}$ at different temperatures. The electric modulus however, display promising relaxation potential at 94-323°C, indicating that the solid-state electrolyte conducts better at low-temperatures. The reproducibility mechanism of the electrolyte at 184-186°C in Figure 5.9 further portrays the electrolyte as highly conducting.

In using $C = (2\pi fR)^{-1}$ where C, f and R represent capacitance, frequency and resistance of the electrolytes, the capacitance can be computed for interpreting the semicircles and their associated resistance.

Table 5-4 Capacitance values and their possible interpretation

Solid-State electrolyte	Frequency (Hz)	Resistance (Ω)	Capacitance (F)	Phenomenon Responsible [179]
$MgCe_4P_6O_{24}$ (184°C)	$2.54x10^5$	$6.79x10^4$	$9.2x10^{-12}$	bulk
	$0.16x10^3$	$2.02x10^5$	$4.9x10^{-9}$	grain boundary

5.2.8 Temperature dependence of ionic conductivity

Figure 5.10 shows the ionic conductivity of $MgM_4P_6O_{24}$ (M = Hf, Ce) end-members solid-state electrolytes as a function of temperature. Several interesting points clearly stand out from the ionic conductivity plots of $MgHf_4P_6O_{24}$ and $MgCe_4P_6O_{24}$ solid-state electrolytes.

The $MgHf_4P_6O_{24}$ electrolyte exhibits an ionic conductivity of 4.52×10^{-4} Scm^{-1} at 747°C whereas, $MgCe_4P_6O_{24}$ electrolyte exhibits 2.14×10^{-3} Scm^{-1} at 744°C. The bulk activation energy E_a of $MgHf_4P_6O_{24}$ and $MgCe_4P_6O_{24}$ electrolytes are 0.74±0.04eV and 0.53±0.02eV, respectively. The $MgCe_4P_6O_{24}$ solid-state electrolyte with lower E_a = 0.53±0.02eV has a higher mobility of Mg^{2+}-cations exhibiting a higher conductivity ($\sigma_{ac} = 2.14 \times 10^{-3}$ Scm^{-1}) at 744°C, while $MgHf_4P_6O_{24}$ solid-state electrolyte with E_a = 0.74±0.04eV, has $\sigma_{ac} = 4.52 \times 10^{-4}$ Scm^{-1} at 747°C. The conductivity data of both electrolytes in Figure 5.10 therefore shows that the $MgCe_4P_6O_{24}$ solid-state electrolyte measured between 94-744°C is a much better conducting electrolyte than $MgHf_4P_6O_{24}$ measured between 182-747°C. However, both solid-state electrolytes sample pellets have displayed very high chemical stability at high-temperatures.

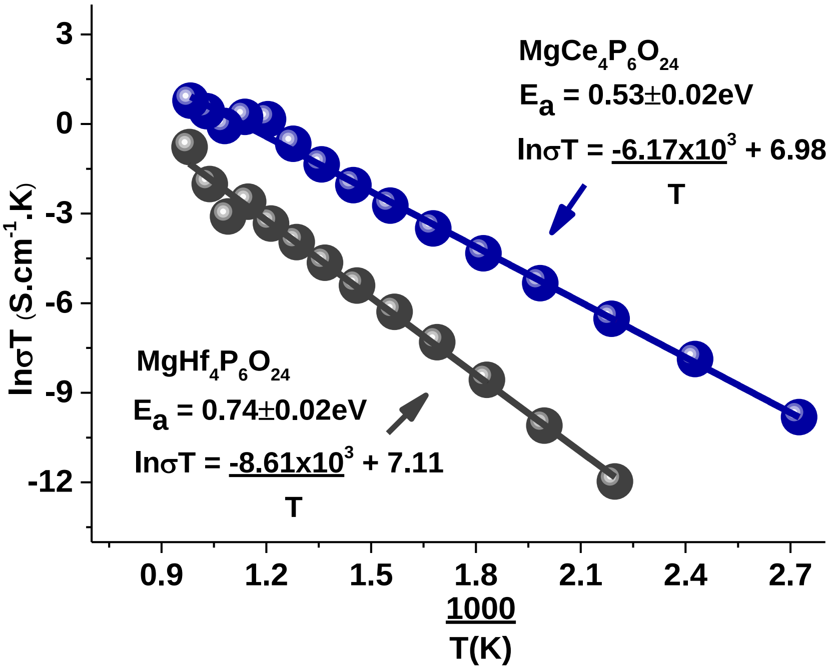

Figure 5-10 Bulk ionic conductivity of both $MgHf_4P_6O_{24}$ and $MgCe_4P_6O_{24}$ solid-state electrolytes as a function of temperature

5.2.9 Frequency dependence of ionic conductivity

Figure 5.11 demonstrates the characteristic frequency dependence of real impedance (ReZ) of $MgCe_4P_6O_{24}$ solid-state electrolytes at different temperatures. The spectral analysis in Figure 5.11 is compared with the spectral of $MgHf_4P_6O_{24}$ and $MgZr_4P_6O_{24}$ electrolytes and it shows clearly that the $MgCe_4P_6O_{24}$ electrolyte possess the potentials of both ionic and electronic conductivity when compared with the other end-members solid-state electrolytes that has shown the capacity to function as an ionic conductor.

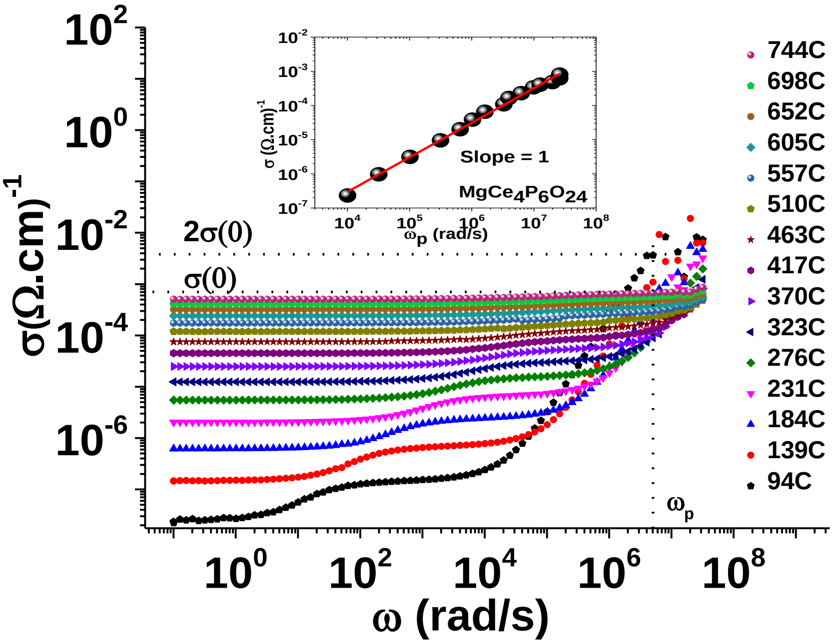

Figure 5-11 Ionic conductivity dispersion plots of $MgCe_4P_6O_{24}$ solid-state electrolyte at various temperatures. Insert is a plot of logσ vs logω_p

Figure 5.12 demonstrates the comparison of a dc-conductivity extracted from the low frequency plateau with ionic conductivity data determined by Arrhenius relation for $MgHf_4P_6O_{24}$ and $MgCe_4P_6O_{24}$ solid-state electrolytes. The conductivity behaviour of $MgHf_4P_6O_{24}$ solid-state electrolyte shows the tendency of the electrolyte exhibiting a total conductivity comparable with $MgZr_4P_6O_{24}$ solid-state electrolyte[24] which is purely ionic, while $MgCe_4P_6O_{24}$ solid-state electrolyte has the potential for both ionic and electronic conductivity [242]. This perhaps, could explain why the measured dc-conductivity of $MgCe_4P_6O_{24}$ solid-state electrolyte is lower than the ionic conductivity data measured on the same solid-state electrolyte with similar activation energy.

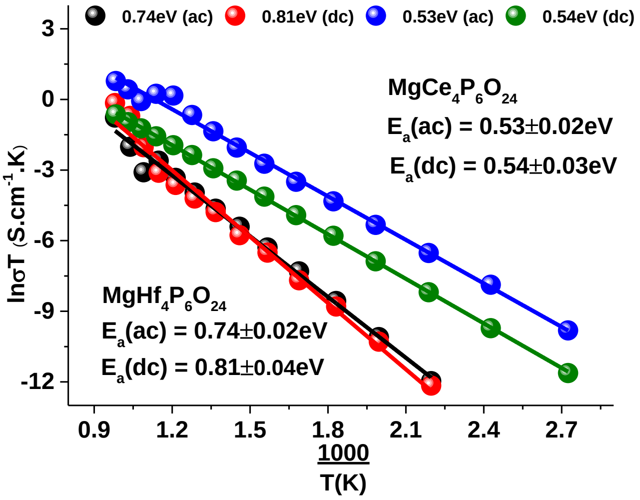

Figure 5-12 Comparison of dc-conductivity obtained from the low frequency plateau with ionic conductivity of $MgHf_4P_6O_{24}$ and $MgCe_4P_6O_{24}$ samples

5.2.10 Comparison of ionic conductivity profiles

Figure 5.13 shows the ionic conductivity profiles of $MgZr_4P_6O_{24}$ (MZP), $MgHf_4P_6O_{24}$ (MHfP), $MgCe_4P_6O_{24}$ (MCeP-1) and $MgCe_4P_6O_{24}$ (MCeP-2). The activation energy, E_a of the conductivity profile of the comparing electrolytes are equally presented as;

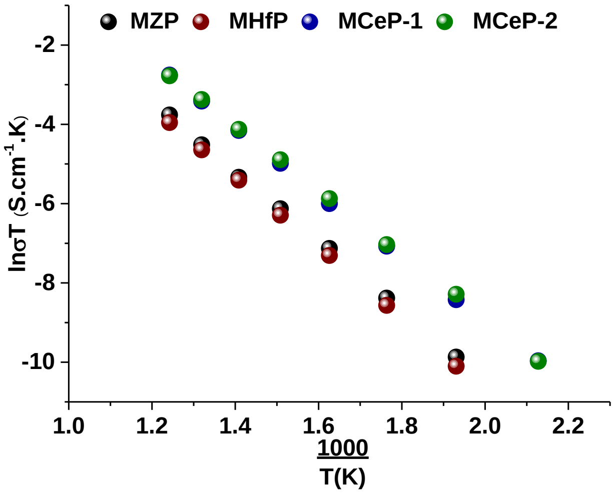

Figure 5-13 Comparison of ionic conductivity profiles of $MgZr_4P_6O_{24}$, $MgHf_4P_6O_{24}$, $MgCe_4P_6O_{24}$ (S1300C) and $MgCe_4P_6O_{24}$ (S1350C) obtained from Arrhenius relation

Figure 5.13 shows the correlation between these electrolytes; the conductivity profiles of $MgZr_4P_6O_{24}$ and $MgHf_4P_6O_{24}$ are believed to be in perfect agreement and their E_a are relatively close too. But, $MgCe_4P_6O_{24}$ (MCeP-1 and MCeP-2) connotes the same solid-state electrolyte, with different sintering temperatures. MCeP-1 was sintered at 1300°C like the $MgZr_4P_6O_{24}$ and $MgHf_4P_6O_{24}$ solid-state electrolytes while, MCeP-2 was then sintered at 50°C more, i.e., 1350°C in order to monitor the conductivity trend within the same electrolyte. Based on the conductivity data reported in Figure 5.13, it shows therefore that sintering temperatures has some direct effect on the conductivity rate of the $MgCe_4P_6O_{24}$ solid-state electrolytes.

Table 5-5 Conductivity profiles and activation energy of $MgZr_4P_6O_{24}$, $MgHf_4P_6O_{24}$ and $MgCe_4P_6O_{24}$ solid-state electrolyte (x = 0, 1)

Solid-State Electrolyte	E_a (eV)	σ_{bulk} (S cm^{-1})	T(K)
$MgZr_4P_6O_{24}$	0.84 ± 0.04	7.23×10^{-3}	998 [24]
$MgHf_4P_6O_{24}$	0.74 ± 0.02	4.52×10^{-4}	1020
MCeP-1	0.53 ± 0.02	1.72×10^{-3}	901
MCeP-2	0.52 ± 0.04	2.14×10^{-3}	1017

5.3 Solid-State Solutions

5.3.1 Temperature dependence of ac-conductivities

The conductivity behaviour of solid-state solutions presented in Figure 5.14 shows a trend at an increasing doping concentration. The comparison between Hf-doping and Ce-doping to the $MgZr_4P_6O_{24}$ solid-state electrolyte provides relevant conductivity trend that influences the conductivity rate of solid-state electrolytes in this research by either creating vacancies or interstitials thereby changing the structural orientation of the electrolytes. Moreso, the $MgZr_{3.6}Hf_{0.4}P_6O_{24}$ and $MgZr_{3.6}Ce_{0.4}P_6O_{24}$ (x = 0.1) solid-state solution demonstrates that the $MgZr_{3.6}Ce_{0.4}P_6O_{24}$ has a better conductivity and E_a than $MgZr_{3.6}Hf_{0.4}P_6O_{24}$. However, as doping increased to x = 0.2, $MgZr_{3.2}Hf_{0.8}P_6O_{24}$ becomes more conducting than $MgZr_{3.2}Ce_{0.8}P_6O_{24}$ with E_a showing improvement from

E_a = 1.02±0.04eV to 0.86±0.03eV, thereby allowing for more mobility of Mg^{2+}-cation in the solid-state solution. Furthermore, the crossover point of $MgZr_{2.8}Hf_{1.2}P_6O_{24}$ and $MgZr_{2.8}Ce_{1.2}P_6O_{24}$ (when x = 0.3) bulk ionic conductivity is at 352°C, whereas, the solid-state solutions, $MgZr_{2.8}Hf_{1.2}P_6O_{24}$ and $MgZr_{2.8}Ce_{1.2}P_6O_{24}$ demonstrates the same ionic conductivity at a temperature lower than 352°C. $MgZr_{2.8}Hf_{1.2}P_6O_{24}$ is however a marginally better ionic conductor at temperatures higher than 352°C and at 727°C, the $MgZr_{2.8}Ce_{1.2}P_6O_{24}$ shows a low conductivity at 441-560°C temperature range, hence, $MgZr_{2.8}Hf_{1.2}P_6O_{24}$ is considered a better material at high-temperatures. As the dopant increases, the $MgZr_{2.4}Hf_{1.6}P_6O_{24}$ (when x = 0.4) becomes a better ionic conductor at increasing temperature, but no defined crossover point between the $MgZr_{2.4}Hf_{1.6}P_6O_{24}$ and $MgZr_{2.4}Ce_{1.6}P_6O_{24}$ electrolytes. The $MgZr_2Hf_2P_6O_{24}$ and $MgZr_2Ce_2P_6O_{24}$ (when x = 0.5), it shows a crossover point at 352°C. $MgZr_2Hf_2P_6O_{24}$ is however a marginally better ionic conductor at temperatures lower than 352°C, than $MgZr_2Ce_2P_6O_{24}$ which is better at temperatures higher than 352°C. As the dopant further increases (x = 0.6), $MgZr_{1.6}Hf_{2.4}P_6O_{24}$ and $MgZr_{1.6}Ce_{2.4}P_6O_{24}$ solid-state solutions demonstrate the same ionic conductivity observed from 227°C to the crossover point at 560°C, therefore, the $MgZr_{1.6}Hf_{2.4}P_6O_{24}$ becomes a marginally better ionic conductor. The behaviour of $MgZr_{1.2}Hf_{2.8}P_6O_{24}$ and $MgZr_{1.2}Ce_{2.8}P_6O_{24}$ solid-state solutions (x = 0.7) shows that the $MgZr_{1.2}Hf_{2.8}P_6O_{24}$ and $MgZr_{1.2}Ce_{2.8}P_6O_{24}$ solid-state solutions have the same ionic conductivity at 283-333°C. However, $MgZr_{1.2}Hf_{2.8}P_6O_{24}$ becomes a better ionic conductor at temperature higher than 333°C. As the solid-state ceramic solutions tend towards their respective solid-state electrolytes end-members, it becomes clearer that $MgZr_{0.8}Ce_{3.2}P_6O_{24}$ and $MgZr_{0.4}Ce_{3.6}P_6O_{24}$ (x = 0.8 and 0.9), respectively are better ionic conductor than their respective Hf-doped at x = 0.8 and 0.9, respectively. The different behaviour by these solid-state solutions described in this research could be largely due to the enhancement of ionic conductivity owing to space-charge region effect [240] by solid-state solutions at corresponding temperatures.

x = 0.1 and x = 0.2

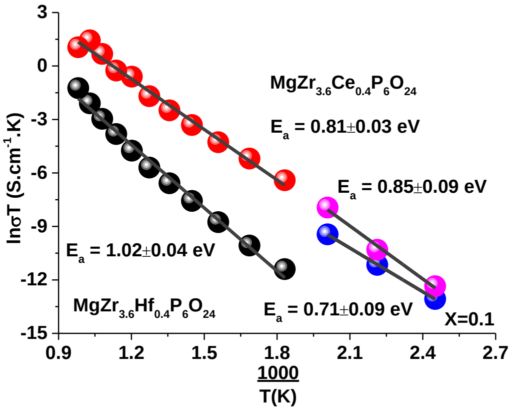

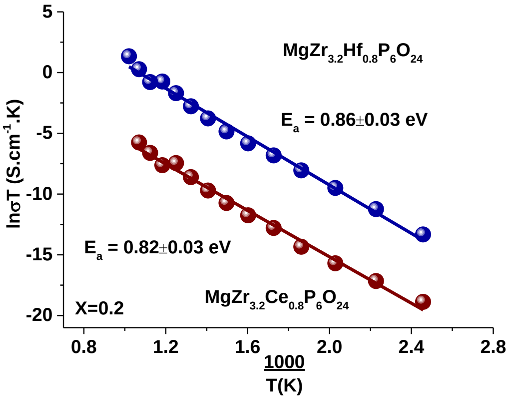

x = 0.3 and x = 0.4

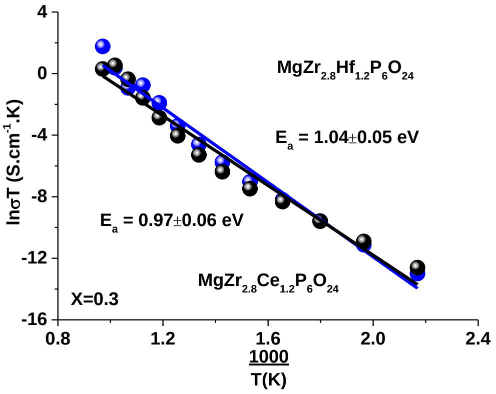

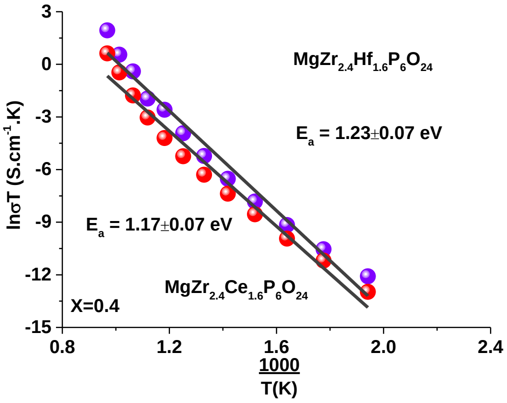

x = 0.5 and x = 0.6

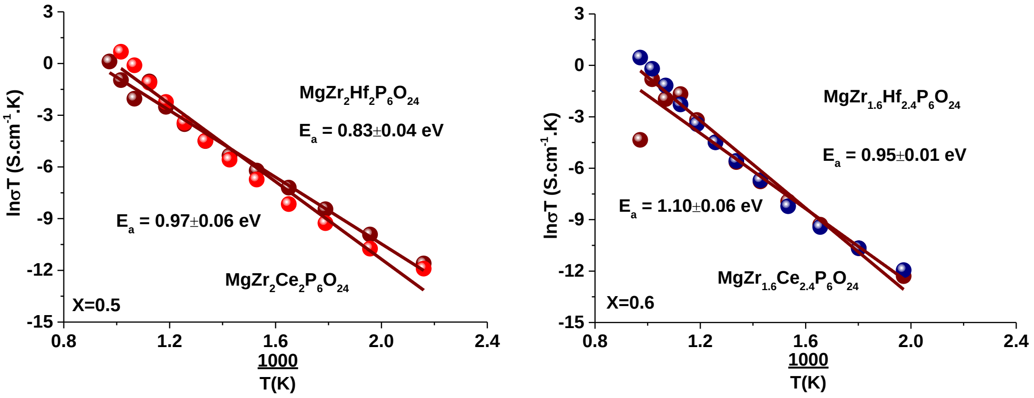

x = 0.7 and x = 0.8

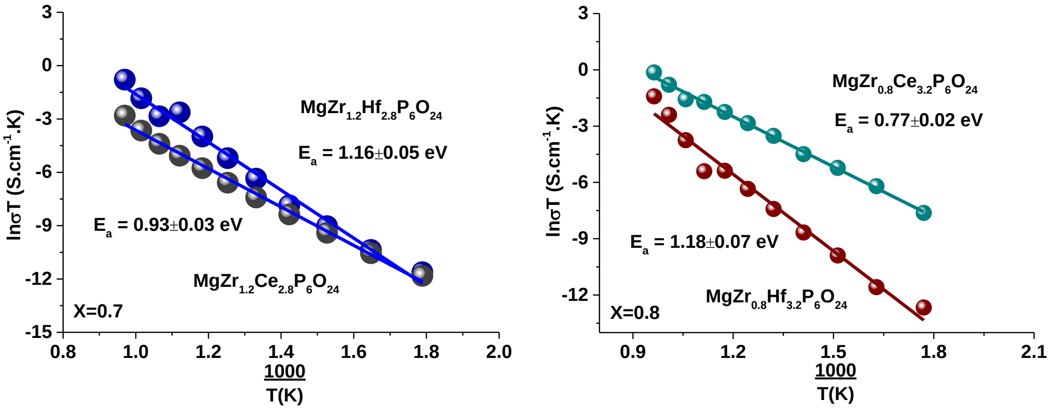

x = 0.9

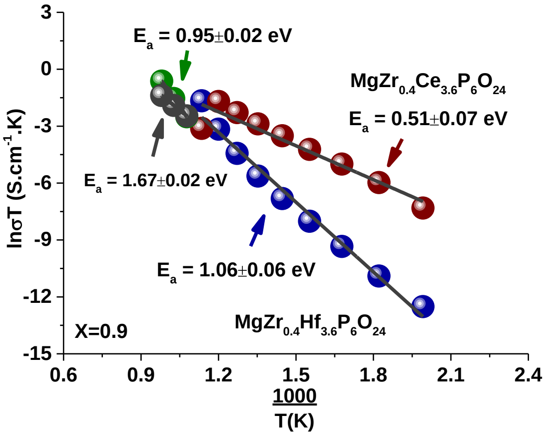

Figure 5-14 Comparison of E_a and ionic conductivity of the $MgZr_{4(1-x)}M_{4x}P_6O_{24}$ solid-state solution series in the composition range $0.1 \leq x \leq 0.9$

5.4 Conclusions

The electrical properties of $MgZr_4P_6O_{24}$, $MgHf_4P_6O_{24}$, $MgCe_4P_6O_{24}$ and the solid-state solutions were characterised for their electrical properties using impedance analysis. This technique provided insight into the resistance of the bulk, R_b and grain boundary, R_{gb} by fitting the Nyquist plots to determine ionic conductivity of the sample pellets.

The impedance measurement of $MgZr_4P_6O_{24}$ electrolyte shows bulk conductivity of a composite electrolyte of pure ionic conductivity at 390-391°C while at 764-765°C, a depressed semicircle not starting from origin indicating there is a finite resistance, R_s which represent a lumped electrode-electrolyte interfacial resistance in series with a parallel combination of R_b and CPE_b. The ionic conductivity derived by the Arrhenius equation and dc-conductivity extracted from the intermediate plateau during spectral analysis tend to agree excellently well considering that their E_a is closely related i.e., $E_a(ac) = 0.84 \pm 0.04eV$ and $E_a(dc) = 0.87\pm0.04eV$.

The impedance analysis of $MgHf_4P_6O_{24}$ solid-state electrolyte is quite similar to the $MgZr_4P_6O_{24}$ solid-state electrolyte because as transition elements, they belong to the same periodic group, hence, they promote the same structural properties. However, $MgHf_4P_6O_{24}$ solid-state electrolyte maintains bulk resistance at 182-747°C, the ac- and dc-conductivities of $MgHf_4P_6O_{24}$ solid-state electrolyte shows $E_a(ac) = 0.74\pm0.02eV$ and $E_a(dc) = 0.81\pm0.03eV$, which is similar to $MgZr_4P_6O_{24}$ solid-state electrolyte with a crossover point at 394°C, showing that the $MgZr_4P_6O_{24}$ has a marginally better ionic conductivity at temperatures greater than 394°C whereas, the $MgHf_4P_6O_{24}$ solid-state electrolyte has a better ionic conductivity at temperatures lower than 394°C.

The impedance analysis of $MgCe_4P_6O_{24}$ shows more than one semicircle at 184-186°C which indicates the presence of bulk and grain boundary resistance. However, the electrolyte is highly conductive with a very low activation energy, $E_a = 0.53\pm0.02eV$.

The solid-state solutions doped respectively with Hf and Ce, shows some consistency in the conductivity of the electrolytes. The E_a of $MgZr_2Hf_2P_6O_{24}$ (0.83±0.04eV) and $MgZr_2Ce_2P_6O_{24}$ (0.97±0.06eV) are quite close showing similar electrical behaviour. The solid-state solutions displaying a crossover point at 352°C shows $MgZr_2Hf_2P_6O_{24}$ as a better ionic conductor at temperatures lower than 352°C while $MgZr_2Ce_2P_6O_{24}$ is a better ionic conductor at temperatures greater than 352°C.

Chapter 6

Thermodynamics Studies and Sensor Testing

6.1 Thermodynamics Studies

6.1.1 Synopsis

The use of galvanic cells to determine thermodynamic properties of ceramic materials by electromotive force (emf) method is described in this research. Two basic types of this method are distinguished: Those employing liquid electrolytes and those based on solid ion-conducting electrolytes. Liquid electrolytes can be aqueous solutions, meanwhile for thermodynamic measurements in metallic materials, molten salt mixtures with the addition of corresponding charge-carrying ion are mostly used. Solid-state electrolytes applied in the thermochemistry of alloys and ceramic materials are usually based on oxides, such as ZrO_2 as O^{2-}-ion conductors, on β- or β''-alumina as Na^+-cation conductors (with the possibility to exchange sodium cations by other cations), or on fluorides, such as CaF_2 as F^{-1}-ion conductors and recently, $MgM_4P_6O_{24}$ (M = Zr, Ti, Hf, Ce) as Mg^{2+}-cation conductor.

In general, three experimental methods for determining the thermodynamic properties of electroceramics and other solid-state materials can be expressed using;

i. calorimetry
ii. vapour pressure measurements

iii. electromotive force (emf).

The emf method however, is deployed in this research because it is considered the most accurate method for determining partial Gibbs energy, ΔG [71, 243]. The solid-state electrolytes for thermodynamic measurements are expected to have the transport number, $t_{ion} \geq 0.99$, this enables the cell to only conduct migrating ions from the solid-state electrolytes while the electrons move through the external circuit. In this research however, the flow has to be stopped to create an open circuit voltage between the two electrodes ($MgCr_2O_4$+Cr_2O_3 and $MgFe_2O_4$+α-Fe_2O_3) of the cell, and this corresponds to the state of thermodynamic equilibrium potential. In order to achieve this, a high impedance measuring device, Keithley 6517A with an internal impedance $> 10^{14}\Omega$ was used to measure the voltage across the open circuit. Furthermore, thermodynamic measurements offer important tool for the determination of compatibility and chemical stability of the various high-temperature electroceramic materials.

Thermodynamic and kinetic measurements are two common types of measurements using the solid-state electrolytes. The use of solid-state electrolytes for thermodynamic measurements by the emf method originates from the work of Kikuola and Wagner [23, 113, 114] and Peters *et al.* [244, 245]. Further, the pioneering work of Kikuola and Wagner [113, 114] encouraged the use of solid oxide and halide electrolytes for measuring thermodynamic properties of electroceramic materials [23, 246]. However, the most used solid-state electrolyte in a previous research is the stabilised zirconia which is an oxide-ion conductor.

6.1.2 Procedure

In this research, $MgM_4P_6O_{24}$ (M = Zr, Hf, Ce) was used as solid-state electrolytes for electrochemical cells. Biphasic power mixtures of $MgCr_2O_4$+Cr_2O_3 and $MgFe_2O_4$+α-Fe_2O_3 were synthesised using the conventional solid-state method and then used as reference electrodes. The $MgCr_2O_4$ and $MgFe_2O_4$ spinel were selected because MgO activity in the spinel are well known [123], therefore, the biphasic powder mixture of $MgCr_2O_4$+Cr_2O_3 and $MgFe_2O_4$+α-Fe_2O_3 were prepared in the 1:1 ratio in order to reduce the activity of MgO in both $MgCr_2O_4$ and $MgFe_2O_4$ spinel, thereby stabilising the working electrode. Some pellets were pressed from the powders, $MgCr_2O_4$+Cr_2O_3

and $MgFe_2O_4$+α-Fe_2O_3 and later sintered at 1090°C for 144h as shown in the previous chapters, the respective phases in the sample powders and pellets were identified using x-ray diffraction analysis as presented in Figure 4.24. Meanwhile, the pellets were not well sintered at 1090°C for 24h long annealing time but they could be used as reference electrode, in as much as the solid-state electrolyte is well sintered. Platinum paste was then applied on one side of the pellets and allowed to dry, then heat treated at 800°C for 0.5h. The other side of the reference electrodes was ground flat to align with the contacting face of the solid-state ceramic electrolyte whereby a perfect connection is established and for the interface reactions to be monitored. The emf measurement rig was inserted into a Faraday cage within a horizontal Lenton LTF 1200 tube furnace shown in Figure 3.22, this procedure ensures shield from any induced Faraday emf.

6.1.3 Measurement

The cell arrangement based on the pellets and reference electrodes were connected according to the notations in cell I - cell III. The sign of the electrodes is indicated in parenthesis;

$$\text{Cell I: } (-)\ O_2,\ MgFe_2O_4+\alpha\text{-}Fe_2O_3/MgZr_4P_6O_{24}/MgCr_2O_4+Cr_2O_3,\ O_2\ (+) \quad (6.1)$$

$$\text{Cell II: } (-)\ O_2,\ MgFe_2O_4+\alpha\text{-}Fe_2O_3/MgHf_4P_6O_{24}/MgCr_2O_4+Cr_2O_3,\ O_2\ (+) \quad (6.2)$$

$$\text{Cell III: } (-)\ O_2,\ MgFe_2O_4+\alpha\text{-}Fe_2O_3/MgCe_4P_6O_{24}/MgCr_2O_4+Cr_2O_3,\ O_2\ (+) \quad (6.3)$$

The electrochemical cell can also be written as;

$$(-)\ O_2,\ MgFe_2O_4+\alpha\text{-}Fe_2O_3/MgM_4P_6O_{24}/MgCr_2O_4+Cr_2O_3,\ O_2\ (+) \quad (6.4)$$

when M = Zr, Hf, Ce.

The emf of the measurement cell was measured as a function of the temperature range, $300 \leq T/^{o}C \leq 800$ using high impedance Keithley 6517A electrometer. The cell electrodes were connected to the Keithley electrometer which was interpreted through the LabVIEW interface. The actual measurement temperature was determined using K-type thermocouple attached very close to the cell in the furnace. The temperature started at 800°C and then decreased accordingly until 300°C at a 100°C interval which was later increased upward at 50°C interval until 800°C is achieved both ways in order to monitor the reversibility of the solid-state electrolytes. The temperature-time profile is then analysed to determine the corresponding emf data at every temperature point. The measured emf in this research is compared with the standard free energies (ΔG^o) for the formation of spinel $MgFe_2O_4$ and $MgCr_2O_4$ biphasic reference electrodes from the component oxides. In general, electrochemical cells have a concentration gradient of conducting species across solid-state electrolytes. Moreover, semi permeability flux of the conduction ions would likely result when there is a large chemical potential gradient resulting in mass transport across the electrolyte from one electrode to another subsequently resulting in small compositional change in the electrode and electrolyte. However, the biphasicity nature of the reference electrode ensures continuous buffing of the cell.

6.1.4 Theoretical considerations

The anodic reaction at the $MgZr_4P_6O_{24}/MgFe_2O_4+\alpha\text{-}Fe_2O_3$ interface in the galvanic cell shown in cell I - cell III is illustrated as;

$$MgFe_2O_4(sp) = Mg^{2+} + \frac{1}{2}O_2(g) + \alpha\text{-}Fe_2O_3(cor) + 2e^- \qquad (6.5)$$

The Mg^{2+}-ions migrate through the $MgZr_4P_6O_{24}/MgCr_2O_4+Cr_2O_3$ interface where they react with oxygen in the cathodic reaction as;

$$Mg^{2+} + 2e^- + \frac{1}{2}O_2(g) = MgO \qquad (6.6)$$

Because the O_2 atmosphere, (P_{O_2}) is common to both electrodes of the cell, the net cell reaction from equation (6.5) and equation (6.6) is as shown in equation (6.7);

$$MgFe_2O_4(sp) = MgO(s) + \alpha\text{-}Fe_2O_3(cor) \qquad (6.7)$$

Equation (6.7) therefore can be said to represent the overall virtual cell reaction shown in equation (6.8);

$$MgFe_2O_4 + Cr_2O_3 = MgCr_2O_4 + \alpha\text{-}Fe_2O_3 \qquad (6.8)$$

The emf generated as a result of electrode reactions in equation (6.7) is related to the difference in chemical potential of MgO between the reference and working electrode through the relation;

$$E = - RT\ln\frac{a_{MgO(RE)}}{a_{MgO}(WE)} \qquad (6.9)$$

at constant temperature, where z, F are the electrons transferred and Faraday's constant (96485 C mol^{-1}), respectively, since the chemical potential, $\mu_{ion} = RT\ln a_{ion}$.

6.1.5 Results

Figure 6.1(a) showing the equilibration of an electrochemical cell during typical emf measurements. The emf data at 606-938K region is presented in Figure 6.1(b).

Cell I: (-) O_2, $MgFe_2O_4$+α-Fe_2O_3/$MgZr_4P_6O_{24}$/$MgCr_2O_4$+Cr_2O_3, O_2 (+)

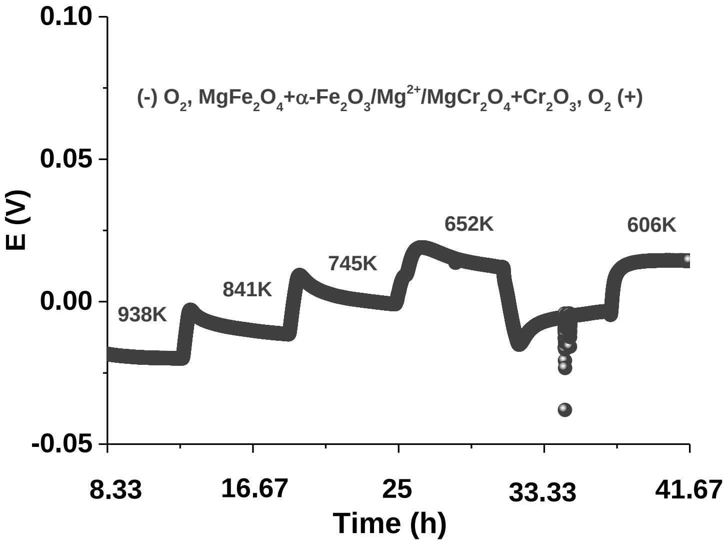

Figure 6-1(a) Typical equilibration of the cell during emf measurements

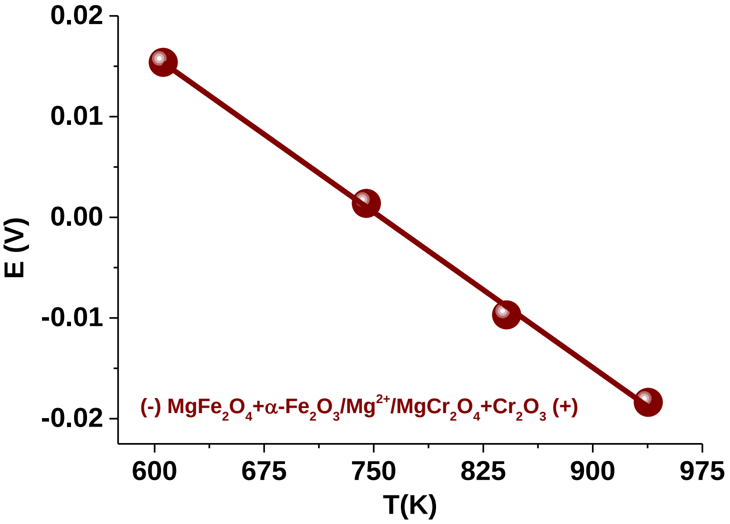

Figure 6-1(b) Measured emf using cell I including the linear fits at 606 - 938K region

The emf from Figure 6.1(a) is linear in the temperature region, $606 \leq T/K \leq 938$. From linear regression analysis, the measured emf is presented as equation (6.10),

$$E\ (mV) = 77.7 - 0.1029\ (\pm 0.002)\ T \tag{6.10}$$

The standard emf from JANAF [247] and Barin [248, 249] thermochemical data shows linearity at two temperature regions, $500 \leq T/K \leq 700$ and $900 \leq T/K \leq 1200$, often referred to as low-temperature (LT) and high-temperature (HT) regions, respectively. From linear regression analysis, however, the standard emf obtained is as presented in equation (6.11) and (6.12)

$$E_{HT}\ (mV) = (-0.09 \pm 0.005) - (8.35E\text{-}5 \pm 4.99E\text{-}6)\ T \tag{6.11}$$

$$E_{LT}\ (mV) = (-0.19 \pm 0.005) + (3.78E\text{-}5 \pm 7.97E\text{-}6)\ T \tag{6.12}$$

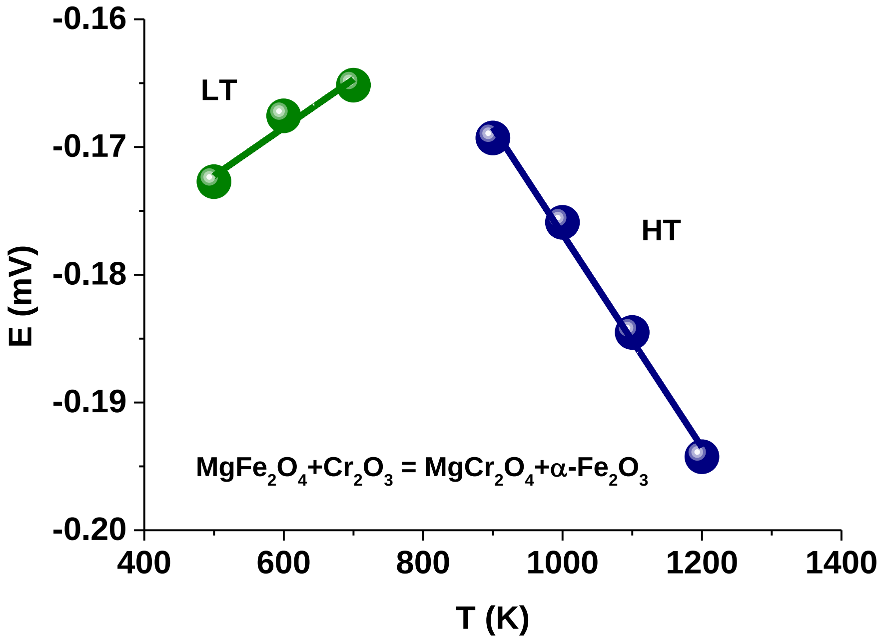

Figure 6-2 EMF standard data calculated from JANAF[247] and Barin [248, 249] thermochemical data

Cell II: (-) O_2, $MgFe_2O_4+\alpha\text{-}Fe_2O_3/MgHf_4P_6O_{24}/MgCr_2O_4+Cr_2O_3$, O_2 (+)

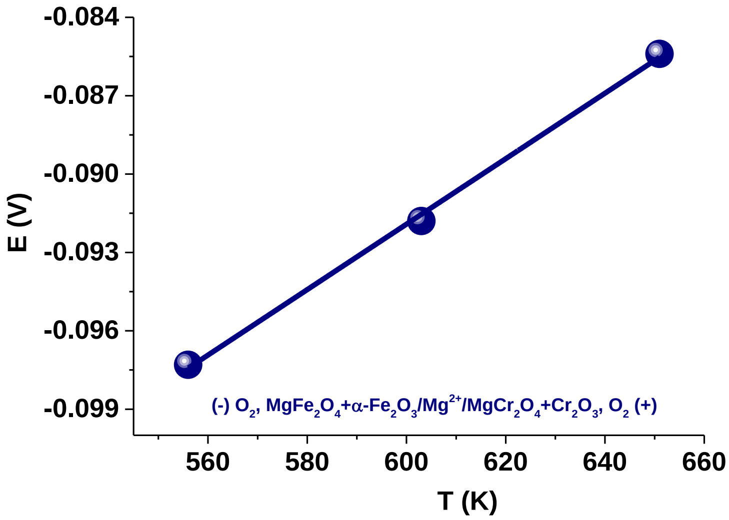

Figure 6-3 Measured emf using cell II including the linear fits at 556-651K region

The measured emf cell with $MgHf_4P_6O_{24}$ as the solid-state electrolyte is as presented;

$$E\ (V) = (-0.1671 \pm 0.003) + (1.2529E\text{-}4 \pm 4.71E\text{-}6)\ T \qquad (6.13)$$

6.2 Sensor Testing

In this research, the design, fabrication and testing of solid-state Mg-sensor have been achieved. The component materials for the design, fabrication and testing of the high-temperature electrochemical sensors are as presented;

i. High-conductive solid-state ceramic electrolytes and the corresponding solid-state solutions, using the $MgZr_{4(1-x)}M_{4x}P_6O_{24}$ (when M = Hf, Ce; $0.1 \leq x \leq 0.9$) composition solid-state electrolytes series.
ii. Stable reference electrode (i.e., biphasic powder mixture of $MgCr_2O_4+Cr_2O_3$).
iii. Non-ferrous metallic alloys (i.e., Al-Mg and Cu-Mg alloys).

6.2.1 Stability testing

The synthesised solid-state electrolytes characterised for the design and fabrication of solid-state Mg-sensors were subjected to a stability test in molten pure Al at 700±5°C for 8h and 24h, respectively. Similarly, some sets of sample pellets were immersed in OFHC-Cu and Cu-0.5 wt.% Mg for 2h and 6.5h, respectively at 1250°C to determine the stability of the solid-state electrolytes and the corresponding solid-state solutions. After phase identification and further characterisations, the characterised solid-state electrolytes sample pellets were used in the fabrication of solid-state Mg-sensors using biphasic powder mixture of $MgCr_2O_4$+Cr_2O_3 as a reference electrode, while the other pellets were used in thermodynamic and kinetic measurement.

6.2.1.1 Al + 0.02 wt.% Si

Figures 6.4 (a-e) shows the behaviour of solid-state electrolytes and the corresponding solid-state solutions (x = 0.5) in molten pure Al for 8h. The X-ray diffraction profiles of these materials compare accurately with pellets of the same composition sintered at 1300°C, initially characterised for both impedance measurement and sensor testing.

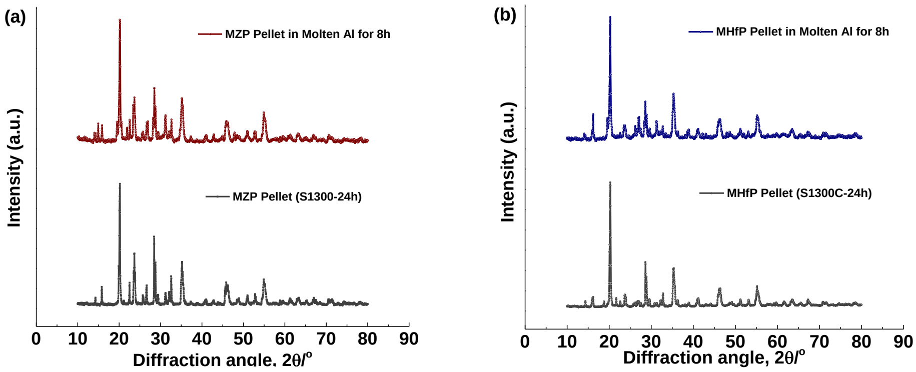

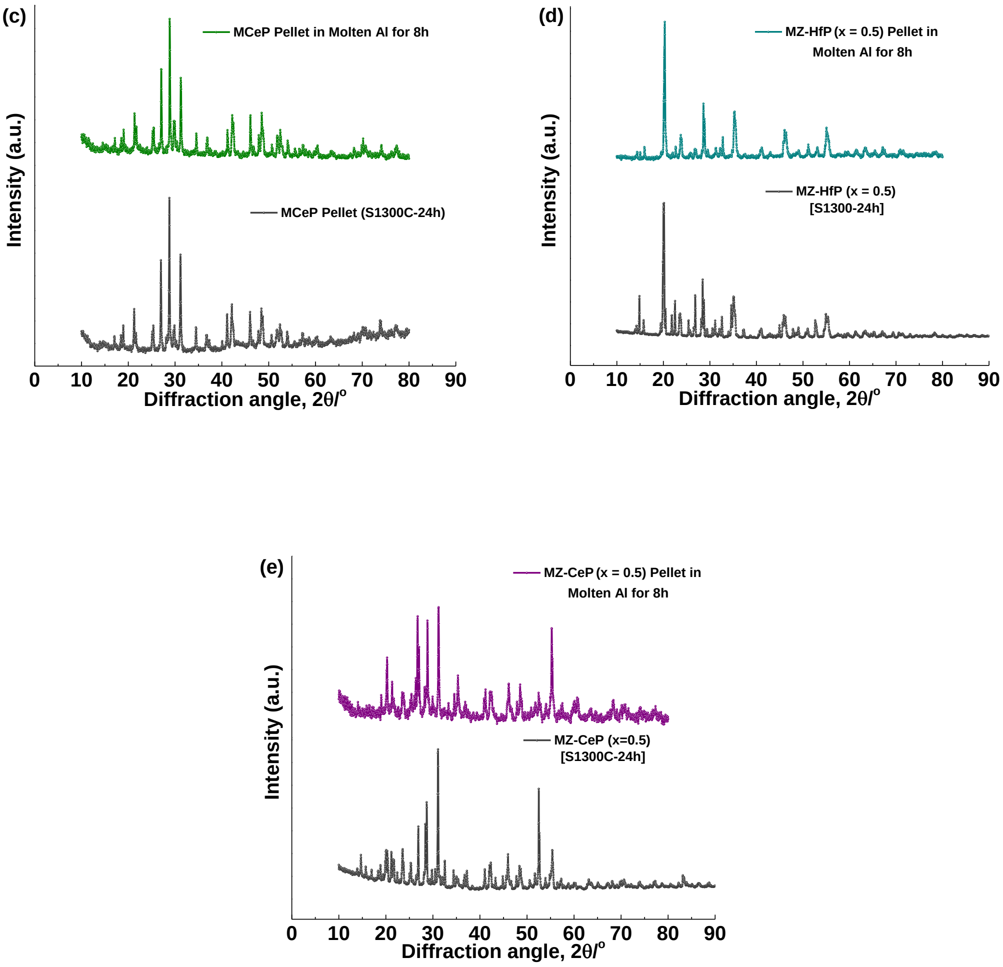

Figure 6-4 Stability testing of the (a) $MgZr_4P_6O_{24}$ (b) $MgHf_4P_6O_{24}$ (c) $MgCe_4P_6O_{24}$ (d) $MgZr_2Hf_2P_6O_{24}$ (e) $MgZr_2Ce_2P_6O_{24}$ in molten pure Al for 8h

Figure 6.5 shows solid-state electrolytes and the solid-state solutions sample pellets in pure molten Al for 24h. The sample pellets in Figure 6.5(a), Figure 6.5(c) and Figure 6.5(d) agrees perfectly but, Figure 6.5(b) shows an intense peak at 16.1^0 2θ signifying the presence of $Zr_2(PO_4)_2O$ coexistent second phase. Furthermore, Figures 6.5(a) and 6.5(d) are both $MgZr_4P_6O_{24}$ solid-state electrolytes sintered at different temperature. It implies therefore that all the sample pellets were stable in molten Al for 24h.

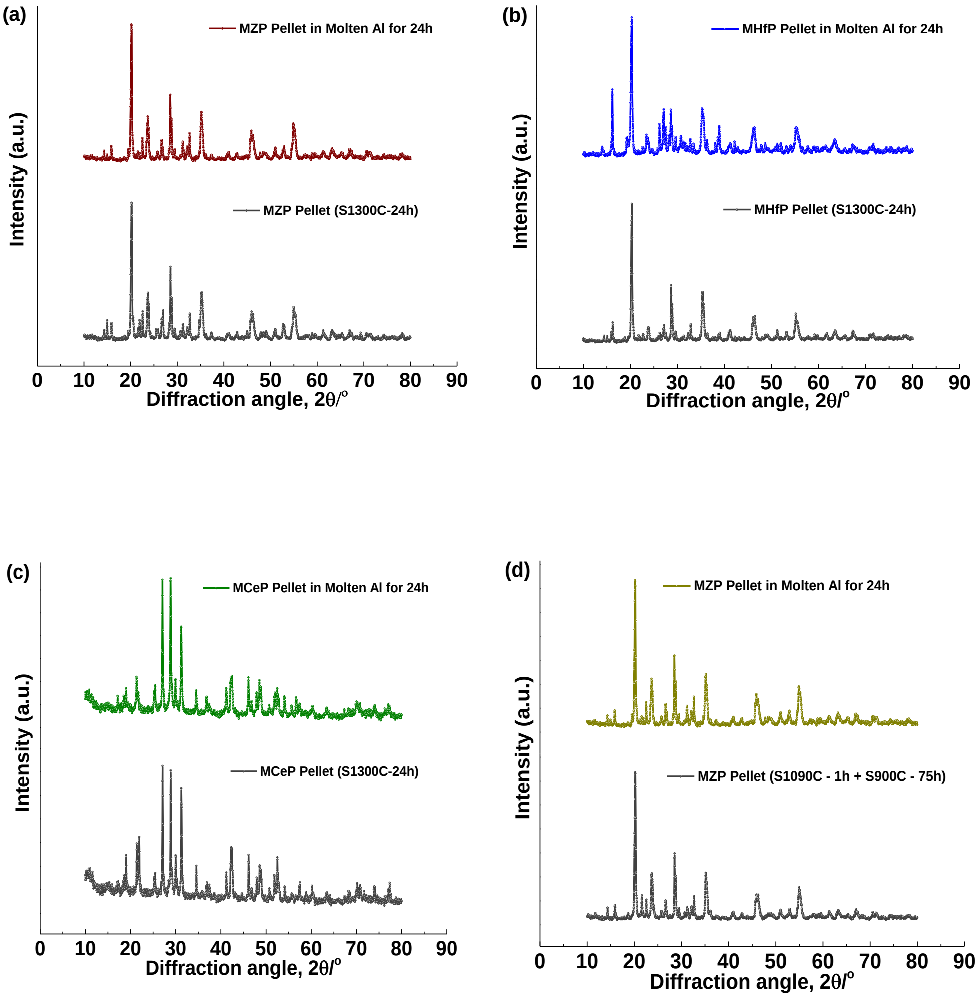

Figure 6-5 Stability testing of the (a) $MgZr_4P_6O_{24}$ (b) $MgHf_4P_6O_{24}$ (c) $MgCe_4P_6O_{24}$ (d) $MgZr_4P_6O_{24}$ in molten pure Al for 24h

6.2.1.2 OFHC and Cu-0.5 wt.% Mg

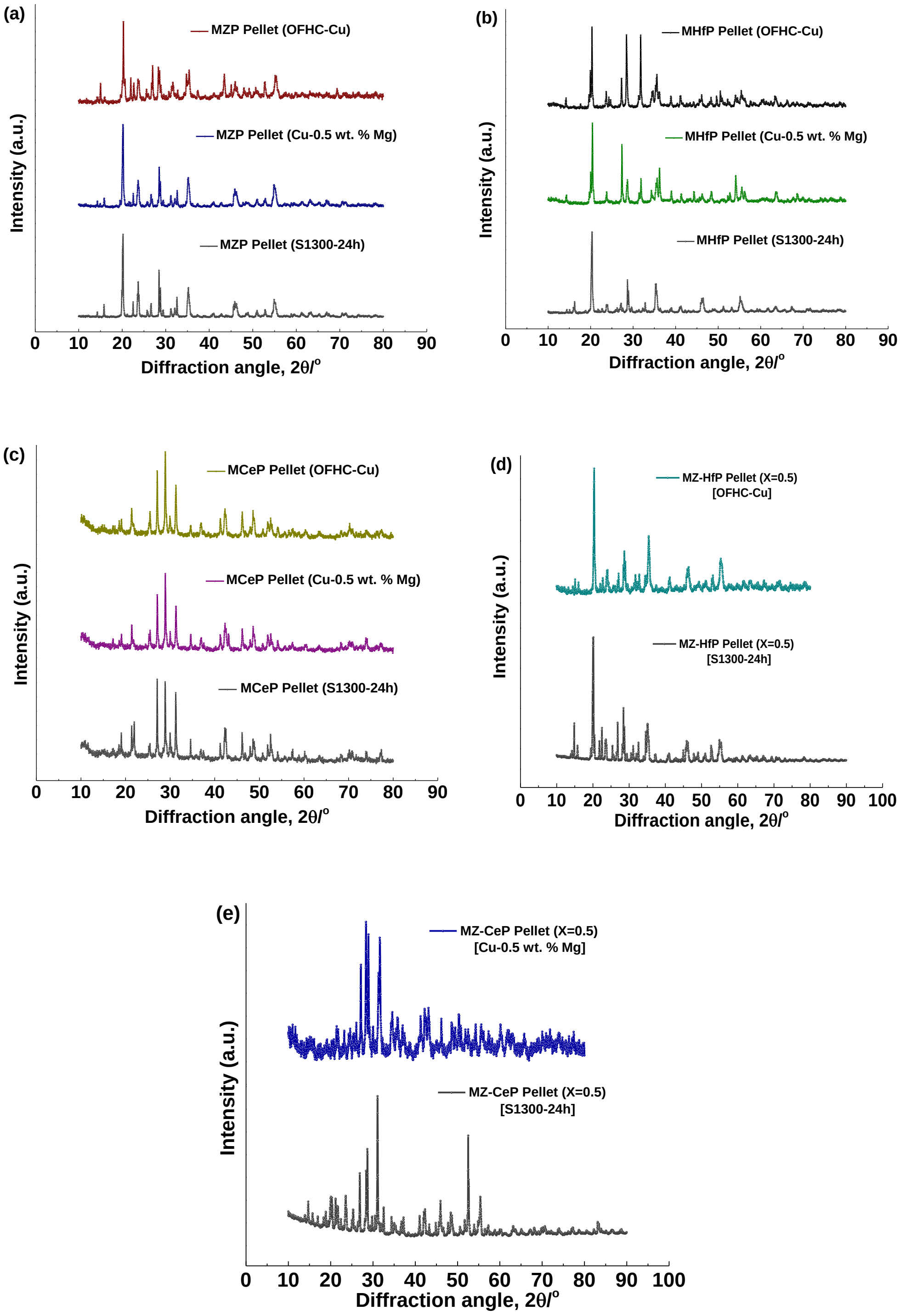

Figure 6-6 Stability testing of the (a) $MgZr_4P_6O_{24}$ (b) $MgHf_4P_6O_{24}$ (c) $MgCe_4P_6O_{24}$ (d) $MgZr_2Hf_2P_6O_{24}$ (e) $MgZr_2Ce_2P_6O_{24}$ in molten OFHC-Cu and Cu-0.5 wt.% Mg for 2h and 6.5h, respectively at 1250°C

Figure 6.6 shows chemical stability testing of solid-state electrolytes and solid-state solutions in OFHC-Cu and Cu-0.5 wt.% Mg for 2h and 6.5h, respectively at 1250°C. Moreso, Figure 6.6(a) and Figures 6.6(c-d) shows all the corresponding peak profiles in perfect alignment. However, Figure 6.6(b) and Figure 6.6(e) has some transformed peaks which could represent a sample shape and surface distortion which occurred as a result of the difficulty in extracting some pellets from a graphite holder when testing electrolytes and solid-state solutions sample pellets in pure Cu and Cu-0.5 wt.% Mg alloys for 2h and 6.5h, respectively at 1250°C in graphite crucible melting furnace, respectively. The Cu and Cu-0.5 wt.% Mg alloys were held in a graphite crucible with graphite flake on top of the melt to prevent oxidation. The melting furnace lid was closed throughout the entire experiment to prevent oxidation also.

6.2.2 Al-Foil

In considering the volatile and explosive nature of solid Mg, inserting solid Mg-rod in molten Al at high-temperature (i.e., 700±5°C) is risky and dangerous therefore the need for professional handling. The indexing of Al-foil shown in Figure 6.7 reveals that the foil-sheet used in this research is made of a single phase Al. The foil was thereafter used in wrapping Mg-rods after measurement in gram before dropping it in the molten Al at a melting temperature of 750±5°C.

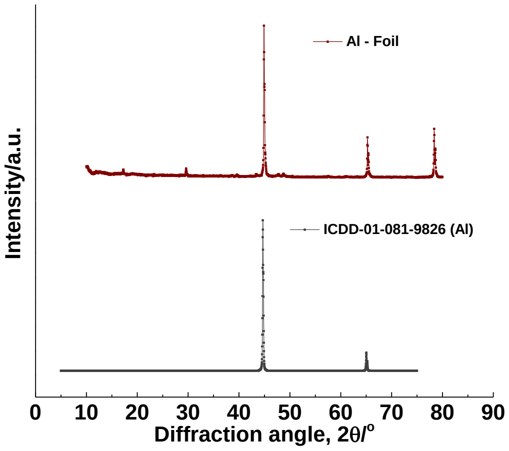

Figure 6-7 X-ray diffraction of Al-foil revealing the intensity of Al in the foil sheet

6.2.3 SEM-EDS

Al-Si-Mg Alloy:

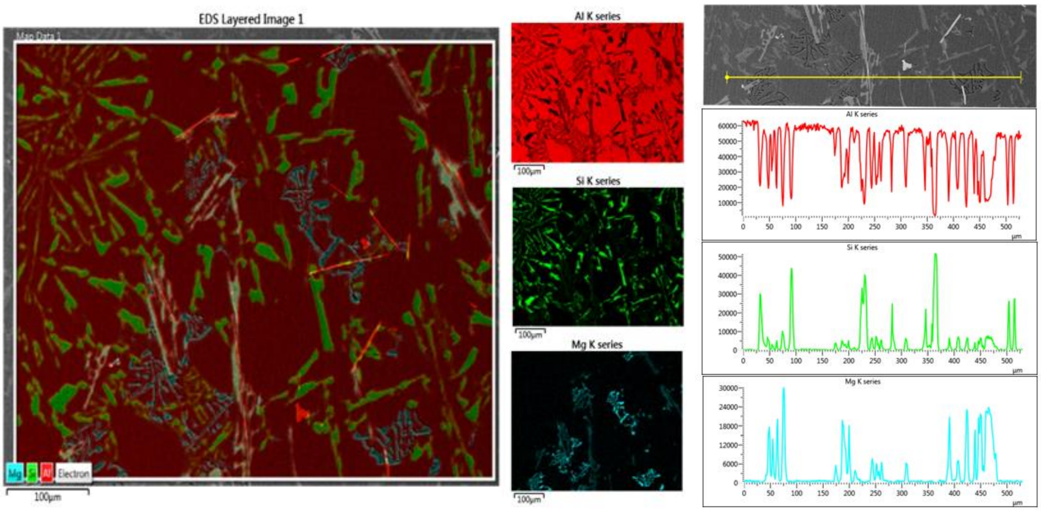

Figure 6-8(a) Elemental-Maps and Linescan of Al-Si-Mg Alloy

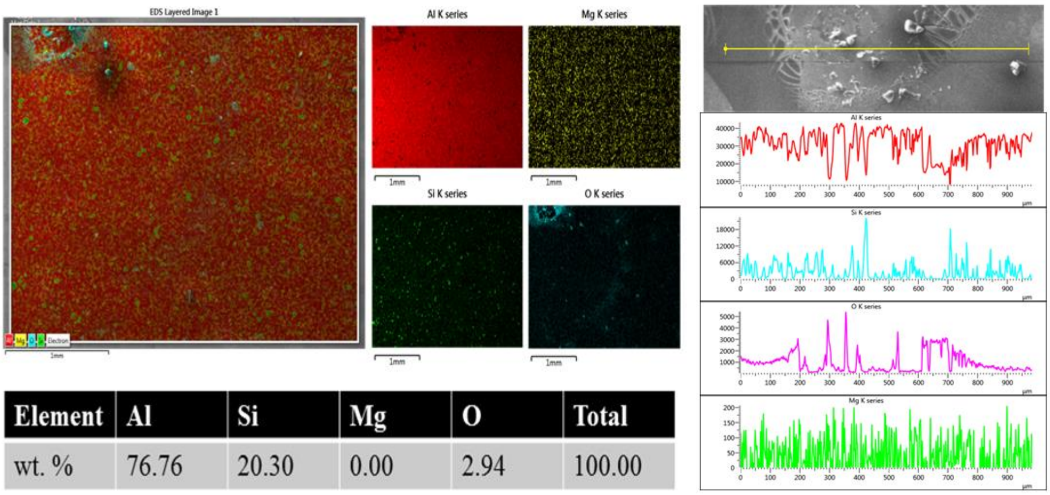

Element	Al	Si	Mg	O	Total
wt. %	76.76	20.30	0.00	2.94	100.00

Figure 6-8(b) Elemental-Maps and Linescan of Al-Si-Mg Alloy (20.30 wt.% Si)

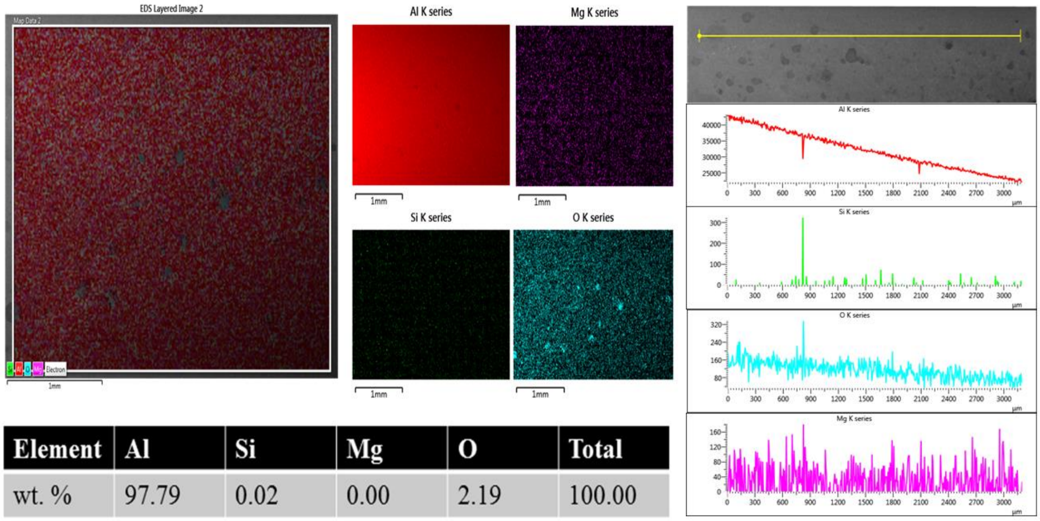

Element	Al	Si	Mg	O	Total
wt. %	97.79	0.02	0.00	2.19	100.00

Figure 6-8(c) Elemental-Maps and Linescan of Al-Mg Alloy (0.02 wt.% Si)

In Figures 6.8(a-c), the elemental-maps and linescan across different Al-sample blocks characterised for possible alloying with Mg are presented. However, Figure 6.8(a) has shown substantial amount of Si and Mg in the Al-block, believing the sample block to be Al-Si-Mg alloy instead of pure Al. Figure 6.8(b) also shows that the Al-block has 20.30 wt.% Si which is substantial for this research. Further analysis on a different Al-sample block revealed a sample with 0.02 wt.% Si which is considered adequate for making Al-Mg alloy. The amount of Si in molten Al is essential, and considering that the solid-state Mg-sensor is designed for sensing Mg, the possibility of Si interference could influence the final outcome. The third sample block was used in making Al-Mg alloy in this research while Al-Si-Mg alloy and other alloys are proposed for further studies in the nearest future.

6.2.4 Sample preparation for AAS

Sample preparation for Atomic Absorption Spectroscopy (AAS) analysis is essential for determining the actual amount of Mg in molten Al on the samples extracted from the molten alloy during sensor testing. The preparation steps observed here are in two stages as;

i. Samples of Al-Mg alloy at different nominal wt.% Mg are weighed and placed in separate beakers. Label the separate beakers for easy identification.
ii. Add 5 mL of concentrated HCl and heat up for ~ 20-30 minutes on a hot-plate to allow the samples digest in the acid.
iii. Pour the digested samples in different graduated cylinder and dilute to 20 mL with deionised H_2O each, and then allow the solution to cool down. Store the dilute samples in their labelled container bottles.

Preparation of Mg-standard solution

i. Measure 1 mL of 1000 ppm (i.e., 1000 µg/mL) of Mg solution in 100 mL flat-bottom flask.
ii. Dilute the 100 mL Mg solution with deionised H_2O to make 10 ppm.
iii. Use Accumax PRO volume pipettes (GH Zeal Limited, Merton, London) to measure 0.5, 2, 4, 6 and 10 vol/mL, respectively, into different 100 mL flask and dilute with the 10 ppm solution accordingly.
iv. The Mg-standard solutions are then stored and labelled.
v. The Mg-standard solutions are used for calibrating the AAnalyst 400 while the equipment maintains baseline in 5% HNO_3.
vi. The measurement flame is powered with combined acetylene and compressed air.
vii. After the AAS analysis, the obtained data are calculated for the exact wt.% Mg in molten Al using ;

$$\text{wt.\%} = \frac{C * V * d}{W * 10{,}000} \tag{6.14}$$

where C = Concentration of solution by AAS in ppm (i.e., $mgdm^{-3}$)
V = Volume of original flask (mL)
d = Dilution factor (note: no dilution = 1)
W = Weight (g)

6.3 Sensor Evaluation and Performance

Figure 3.32 describes the solid-state Mg-sensor for measuring Mg dissolved in molten Al at 700±5°C as potentiometric sensor which relies on the Nernst equation that relates measured open-circuit voltage or emf logarithmically to the concentration of dissolved Mg in molten Al at a fixed temperature of 700±5°C. That, as a result of this logarithmic relationship, potentiometric sensor is more likely to be an accurate and faster analytical tool in the dilute concentration region compared to most of the other analytical tools currently used in the metallurgical industry worldwide [44].

Therefore, the required skills in designing and fabricating solid-state Mg-sensors for monitoring Mg concentration dissolved in molten Al lies in making an appropriate choice of a solid-state electrolyte and reference electrode system from already-known and available sintered ceramic materials or new synthesised materials. In this research however, $MgZr_4P_6O_{24}$, $MgHf_4P_6O_{24}$, $MgCe_4P_6O_{24}$ solid-state ceramic electrolytes and $MgCr_2O_4$+Cr_2O_3 reference electrode were used in fabricating solid-state Mg-sensors. The solid-state electrolytes therefore were characterised as a highly-conducting Mg^{2+}-cation conductor while, the reference electrode is found to be stable and non-reactive.

6.3.1 Solid-State Electrolyte: $MgZr_4P_6O_{24}$

The schematic diagram in Figure 3.32 displays a simplified sensor design using solid-state electrolyte and reference electrode. Solid-state electrolytes are vital for designing electrochemical sensors unlike using molten electrolyte, where the electrolyte must be kept separate from the reference electrode and electrically isolated from the connecting wire to ensure establishment of the appropriate reference potential. This requirement however is not needed when using solid-state electrolyte since the reference electrode is the only material deposited inside the solid-state electrolyte tube or alternatively, in direct contact with the solid-state electrolyte pellets. The solid-state electrolytes used in designing the electrochemical sensor for sensing Mg in molten non-ferrous alloys is as presented in equation (6.15);

Electrochemical cell showing the working principle of Mg-sensor measuring element M in molten Al is written as shown in cell I;

wire, M(Re)/M ion conductor/M(in Al), wire (6.15)

Using M solid-state electrolyte as Mg^{2+}-cation conductor shown in equation (6.15);

(+) air, $MgCr_2O_4 + Cr_2O_3(s)/Mg^{2+}$-cation conductor(s)/Al-Mg(l) (-) (6.15)

M representing $MgZr_4P_6O_{24}$, $MgHf_4P_6O_{24}$, $MgCe_4P_6O_{24}$ solid-state electrolytes and the corresponding solid-state solutions, considered the heart of all the electrochemical sensors;

The anodic and cathodic half-cell reactions of the Mg-sensors are as presented in equation (6.16) and equation (6.17);

$$MgCr_2O_4(sp) \rightarrow Mg^{2+} + \frac{1}{2}O_2(g) + Cr_2O_3(cor) + 2e^- \qquad (6.16)$$

$$Mg^{2+} + 2e^- \rightarrow Mg\text{-}Al(l) \qquad (6.17)$$

Therefore, the net cell reaction of the Mg-sensor can be written as:

$$MgCr_2O_4(sp) \rightarrow Mg\text{-}Al(l) + \frac{1}{2}O_2(g) + Cr_2O_3(cor) \qquad (6.18)$$

where sp is defined as spinel and cor is defined as corundum in equation (6.16) and equation (6.18), respectively.

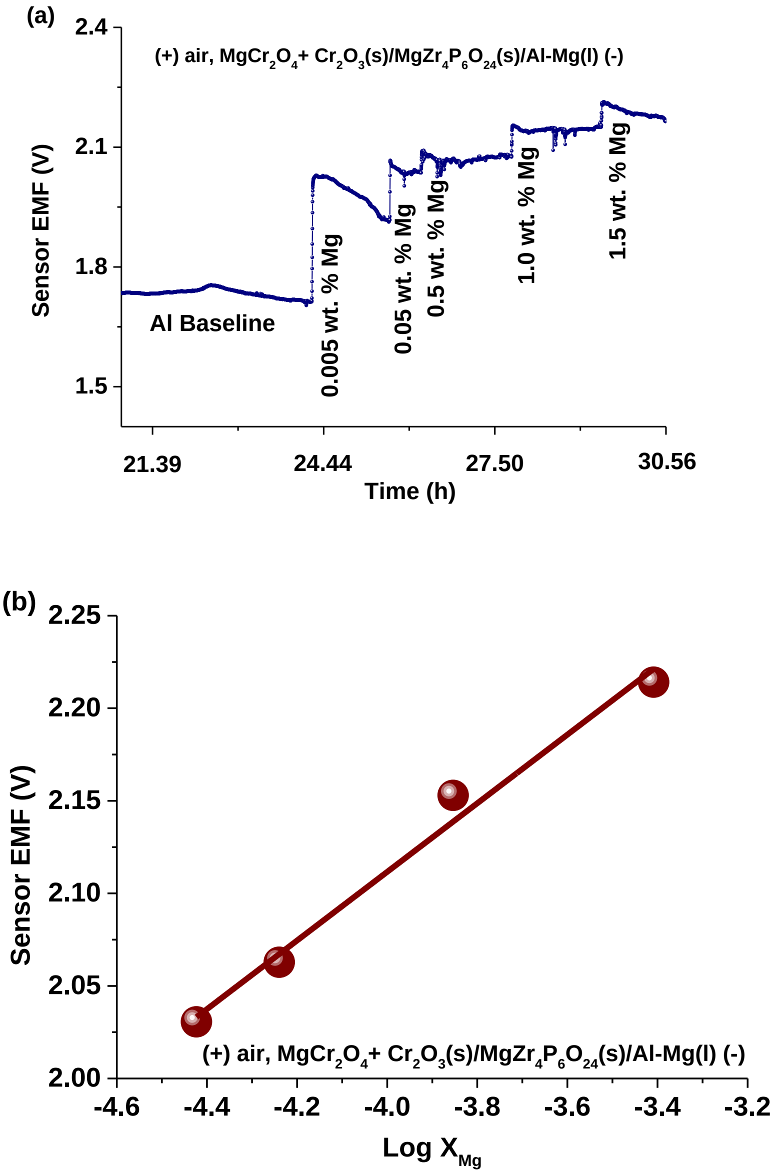

Figure 6-9 (a) Response of solid-state Mg-sensor, (b) Sensor EMF variation of the solid-state Mg-sensor as a function of concentration of Mg in molten Al at 700±5°C, using $MgZr_4P_6O_{24}$ solid-state electrolyte and $MgCr_2O_4$+Cr_2O_3 reference electrode

Figure 6.9(a) shows the response of Mg-sensor to changes in the concentration of Mg in molten Al at 700±5°C, using $MgCr_2O_4$+Cr_2O_3 biphasic powder mixture as reference electrode. Each upward step in Figure 6.9(a) correspond to the addition of Mg in molten Al. It shows therefore that as the concentration of Mg increases in molten Al, sensor EMF also increases at fixed temperature of 700±5°C thereby indicating positive response of Mg-sensor to Mg concentration in molten Al which agrees perfectly with a recent research [44]. The response plot of emf vs. time in Figure 6.9(a) further shows that the solid-state ceramic electrolyte is chemically stable in molten Al at 700±5°C considering that the Mg-sensor respond as anticipated to the sensing electrode as a function of time and at a fixed temperature. Furthermore, no drift in sensor emf during the experiment since the emf attained equilibrium value rapidly and consistently with time. The sensor emf vs. mole fraction of Mg plot (using data from atomic absorption spectroscopy, AAS), in Figure 6.9(b) indicates that the sensor emf varies linearly as a function of the concentration of Mg concentration in molten Al which is in accordance with the Nernst equation presented in equation (6.19);

$$E = -\frac{1}{nF}\int_{\mu_{ion}^{i}}^{\mu_{ion}^{ii}} t_{ion}\, d\mu_{Mg} \qquad (6.19)$$

where E is the measured open circuit voltage in V, R is the universal gas constant in J $mol^{-1}K^{-1}$, F is the Faraday constant in Coulombs mol^{-1}, n is the number of electrons participating in the electrode reaction (that is, n = 2), t_{ion} is the transport number of the conducting species (Mg^{2+}), usually ~1, μ_{Mg} is the chemical potential of Mg defined as $RT\ln a_{Mg}$, where a_{Mg} is the thermodynamic activity of Mg, the neutral form of the conducting species in the electrolyte. It is apparent from the polarity of the cell and emf response of the sensor that, the chemical potential of Mg at the reference electrode (μ^{ii}_{Mg}) is lower than that at the molten alloy sensing electrode (μ^{i}_{Mg}).

However, for the chemical potential phenomenon to be applicable, the chemical potential of Mg in the molten alloy must be greater than that at the reference electrode;

$$\mu^{i}_{Mg} > \mu^{ii}_{Mg} \qquad (6.20)$$

6.3.2 Solid-State Electrolyte: $MgHf_4P_6O_{24}$

Figure 6.10(a) and Figure 6.10(a') illustrates the response of Mg-sensor to change in Mg concentration at a particular time, while holding the experiment temperature at 700±5°C. It further shows that while adding Mg-rod wrapped in Al-foil to the pure molten Al at certain intervals, the upward stepwise pattern of Mg-sensor emf signal demonstrating the response of the solid-state Mg-sensor. Moreso, the solid-state Mg-sensor and other electrochemical sensors with similar configuration respond rapidly to Mg concentration on the first dipping, leading to fast equilibration at a short time. The equilibrium emf however, present an accurate amount of Mg concentration in molten Al. Furthermore, it should be of interest knowing that the data presented in Figure 6.10(a') was extracted from Figure 6.10(a), showing the response of solid-state Mg-sensor by adding 0.005-0.05 wt.% Mg concentration at 700±5°C. Although, the Mg-sensor reached a stable emf of 1.92V in about 0.5h, the emf reading remained for much longer to achieve proper equilibration. However, the sensor emf increased by 30mV after increasing the Mg concentration by further adding 0.05 wt.%. The Mg-sensor thereafter equilibrates for a further 0.5h to attain a stable emf of 1.95V. Further, as the Mg concentration increased by 0.5 wt.% Mg, the sensor emf increased to about 2.1V which is an increase of about 150mV. The sensor emf remained stable at this emf value and then returned to zero or baseline when the sensor measurement is discontinued indicating that this Mg-sensor has a good recovery time. Figure 6.10(b) showing a straight line relation indicating that as the Mg concentration in Mg-Al alloy increases, sensor emf also increases in somewhat proportional ratio which therefore obeys the Nernst equation. Mg-sensor in this research produced a voltage proportional to the logarithm of the Mg concentration with appropriate sensitivity.

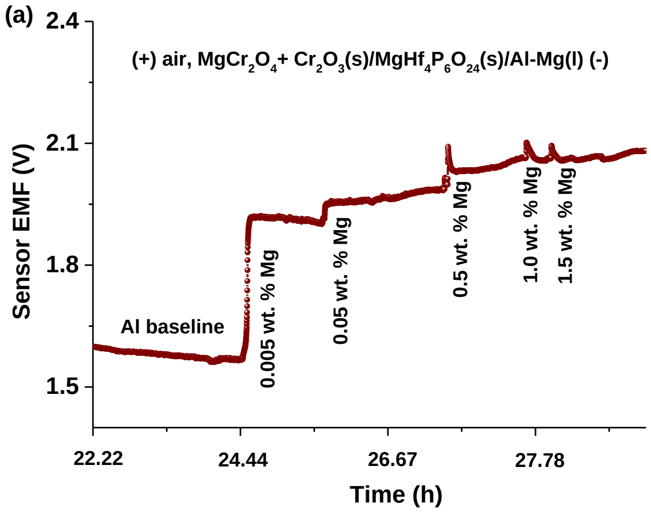
(a)
(+) air, MgCr2O4+ Cr2O3(s)/MgHf4P6O24(s)/Al-Mg(l) (-)
Sensor EMF (V)
2.4
2.1
1.8
1.5
Al baseline
0.005 wt. % Mg
0.05 wt. % Mg
0.5 wt. % Mg
1.0 wt. % Mg
1.5 wt. % Mg
22.22
24.44
26.67
27.78
Time (h)

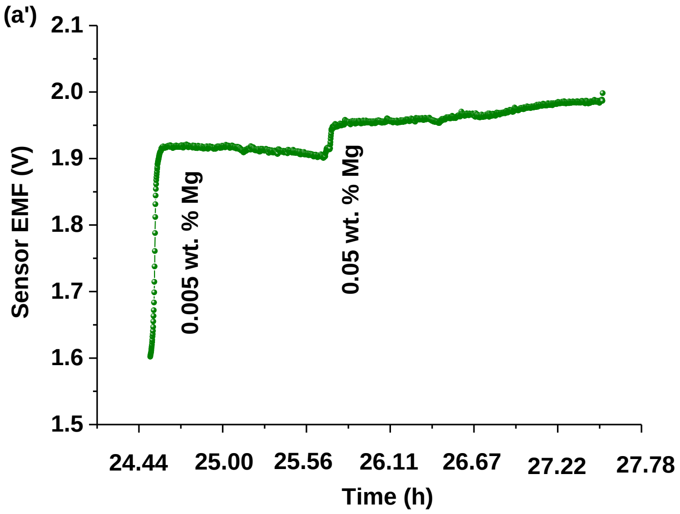
(a')
Sensor EMF (V)
2.1
2.0
1.9
1.8
1.7
1.6
1.5
0.005 wt. % Mg
0.05 wt. % Mg
24.44
25.00
25.56
26.11
26.67
27.22
27.78
Time (h)

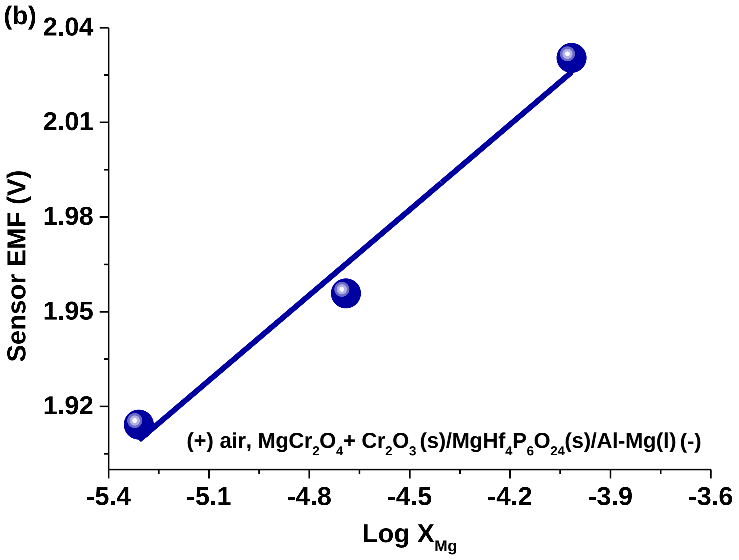

Figure 6-10 (a-a') Response of solid-state Mg-sensor (b) Sensor EMF variation of the solid-state Mg-sensor as a function of concentration of Mg in molten Al at 700±5°C, using $MgHf_4P_6O_{24}$ solid-state electrolyte and $MgCr_2O_4$+Cr_2O_3 reference electrode

6.3.3 Solid-State Electrolyte: $MgCe_4P_6O_{24}$

Figure 6.11 depicts the response of Mg-sensor to change in Mg concentration at a specific time with a fixed temperature of 700±5°C. After long equilibration of the Mg-sensor in pure molten Al to determine the baseline of molten Al before adding Mg, the subsequent change in Mg concentration in molten Al was made *in situ* by the addition of 0.005-1.0 wt.% Mg wrapped in Al-foil sheet to the pure molten Al. In terms of performance, this Mg-sensor reached a stable emf of 1.5V after 0.005 wt.% Mg was added, the emf further increased to 1.75V and then 2.25V after the Mg concentration was increased to 1.0 wt.% at an interval of 250mV after each stage of Mg addition.

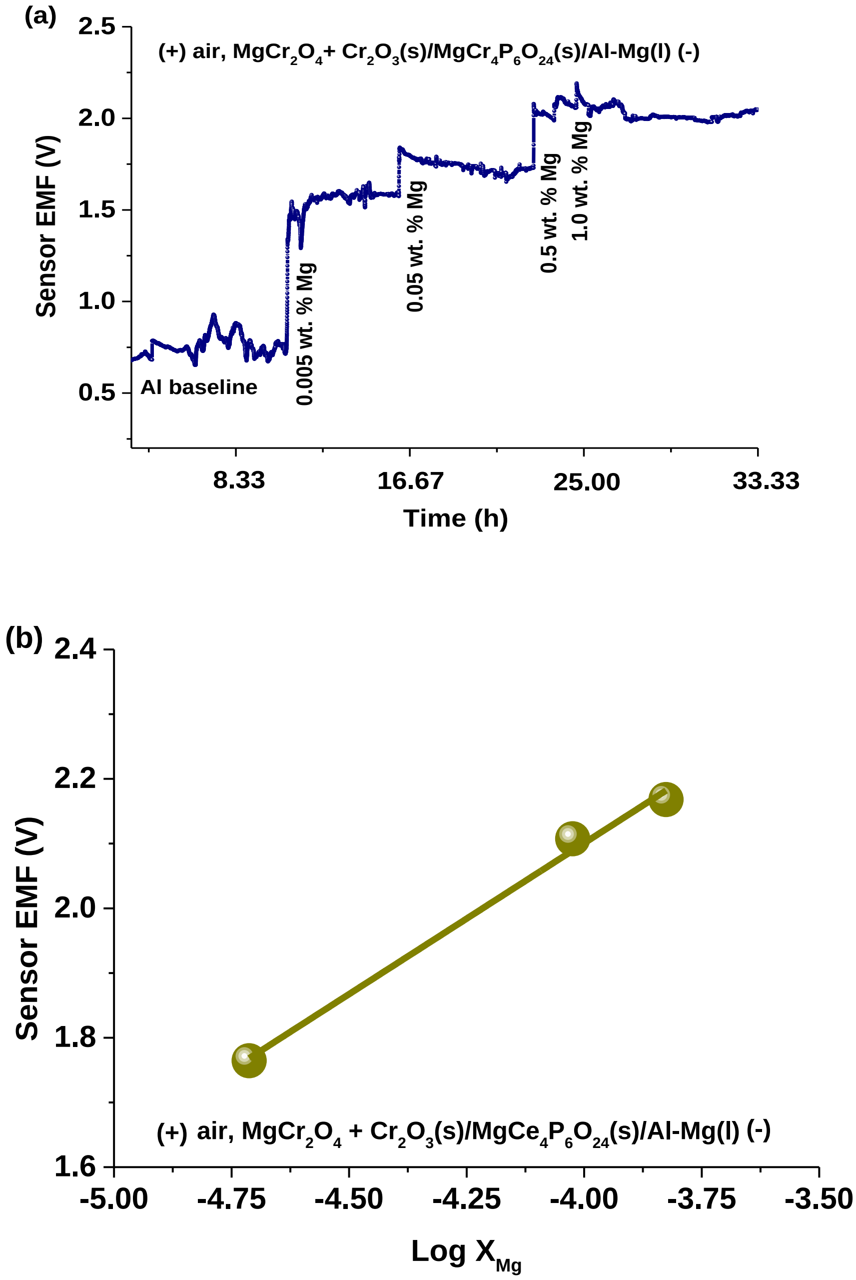

Figure 6-11 (a) Response of solid-state Mg-sensor (b) Sensor EMF variation of the solid-state Mg-sensor as a function of concentration of Mg in molten Al at 700±5°C, using $MgCe_4P_6O_{24}$ solid-state electrolyte and $MgCr_2O_4$+Cr_2O_3 reference electrode

6.4 Thermodynamic Activity Calculation

The thermodynamic activity of Mg in molten Al was calculated by emf method using the net cell reaction equation of solid-state Mg-sensor. The standard Gibbs free energy of formation, ΔG_f^o of spinel $MgCr_2O_4$ and MgO have been derived by potentiometric measurements on reversible solid-state electrochemical cells, these have been reported by Jacob [122] and Fujii [123].

The net cell reaction equation of solid-state Mg-sensor derived in this research, depicts the working of electrochemical Mg-sensors as presented;

$$(+)\ \text{air},\ MgCr_2O_4 + Cr_2O_3(s)/Mg^{2+}\text{-cationic conductor}(s)/Al\text{-}Mg(l)\ (-) \qquad (6.21)$$

According to Jacob [122];

$$MgO(s) + Cr_2O_3(cor) = MgCr_2O_4(sp),\ \Delta G_f^o = -45{,}200 + 5.36T(\pm 400)\ Jmol^{-1} \quad (6.22)$$

Equation (6.22) can be rearranged to give:

$$MgCr_2O_4(sp) = MgO(s) + Cr_2O_3(cor),\ \Delta G_f^o = +45,\ 200 - 5.36T(\pm 400)\ Jmol^{-1} \quad (6.23)$$

At the experiment melting temperature of 973 K, equation (6.23) becomes;

$$\Delta G_f^o = +45{,}200 - 5.36T(\pm 400)\ Jmol^{-1} \qquad (6.24)$$

Therefore, the standard free energy of spinel $MgCr_2O_4$ at T = 973K is determined as;

$\Delta G^o_{973K} = +39984.72(\pm 400)\ Jmol^{-1}$

Similarly, the standard free energy of formation of MgO according to Fujii [123];

$$Mg(l) + \frac{1}{2}O_2(g) = MgO(s),\ \Delta G_f^o = -669, 350 + 135.0T\ Jmol^{-1} \tag{6.25}$$

Equation (6.25) can be rearranged to give:

$$MgO(s) = Mg(l) + \frac{1}{2}O_2(g),\ \Delta G_f^o = +669, 350 - 135.0T\ Jmol^{-1} \tag{6.26}$$

At the experiment melting temperature of 973 K, equation (6.26) becomes;

$\Delta G_f^o = +669, 350 - 135.0T\ Jmol^{-1}$

Therefore, the standard free energy of MgO at T = 973K is determined as;

$\Delta G^o_{973K} = +537995\ Jmol^{-1}$

The net cell reaction equation derived from anodic and cathodic reactions is written as presented;

$$MgCr_2O_4(sp) = Mg(l) + Cr_2O_3(cor) + \frac{1}{2}O_2(g),\ \Delta G^o_{973K} = +577979.72\ Jmol^{-1} \tag{6.27}$$

The thermodyamic activity of Mg in molten Al is determined from the notation;

$$-nEF = \Delta G = \Delta G^o + RTlna_{Mg} \tag{6.28}$$

Equation (6.28) is rearranged to give:

$$-2EF = \Delta G^{o} + RT\ln a_{Mg} \tag{6.29}$$

Therefore,

$$\text{Log } a_{Mg} = \frac{-2EF - \Delta G^{o}_{973K}}{RT(2.3026)} \tag{6.30}$$

where E is the measured open circuit voltage in V, F is the Faraday constant in Coulombs mol^{-1} (F = 96485.33 C mol^{-1}), R is the universal gas constant in J mol^{-1} K^{-1} (R = 8.314 J mol^{-1} K^{-1}) and T is the experiment temperature in K (T = 973 K).

The relation between measured open voltage, E and thermodynamic activity, a_{Mg} of the reaction as a function of Mg concentrations from equation (6.31) is determined as;

$$\text{Log } a_{Mg} = -10.3598E - 31.0292 \tag{6.31}$$

The activity of Mg in molten Al as a function of concentration at 973K using the cell in equation (6.32) is as shown in Figure 6.12;

$$(+)\text{ air, } MgCr_2O_4 + Cr_2O_3(s)/MgZr_4P_6O_{24}(s)/Al\text{-}Mg(l)\ (-) \tag{6.32}$$

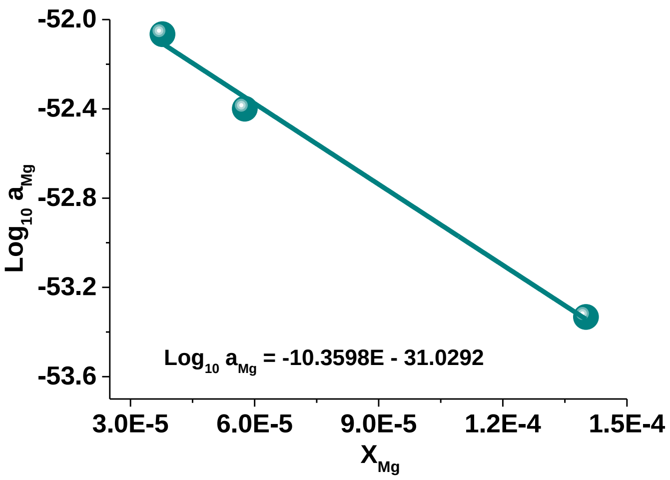

Figure 6-12 Variation of activity of Mg in molten Al as a function of concentration at 973K using $MgZr_4P_6O_{24}$ solid-state electrolyte in Mg-sensor fabrication

The activity of Mg in molten Al as a function of concentration at 973K using the cell in equation (6.33) is as shown in Figure 6.13;

(+) air, $MgCr_2O_4 + Cr_2O_3(s)/MgHf_4P_6O_{24}(s)/Al\text{-}Mg(l)$ (-) (6.33)

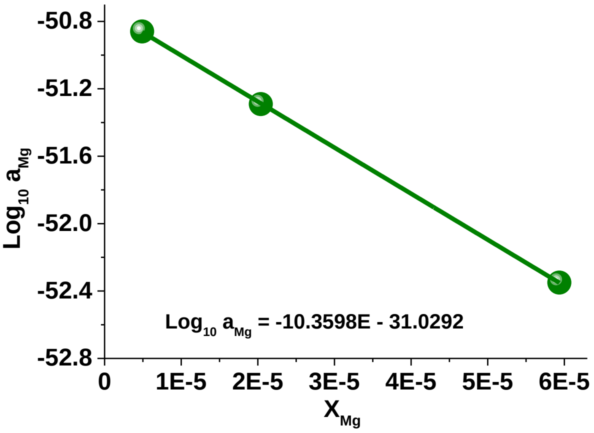

Figure 6-13 Variation of activity of Mg in molten Al as a function of concentration at 973K using $MgHf_4P_6O_{24}$ solid-state electrolyte in Mg-sensor fabrication

The activity of Mg in molten Al as a function of concentration at 973K using the cell in equation (6.34) is as shown in Figure 6.14;

$$(+)\ \text{air},\ MgCr_2O_4 + Cr_2O_3(s)/MgCe_4P_6O_{24}(s)/Al\text{-}Mg(l)\ (-) \qquad (6.34)$$

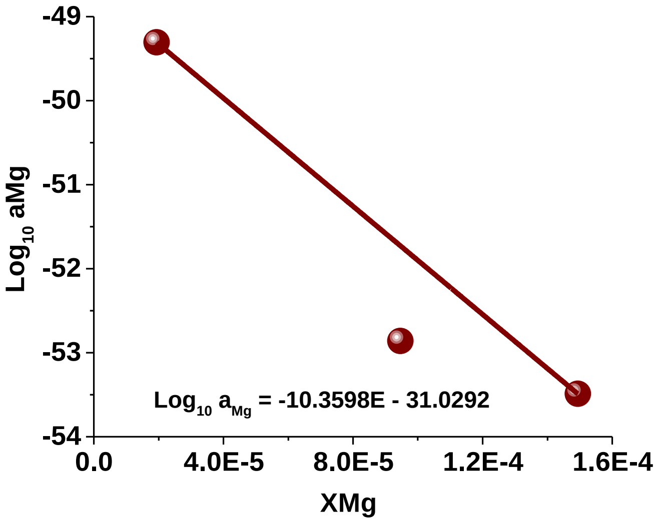

Figure 6-14 Variation of activity of Mg in molten Al as a function of concentration at 973K using $MgCe_4P_6O_{24}$ solid-state electrolyte in Mg-sensor fabrication

The variation of activity of Mg in molten Al as a function of concentration at 700±5°C (973K) in Figure 6.12 and Figure 6.13 for the solid-state Mg-sensor, respectively fabricated with the solid-state electrolytes $MgZr_4P_6O_{24}$ and $MgHf_4P_6O_{24}$ and reference electrode $MgCr_2O_4$+Cr_2O_3 define a non-ideal behaviour of Mg in molten Al-Mg alloy. Furthermore, the activity of Mg in the molten alloy at 973K during each sensor testing process was found to exhibit strong negative deviation from Raoult's law. Meanwhile, since the activity of Mg in molten Al is relatively low, it shows therefore that the molten Al-Mg alloy is thermodynamically stable. Three activity points were identified in Figure 6.12 and Figure 6.13, showing the relationship between $Log_{10}\ a_{Mg}$ and X_{Mg} in molten alloy. This relationship further shows that thermodynamic activity reduces, while concentration of Mg in molten Al increases. This confirms the thermodynamic stability of the molten Al-Mg alloy.

Similarly, Figure 6.14 has shown strong negative deviation from Raoult's law as well, which can be identified using the two activity points and one outliers. The relationship between logarithmic activity and Mg concentration (mole fraction) reveals that while the concentration of Mg in molten Al increases, the activity reduces which defines the molten Al-Mg alloy as thermodynamically stable.

6.5 Sensor for Mg in liquid Al

The solid-state Mg-sensor designed in this research can be schematically presented as;

$$\text{(+) air, Fe-Cr, } MgCr_2O_4+Cr_2O_3(s)/MgZr_4P_6O_{24}(s)/Al\text{-}Mg(l),\ \text{Mo (-)} \qquad (6.35)$$

The measured open circuit voltage of the sensor at different Mg concentrations is given in Figure 6.9(b) for $MgZr_4P_6O_{24}$; Figure 6.10(b) for $MgHf_4P_6O_{24}$; Figure 6.11(b) for $MgCe_4P_6O_{24}$ measurements, respectively. However, the measured open circuit voltage of Mg-sensor at different Mg concentrations in Figure 6.9(b) can be represented as Equation (6.36):

$$E/V\ (\pm 0.009) = 2.446 + 0.1265 \log X_{Mg} \qquad (6.36)$$

The voltage generated between the dissimilar metal leads from the two electrodes (Mo(+) - Fe-Cr(-)) at 700±5^{o}C measured independently is -0.0093V. The emf of the cell corrected for thermo-emf is given by:

$$E/V\ (\pm 0.009) = 2.437 + 0.1265 \log X_{Mg} \qquad (6.37)$$

The activity of Mg is relatively high at the alloy electrode and very low at the ceramic electrode exposed to air. The electrochemical reaction at the alloy electrode on the right-hand side of the cell is:

$$\{Mg\}_{Al(l)} \rightarrow Mg^{2+} + 2e^{-} \qquad (6.38)$$

At the reference electrode on the left-hand side, the electrochemical reaction is:

$$Mg^{2+} + 0.5O_2(g) + Cr_2O_3(cor) + 2e^{-} \rightarrow MgCr_2O_4(sp) \qquad (6.39)$$

If it is assumed that the transport number of Mg^{2+}-cation in $MgZr_4P_6O_{24}$ is unity, emf of Mg-sensor can be calculated from the thermodynamic activity of Mg in molten Al. The Gibbs energy of formation of $MgCr_2O_4$(sp) from its component binary oxides according to Jacob [122] is given as;

$$MgO(rs) + Cr_2O_3(cor) = MgCr_2O_4(sp) \qquad (6.40)$$

$$\Delta G^{o}_{f(ox)}\ (\pm 400)/Jmol^{-1} = -\ 45{,}200 + 5.36(T/K) \qquad (6.41)$$

At 700°C (973K);

$\Delta G^{o} = -39985 Jmol^{-1}$

Combining this with the Gibbs energy of formation of MgO at the same temperature

$$Mg(l) + 0.5O_2(g) = MgO(s),\ \Delta G^{o}_{f} = -501401 Jmol^{-1} \qquad (6.42)$$

The Gibbs energy change associated with the virtual cell reaction at 700°C is as shown;

$$Mg(l) + Cr_2O_3(cor) + 0.5O_2(g) = MgCr_2O_4(sp),\ \Delta G^o = -541386 Jmol^{-1} \qquad (6.43)$$

The estimated uncertainty in the value of Gibbs energy change for Equation (6.43) is 5 $Jmol^{-1}$. The emf of the sensor is related to the activity of Mg in molten Al by the relation;

$$-2FE = \Delta G = \Delta G^o + RT\ln a_{Mg} + 0.5RT\ln p_{O2} \qquad (6.44)$$

Thus, the theoretical emf of the sensor at 700°C can be calculated as;

$$E_{th}(\pm 0.026)/V = 2.7728 + 0.09653\log a_{Mg} \qquad (6.45)$$

Aghdam and Soltanieh [250] have recently measured the activity of Mg in liquid Al using an electrochemical cell with eutectic mixture of $MgCl_2$-$CaCl_2$ as the electrolyte in the temperature range from 700 to 800°C and composition range from 0.07 to 12.1. The activity coefficient of Mg at 700°C for dilute alloys up to 1.4 atom % Mg can be expressed by the relation,

$$\log\gamma_{Mg} = -0.7624 + 23.183X_{Mg} \qquad (6.46)$$

Expressing activity of Mg in Equation (6.45) as a product of mole fraction and activity coefficient, one obtains;

$$E_{th}(\pm 0.03)/V = 2.6992 + 2.2379X_{Mg} + 0.09653\log X_{Mg} \qquad (6.47)$$

The theoretical emf is compared with the measured values in Figure 6.15. On the average, the measured values are lower by ~0.359±0.022V. An average transport number at 700±5°C for Mg^{2+}-cations over the range of chemical potential at the two electrodes can be computed from the calculated difference between experimental emf and theoretical emf assuming that the electrodes are not polarised.

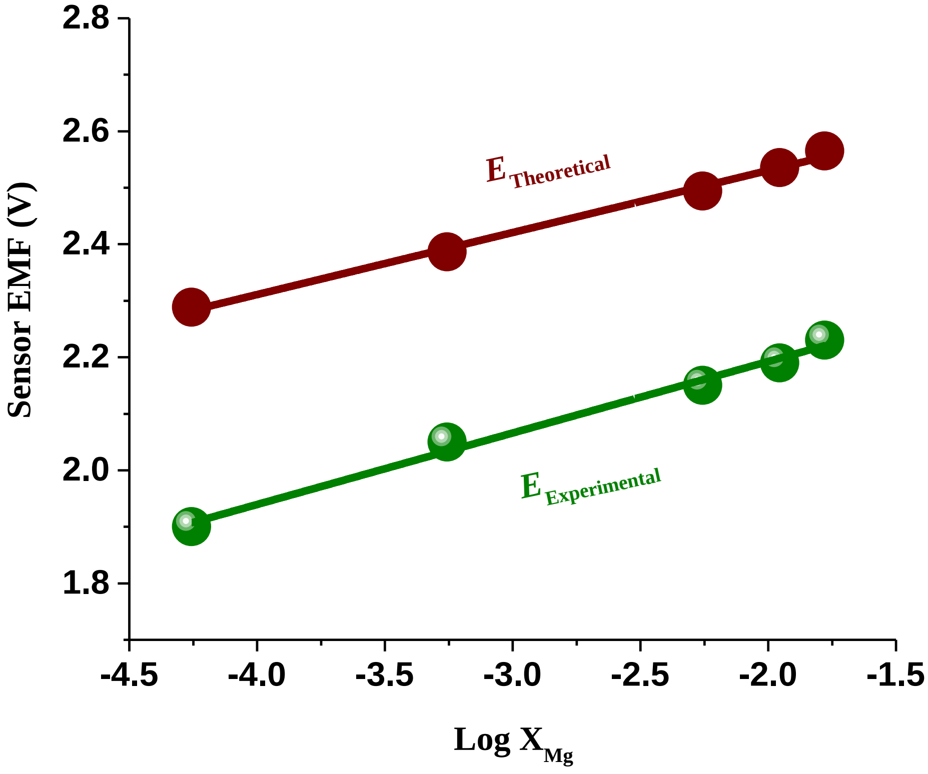

Figure 6-15 Comparison of the experimental voltage of the sensor with the theoretical emf

$$t_{ion} = \frac{E_{exp}}{E_{th}} \tag{6.48}$$

The average transport number for Mg^{2+}-cation in the solid-state electrolyte according to Figure 6.15 is 0.85±0.03. This is further presented in Figure 6.16 as a function of Mg concentration.

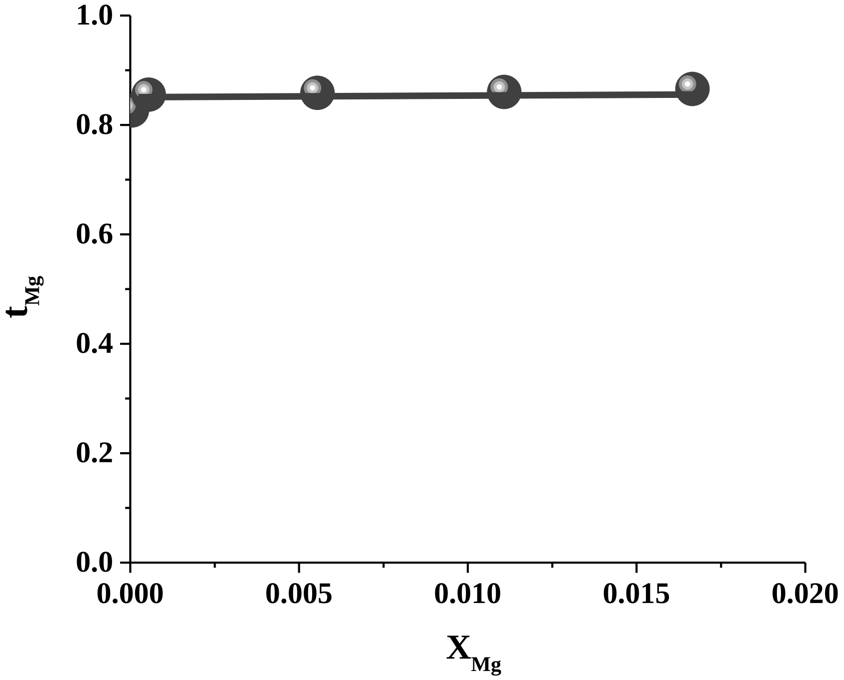

Figure 6-16 Variation of the average transport number of Mg^{2+}-cation in $MgZr_4P_6O_{24}$ solid-state electrolyte at 700°C

The data in this research compares excellently with the activity of Mg in liquid Al reported by Aghdam and Soltanieh [250]. However, it is likely that the experimental emf is affected by the relatively large electron and/or hole transport in the solid-state electrolyte and the large difference in chemical potential of Mg at the two electrodes leading to polarisation of the biphasic powder mixture reference electrodes. Hence, testing of the ceramic solid-state electrolyte with other reference electrodes with much higher Mg chemical potential is recommended.

6.6 Conclusions

This chapter discusses thermodynamics studies of contact reaction between solid-state electrolytes and reference electrodes using electrochemical method. Sensor testing, performance and evaluation was equally studied with emphasis on thermodynamic activity of Mg in molten Al at 973K. The electrochemical method was preferred to others because it is the most accurate and reliable method in terms of determining the both measured and theoretical emf in chemical reactions. The procedure was outlined, and it is important to follow the set procedure in order to achieve a pure homogeneous phase of the spinel chromate before a biphasic powder mixture in ratio of 1:1 follows. Before fabricating Mg-sensor using the solid-state electrolytes characterised in this research, of importance is acquiring adequate knowledge set on the stability of these electrolytes before subjecting them to a high-temperature functionality, the stability tests however, proved that the electrolytes are stable and are right for high-temperature functionality. Sensor testing was perfect and the sensor response looks very promising. However, the thermodynamic activity of Mg in molten Al indicates a strong negative deviation from the Raoult's law but, the activity is very small showing that the working environment is stable. The actual amount of Mg in molten Al during sensor testing was analysed using the Atomic absorption spectroscopy, AAS and the acquired data looks very promising as well. Furthermore, Mg concentration data extracted by AAS were used to compute the mole fraction of Mg in molten Al and that, the relationship between sensor emf and logarithmic mole fraction looks better than the nominal data presented in the appendix section. The end-members solid-state electrolytes used in fabricating solid-state Mg-sensor shows that they are good electroceramic materials with sufficiently high ionic conductivity properties necessary for sensors and other electrochemical devices. Subsequently, structural characterisation on the component electrodes for sensor fabrication reveals the potential suitability of these components, with adequate stability, they can function in high-temperature environment, harsh and corrosive atmosphere.

Sintered $MgZr_4P_6O_{24}$ was stable at 700±5°C in molten Al and Al-Mg alloys in the range from 0.005 to 1.5 wt.% Mg. The $MgZr_4P_6O_{24}$ pellets were deployed to fabricate solid-state sensors for measuring Mg concentration in molten Al. A biphasic powder mixture $MgCr_2O_4+Cr_2O_3$ in air was used as the reference electrode. The sensor voltage was a linear function of logarithm of Mg concentration; this shows that a practical sensor can be developed for re-melting and casting applications. However, the sensor emf was consistently below the theoretical value suggesting an average ionic transport number of 0.85±0.03 for the solid-state electrolyte in the temperature and Mg chemical potential range covered in this research.

.

Chapter 7

Conclusion, Recommendations and Future Works

7.1 Conclusion

The main achievements of this research are presented in Summary;

In an attempt to fabricate a relatively cheap solid-state Mg-sensor, sol-gel procedure adapted in this research was modified to suit our research need. The modified sol-gel method developed in our laboratory at University of Leeds enables the solid-state electrolytes to be formed at 800-900°C for 0.5h by calcining and for the sample pellets prepared using the calcined solid-state electrolytes to be sintered at an equally lower sintering temperature of 1300°C. The sintering process however was modelled in such a way to prevent volatilisation of the phosphate phase in the pellets at high-temperature during sintering. This was achieved by placing the green pellets on droplets of powders of the same composition in a boat crucible while the entire bulk of the pellet is covered by this atmosphere powder, and the entire assembly is covered with alumina crucible before insertion into the furnace.

This research was classified into structural and electrical characterisation for purpose of application, and sensor testing. The modified sol-gel technique adapted in this research reveals some novelty in structural and ionic conductivity to reckon with. The $MgZr_4P_6O_{24}$ solid-state electrolyte characterised in an earlier research was reported to exhibit an ionic conductivity of 6.92×10^{-3} S cm^{-1} at 800°C [224], whereas, our recent report on synthesised $MgZr_4P_6O_{24}$ solid-state electrolyte reveals an ionic conductivity of 7.23 x 10^{-3} S cm^{-1} at 725°C, which is believed to be a much lower temperature [24]. This finding however, opens vista of research interest in solid-state ionics, materials and electrochemistry. In furtherance of this research, solid-state solutions by chemical doping (i.e., doping by substitution) was pursued and the product of this synthesis have been characterised and reported in this thesis. It appears therefore that the doped solid-state electrolytes have shown a trend to further the electrical characterisation research for onward application in sensor fabrication. The solid-state solutions at x = 0.5 have been found to possess high stability in both molten Al, OFHC- CU, Cu-0.5 wt.% Mg alloy and recently, in Al-Mg alloy, seen in Figure 6.4 and Figure 6.6, respectively.

The solid-state Mg-sensors developed in this research finds useful applications in our automobiles, aerospace, chemical and process industries, and of particular interest, the metallurgical industries for applications in casting, refining and recycling processes. Thermodynamics of the reference electrodes, $MgCr_2O_4$+Cr_2O_3 and $MgFe_2O_4$+α-Fe_2O_3 using emf method revealed novel information that may have been ignored in recent past. The negative deviation of the thermodynamic activity of Mg in molten Al from the Raoult's law negates the conventional Raoult's law as it applies to both ideal and non-ideal situation. In an earlier research, $MgCr_2O_4$+Cr_2O_3 and $MgFe_2O_4$+α-Fe_2O_3 have been used as reference electrode for sensing Mg in molten Al [44], the measured emf data in this thesis has shown improvement in terms of sensor sensitivity, response and recovery rate. Furthermore, the accuracy of Mg concentration from the AAS method should be relied upon. The possibility of losing Mg to oxidation and other experimental error is high which could affect the nominal experimental data.

The structural properties of monoclinic $MgZr_4P_6O_{24}$ and $MgHf_4P_6O_{24}$ electrolytes are similar, this is probably because they belong to the same group on the periodic table with the same chemical properties, unlike $MgCe_4P_6O_{24}$, a lanthanide that could sinter at a very low temperature with a monazite structure characteristic of the phosphates of *f*-elements, as observed in $A_3R_2(PO_4)_3$ with A = Na, K and R = Ce-Gd, Pu(III), Am, and Cm [251, 252].

Structural Characterisation:

i. The morphology of the ceramic pellets was achieved on fracture surface of a cracked pellet and on cross-sectional polished sample surface. In both cases, it shows that the solid-state electrolytes were dense with little porosity which was established by the density-porosity measurements at about 94-99.0% density and 6.0-1.0% porosity, respectively in the sintered pellets.

ii. HR-TEM evaluates the formation of a pure, homogeneous single phase of the solid-state electrolytes nanoparticles and pellets at $900 \leq T/^oC \leq 1300$. The EDS spectra further revealed the spatial distribution of the constituent elements in appropriate stoichiometric ratio in $MgZr_4P_6O_{24}$. In the case of $MgHf_4P_6O_{24}$ and $MgCe_4P_6O_{24}$, a non-stoichiometric relation was established.

iii. SAED analysis revealing nanoparticles with either amorphous or crystallinity orientation which was used to further predict the calcination temperature. In this research, the SAED shows single crystallinity for $MgCe_4P_6O_{24}$ and traces of amorphous nanoparticles for $MgZr_4P_6O_{24}$ and $MgHf_4P_6O_{24}$.

Electrical Characterisation:

i. The impedance analysis of $MgZr_4P_6O_{24}$ and $MgHf_4P_6O_{24}$ samples are similar. That of $MgCe_4P_6O_{24}$ however is different. The $MgZr_4P_6O_{24}$ and $MgHf_4P_6O_{24}$ analysis revealed a single semicircle for bulk measurement, $MgCe_4P_6O_{24}$ has consistently shown two semicircles at both low and high-temperature region. The Nyquist plots of $MgZr_4P_6O_{24}$ samples measured at HT-region (764-765°C) and LT-region (390-391°C) revealed that as the temperature increases towards 764°C, there seem to be depressed bulk semicircle that gradually move away from the origin, zero indicating a finite resistance, R_s which represent lumped electrode-electrolyte interfacial assistance in series with a parallel combination of R_b and CPE_b. Similarly, for the $MgHf_4P_6O_{24}$ samples measured from 273°C to 747°C, a perfect Nyquist plot was observed at the LT-region (273°C) while the plots was found to also shift away from the origin at the HT-region. In this case, as the impedance temperature increases, the depressed bulk semicircles gradually becomes smaller and the inclined spike on the electrode-electrolyte interface gradually bent downward tending towards depressed semicircle. The $MgCe_4P_6O_{24}$ sample shows a different behaviour, the Nyquist plots in the Ce-based phosphate materials shows double semicircles at both HT and LT-region with no visible electrode-electrolyte spike, this shows that electrode effect was not possible in this material at any temperature. The electric modulus was used to determine the relaxation points of these materials. It shows therefore that for all the sample pellets, relaxation frequency diminishes as frequency increases towards 32MHz. It was further observed that all the samples displayed a good reproducibility behaviour which makes these Mg-phosphate based solid-state electrolytes suitable in sensor fabrication.

ii. In comparison, it has been observed that $MgZr_4P_6O_{24}$ and $MgHf_4P_6O_{24}$ behave differently at different temperature. It was observed therefore that $MgZr_4P_6O_{24}$ is a marginally better material to use for HT activities than $MgHf_4P_6O_{24}$ which could be owned to the enhancement of ionic conductivity due to space-charge region effect considering that $MgZr_4P_6O_{24}$ is a composite electrolyte, whereas, solid-state electrolyte, $MgHf_4P_6O_{24}$ is considered a single phase electrolyte at HT-region, respectively. Temperature dependence on ionic conductivity of $MgHf_4P_6O_{24}$ and $MgCe_4P_6O_{24}$ samples expressed $MgCe_4P_6O_{24}$ as a better ionic conductor than $MgHf_4P_6O_{24}$, however, they have both remained chemically stable at high-temperatures.

Thermodynamics Consideration:

In using the virtual cell reaction: $MgFe_2O_4 + Cr_2O_3 = MgCr_2O_4 + \alpha\text{-}Fe_2O_3$, measured emf, E determined from E (mV) = 77.7 – 0.1029 (±0.002) T at the 600-938K region gives 15.96±0.002mV and -18.82±0.002mV at 600K and 938K, respectively, when using $MgZr_4P_6O_{24}$ as the Mg^{2+}-cation conductor.

However, if $MgHf_4P_6O_{24}$ is the Mg^{2+}-cation conductor, the measured emf at 600-938K can be determined using the cell, E (V) = -0.1671 + 1.2529E-4 (±4.71E-6) T which results in -91.93±0.003mV and -49.58 ±0.003mV, for 600K and 938K, respectively.

It shows therefore that the emf of both materials are different, $MgZr_4P_6O_{24}$ seem to produce better emf. The standard emf determined from equation (6.11) and equation (6.12) for both the LT and HT-regions are -0.16±0.005mV, respectively which is short off the measured emf.

Sensor Performance:

The electrochemical Mg-sensor fabricated in this research have shown excellent response to the amount of Mg concentration in the molten Al alloys. It shows that the emf increases as Mg concentration increases and decreases as the measurand was removed. The Mg-sensor fabricated using $MgHf_4P_6O_{24}$ shows an increase of 30mV the moment Mg concentration was increased from 0.005 wt.% to 0.05 wt.% and then increased to 2.1V as the Mg concentration was increased to 0.5 wt.% which is an increase of 150mV. After equilibration for 0.5h, the measurand was removed and the emf returned to zero. The Mg-sensor fabricated with $MgCe_4P_6O_{24}$, shows an increment of about 250mV as the Mg concentration was increased from 0.005 wt.% to 1.0 wt.%, respectively.

7.2 Recommendations

7.2.1 Lattice constant

The lattice constant in Figure 4.20 shows deviation from their respective linearity at x = 0.1 and 0.4 and, x = 0.2 and 0.5 for $MgZr_{4(1-x)}Hf_{4x}P_6O_{24}$ and $MgZr_{4(1-x)}Ce_{4x}P_6O_{24}$ solid-state solution series, respectively. As a result, the identified solid-state solutions in Figure 4.20 needs further characterisation so as to compare data with those reported in this research. The data presented in this research are novel, as there are no similar data to compare with at the moment.

7.2.2 Sensor probe

The main problem in a typical sensor making process is selecting suitable electrolytes and reference materials [253]. However, in this research, the design, fabrication and testing of electrochemical Mg-sensors using the end-members solid-state electrolytes; $MgZr_4P_6O_{24}$, $MgHf_4P_6O_{24}$, $MgCe_4P_6O_{24}$ and the solid-state solutions, $MgZr_2Hf_2P_6O_{24}$ and $MgZr_2Ce_2P_6O_{24}$ ($x = 0.5$) have been characterised showing adequate stability in molten Al, OFHC-Cu, and Cu-0.5 wt.% Mg working environment. $MgCr_2O_4$+Cr_2O_3 reference electrode have been found to be stable and non-reactive with the solid-state electrolytes in this research. However, the $MgFe_2O_4$+α-Fe_2O_3 and $MgAl_2O_4$+α-Al_2O_3 can be further analysed for possible use as reference electrode in the electrochemical solid-state Mg-sensors. Therefore, the precursor materials selected for synthesis and characterisation of both the solid-state electrolytes and reference electrodes, and then the working electrodes are considered appropriate and adequate.

7.2.3 Phase identification

X-ray diffraction and SEM-EDS have been used for phase identification analysis of critical components in this research. The Al-foil for wrapping Mg-rod before dropping off in molten Al was identified by XRD analysis, knowing that labels ordinarily might not define the actual composition requirements. Tin-foil (SnO_2) might have been used instead which could initiate contamination of the working composition and possibly, in sensor damage. Sensors for multiple sensing might be necessary in future. Since the sensor designed in this research is for specific sensing, the working environment, Al-Mg and Cu-Mg alloys need to be of required composition. SEM-EDS further revealed the presence of 20.30 wt.% Si in Al-block which might have affected the performance of the Mg-sensor. In this research however, the interesting thing is, the sensor sensed Mg in this alloy which indicates that Si has no immediate effect on the life of the Mg-sensor. Response of the solid-state Mg-sensor with time and sensor emf variation of the solid-state sensor as a function of Mg concentration in the molten Al + 20.30 wt.% Si is presented as Figure A-9(a-b) in appendix A-8.

7.3 Future Works

There are potentials to expand the scope of this research and to build on the knowledge direction of the research focus. Such areas of possible research expansion in future are as discussed;

7.3.1 Co-doping

The modified sol-gel synthesis method adapted in this research achieved $MgZr_4P_6O_{24}$, $MgHf_4P_6O_{24}$, $MgCe_4P_6O_{24}$ solid-state electrolytes and the corresponding solid-state solutions. The stoichiometric series of $MgZr_{4(1-x)}M_{4x}P_6O_{24}$ (M = Hf, Ce; $0.1 \leq x \leq 0.9$) for solid-state ceramic synthesis achieved 18-different solid-state solutions by partial substitution or doping process. In this regard, Zr^{4+} in $MgZr_4P_6O_{24}$ B-site was partially substituted with Hf^{4+} (HfO_2) and Ce^{4+} (CeO_2), respectively, to complete the doping of $MgZr_4P_6O_{24}$, $MgHf_4P_6O_{24}$, and $MgCe_4P_6O_{24}$ presented in Figure 7.1. In furtherance of this research, co-doping of $MgZr_4P_6O_{24}$ with $MgHf_4P_6O_{24}$ and $MgCe_4P_6O_{24}$ should be pursued using the synthesis series illustrated in Figure 7.1 to complete the triangle of synthesis for the solid-state solutions.

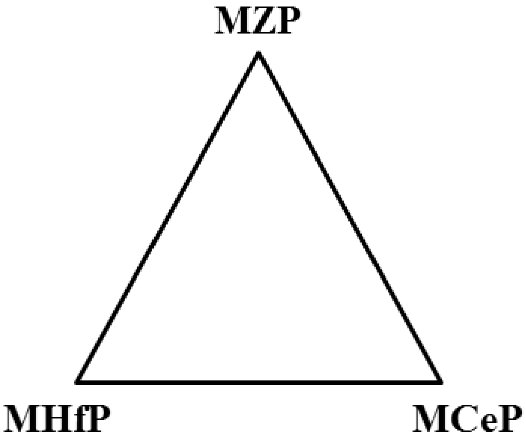

Figure 7-1 Triangle of synthesis for solid-state solutions

7.3.2 Sensor testing

The discrete analytical techniques earlier used in foundry and other process industries are believed to be fast, but considering the time spent in taking samples for analytical examination and, during this time period, the composition of the melt may be changing either owing to refining, casting, alloying reaction or interaction with the environment [253]. As a consequence, the fabrication of the electrochemical sensors in this research as an in-line monitoring technique comes with a potential advantage. Meanwhile, in order to perform very satisfactorily in a foundry, alloying and recycling environment, the sensor measuring technique would have to be rugged, reliable, inexpensive, have a quick response, and also be implemented by a relatively unskilled workforce [253]. These criteria are particularly demanding and no single technique is likely to satisfy all the requirements. A method which offers the possibility of meeting some of them is an electrochemical one based upon a simple thermodynamic measurement [253].

Meanwhile, the solid-state Mg-sensors characterised in this research were fabricated using the solid-state electrolytes, $MgZr_4P_6O_{24}$, $MgHf_4P_6O_{24}$, $MgCe_4P_6O_{24}$ and solid-state solutions, $MgZr_{4(1-x)}M_{4x}P_6O_{24}$ ($M = Hf$, Ce; $0.1 \leq x \leq 0.9$), with biphasic powder mixture, $MgCr_2O_4+Cr_2O_3$, as the reference electrode. The pelletised biphasic powder mixtures, $MgFe_2O_4+\alpha\text{-}Fe_2O_3$, $MgAl_2O_4+\alpha\text{-}Al_2O_3$ and $MgCr_2O_4+Cr_2O_3$ were already used as reference electrodes in different combinations during thermodynamics studies by electrochemical method. Furthermore, these biphasic powder mixture could also be used as reference electrodes in fabricating Mg-sensors as observed earlier. The data however could be compared with the variation of emf of Mg-sensor as a function of Mg concentration published earlier [44].

7.3.3 Solid-state electrolytes for magnesium-ion batteries

Recent attempt at characterising solid-state Mg^{2+}-cation batteries can be adjudged and considered a direct challenge to the dominance of Li^{+}-cation batteries, believed to be the top dog of the battery world at the moment.

In considering the safety and energy density limitations faced by current Li^{+}-cation technology, the Mg^{2+}-cation batteries can have a good chance in the market today.

In making a case for Mg^{2+}-cation batteries however, Ikeda *et al.* [254] asserted that if the multivalent cationic conductors of relatively light elements are developed, there is a promise that the higher-energy density solid-state batteries will be fabricated. In recent time, the sulphide, oxide, phosphate and silicate based solid electrolytes have emerged in solid-state batteries [255-262]. More so that most known electrolytes have shown some deficiencies; ranging from low ionic conductivity, poor electrochemical and chemical stabilities. The electrochemical window is also a very important property for solid-state batteries, because solid electrolytes in all the solid-state batteries contact with highly oxidised cathode material and highly reduced anode material. In this study however, the $MgHf_4P_6O_{24}$, $MgCe_4P_6O_{24}$ and $MgZr_4P_6O_{24}$ solid state electrolytes have shown high ionic conductivities with increasing voltage capacity in concentrations.

No doubt, Li^+-cation batteries have an unmatchable combination of high energy and power density, making it the technology of choice for portable electronics, power tools, and hybrid-full electric vehicles [263], so much that if electric vehicles (EVs) replace the majority of gasoline powered transportation, Li^+-cation batteries would have significantly reduced greenhouse emissions [264].

The objective of this proposed research is to develop a rechargeable Mg-battery by fabricating a well-defined, thin, inorganic Mg solid-state electrolyte on the surface of a portion of Mg metal, and thus prevent chemical reaction between the electrolyte and the bulk Mg metal which avoids the undesirable formation of an ion-blocking layer.

The structure of Mg-batteries based on this principle would essentially be solely solid-state and thus would be intrinsically safer than a liquid-type Mg-battery. A prerequisite for developing such a system is centred on fabricating Mg^{2+}-cation conductors. This is problematic as well knowing that only few solid-state electrolytes exhibit Mg-conductivity and this conduction is only observed at high temperatures ($10^{-6}Scm^{-1}$ at 500°C) [26, 265]. The research, therefore, depends on $MgHf_4P_6O_{24}$, $MgCe_4P_6O_{24}$ and $MgZr_4P_6O_{24}$ solid-state electrolytes and the various solid-state solutions as source of novel Mg^{2+}-cation conductor.

With the doubt that Li^+-cation batteries will be able to power the needs of our world today, for portable energy storage in the long run, other types of batteries becomes expedient considering that the shortage of Li and some transition metals currently used in Li^+-cation batteries may one day become a serious issue of concern [266].

It is believed that multivalent-cations based batteries (i.e., Mg^{2+}, Zn^{2+}, Ca^{2+} and Al^{3+}) have developed their own niche with the capability to achieve at least twice the energy density of most monovalent-cation systems such as the Li^+-cation and Na^+-cation batteries. Among the multivalent-cation battery candidates, the Mg-batteries appear a viable alternative to overcome the safety and energy density limitations faced by current Li^+-cation technology [267]. In contrast, the Mg-based electrolytes display high electrode potential, superior safety, wide electrochemical window and with high abundance of the Mg-metal, Mg-batteries should be a viable alternative however, the development of a competitive Mg-battery technology today is plagued by a generally perceived obstacle and notion of low mobility of Mg^{2+}-cation solids [267-269], and the limited development in Mg^{2+}-cation solid-state electrolytes and cathodes has prevented their commercialisation to date. Indeed, a poor mobility of the Mg^{2+}-cation and other multivalent cations [270] earlier characterised, prevents the development of a broad spectrum of cathode materials for Mg-batteries, as are readily available to both the Li^{+}-cation batteries and Na^{+}-cation batteries technology.

Chapter 8

Conferences, Publications and Recognition

8.1 Conferences

1. Mohammed Adamu and Girish M. Kale, New Insight into the Electrical Properties of Ceria Based Solid-state electrolyte Using Sol-Gel Method, *6th EuCheMS Chemistry Congress, 2016, Seville, Spain.*

2. Mohammed Adamu and Girish M. Kale, A Study of the Effect of Sol-Gel Synthesis on Ionic conductivity of $MgZr_4P_6O_{24}$, *MSE 2016 - Materials Science and Engineering, 2016, Darmstadt, Germany.*

3. Mohammed Adamu and Girish Kale, Characterisation of Novel Mg^{2+}-Cation Conducting Double $Mg_{0.5}M_2P_3O_{12}$ (M = Zr, Ce) for Fabricating Solid-State Mg-Sensor, *MRS Spring Meeting & Exhibit, 2017, Phoenix, Arizona.*

4. Mohammed Adamu and Girish Kale, Mg^{2+}-Cation Conducting $MgCe_4P_6O_{24}$ Solid-State Electrolyte for High-Temperature Electrochemical Devices, *MRS Fall Meeting & Exhibit, 2017, Bolton, Massachusetts.*

5. Mohammed Adamu and Girish Kale, Sol-Gel Synthesis and Electrical Properties of $MgZr_4P_6O_{24}$ Composite Solid Electrolyte and its Application for Sensing Mg in Molten Al, *42nd International Conference & Exposition on Advanced Ceramics and Composites, 2018, Daytona Beach, Florida.*

8.2 Publications

8.2.1 Published article

1. Mohammed Adamu and Girish Kale. Novel Sol-Gel Synthesis of $MgZr_4P_6O_{24}$ Composite Solid-state electrolyte and Newer Insight into the Mg^{2+}-Ion Conducting Properties Using Impedance Spectroscopy. *Journal of Physical Chemistry C, 2016,* ***120,*** *17909-17915.*

8.2.2 Potential publications

1. Mohammed Adamu and Girish Kale. Novel Mg^{2+}-Cation Conducting Solid-State Electrolyte for Fabricating High-Temperature Mg-Sensors. (*Submitted to 14th International Conference on Materials Chemistry, (MC14) Birmingham, United Kingdom*).

2. Mohammed Adamu and Girish Kale. Assessment of $MgZr_4P_6O_{24}$ Composite Electrolyte for Fabricating Solid-State Mg-Sensor and Sensing Mg in Liquid Al (*Submitted to 2019 MRS Fall Meeting & Exhibit, Bolton, Massachusetts*).

3. Mohammed Adamu, Kallarackel Thomas Jacob and Girish Kale. Assessment of $MgZr_4P_6O_{24}$ as a Solid Electrolyte for Sensing Mg in Molten Non-Ferrous Alloys (*Submitted to Journal of The Electrochemical Society; ECS Journal of Solid State Science and Technology*).

4. Mohammed Adamu and Girish Kale. $MgZr_2Hf_2P_6O_{24}$ Solid-State Electrolyte in Sensor Fabrication (*Pending submission*) - from Chapter 3 & 4.

5. Mohammed Adamu and Girish Kale. Novel $MgZr_2Ce_2P_6O_{24}$ high-Conducting Electrolyte in Sensor Fabrication (*Pending submission*) - from Chapter 3 & 4.

6. Mohammed Adamu and Girish Kale. New $MgZr_{4(1-x)}Hf_{4x}P_6O_{24}$ $(0.1 \leq x \leq 0.9)$ Solid-State Solution as Ionic Conductor in High-Temperature Electrochemical Devices (*Pending submission*) - from Chapter 3 & 5.

7. Mohammed Adamu and Girish Kale. Potential Application of Mg^{2+}-Cation Conducting $MgHf_4P_6O_{24}$ Electrolyte in High-Temperature Electrochemical Sensor (*Pending submission*) - from Chapter 3 & 6.

8.2.3 Recognition and Grants

1. Travel Grants for PhD Students & Early Career Scientist. Materials Chemistry Division (MCD), RSC Travel Grant Number (T19 - 4439).
   Research Paper: Promising $MgZr_4P_6O_{24}$ Composite Solid-State Electrolyte for Sensing Mg in Molten Non-Ferrous Alloys. *2019 MRS Spring Meeting and Exhibit, Phoenix, Arizona, United States of America. April 22-26, 2019.*

2. Travel Grants for PhD Students & Early Career Scientist. Materials Chemistry Division (MCD), RSC Travel Grant Number (T19 - 1604)
   Research Paper: Novel Mg^{2+}-Cation Conducting Solid-State Electrolyte for Fabricating High-Temperature Mg-Sensors. *14th International Conference on Materials Chemistry (MC14), Birmingham, United Kingdom. July 8-11, 2019.*

3. Travel Grants for PhD Students & Early Career Scientist. Materials Chemistry Division (MCD), Royal Society of Chemistry (RSC).
   Research Paper: Effect of Sol-Gel Synthesis on Ionic Conductivity of Ceramic $MgZr_4P_6O_{24}$. *Materials Science and Engineering (MSE-2016), Darmstadt, Germany. September 27-29, 2016.*

4. University Conference Grant. School of Chemical and Process Engineering.
   Research Paper: New Insight into the Electrical Properties of Ceria-Based Solid Electrolyte Using Sol-Gel Method. *6th EuCheMS Chemistry Congress, Seville, Spain. September 11-15, 2016.*

References

1. Smith CS. On material structure and human history. *Annu. Rev. Mater. Sci.* 1986;16(1):1-12.

2. Kelly MJ. Mesoscopic systems: Will they ever be manufacturable? *Adv. Mater.* 1997;9(11):857-860.

3. Abraham T. Electronics and environmental applications push overall use of advanced ceramics. *Ceram. Indus.* 1997;9:84-88.

4. Newnham RE, Ruschau GR. Smart electroceramics. *J. Am. Ceram. Soc.* 1991; 74(3):463-480.

5. Swartz S. Topics in electronic ceramics. IEEE Transactions on Electrical Insulation. 1990;25(5):935-987.

6. Avedesian MM, Baker H. ASM specialty handbook: Magnesium and magnesium alloys. ASM international, 1999.

7. Hirsch J, Al-Samman T. Superior light metals by texture engineering: optimized aluminum and magnesium alloys for automotive applications. *Acta Materialia.* 2013;61:818-843.

8. Joost WJ, Krajewski PE. Towards magnesium alloys for high-volume automotive applications. *Scripta Materialia.* 2017;128:107-112.

9. Friedrich H, Schumann S. Research for a "new age of magnesium" in the automotive industry. *J. Mater. Process. Technol.* 2001;117(3):276-281.

10. Tiwari BL. Demagging processes for aluminum alloy scrap. *JOM.* 1982;34(7): 54-58.

11. Fergus JW, Hui S. Solid electrolyte sensor for measuring magnesium in molten aluminum. *Metall. Mater. Trans. B.* 1995;26(1):1289-1291.

12. Kale G, Kurchania R. On-line electrochemical sensors in molten metal processing technology: A Review. *ChemInform*. 2000;31(6).

13. Fergus JW. Using chemical sensors to control molten metal processing. *JOM*. 2000;52(10):14.

14. Tarascon JM, Armand M. Issues and challenges facing rechargeable lithium batteries. *Nature*. 2001;414(6861):359-367.

15. Armand M, Tarascon JM. Building better batteries. *Nature*. 2008;451(7179): 652-657.

16. Owen JR. Rechargeable lithium batteries. *Chem. Soc. Rev*. 1997;26(4):259-267.

17. Inaba H, Tagawa H. Ceria-based solid electrolytes. *Solid State Ionics*. 1996; 83(1):1-16.

18. Knauth P. Inorganic solid Li ion conductors: An overview. *Solid State Ionics* 2009;180(14):911-916.

19. Fergus JW. Ion transport in sodium ion conducting solid electrolytes. *Solid State Ionics*. 2012;227:102-112.

20. Tamura S, Mori A, Imanaka N. Li^+-ion conduction in (Gd, La)$_2$O$_3$–LiNO$_3$ system. *Solid State Ionics*. 2004. 175(1):467-470.

21. Tamura S, Yamane M, Hoshion Hoshomo. Highly conducting divalent Mg^{2+}-ion solid electrolytes with well-ordered three-dimensional network structure. *J. Solid State Chem*. 2016;235:7-11.

22. Aono H, Imanaka N, Adachi G. High Li^+ conducting ceramics. *Acc. Chem. Res*. 1994;27(9):265-270.

23. Pratt J. Applications of solid electrolytes in thermodynamic studies of materials: a review. *Metall. Trans. A*. 1990;21(5):1223-1250.

24. Adamu M, Kale GM. Novel sol-gel synthesis of $MgZr_4P_6O_{24}$ composite solid electrolyte and newer insight into the Mg^{2+}-ion conducting properties using impedance spectroscopy. *J. Phys. Chem. C*. 2016;120(32):17909-17915.

25. Kazakos-Kijowski A, Komarneni S, Agrawal D, Roy R. Synthesis, crystal data and thermal stability of magnesium zirconium phosphate [$MgZr_4(PO_4)_6$]. *Mat. Res. Bull.* 1988;23(8):1177-1184.

26. Ikeda S, Takahashi M, Ishikawa J, Ito K. Solid electrolytes with multivalent cation conduction. 1. Conducting species in Mg-Zr-PO_4 system. *Solid State Ionics.* 1987;23(1-2):125-129.

27. Shannon RD. Revised effective ionic radii and systematic studies of interatomic distances in halides and chalcogenides. *Acta Crystallogr., Sect. A: Cryst. Phys., Diffr., Theor. Gen. Crystallogr.* 1976;32(5):751-767.

28. Barth S, Olazcuaga S, Gravereau P. $Mg_{0.5}Ti_2(PO_4)_3$ - A new member of the NASICON family with low thermal expansion. *Mater. Lett.* 1993;16(2-3):96-101.

29. Pet'kov VI, Kurazhkovskaya VS, Orlova AI, Spiridonova ML. Synthesis and crystal chemical characteristics of the structure of $M_{0.5}Zr_2(PO_4)_3$ phosphates. *Crystallogr. Rep.* 2002;47(5):736-743.

30. Orlova A, Artem'eva GY, Korshunov I. Double phosphate of hafnium and the alkaline-earth elements [Mg, Ca, Sr, Ba]. *Zh. Neorg. Khim.* 1990;35(5):1091-1094.

31. Takahashi H, Takamura H. Preparation and ionic conductivity of Al-doped $Mg_{0.5}Ti_2 (PO_4)_3$. *Mater. Trans.* 2012;53(5):932-935.

32. Ikeda S, Takahashi M, Ishikawa J, Ito K. Solid electrolytes with multivalent cation conduction. 1. Conducting species in Mg-Zr-PO_4 system. *Solid State Ionics.* 1987;23(1-2):125-129.

33. Nomura K, Ikeda S, Ito K, Einaga H. Framework structure, phase transition, and transport properties in $M^{II}Zr_4(PO_4)_6$ compounds (M^{II}=Mg, Ca, Sr, Ba, Mn, Co, Ni, Zn, Cd, and Pb). *Bull. Chem. Soc. Jpn.* 1992;65(12):3221-3227.

34. Imanaka N, Okazaki Y, Adachi G. Divalent magnesium ionic conduction in $Mg_{1-2x}(Zr_{1-x} Nb_x)_4P_6O_{24}$ (x = 0-0.4) solid solutions. *Electrochem. Solid State Lett.* 2000;3(7):327-329.

35. Imanaka N, Okazaki Y, Adachi G. Optimization of divalent magnesium ion conduction in phosphate based polycrystalline solid electrolytes. *Ionics,* 2001; 7(4-6):440-446.

36. Anuar N, Adnan S, Mohamed N. Characterization of $Mg_{0.5}Zr_2(PO_4)_3$ for potential use as electrolyte in solid state magnesium batteries. *Ceram. Int.* 2014;40(8):13719-13727.

37. Omote A, Yotsuhashi S, Zenitani Y, Yamada Y. High ion conductivity in $MgHf(WO_4)_3$ solids with ordered structure: 1-D alignments of Mg^{2+} and Hf^{4+} Ions. *J. Am. Ceram. Soc.* 2011;94(8):2285-2288.

38. Higashi S, Miwa K, Aoki M, Kensuke T. A novel inorganic solid state ion conductor for rechargeable Mg batteries. *Chem. Commun.* 2014;50(11):1320-1322.

39. Kajihara K, Nagano H, Tsujita T, Munakata H, Kanamura K. High-temperature conductivity measurements of magnesium-ion-conducting solid oxide $Mg_{0.5-x}(Zr_{1-x}Nb_x)_2(PO_4)_3$ (x = 0.15) using Mg metal electrodes. *J. Electrochem. Soc.* 2017;164(9):A2183-A2185.

40. Goodenough JB, Hong HYP, Kafalas JA. Fast Na^+-ion transport in skeleton structures. *Mater. Res. Bull.* 1976;11(2):203-220.

41. Mustaffa NA, Mohamed NS. Zirconium-substituted $LiSn_2P_3O_{12}$ solid electrolytes prepared via sol–gel method. *J. Sol-Gel. Sci. Technol.* 2016;77(3):585-593.

42. Zhang L, Fray DJ, Vangrunderbeek J, de Schutter F. Electrochemical sensor for measuring magnesium content in molten aluminium. *J. Appl. Electrochem.* 1996;26(3):269-275.

43. Fergus JW. Sensors for monitoring the quality of molten aluminum during casting. *J. Mater. Eng. Perform.* 2005;14(2):267-275.

44. Kale GM, Wang L, Hong Y. High-temperature sensor for in-line monitoring of Mg and Li in molten Al employing ion-conducting ceramic electrolytes. *Int. J. Appl. Ceram. Technol.* 2004;1(2):180-187.

45. DeYoung DH, Moreland JB, Mutharasan R. "Closed loop melt composition control by in-line computer-aided alloying," *Light Metals 1995,* ed. Evans J (Warrendale, PA: *TMS,* 1995), 840-850.

46. Howie BJ, Tiwari BL. "Determination of magnesium in molten aluminium alloy using an electrochemical sensor," *Light Metals 1989,* ed. Campbell PG (Warrendale, PA: *TMS,* 1989), 895-902.

47. Tiwari BL, Howie BJ. "Electrochemical probe for measuring magnesium concentration in molten aluminium," U.S. patent 4,601,810 (22 July 1986).

48. Belton GR, Rao YK. A galvanic cell study of activities in Mg-Al liquid alloys. *Trans. Metall. Soc. AIME,* 1969;245:2189-2193.

49. Tsyplakova MM, Strelets Kh.L. Study of the thermodynamic properties of the magnesium-aluminum system by the EMF method. *J. Appl. Chem. USSR.* 1969;42(11):2354-2359.

50. Larose S, Dubreuil A, Pelton AD. Solid electrolyte probes for magnesium, calcium and strontium in molten aluminum. *Solid State Ionics.* 1991;47(3-4): 287-295.

51. Fergus JW. Electrochemical magnesium sensors for use in aluminum processing. *JOM.* 1995;47(11):36-40.

52. Fraden J. "Handbook of Modern Sensors: Physics, designs and applications," Springer Science and Business Media, New York, 2004.

53. Livage J, Henry M, Sanchez C. Sol-gel chemistry of transition metal oxides. *Prog. Solid State Chem.* 1988;18(4):259-341.

54. Hu L, Yoko T, Kozuka H, Sakka S. Effects of solvent on properties of sol-gel-derived TiO_2 coating films. *Thin Solid Films.* 1992;219(1-2):18-23.

55. Brinker CJ, Scherer GW. Sol-gel science: The physics and chemistry of sol-gel processing. Academic Press, New York, 2013, 912.

56. Brinker CJ, Frye GC, Hurd AJ, Ashley CS. Fundamentals of sol-gel dip coating. *Thin Solid Films.* 1991;201(1):97-108.

57. Dislich H. New Routes to multicomponent oxide glasses. *Angew. Chem. Internat. Edit.* 1971;10(6):363-370.

58. Zelinski B, Uhlmann DRJ. Gel technology in ceramics. *J. Phys. Chem. Solids.* 1984;45(10):1069-1090.

59. Mackenzie JD. Unusual Non-crystalline solids from gels in 2004. *J. Non-Cryst. Solids.* 1985;73(1-3):631-637.

60. Iler RK. "The Chemistry of silica: Solubility, polymerisation, colloid and surface properties and biochemistry," John Wiley and Sons, New York, 1979, 30-62.

61. Bradley DC, Mehrotra RC, Gaur DP. "Metal alkoxides," Academic Press, London, 1978.

62. Nishio K, Sei T, Tsuchiya T. Preparation and electrical properties of ITO thin films by dip-coating process. *J. Mater. Sci.* 1996;31(7):1761-1766.

63. Nishio K, Miyake S, Sei T, Watanabe Y, Tsuchiya T. Preparation of highly oriented thin film exhibiting transparent conduction by the sol-gel process. *J. Mater. Sci.* 1996;31(14):3651-3656.

64. Nishio K, Kudo C, Nagahama T, Manabe T. Preparation and characterisation of epitaxial Bi_2WO_6 thin films prepared by a sol-gel process. MRS Online proceedings library archive. 2000;623 (Symposium U).

65. Nishio K, Tsuchiya T. Sol-gel processing of thin films with metal salts. "Handbook of sol-gel science and technology: Processing, characterisation and applications," Kluwer Academic Publishers, Boston, 2005, 59-76.

66. Nishio K, Watanabe Y, Tsuchiya T. Epitaxial growth of $Sr_xBa_{1-x}Nb_2O_6$ thin films prepared from sol-gel process. *J. Sol-Gel Sci. Technol.* 2003;26(1-3):245-250.

67. Kodaira T, Nishio K, Yamaguchi I, Suzuki S, Tsukada K, Tsuchiya T. Synthesis and properties of highly conductive thin films as buffer layer from sol-gel process. *J. Sol-Gel Sci. Technol.* 2003;26(1-3):1049-1053.

68. Brinker CJ, Scherer GW, Roth EP. Sol→gel→glass: II. Physical and structural evolution during constant heating rate experiments. *J. Non-Cryst. Solids.* 1985;72(2-3):345-368.

69. Scherer GW, Brinker CJ, Roth EP. Sol→gel→glass: III. Viscous sintering. *J. Non-Cryst. Solids.* 1985;72(2-3):369-389.

70. Scherer GW. Drying gels: I. General theory. *J. Non-Cryst Solids.* 1986;87(1-2):199-225.

71. Ipser H, Mikula A, Katayama I. Overview: The emf method as a source of experimental thermodynamic data. *Calphad.* 2010;34(3):271-278.

72. Hagenmuller P, Van Gool W. "Solid Electrolytes: General principles, characterisation, materials, applications," Academic Press, New York, 1978.

73. Subbarao EC. "Solid electrolytes and their applications," Plenum Press, New York, 1980.

74. Rickert H. "Electrochemistry of Solids: An introduction," Springer-Verlag, Berlin, 1982.

75. Goto KS. "Solid state electrochemistry and its applications to sensors and electronic devices," Elsevier, Amsterdam, 1988.

76. Takehiko T (ed). "High conductivity solid ionic conductors: Recent trends and applications," World Scientific, Hong Kong, 1989.

77. Fischer WA, Janke D. "Metallurgische Elektrochemie," Verlag Stahleisen, Dusseldorf, 1975.

78. Hladik J. "Physics of Electrolytes: Thermodynamics and electrode processes in solid state electrolytes (Vol. 2)," Academic Press, London, 1972.

79. Chang YA, Sommer F. "Thermodynamics of Alloy Formation, in: *TMS* 1997. Warrendale, 77, 1997.

80. Kummer JT. β-alumina electrolytes. *Prog. Solid State Chem.* 1972;7:141-175.

81. Stevens R, Binner J. Structure, properties and production of β-alumina. *J. Mater. Sci.* 1984;19(3):695-715.

82. Collongues R, Gourier D, Kahn A, Boilot JP, Colomban Ph, Wicker A. β alumina, a typical solid electrolyte: Latest developments in fundamental approach and in battery utilsation. *J. Phys. Chem. Solids.* 1984;45(10):981-1013.

83. West AR. Solid electrolytes. *Ber. Bunsenges. Phys. Chem.* 1989;93(11):1235-1241.

84. Ferloni P, Magistris A. New materials for solid state electrochemistry. *J. Phys. IV France.* 1994;4:C1-3-C1-15.

85. Hara N, Macdonald DD. Development of Dissolved Hydrogen Sensors Based on Yttria-Stabilized Zirconia Solid Electrolyte with Noble Metal Electrodes. *J. Electrochem. Soc.* 1997;144(12):4152-4157.

86. Tan Y, Tan T. Characteristics and modeling of a solid state hydrogen sensor. *J. Electrochem. Soc.* 1994;141(2):461-467.

87. Zheng M, Zhen X. Hydrogen probe equipped with $SrCeO_3$-based proton conductor and Ca/CaH_2 reference electrode. *Metall. Mater. Trans. B.* 1993;24(5):789-794.

88. Fukatsu N, Kurita N, Yajima T, Koide K, Ohashi T. Proton conductors of oxide and their application to research into metal-hydrogen systems. *J. Alloys Compd.* 1995;231(1-2):706-712.

89. Casciola M, Palombari R. Proton-metal ion conduction in monoalkali salt forms of α-zirconium phospate. *Solid State Ionics.* 1991;47(1-2):155-159.

90. Chehab SF, Canaday JD, Kuriakose AK, Wheat TA, Ahmad A. A hydrogen sensor based on bonded hydronium NASICON. *Solid State Ionics.* 1991;45(3-4):299-310.

91. Schwandt C, Fray DJ. Hydrogen sensing in molten aluminium using a commercial electrochemical sensor. *Ionics.* 2000;6(3):222-229.

92. Zhang L, Fray DJ, Dekeyser JC, De Schutter F. Reference electrode of simple galvanic cells for developing sodium sensors for use in molten aluminum. *Metall. Mater. Trans. B.* 1996;27(5):794-800.

93. Dekeyser JC, De Schutter F, Van der Poorten C, Zhang L, Fray DJ. An electrochemical sodium sensor for aluminium melts. *Sens. Actuator B-Chem.* 1995;24(1-3):273-275.

94. Kirchnerovà J, Pelton AD. Solid electrolyte probes for strontium employing a $SrCl_2$-AgClAg reference and thermodynamic evaluation of the $SrCl_2$-AgCl system. *Solid State Ionics.* 1996;93(1-2):165-170.

95. Zhang Q. "Fluoride-based sodium sensor for use in molten aluminum," M.S Thesis, Auburn University, 1998.

96. Smart LE, Moore EA. "Solid state chemistry: An introduction (4th ed).," CRC press, 2012, 494.

97. Wagner C. Mechanism of electric conduction in Nernst glower. *Sci. Nat.* 1943;31(23):265-268.

98. Gobechiya ER, Sukhanov MV, Pet'kov VI, Kabalov Yu K. Crystal structure of the double magnesium zirconium orthophosphate at temperatures of 298 and 1023K. *Crystallogr. Rep.* 2008;53(1):53-59.

99. Lee WC, Huang CY, Tsao Liang-K, Wu Yu-C. Chemical composition and tolerance factor at the morphotropic phase boundary in $(Bi_{0.5}Na_{0.5})TiO_3$-based piezoelectric ceramics. *J. Eur. Ceram. Soc.* 2009;29(8):1443-1448.

100. Wang L, Kumar RV. A new SO_2 gas sensor based on an Mg^{2+} conducting solid electrolyte. *J. Electroanal. Chem.* 2003;543(2):109-114.

101. Ikeda S, Kato S, Nomura K, Ito K, Einaga H, Saito S, Fujita Y. Carbon dioxide sensor using solid electrolytes with zirconium phosphate framework. *Solid State Ionics.* 1994;70-71:569-571.

102. Nomura K, Ikeda S, Ito K, Einaga H. Framework structure, phase transition and ionic conductivity of $MgZr_4(PO_4)_6$ and $ZnZr_4(PO_4)_6$. *J. Electroanal. Chem.* 1992;326(1-2):351-356.

103. Shannon RT, Prewitt CT. Effective ionic radii in oxides and fluorides. *Acta Crystallogr. B.* 1969;25(5):925-946.

104. Mullica DF, Lok CKC, Grossie DA. A new nine-coordination system: pentagonal interpenetrating tetrahedral polyhedron. *J. Solid State Chem.* 1986;63(3):452-454.

105. Zubkova NV, Kabalov Yu K, Orlova AI, Kitaev DB, Kurazhkovskaya VS. The synthesis and structure of alkaline earth and cerium (IV) phosphates (Ce, B,□)$[PO_4]$(B= Mg, Ca). *Crystallogr. Rep.* 2003;48(3):401-405.

106. Kroger FA, Vink HJ. "Relations between concentrations of imperfections in crystalline solids, in: Solid State Physics, Volume 3, Ed., Seitz F and Turnbull D," Academic Press, New York, 1956.

107. Kröger FA, Vink HJ. Relations between the concentrations of imperfections in solids. *J. Phys. Chem. Solids.* 1958;5(3):208-223.

108. Anderson JC, Leaver KD, Rawlings RD, Alexander JM. "Microstructure and properties (4th ed) ed. Materials Science," 1990, Chapman and Hall, London, 1990.

109. Norton HN. "Handbook of transducers," Prentice Hall, London, 1989, 480.

110. Fraden J. Handbook of Modern Sensors: Physics, Designs and Applications. Springer, San Diego, 2003;17(2), 499-501.

111. Vetelino J, Reghu A. "Introduction to sensors," CRC Press, Boca Raton, 2017.

112. Park C, Akbar S, Weppner W. Ceramic electrolytes and electrochemical sensors. *J. Mater. Sci.* 2003;38(23):4639-4660.

113. Kiukkola K, Wagner C. Measurements on galvanic cells involving solid electrolytes. *J. Electrochem. Soc.* 1957;104(6):379-387.

114. Kiukkola K, Wagner C. Galvanic cells for the determination of the standard molar free energy of formation of metal halides, oxides, and sulfides at elevated temperatures. *J. Electrochem. Soc.* 1957;104(5):308-316.

115. Brett CMA. "Electrochemistry: Principles, Methods and Applications," Oxford University Press, New York, 1994.

116. Alcock C. Solid state sensors and process control. *Solid State Ionics.* 1992;53: 3-17.

117. Stradiotto NR, Yamanaka H, Zanoni MVB. Electrochemical Sensors: A Powerful Tool in Analytical Chemistry. *J. Braz. Chem. Soc.* 2003;14(2):159.

118. Sato H. "Solid Electrolytes," Springer-Verlag, Berlin, 1977.

119. Collin G, Boilot JP. "Superionic Solids and Solid Electrolytes," Academic Press, San Diego, 1989.

120. Wang L, Kumar RV. Cross-sensitivity effects on a new carbon dioxide gas sensor based on solid bielectrolyte. *Meas. Sci. Technol.* 2004;15(5):1005.

121. Holzinger M, Maier J, Sitte W. Potentiometric detection of complex gases: application to CO_2. *Solid State Ionics.* 1997;94(1-4):217-225.

122. Jacob KT. Potentiometric Determination of the Gibbs Free Energy of Formation of Cadmium and Magnesium Chromite. *J. Electrochem. Soc.* 1977;124:1827-1831.

123. Fujii K, Nagasaka T, Hino M. Activities of the constituents in spinel solid solution and free energies of formation of MgO, $MgO{\cdot}Al_2O_3$. *ISIJ Int.* 2000;40(11):1059-1066.

124. Alper AM, McNally RN, Doman RC, Keihn FG. Phase Equilibria in the System $MgO\text{-}MgCr_2O_4$. *J. Am. Ceram. Soc.* 1964;47(1):30-33.

125. Yao PC, Fray DJ. Determination of the lithium content of molten aluminum using a solid electrolyte. *Metall. Trans. B.* 1985;16(1):41-46.

126. Fray, DJ. Possible uses of sensors in the aluminium industry. *Mater. Sci. Technol.* 1987;3(1):61-65.

127. Fray DJ. Developments in on-line sensing in molten metals using solid electrolytes. *ATB Metall.* 1990;30(3):63-68.

128. Pathak A, Pramanik P. Nano-particles of oxides through chemical methods. *Proc. Natl. Acad. Sci. India A.* 2001;67(1):47-70.

129. Segal DL. "Processing of Ceramics, in: Materials Science and Technology: A Comprehensive Treatment," Brook RJ (ed) Volume 17A. Weinheim, VCH Publishers, 1996, 69.

130. Segal D. Chemical synthesis of ceramic materials. *J. Mater. Chem.* 1997;**7**(8): 1297-1305.

131. Mielewczyk A, Molin S, Gdula K, Jasinski G, Kusz B, Jasinski P, Gazda M. Structure and electric properties of double magnesium zirconium orthophosphate. *Mater. Chem.* 2010;62(4):477-480.

132. Jolivet JP, Henry M, Livage J. "Metal oxide chemistry and synthesis - from solution to solid state," John Wiley and Sons Ltd., England, 2000.

133. Fray DJ. The use of solid electrolytes as sensors for applications in molten metals. *Solid State Ionics.* 1996;86-88(2):1045-1054.

134. Seetharaman S, Sichen D. "Development and Application of Electrochemical Sensors for Molten Metals Processing. Emerging Separation Technologies for Metals II," 1996:317-340.

135. Fray DJ. Potentiometric gas sensors for use at high temperatures. *Mater. Sci. Technol.* 2000;16(3):237-242.

136. Hench LL, West JK. The sol-gel process. *Chem. Rev*. 1990;90(1):33-72.

137. Livage J, Ganguli D. Sol-gel electrochromic coatings and devices: a review. *Sol. Energy Mater. Sol. Cells.* 2001;68(3):365-381.

138. Pierre AC. "Introduction aux procedes sol-gel," Septima, Paris, 1992.

139. Hong HYP. Crystal structures and crystal chemistry in the system $Na_{1+x}Zr_2Si_xP_{3-x}O_{12}$. *Mater. Res. Bull.* 1976;11(2):173-182.

140. Bakker E, Qin Y. Electrochemical sensors. *Anal. Chem*. 2006;78(12):3965-3984.

141. Singhal SC, Kendall K. "High-temperature solid oxide fuel cells: Fundamentals, design and applications," Elsevier, 2003:406.

142. Keith M. Phase Equilibria in the System $MgO-Cr_2O_3-SiO_2$. *J. Am. Ceram. Soc.* 1954;37(10):490-496.

143. Wilde W, Rees W. The Ternary System $MgO-Al_2O_3-Cr_2O_3$. *Brit. Ceram. Trans.* 1943;42(7):123-155.

144. Warshaw I, Keith ML. Solid Solution and Chromium Oxide loss in part of the system $MgO-Al_2O_3-Cr_2O_3-SiO_2$. *J. Ame. Ceram. Soc.* 1954;37(4):161-168.

145. Hallstedt B.Thermodynamic assessment of the system $MgO-Al_2O_3$. *J. Am. Ceram. Soc.* 1992;75(6):1497-1507.

146. Mackenzie RC. *Note.* Talanta, 1969;16(8):1227-1230.

147. Thompson H. Recommendations for nomenclature of thermal analysis (IUPAC Recommendations 1973). *Pure Appl. Chem*. 1974;37:439-444.

148. Hill JO. "For better thermal analysis and calorimetry. International Confederation for Thermal Analysis," 1991.

149. Capurso G. Innovative materials and systems for solid state hydrogen storage. *PhD thesis*, University of Padova, 2013.

150. Höhne GWH, Hemminger W, Flammersheim HJ. "Theoretical Fundamentals of Differential Scanning Calorimeters, in Differential Scanning Calorimetry," Springer, 1996, 21-40.

151. Gilfrich J. "Structural and chemical analysis of materials: X-ray, electron and neutron diffraction, ion spectrometry and electron microscopy, ed. JP Eberhart John Wiley and Sons Ltd., Chichester,"1993;22(2):119-120.

152. Eberhart J. Structural and chemical analysis of materials. X-ray, electron, and neutron diffraction; X-ray, electron, and ion spectrometry; electron microscopy. *J. Appl. Crystallogr.* 1993;26:145.

153. Hammond C. "Introduction to Crystallography, Microscopy Handbooks. Vol. 19," Oxford University Press, Oxford, 1997.

154. Bish DL, Howard S. Quantitative phase analysis using the Rietveld method. *J. Appl. Crystallogr.* 1988;21(2):86-91.

155. Larson AC, Von-Dreele RB. General Structure Analysis System (GSAS). *In Los Alamos National Laboratory Report - LAUR.* 2004:86-748.

156. Toby BH, EXPGUI. A graphical user interface for GSAS. *J. Appl. Crystallogr.* 2001;34(2):210-213.

157. Jenkins, R. and R. Zinder. "Introduction to X-ray Powder Difrattometry," John Wyley and Sons, 1996.

158. Jenkins R, Snyder RL. "Diffraction theory: Introduction to X-ray Powder Diffractometry," Vol.138, 1996:47-95.

159. Cullity BD. "Answers to Problems: Elements of X-ray Diffraction," Addison-Wesley, 1978.

160. Klung H, Alexander L. "X-ray diffraction procedures," Wiles, New York, 1974:687.

161. Swartz S, Shrout TR. Fabrication of perovskite lead magnesium niobate. *Mater. Res. Bull.* 1982;17(10):1245-1250.

162. Shrout TR, Halliyal A. Preparation of lead-based ferroelectric relaxors for capacitors. *Am. Ceram. Soc. Bull.* 1987;66(4):704-711.

163. Chen J, Harmer MP. Microstructure and dielectric properties of Lead Magnesium Niobate-Pyrochlore diphasic mixtures. *J. Am. Ceram. Soc.* 1990;73(1):68-73.

164. Shrout T, Swartz S. Dielectric properties of pyrochlore lead magnesium niobate. *Mater. Res. Bull.* 1983;18(6):663-667.

165. Ananta S, Thomas N. A modified two-stage mixed oxide synthetic route to lead magnesium niobate and lead iron niobate. *J. Eur. Ceram. Soc.* 1999;19(2): 155-163.

166. Ananta S, Thomas N. Relationships between sintering conditions, microstructure and dielectric properties of lead magnesium niobate. *J. Eur. Ceram. Soc.* 1999;19(5):629-635.

167. Cullity BD, Cullity SR, Stock S. Elements of X-ray Diffraction, Third Edition, Prentice Hall, New York, 2001.

168. Stokes A, Wilson A. The diffraction of X rays by distorted crystal aggregates-I. Proceedings of the Physical Society, 1944;56(3):174.

169. Bushroa, AR, Rahbari RG, Muhamad MR. Approximation of crystallite size and microstrain via XRD line broadening analysis in TiSiN thin films. *Vacuum.* 2012;86(8):1107-1112.

170. Holzwarth U, Gibson N. The Scherrer equation versus the 'Debye-Scherrer equation'. *Nat. Nanotechnol.* 2011;6(9):534-534.

171. Singh L, Rai U, Mandal, K. Dielectric, modulus and impedance spectroscopic studies of nanostructured $CaCu_{2.70}Mg_{0.30}Ti_4O_{12}$ electro-ceramic synthesized by modified sol–gel route. *J. Alloys Compd.* 2013;555:176-183.

172. Lin HL, Zhang GC, Huang YT, Lin SY. An Investigation of Indomethacin–Nicotinamide Cocrystal Formation Induced by Thermal Stress in the Solid or Liquid State. *J. Pharm. Sci.* 2014;103(8):2386-2395.

173. Lin HL, Wu TK, Lin SY. Screening and characterization of cocrystal formation of metaxalone with short-chain dicarboxylic acids induced by solvent-assisted grinding approach. *Thermochim Acta.* 2014;575:313-321.

174. Gul I, Maqsood A. Structural, magnetic and electrical properties of cobalt ferrites prepared by the sol-gel route. *J. Alloys Compd.* 2008;465(1):227-231.

175. Valdes LB. Resistivity measurements on germanium for transistors. Proceedings of the IRE, 1954;42(2):420-427.

176. Schroder DK. "Semiconductor material and device characterization," John Wiley and Sons, 2006.

177. Dimos D, Chaudhari P, Mannhart J, LeGoues FK. Orientation dependence of grain-boundary critical currents in $YBa_2Cu_3O_{7-\delta}$ bicrystals. *Phys. Rev. Lett.* 1988;61(2):219.

178. Sumino H, Sakurai O, Shinozaki K, Kato M, Mizutani N. A new instrument to measure the electrical properties in very narrow regions in ceramics. *J. Mater. Sci. Lett.* 1991;10(17):1026-1028.

179. Irvine JT, Sinclair DC, West AR. Electroceramics: characterisation by impedance spectroscopy. *Adv. Mater.* 1990;2(3):132-138.

180. Sinclair DC. Characterisation of electro-materials using ac impedance spectroscopy. *Bol. Soc. Esp. Ceram. V.* 1995;34(2):55-65.

181. Lai W, Haile SM. Impedance spectroscopy as a tool for chemical and electrochemical analysis of mixed conductors: a case study of ceria. *J. Am. Ceram Soc.* 2005;88(11):2979-2997.

182. Bauerle J. Study of solid electrolyte polarization by a complex admittance method. *J. Phys. Chem. Solids.* 1969;30(12):2657-2670.

183. Macdonald JR. Simplified impedance/frequency-response results for intrinsically conducting solids and liquids. *J. Chem. Phys.* 1974;61(10):3977-3996.

184. Jonscher A. Analysis of the alternating current properties of ionic conductors. *J. Mater. Sci.* 1978;13(3):553-562.

185. McDonald, JR. Superionic Conductors, ed. G.D. Mahan GD, Roth WL. Plenum Press, New York, 1976:81.

186. Kurzydlowski KJ, Ralph B. The quantitative description of the microstructure of materials. Vol. 3. CRC Press, London, 1995.

187. Allen JL, Thompson T, Sakamoto J, Becker CR, Jow R, Wolfenstine J. Transport properties of $LiCoPO_4$ and Fe-substituted $LiCoPO_4$. *J. Power Sources.* 2014;254:204-208.

188. Austin LB. Evaluation and optimisation of diamond-like carbon for tribological applications. University of Leeds, 2014.

189. Jung SM, Sohn I, Min DJ. Chemical analysis of argon-oxygen decarburization slags in stainless steelmaking process by X-ray fluorescence spectrometry. *X-Ray Spectrom.* 2010;39(5):311-317.

190. Buhrke VE, Jenkins R, Smith DK. "A practical guide for the preparation of specimens for x-ray fluorescence and x-ray diffraction analysis," Wiley-VCH, 1998.

191. Mori M, Suda E, Pacaud B, Murai K, Moriga T. Effect of components in electrodes on sintering characteristics of $Ce_{0.9}Gd_{0.1}O_{1.95}$ electrolyte in intermediate-temperature solid oxide fuel cells during fabrication. *J Power Sources.* 2006;157(2):688-694.

192. Pokol G., T. Leskelä, and L. Niinistö, Thermal behaviour of sulphato and nitrato complexes of cerium (IV). *J. Therm. Anal. Calorim.* 1994;42(2-3):343-359.

193. Guillou N, Auffrédic J, Louër D. An unexpected double valence change for cerium during the thermal decomposition of $CeK_2(NO_3)_6$. *J. Solid State Chem.* 1995;115(1):295-298.

194. Züttel, A. Materials for hydrogen storage. *Mater. Today.* 2003;6(9):24-33.

195. Sugantha M, Varadaraju U. Ionic conductivity of Li^+ ion conductors $Li_2M^{3+}M^{4+}P_3O_{12}$. *Solid State Ionics.* 1997;95(3):201-205.

196. López-Cota FA, Cepeda-Sanchez NM, Diaz-Guillen JA, Dura OJ, Lopez de la Torre MA, Maczka M, Ptak M, Fuentes AF. Electrical and thermophysical properties of mechanochemically obtained lanthanide hafnates. *J. Am. Ceram.* Soc. 2017;100(5):1994-2004.

197. Cançado LG, Takai K, Enoki T, Endo M, Kim YA, Mizusaki H, Jorio A, Coelho LN, Magalhaes-Paniago R, Pimenta MA. General equation for the determination of the crystallite size L_a of nanographite by Raman spectroscopy. *Appl. Phys. Lett.* 2006;88(16):163106.

198. Klug H, Alexander L. "X-Ray Diffraction Procedures," Wiley and Sons, New York, 1974:618-677.

199. Langford JI, Wilson A. Scherrer after sixty years: A survey and some new results in the determination of crystallite size. *J. Appl. Crystallogr.* 1978; 11(2):102-113.

200. Cullity B. "Elements of X-ray Diffraction, *2nd edn.,"* Addision-Wesley, Reading, 1978.

201. Raman S, Katz JL. Handbook of X-Rays, ed. Kaelble EF. New York, McGraw-Hill, 1967.

202. Smith BC, Fundamentals of Fourier Transform Infrared Spectroscopy. Second Ed. Boca Raton, FL, CRC Press, 2011:33487-2742

203. Hanna R. Infrared properties of magnesium oxide. *J. Am. Ceram. Soc.* 1965;48(7):376-380.

204. Chelliah M, Rayappan JBB, Krishnan UM. Synthesis and characterization of cerium oxide nanoparticles by hydroxide mediated approach. *J. Appl. Sci.* 2012;12(16):1734.

205. Lucchesi PJ, Glasson WA. Infrared investigation of bound water in hydrates. *J. Am. Chem. Soc.* 1956;78(7):1347-1348.

206. Kidchob T, Malfatti L, Serra F, Falcaro P, Enzo S, Innocenzi P. Hafnia sol-gel films synthesized from HfCl4: Changes of structure and properties with the firing temperature. *J. Sol-Gel Sci. Technol.* 2007;42(1):89-93.

207. Ansari AA, Solanki PR, Malhotra B. Hydrogen peroxide sensor based on horseradish peroxidase immobilized nanostructured cerium oxide film. *J. Biotechnol.* 2009;142(2):179-184.

208. Kiefer J. Recent advances in the characterization of gaseous and liquid fuels by vibrational spectroscopy. *Energies.* 2015;8(4):3165-3197.

209. Mandair GS, Morris MD. Contributions of Raman spectroscopy to the understanding of bone strength. *Bonekey Rep.* 2015;7(4):620.

210. Zhou B, Shi H, Zhang XD, Su Q, Jiang ZY. The simulated vibrational spectra of HfO_2 polymorphs. *J. Phys. D: Applied Physics.* 2014;47(11):115502.

211. Balakrishnan G, Murugesan RC, Ghosh C, Ramachandran D, Mohandas E, Song J, Bae SI, Kim TG. X-ray diffraction, Raman and photoluminescence studies of nanocrystalline cerium oxide thin films. *Ceram. Int.* 2013;39(7):8327-8333.

212. McBride JR, Hass KC, Poindexter BD, Weber WH. Raman and x-ray studies of $Ce_{1-x}RE_xO_{2-y}$ where RE = La, Pr, Nd, Eu, Gd, and Tb. *J. Appl. Phys.* 1994;76(4):2435-2441.

213. Lin KL. Phase identification using series of selected area diffraction patterns and energy dispersive spectrometry within TEM. *Microsc. Res. Technol.* 2014;2(04):57.

214. Tian J, Wang D, Shan Z. Improved electrochemical performances of $LiSn_2(PO_4)_3$ anode material for lithium-ion battery prepared by solid-state method. *J. Power Sources.* 2017;361:96-104.

215. West AR. "Solid state chemistry and its applications," John Wiley and Sons, 2014.

216. Choudhary C, Maiti H, Subbarao E. "Defect structure and transport properties, in Solid Electrolytes and Their Applications," Springer, 1980:1-80.

217. Ma B, Balachandran U, Park JH, Segre C. Electrical Transport Properties and Defect Structure of $SrFeCo_{0.5}O_x$. *J. Electrochem. Soc.* 1996;143(5):1736-1744.

218. Huggins RA. Simple method to determine electronic and ionic components of the conductivity in mixed conductors a review. *Ionics*. 2002;8(3-4):300-313.

219. MacDonald JR. Impedence Spectroscopy. In: Emphasising Solid Materials and Systems. Wiley-Interscience, John Wiley and Sons: New York. 1987:1-346.

220. Chowdari BVR, Gopalakrishnan R. Impedance and modulus spectroscopy of vitreous AgI-Ag_2O-P_2O_5 system. *Solid State Ionics*. 1986;18:483-487.

221. Zhou DF, Xia YJ, Zhu JX, Meng J. Preparation and electrical properties of new oxide ion conductors $Ce_{6-x}Dy_xMoO_{15-\delta}$$(0.0\leq x\leq 1.8)$. *Solid State Sci*. 2009;11(9): 1587-1591.

222. Yadav P, Bhatnagar MC. Structural studies of NASICON material of different compositions by sol–gel method. *Ceram. Int*. 2012;38:1731-1735.

223. Bo QB, Sun GX, Meng J. Preparation, structure and oxide ion conductivity in $Ce_{6-x}Y_xMoO_{15-\delta}$$(x=0.1\text{-}1.4)$ solid solutions. *J. Phys. Chem. Solids*. 2006;67(4):732-737.

224. Imanaka N, Okazaki Y, Adachi G. Divalent magnesium ion conducting characteristics in phosphate based solid electrolyte composites. *J. Mater. Chem*. 2000;10(6):1431-1435.

225. Jonscher AK. A new model of dielectric loss in polymers. *Colloid Polym. Sci*. 1975;253:231-250.

226. Ivanov-Schitz AK, Bykov AB. Ionic conductivity of the $NaZr_2(PO_4)_3$ single crystals. *Solid State Ionics*. 1997;100:153-155.

227. Jonscher AK. A new understanding of the dielectric relaxation of solids. *J. Mater. Sci*. 1981;16:2037-2060.

228. Ingram MD. Ionic conductivity in glass. *Phys. Chem. Glasses*. 1987;28:215-234.

229. Mariappan C, Govindaraj G, Roling B. Lithium and potassium ion conduction in $A_3TiB'P_3O_{12}$ (A=Li, K; B′= Zn, Cd) NASICON-type glasses. *Solid State Ionics*. 2005;176:723-729.

230. Govindaraj G, Mariappan C. Synthesis, characterisation and ion dynamic studies of NASICON type glasses. *Solid State Ionics.* 2002;147:49-59.

231. Funke K. Jump relaxation in solid electrolytes. *Prog. Solid St. Chem.* 1993;22:111-195.

232. Afifi MA, El-Nahass MM, Bekheet AE, Zedan IT. Dc and ac electrical conductivity of bulk $CdSe_xTe_{1-x}(0\leqslant x\leqslant 0.4)$. *Phys B-Condensed Matter.* 2007;400:248-251.

233. Prakash T. Influence of temperature on ac conductivity of nanocrystalline $CuAlO_2$. *Int. Nano Lett.* 2012;2:1-3.

234. Mariappan CR, Govindaraj G, Rathan SV, Prakash GV. Preparation, characterisation, ac conductivity and permittivity studies on vitreous $M_4AlCdP_3O_{12}$(M= Li, Na, K) system. *Mater. Sci. Eng. B.* 2005;121:2-8.

235. Jonscher AK. The 'Universal' Dielectric Response. *Nature.* 1977;267:673-679.

236. Teo LP, Buraidah MH, Nor AFM, Majid SR. Conductivity and dielectric studies of Li_2SnO_3. *Ionics.* 2012;18(7):655-665.

237. Vijayakumar M, Hirankumar G, Sirakumar B, Subramanian S. Influence of B_2O_3 doping on conductivity of $LiTiO_2$ electrode material. *J. Power Sources.* 2003;117(1):143-147.

238. Savitha T, Selvasekarapandian S, Ramya CS, Bhuvaneswari MS, Hirankumar G, Baskaran R, Angelo PC. Structural and ionic transport properties of $Li_2AlZr(PO_4)_3$. *J. Power Sources.* 2006;157(1):533-536.

239. Abo El Ata AM, Attia SM, Meaz TM. *AC* conductivity and dielectric behavior of $CoAl_xFe_{2-x}O_4$. *Solid State Sci.* 2004;6:61-69.

240. Vaidehi N, Akila R, Shukla AK, Jacob KT. Enhanced ionic conduction in dispersed solid electrolyte systems CaF_2-Al_2O_3 and CaF_2-CeO_2. *Mater. Res. Bull.* 1986;21(8):909-916.

241. Zugmann S, Fleischmann M, Amereller M, Gschwind RM, Wiemhofer HD, Gores HJ. Measurement of transference numbers for lithium ion electrolytes via four different methods, a comparative study. *Electrochim. Acta.* 2011;56(11):3926-3933.

242. Wang S, Kobayashi T, Dokiya M, Hashimoto T. Electrical and ionic conductivity of Gd-doped Ceria. *J. Electrochem. Soc.* 2000;147(10):3606-3609.

243. Moser Z, Fitzner K. The use of experimental thermodynamic data in the phase equilibria verification. *Thermochim. Acta.* 1999;332(1):1-19.

244. Peters H, Möbius H. Electrochemical investigation of equilibria $CO + 0.5O_2 = CO_2$ and $C + CO_2 = 2CO$. *Z physik Chem [Leipzig].* 1958;209:298-309.

245. Peters H, Mann G. Electrochemical Study of Balance $Fe + CO_2 \rightleftarrows FeO + CO$. *Reports of Physical Chemistry of Bunsengesellschaft.* 1959;63(2):244-248.

246. Kubaschewski O, Alcock CB, Spencer PJ. Materials Thermochemistry. 6th ed. Oxford, England, Pergamon Press, 1993.

247. Stull DR, Prophet H. JANAF thermochemical tables. National Standard Reference Data System, 1971.

248. Barin I, Platzki G. Thermochemical data of pure substances. Vol. 304. Wiley Online Library, 1989.

249. Barin I, Knacke O, Kubaschewski O. Thermochemical properties of inorganic substances: *Supplement*. Springer Science and Business Media, 2013.

250. Aghdam GRK, Soltanieh M. Study of the thermodynamic properties of the Al-Mg binary system between 973-1073 K by the emf method. *Can. Metall. Quart.* 2010;49:39-45.

251. Burnaeva AA, Volkov Yu. F, Kryukova AI. Analysis of crystallochemical features of double phosphates of plutonium (3) with sodium cation and of some other phosphates of f-elements. *Radiokhimiya.* 1994;36(4):289-294.

252. Burnaeva AA, Volkov Yu. F, Kryukova AI. Crystal-chemical features of sodium-Pu (III) double phosphates and certain other f-element phosphates. *Radiochemistry.* 1995;36(4):289-294.

253. Fray DJ. Possible Uses of Sensors in the Aluminum Foundry Industry. Foundry Processes: Their Chemistry and Physics, in: Katz S, Landefeld CF (eds)., 1988, Springer, Boston, MA, 243-255.

254. Ikeda S, Kanbayashi Y, Nomura K, Kasai A, Ito K. Solid electrolytes with multivalent cation conduction (2) zinc ion conduction in Zn-Zr-PO_4 system. *Solid State Ionics.* 1990;40:79-82.

255. Murugan R, Thangadurai V, Weppner W. Fast lithium ion conduction in garnet-type $Li_7La_3Zr_2O_{12}$. *Angew. Chem. Int. Ed.* 2007;46(41):7778-7781.

256. Minami T, Hayashi A, Tatsumisago M. Recent progress of glass and glass-ceramics as solid electrolytes for lithium secondary batteries. *Solid State Ionics.* 2006;177(26-32):2715-2720.

257. Hayashi A, Sakuda A, Tatsumisago M. Development of sulfide solid electrolytes and interface formation processes for bulk-type all-solid-state Li and Na batteries. *Front. Energy Res.* 2016;4(25):1-13.

258. Inaguma Y, Liquan C, Itoh M, Nakamura T. High ionic conductivity in lithium lanthanum titanate. *Solid State Commun.* 1993;86(10):689-693.

259. Aono H, Sugimoto E, Sadaoka Y, Imanaka N. Ionic conductivity of solid electrolytes based on lithium titanium phosphate. *J. Electrochem. Soc.* 1990;137(4):1023-1027.

260. Bates JB, Dudney NJ, Gruzalski GR, Zuhr RA. Electrical properties of amorphous lithium electrolyte thin films. *Solid State Ionics.* 1992;53:647-654.

261. Wang B, Bates JB, Hart FX, Sales BC. Characterization of thin-film rechargeable lithium batteries with lithium cobalt oxide cathodes. *J. Electrochem. Soc.* 1996;143(10):3203-3213.

262. Ohtsuka H, Yamaki J. Electrical characteristics of Li_2O-V_2O_5-SiO_2 thin films. *Solid State Ionics.* 1989;35(3-4):201-206.

263. Tarascon JM, Armand M. Issues and challenges facing rechargeable lithium batteries, in Materials for Sustainable Energy: A collection of peer-reviewed research and review articles from Nature Publishing Group. World Scientific. 2011:171-179.

264. Pacala S, Socolow R. Stabilization wedges: solving the climate problem for the next 50 years with current technologies. *Science.* 2004;305(5686):968-972.

265. Kawamura J, Morota K, Kuwata N, Nakamura Y, Maekawa H, Hattori T, Inamaka N, Okazaki Y, Adachi GY. High temperature 31P NMR study on Mg^{2+}-ion conductors. *Solid State Commun.* 2001;120(7-8):295-298.

266. Vikström H, Davidsson S, Höök M. Lithium availability and future production outlooks. *Appl. Energy.* 2013;110:252-266.

267. Canepa P, Bo SH, Gautam GS, Key B, Richards WD, Shi T, Tian Y, Wang Y, Li J, Ceder G. High magnesium mobility in ternary spinel chalcogenides. *Nat. Commun.* 2017;8(1):1759.

268. Levi E, Gofer Y, Aurbach D. On the way to rechargeable Mg batteries: the challenge of new cathode materials. *Chem. Mater.* 2009;22(3):860-868.

269. Huie MM, Bock DC, Takeuchi ES, Marschilok AC, Takeuchi KJ. Cathode materials for magnesium and magnesium-ion based batteries. *Coord. Chem. Rev*. 2015;287:15-27.

270. Kundu D, Adams BD, Duffort V, Vajargah SH, Nazar LF. A high-capacity and long-life aqueous rechargeable zinc battery using a metal oxide intercalation cathode. *Nat. Energy.* 2016;1(10):16119.

Appendix

A-1

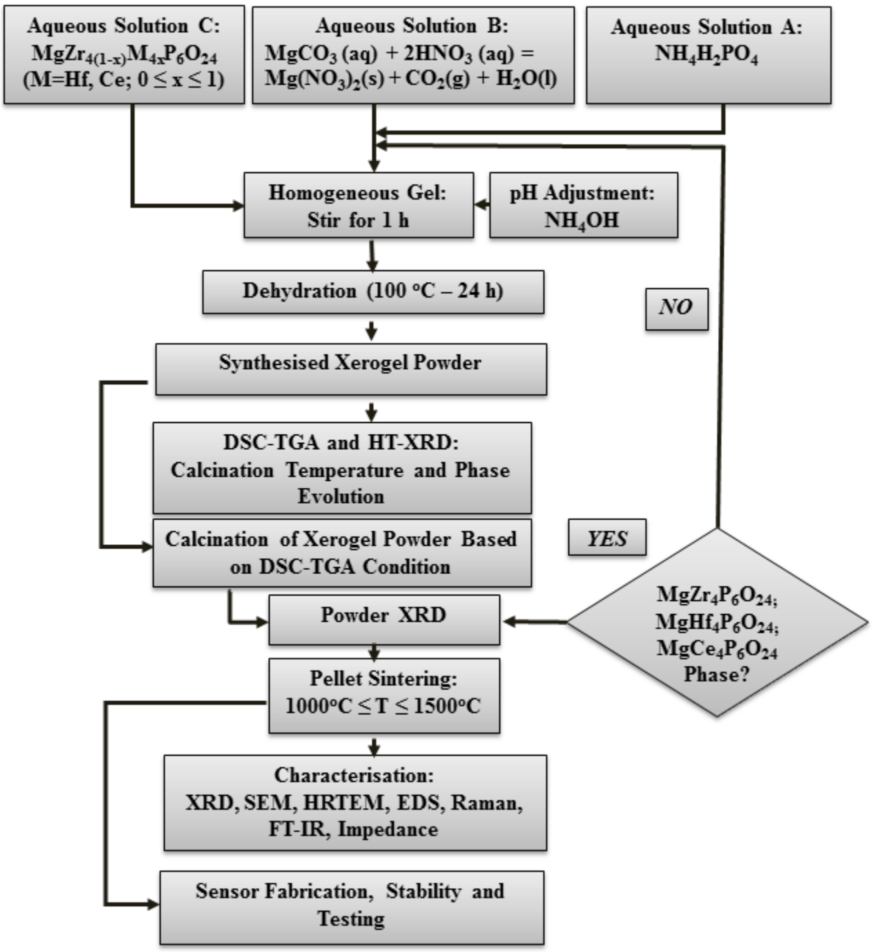

Figure A-1 Flowchart showing sol-gel synthesis procedure

A-2

Table T-1 Atomic coordinates, occupancies of the q positions, and displacement parameters of U_{iso}/U_e*100 in $MgZr_4P_6O_{24}$ structures.

Atom	x	y	z	U_{iso}/U_e*100	q
Mg	0.1616	0.2183	0.7182	12.21	0.6902
Zr(1)	0.1153	0.0293	0.2530	2.52	1.0000
Zr(2)	0.3882	0.0290	0.7466	1.50	1.0000
P(1)	0.4864	0.2846	0.4500	4.92	0.6292
P(2)	0.1481	0.3731	0.3848	5.96	0.7925
P(3)	0.3537	0.3838	0.8720	9.89	0.7905
O(1)	0.5570	0.2953	0.5872	14.61	1.0000
O(2)	0.5768	0.1783	0.3516	4.13	1.0000
O(3)	0.3875	0.3820	0.2995	6.65	1.0000
O(4)	0.4796	0.1333	0.5788	12.41	1.0000
O(5)	0.1918	0.2035	0.3488	7.25	1.0000
O(6)	0.0395	0.4268	0.3542	11.86	1.0000
O(7)	0.1379	0.4241	0.5780	13.63	1.0000
O(8)	0.2024	0.4983	0.2618	9.43	1.0000
O(9)	0.3311	0.2305	0.8198	12.85	1.0000
O(10)	0.3746	0.3586	0.0556	5.56	1.0000
O(11)	0.4529	0.4608	0.8191	2.71	1.0000
O(12)	0.2526	0.5475	0.8331	9.05	1.0000

A-3

Table T-2 Atomic coordinates, occupancies of the q positions, and displacement parameters of U_{iso}/U_e*100 in $MgHf_4P_6O_{24}$ structures.

Atom	x	y	z	U_{iso}/U_e*100	q
Mg	0.1620	0.2266	0.7224	8.78	0.79(4)
Hf(1)	0.1180	0.0281	0.2504	2.60	0.9612
Hf(2)	0.3910	0.0320	0.7443	2.88	0.9549
P(1)	0.4919	0.2603	0.4526	0.76	0.8656
P(2)	0.1456	0.3816	0.3869	2.39	0.9414
P(3)	0.3480	0.3762	0.8773	4.02	0.9942
O(1)	0.5430	0.3126	0.5406	7.46	1.0000
O(2)	0.5792	0.1799	0.3554	2.15	1.0000
O(3)	0.4032	0.3792	0.3060	6.24	1.0000
O(4)	0.4509	0.1506	0.5747	6.33	1.0000
O(5)	0.1651	0.2112	0.3573	5.49	1.0000
O(6)	0.0407	0.4336	0.3423	5.36	1.0000
O(7)	0.1346	0.4187	0.5593	12.37	1.0000
O(8)	0.2239	0.4908	0.2998	2.04	1.0000
O(9)	0.3508	0.2400	0.8038	5.35	1.0000
O(10)	0.3596	0.3608	0.0515	1.45	1.0000
O(11)	0.4572	0.4522	0.8172	3.17	1.0000
O(12)	0.2664	0.5508	0.8365	6.58	1.0000

A-4

Table T-3 Atomic coordinates, occupancies of the q positions, and displacement parameters of U_{iso}/U_e*100 in $MgCe_4P_6O_{24}$ structures.

Atom	x	y	z	U_{iso}/U_e*100	q
Ce	0.2174(4)	0.1598(5)	0.4000(5)	1.31	0.6886
Mg	0.2174(4)	0.1598(5)	0.4000(5)	1.31	0.1614
P	0.1954(17)	0.1629(16)	0.8867(17)	2.92	0.8616
O(1)	0.2291(34)	0.5014(29)	0.4339(36)	3.13	0.8887
O(2)	0.0251(28)	0.1057(26)	0.6832(28)	1.36	0.8206
O(3)	0.3858(34)	0.2059(34)	0.7970(34)	4.73	0.8198
O(4)	0.1124(23)	0.3359(31)	-0.0053(28)	0.54	0.8781

A-5

The TEM micrographs illustrated in Figure A2(a-b) represent $MgZr_4P_6O_{24}$ solid-state electrolyte calcined at 900°C for 3h. The TEM micrographs presented in Figure A2(a) shows fine nanoparticles which is believed to be amorphous in nature whereas, Figure A2(b) however shows that the large particles are identified as having clear crystalline nanoparticles. The amorphous and crystallite nanoparticles both identified in the same solid-state electrolyte calcined at the same temperature, having the same composition and crystal structure demonstrates a non-stoichiometric reaction during the chemical synthesis of $MgZr_4P_6O_{24}$ solid-state electrolyte, this observation agrees with the EDS-elemental analysis which shows a slight concentration in the amount of percent atomic fraction in the electrolyte. Furthermore, from the corresponding SAED, crystallite size of the amorphous and crystalline nanoparticles were measured and observed, ranging as < 20nm and >100nm, respectively.

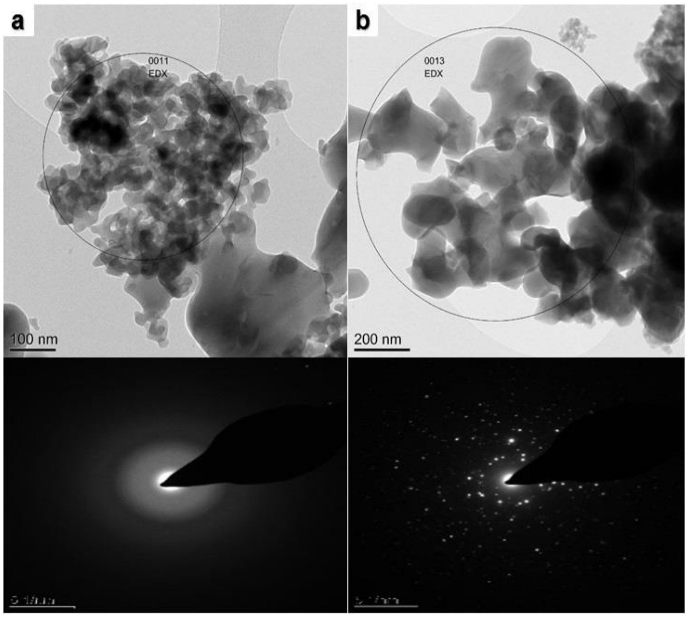

Figure A-2 TEM images of sol-gel synthesised $MgZr_4P_6O_{24}$ nanopowders calcined at 900°C for 3h with corresponding SAED showing (a) amorphous (b) crystalline nanoparticles of $MgZr_4P_6O_{24}$ solid-state electrolyte

A-6

The images shown in Figure A3 suggests that the nanoparticles of $MgHf_4P_6O_{24}$ sample has partially sintered together at temperature as low as 900°C.

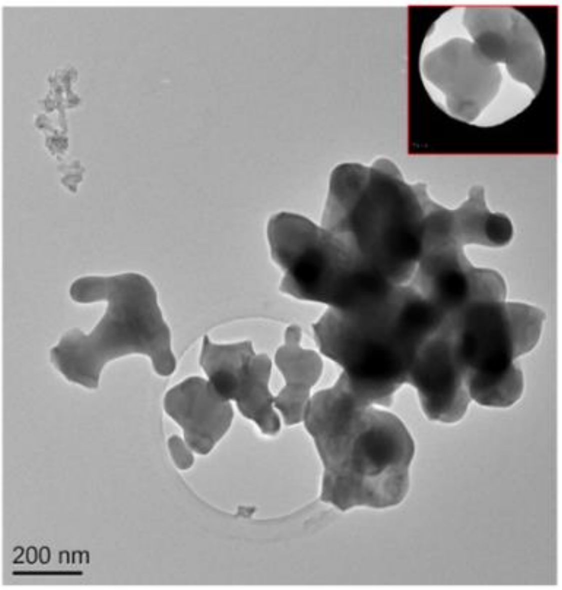

Figure A-3 TEM images of $MgHf_4P_6O_{24}$ nanoparticles calcined at 900°C for 3h

HR-TEM and SAED techniques were used to investigate the particle morphologies of $MgHf_4P_6O_{24}$ nanoparticles. The crystallographic planes of $MgHf_4P_6O_{24}$ could be identified in the HR-TEM images shown in Figure A4(a-b). The crystal lattice fringes, corresponding to the 0.3494nm atomic spacing, are characteristic of a monoclinic $MgHf_4P_6O_{24}$ sample. The SAED pattern in Figure A4(b) can be indexed to the (100) zone axis of monoclinic $MgHf_4P_6O_{24}$, indicating that the sample is a single phase. The d-spacing values obtained from SAED pattern in Figure A4(b) have been compared with HT-XRD and powder XRD data in Figure 4.3(b) and Figure 4.4(b), respectively, and are found to be in excellent agreement.

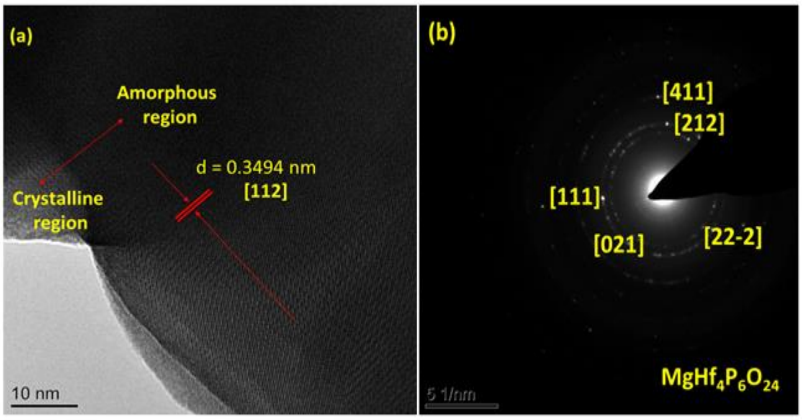

Figure A-4(a-b) HR-TEM profiles and SAED pattern of $MgHf_4P_6O_{24}$ nanopowders calcined at 900°C

Figure A5 depict the elemental maps of $MgHf_4P_6O_{24}$ nanoparticles. The spectra in Figure A5 illustrates a well-defined spatial distribution of the Mg, Hf, P, and O in $MgHf_4P_6O_{24}$ solid-state electrolyte. It further shows that $MgHf_4P_6O_{24}$ appear to be single homogeneous phase as evident from XRD patterns shown in Figure 4.4(b).

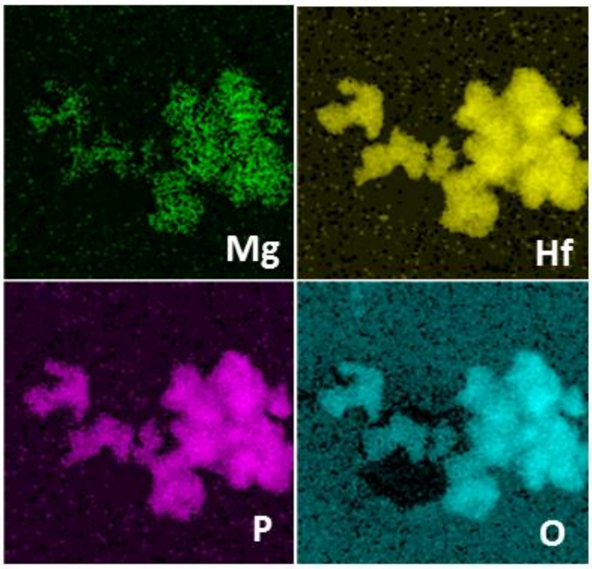

Figure A-5 EDS elemental maps of $MgHf_4P_6O_{24}$ solid-state electrolyte

A-7

The images shown in Figure A6 depicts sintered nanoparticles of $MgCe_4P_6O_{24}$ sample powder at a low calcining temperature of 900°C.

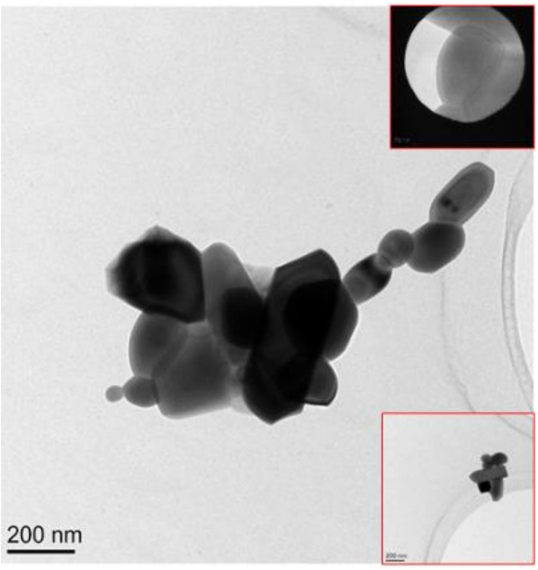

Figure A-6 TEM images of $MgCe_4P_6O_{24}$ nanoparticles calcined at 900°C for 3h

HR-TEM and SAED technique was used to determine the crystallographic planes of $MgCe_4P_6O_{24}$ solid-state electrolyte as shown in Figure A7(a-b). The lattice fringes, corresponding to 0.3108nm atomic spacing, are characteristic of a monoclinic $MgCe_4P_6O_{24}$ sample. The SAED pattern in Figure A7(b) can be indexed to the (100) zone axis of monoclinic $MgCe_4P_6O_{24}$, indicating that the sample nanopowder is a single homogeneous phase. Furthermore, the d-spacing value determined from SAED pattern in Figure A7(b) has been compared with HT-XRD and powder XRD data in Figure 4.3(c) and Figure 4.4(c), respectively, and are in excellent agreement.

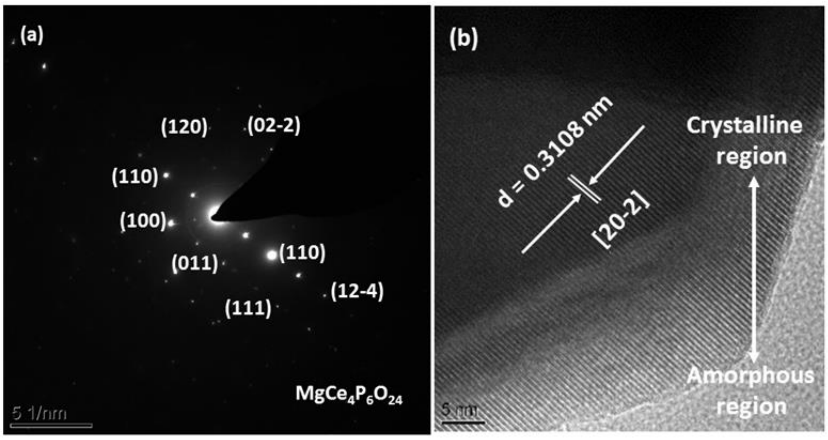

Figure A-7(a-b) HR-TEM profiles and SAED pattern of MgCe$_4$P$_6$O$_{24}$ nanopowders calcined at 900°C

The EDS elemental maps of MgCe$_4$P$_6$O$_{24}$ nanoparticles is presented in Figure A8. The spectra in Figure A8 therefore illustrates a well-defined spatial distribution of the Mg, Ce, P and O component elements in MgCe$_4$P$_6$O$_{24}$ solid-state electrolyte clearly shown in different colouration. Furthermore, it shows the MgCe$_4$P$_6$O$_{24}$ solid-state electrolyte as a single pure homogeneous phase as evident from the HT-XRD and powder XRD profiles presented in Figure 4.3(c) and Figure 4.4(c), respectively.

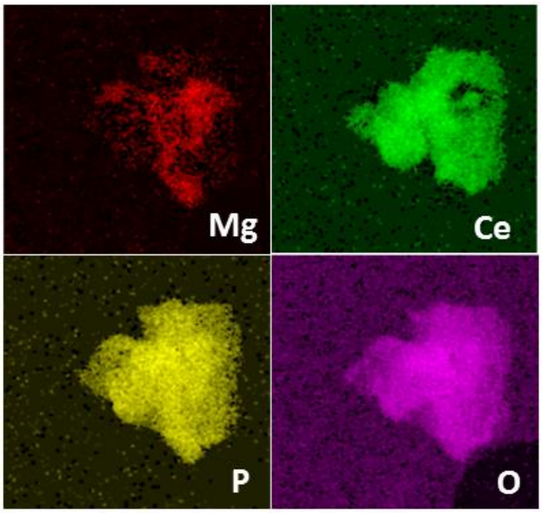

Figure A-8 EDS elemental maps of MgCe$_4$P$_6$O$_{24}$ solid-state electrolyte

A-8

Sensor Testing

Al-Mg-20.30 wt.% Si

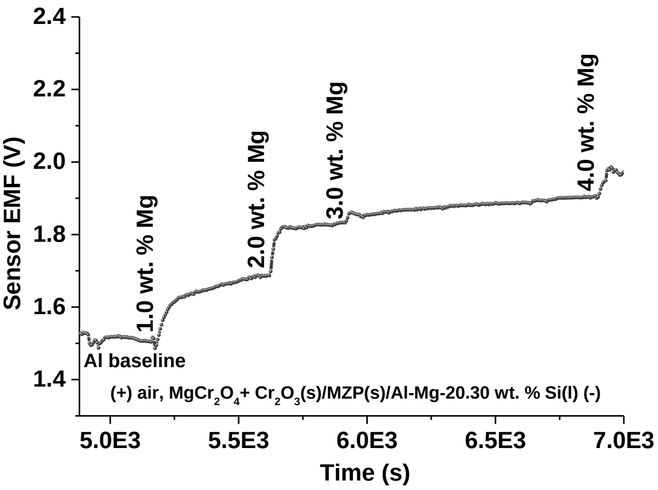

Figure A-9(a) Response of solid-state Mg-sensor with time, using $MgZr_4P_6O_{24}$ solid-state electrolyte and $MgCr_2O_4$+Cr_2O_3 reference electrode for Mg-sensor sensing Mg in molten Mg-Al-20.30 wt.% Si

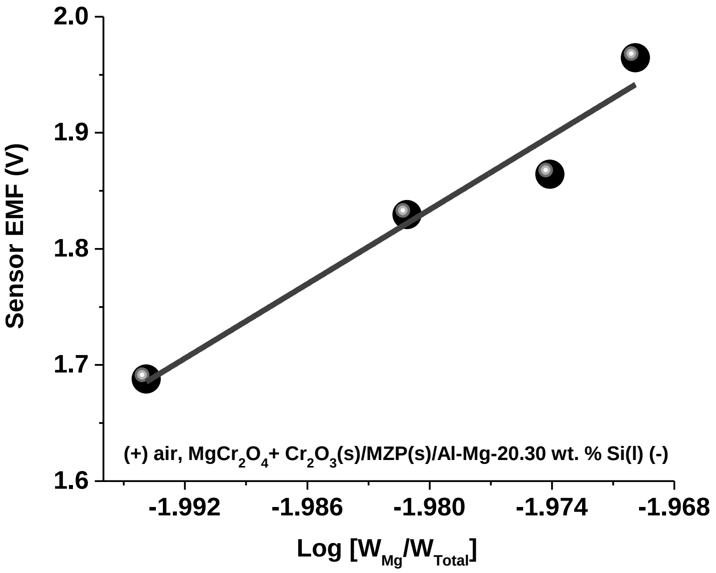

Figure A-9(b) Sensor EMF variation of the solid-state Mg-sensor as a function of Mg concentration in molten Al + 20.30 wt.% Si alloy at 700±5°C, using $MgZr_4P_6O_{24}$ solid-state electrolyte and $MgCr_2O_4$+Cr_2O_3 reference electrode

A-9

Nominal data:

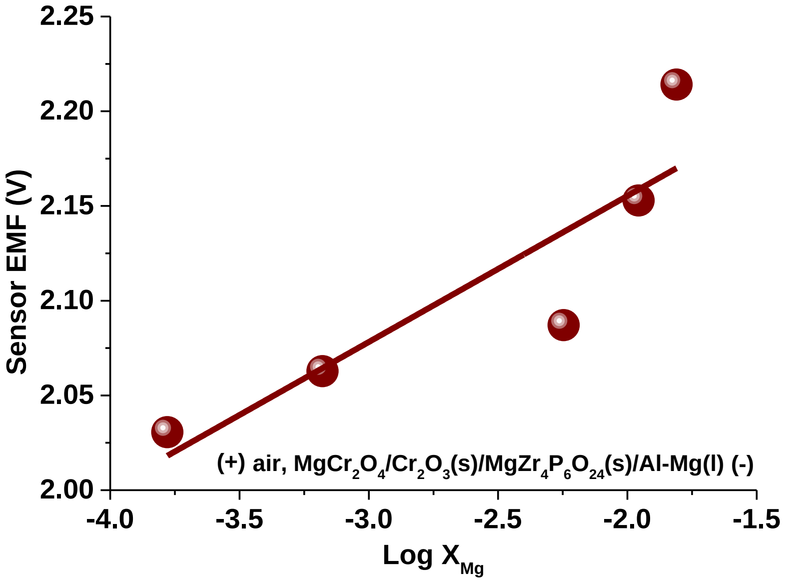

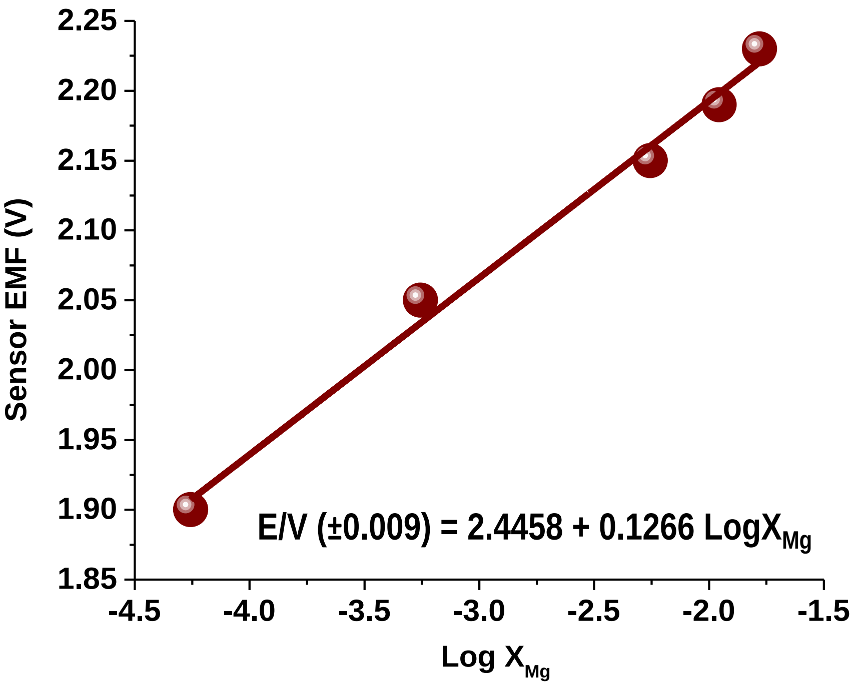

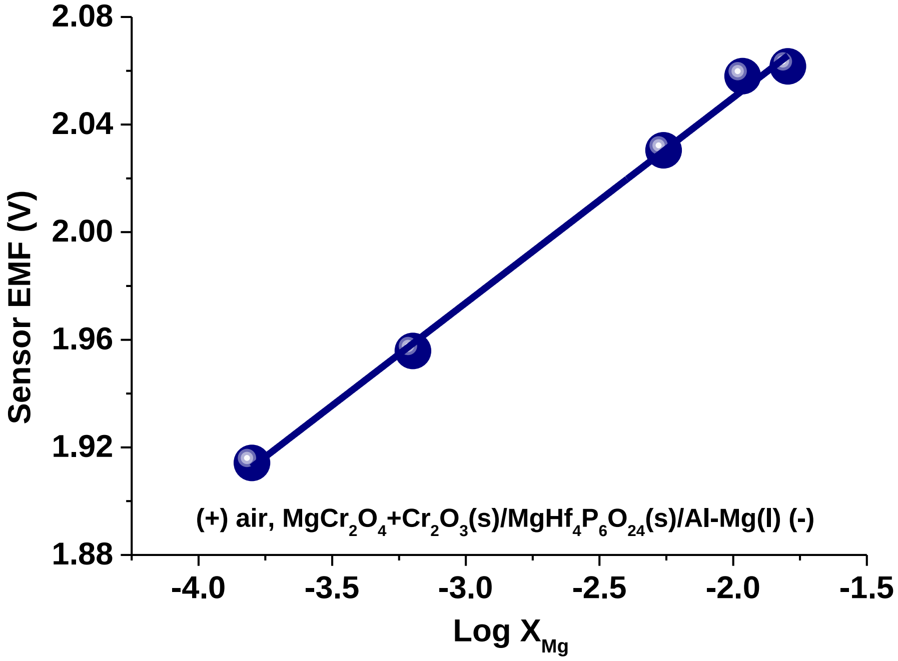
2.08
2.04
2.00
1.96
1.92
1.88
Sensor EMF (V)
(+) air, $MgCr_2O_4+Cr_2O_3(s)/MgHf_4P_6O_{24}(s)/Al-Mg(l)$ (-)
-4.0
-3.5
-3.0
-2.5
-2.0
-1.5
Log X_{Mg}

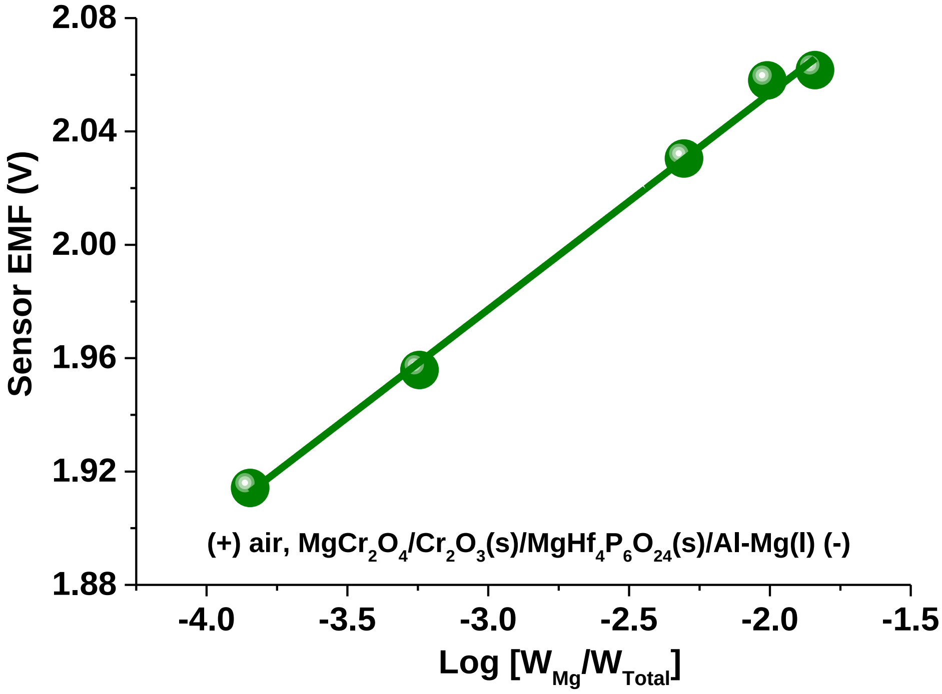
2.08
2.04
2.00
1.96
1.92
1.88
Sensor EMF (V)
(+) air, $MgCr_2O_4/Cr_2O_3(s)/MgHf_4P_6O_{24}(s)/Al-Mg(l)$ (-)
-4.0
-3.5
-3.0
-2.5
-2.0
-1.5
Log $[W_{Mg}/W_{Total}]$

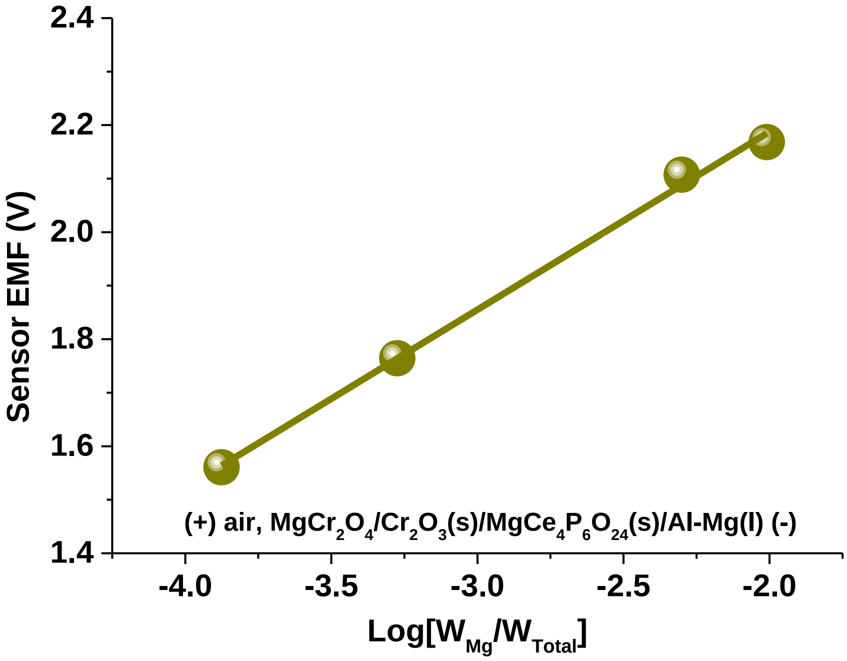

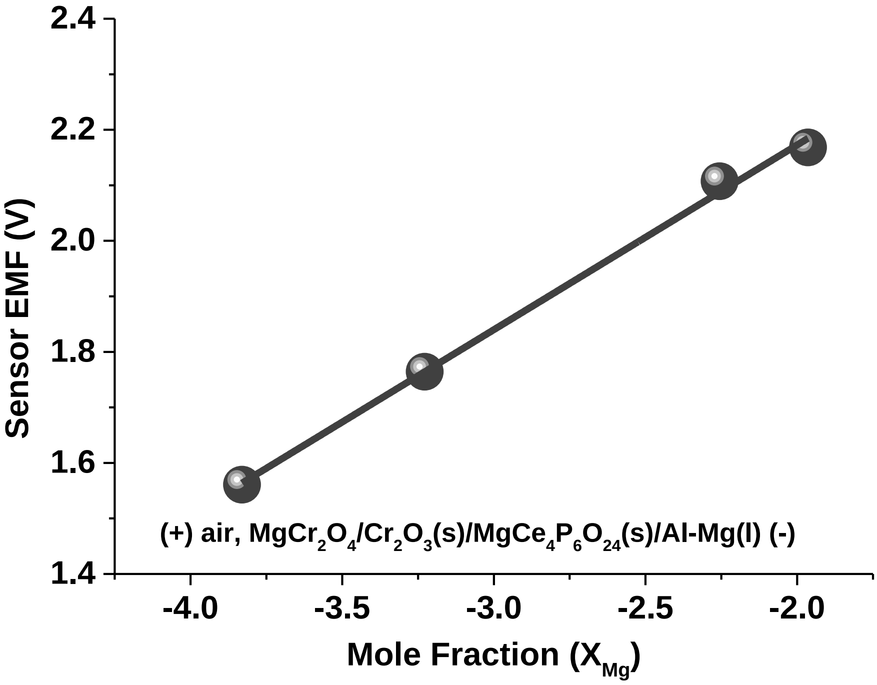

Figure A-10 Sensor EMF variations of the three solid-state Mg-sensors as a function of Mg concentration in molten Al at 700±5°C, using MZP, MHfP and MCeP solid-state electrolytes and biphasic powder mixture of $MgCr_2O_4$+Cr_2O_3 reference electrode for trial different measurements